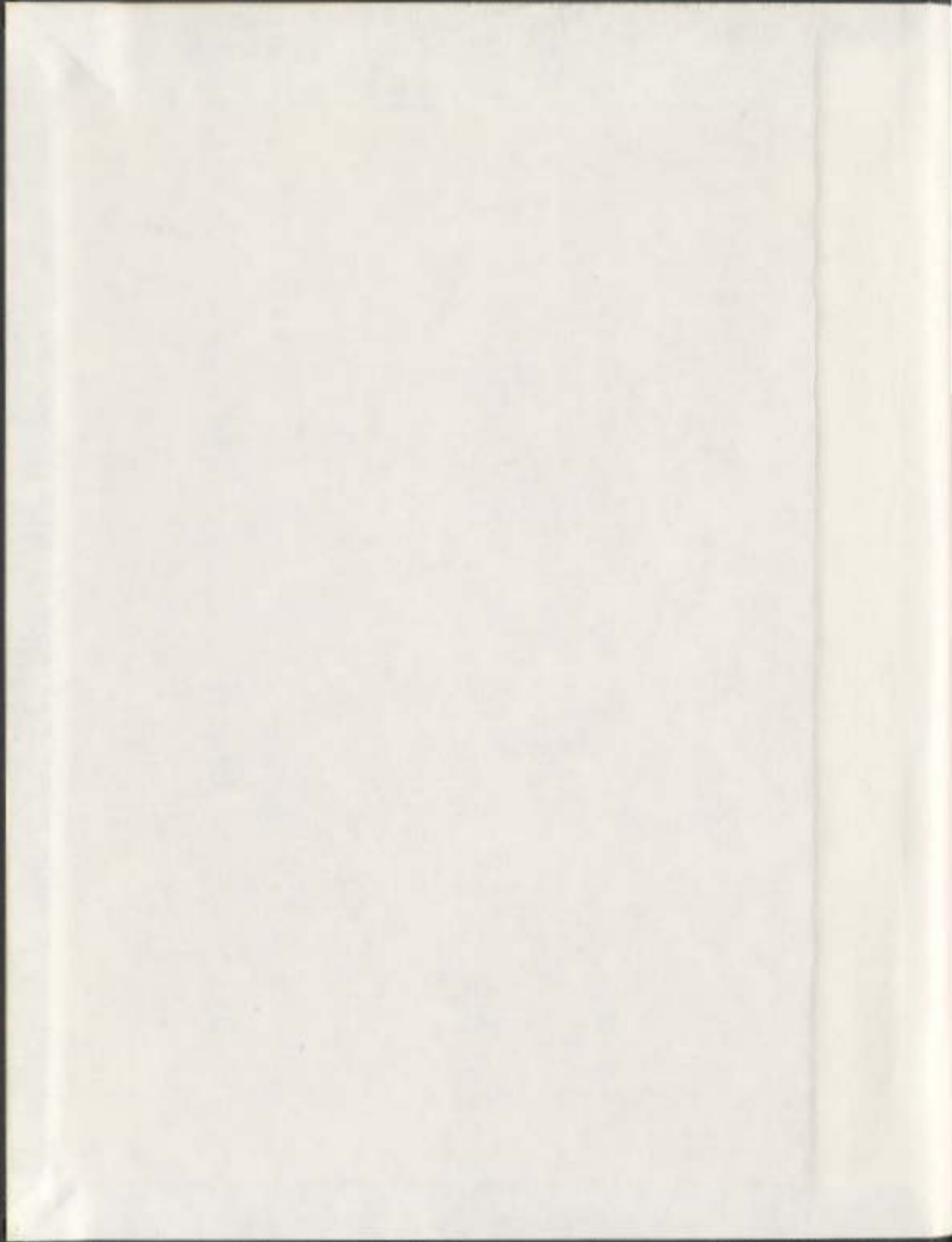# PREDICTION OF PROPELLER PERFORMANCE ON A
MODEL PODDED PROPULSOR IN ICE
(PROPELLER-ICE INTERACTION)

JUNGYONG WANG

PREDICTION OF PROPELLER PERFORMANCE ON A MODEL PODDED PROPULSOR IN ICE (PROPELLER-ICE INTERACTION)

by

© Jungyong Wang, B. Sc., M. Sc.

A thesis submitted to the School of Graduate Studies

In partial fulfillment of the requirements for the degree of

Doctor of Philosophy

Faculty of Engineering and Applied Science

Memorial University of Newfoundland

April 2007

St. John's   Newfoundland   Canada

In compliance with the Canadian Privacy Act some supporting forms may have been removed from this thesis.

Conformément à la loi canadienne sur la protection de la vie privée, quelques formulaires secondaires ont été enlevés de cette thèse.

While these forms may be included in the document page count, their removal does not represent any loss of content from the thesis.

Bien que ces formulaires aient inclus dans la pagination, il n'y aura aucun contenu manquant.

Canada

Abstract

With the increase in popularity of podded propulsors and arctic navigation, understanding the interaction between a podded propulsor and ice has become more important. Propeller-ice interaction itself is a complicated process resulting from the variations associated with the properties of the ice and with the propeller-ice interaction conditions. Model tests provide relatively well-controlled ice properties and interaction conditions to reduce these variations.

The objective of this work is to understand propeller-ice interaction phenomena and develop a numerical method to predict the interaction ice loads. A model podded propulsor was tested in an ice tank with scaled model ice. Three six-component dynamometers and six single-axis dynamometers measured the ice loads acting on various positions of the experimental model. In order to achieve the desired numerical simulations, both a Panel method and empirical formulae were used. The Panel method was suitable for predicting the hydrodynamic loads acting on the propeller blades. The empirical formulae for the ice milling loads were also implemented into the Panel method, thus the hydrodynamic loads and ice milling loads were calculated simultaneously. The ice milling loads model takes into account geometric and kinematic considerations.

Numerical results were compared and validated with the experimental results. The numerical model was valid for the first quadrant operating conditions with various azimuthing (yaw) angles. The numerical results showed a good agreement with experimental results. The findings from this work were then presented and discussed.

Acknowledgements

Table of Contents

List of Tables

List of Figures

List of Abbreviations and Symbols

C_S Shadowing coefficient

D Diameter of the propeller

exp, e Exponential

$F(z)$ Cumulative density function

GFX Longitudinal force at global dynamometer

GFY Transverse (side) force at global dynamometer:

GFZ Vertical force at global dynamometer

$J = \dfrac{V}{nD}$ Advance coefficient

$K_{M\_IPLANE} = \dfrac{M_{IPLANE}}{\rho n^2 D^5}$ In plane bending moment coefficient

$K_{M\_OPLANE} = \dfrac{M_{OPLANE}}{\rho n^2 D^5}$ Out of plane bending moment coefficient

$K_{M\_MX} = \dfrac{M_X}{\rho n^2 D^5}$ Blade moment coefficient on X-axis

$K_{M\_MY} = \dfrac{M_Y}{\rho n^2 D^5}$ Blade moment coefficient on Y-axis

$K_{M\_MZ} = \dfrac{M_Z}{\rho n^2 D^5}$ Blade moment coefficient on Z-axis

$K_{Q\_BLADE} = \dfrac{Q_{BLADE}}{\rho n^2 D^5}$ Blade torque coefficient

$K_{Q\_SHAFT} = \dfrac{Q_{SHAFT}}{\rho n^2 D^5}$ Shaft torque coefficient

$$K_{Q\_SPINDLE} = \frac{Q_{SPINDLE}}{\rho n^2 D^5}$$ Blade spindle torque coefficient

$$K_{T\_BLADE} = \frac{T_{BLADE}}{\rho n^2 D^4}$$ Blade thrust coefficient

$$K_{T\_GFY} = \frac{GFY}{\rho n^2 D^4}$$ Unit transverse (side) force coefficient

$$K_{T\_GFZ} = \frac{GFZ}{\rho n^2 D^4}$$ Unit vertical force coefficient

$$K_{T\_SHAFT} = \frac{T_{SHAFT}}{\rho n^2 D^4}$$ Shaft thrust coefficient

$$K_{T\_UNIT} = \frac{GFX}{\rho n^2 D^4}$$ Unit thrust coefficient

M_{IPLANE} In plane bending moment

M_{OPLANE} Out of plane bending moment

M_X Blade moment on X-axis

M_Y Blade moment on Y-axis

M_Z Blade moment on Z-axis

n Rotational speed of propeller in revolutions per second

P Propeller pitch

P_e Probability

Q_{BLADE} Blade torque

Q_{SHAFT} Shaft torque

$Q_{SPINDLE}$ Blade spindle torque

R, r Propeller radius

r	Proportion of hit
R_e	Reynolds number
T_{BLADE}	Blade thrust
T_{SHAFT}	Shaft thrust
V	Carriage speed
V_A	Advance speed
W	Weight factor
Z	Number of blades, Extreme value
α_G	Geometric angle of attack
α_m	Milling angle
β	Angle of advance
β_i	Hydrodynamic pitch angle
η_{O_SHAFT}	Propeller efficiency
ψ	Azimuthing angle
Θ	Angle between normal vector of panel and α_G
ρ	Density of fluid, in which propeller operates
ρ_i	Density of ice, in which propeller contacts
Ω	Rotational speed
μ	Expected number of interaction per unit time
γ	Number of event
σ	Compressive strength

EFC	Empirical factor for crushing
EFS	Empirical factor for shearing
IOT	Institute for Ocean Technology
rpm	Revolution per minute
rps	Revolution per second
RMS	Root mean square
STD	Standard deviation

Chapter 1 Introduction

1.1. Motivation

1.1.1. The Interest in Ice Covered Waters

Ice covered polar oceans occupy about 7 % of the total ocean area on the planet Earth, or an area greater than that of Europe and North America combined. With the rise of energy prices, the demand is growing for the development of new resources of energy, and developers are exploring non-hospitable areas, including polar oceans. In the Arctic Ocean including Russian territories, vast energy resources have been discovered and developed. For example, the development of oil and gas fields has already been started in the Barents Sea and the Sea of Okhotsk around Sakhalin Island, which are ice covered areas in winter. As a result of the prescribed circumstances, ice class vessels are necessary for transportation of these natural resources all year round. Consequently, a large number of ice class vessels are either being constructed or their construction is expected in the near future.

The Northern Sea Route (NSR) development is also a positive component to increase the interest in the Arctic Ocean. In the 1990s, Russia, Japan and several northern European countries composed a joint project, the International Northern Sea Route Programme (INSROP). One of the missions of the INSROP was to evaluate the NSR as a commercial shipping route. It found the NSR to be about 60 % of the distance of a typical southern sea route when the vessels navigate between the Far East and Europe. This translates to enormous potential economic benefits. When the NSR becomes one of the commercial shipping routes, a significant number of ice class vessels for shipping purposes will be expected.

1.1.2. Propeller in Ice

As the number of vessels capable of navigating in ice covered seas increases, further understanding of propeller-ice interaction becomes important. Most decisions regarding scantlings for an ice class propeller are made by the Arctic Shipping Pollution Prevention Regulations (ASPPR), the Finnish-Swedish Ice Class Rules and various classification society rules. Most ice class rules for a propeller were formulated on the basis of a prescribed ice torque depending on the vessel's particular ice class. Propeller failures, however, are still reported. Nowadays, Finite Element Methods are being used to estimate the stress level of the ice class propeller, but they have not been fully developed due to the weakness of the numerical modeling of ice. As well as the scantling of the ice class propeller, the propeller's performance in ice has not been evaluated clearly.

Propeller-ice interaction may cause problems such as noise, vibration, or even severe bending or failure of the propeller blades. During navigating in ice covered waters, a propeller can be stopped due to various reasons: ice ramming, maneuvering (turning or crash stop) or severe ice loads acting on the propeller. If the vessel has a forward or backward speed without any propeller rotation, the propeller may encounter extremely high ice bending loads. This is one of the exceptional cases and the forward or backward bending moment on the blade may exceed the propeller blade strength.

Besides general strength fixed pitch propellers, controllable pitch propellers have been widely used for ice class propellers because ice class vessels need to operate in both open water and ice covered water. Greater pitch of the propeller in open water provides more speed because of its higher efficiency at lightly loaded conditions, and smaller pitch in ice covered water provides more power because a higher efficiency can be obtained at heavily loaded conditions. Ducted propellers have also been frequently installed in ice class vessels. The duct plays a major role in the protection of the propeller from ice. However, ice blocks sometimes get jammed inside the duct and the blockage effect occurs consequently. Highly skewed controllable pitch propellers have also been used as unconventional propellers for several ice class vessels because highly skewed propellers can reduce propeller-induced noise and vibration so that the propeller performance can be improved.

As electric propulsion is developed, podded propulsors have been highlighted for modern propulsion systems. Especially, azimuthing podded propulsors provide excellent

3

maneuverability in ice covered waters as well as in open water. In particular, a Double

Acting Tanker (DAT), which has an optimized bow and stern shapes for open and ice

covered sea respectively, employed the azimuthing podded propulsors. The DAT

navigates ahead direction in open water and in the astern direction during operation in ice

covered water.

1.2. Objectives

Many studies on propeller-ice interaction have been carried out including full-scale

measurements, model tests, and numerical calculations. Ice loads acting on a propeller

blade are the result of complex processes due to the high rate of revolution of the

propeller, the complex flow at the circumference of the propeller, and the random shape

of the ice contacting with the propeller. Insufficient information on ice properties and

interaction conditions increase the variation of data. Conducting model tests provides

more accurate information regarding ice properties and interaction conditions.

The objective of this thesis is to predict the performance of the propeller on a model

podded propulsor in ice covered water. From both experimental and numerical points of

view, a comprehensive examination about propeller-ice interaction has been performed.

The experimental model, a scaled azimuthing podded propulsor, was tested in an ice tank

and ice loads acting on the various parts of the model were measured. The numerical

model for the propeller-ice interaction loads was developed by using geometric and

kinematic considerations. Both hydrodynamic loads and ice related loads were calculated simultaneously and the results were compared with those from experiments.

This study enables us to predict the ice loads on the propeller with various azimuthing angles during propeller-ice interaction (especially ice milling conditions). This study also helps us to understand how propeller interacts with ice at given operating conditions. Although new propulsion technologies including podded propulsors have become more and more widespread in application for Arctic vessels, the regulations for classifying their use have not kept pace. Consequently, this study will help regulating bodies to update their regulations.

1.3. Approach and Methodology

For better understanding of ice loads acting on a propeller, the author hypothesizes that the loads from ice covered water consist of three components: separable hydrodynamic loads, inseparable hydrodynamic loads and ice milling loads. The separable hydrodynamic loads imply the loads from open water conditions. During the interaction between propeller blade and ice, however, as the blade lift may not fully develop when the blade is in the ice or immediately after the blade exits the ice, the separable hydrodynamic loads are only approximated values. The inseparable hydrodynamic loads are mainly generated by a blockage effect, proximity effect, and cavitation due to the presence of ice. The ice milling loads are the contact loads when the blade physically

contacts with ice. The inseparable hydrodynamic loads and ice milling loads combined are called ice related loads and they are defined when the blades are in contact with ice. This classification helps not only to evaluate accurate ice loads on the blade, but also to develop the ice contact model.

Total Loads in ice (Propeller-Ice Interaction loads) = Ice Milling Loads

+ Separable Hydrodynamic Loads + Inseparable Hydrodynamic Loads

Ice Related Loads = Ice Milling Loads + Inseparable Hydrodynamic Loads

1.3.1. Experiments in Ice Tank

The experiments were carried out in the ice tank at the National Research Council Canada's Institute for Ocean Technology. The objective of the experiments was to accurately measure the ice loads acting on the propeller blade and podded propulsor. As an experimental methodology for assessment of ice loads during propeller-ice interaction, steady milling conditions were designed and performed by using pre-sawn ice sheets. Model ice properties including flexural and compressive strength were measured approximately every two hours. The information about forces and moments acting on one of the propeller blades, forward and aft bearings of the propeller drive shaft, and the whole system was provided by three six-component dynamometers and six one-axis dynamometers. Parametric tests were carried out regarding key parameters such as depth

6

of cut, azimuthing angle, carriage speed and propeller rotating speed. The key parameters were found from a dimensional analysis. Most results are presented with non-dimensional force and moment coefficients against advance coefficients.

1.3.2. Numerical Considerations

The objective of the numerical calculations is to provide an appropriate method to estimate the propeller-ice interaction loads. The numerical study takes into account crushing pressure and shearing force due to ice. A mesh of each propeller blade was generated. The crushing pressure and shearing force were calculated at each panel, and summed up for total forces and moments. In order to decide the magnitude of crushing pressure and shearing force, a constant ice reference pressure, which was same as the ice compressive strength measured during experiments, was used with multiplying empirical factors. The present numerical model is able to calculate the ice loads on the propeller at any azimuthing angle (yaw angle) of the podded propulsor in the first quadrant operating condition. The numerical results provided in this thesis are for the limited ice condition (steady ice milling condition in the first quadrant) and do not consider the kinetics of ice (e.g. ice mass and inertia forces). Fracture and cracking of ice are also ignored.

1.3.3. Scope

In Chapter 2, a historical review of podded propellers and a review of ice-propeller interaction are shown. Several existing theoretical models are introduced. In Chapter 3,

the experimental test concepts and procedures are described. In order to compare ice

loads with hydrodynamic loads, open water tests without ice were carried out as well. The

methodology of data analysis is explained and results are shown. In Chapter 4, a

numerical model for propeller-ice interaction is introduced. The detailed procedure for the

model is addressed. In Chapter 5, comparisons between numerical results and

experimental results are made. Finally in Chapter 6, conclusions of the present study are

provided.

Chapter 2 Literature Reviews

The objective of this chapter is to introduce the podded propulsion system and review propeller-ice interaction studies. The characteristics of the podded propulsion system are shown. Full-scale measurements, model tests and theoretical calculations for the propeller-ice interaction loads are reviewed.

2.1. Podded Propulsors

In the middle of the 1980s, an attempt to use a podded propulsion system was performed by ABB Industry of Finland and Kvaerner Masa-Yards Inc. A podded propulsion system consists of three parts: a strut, a pod with electric motor, and one or two propellers. The propeller is on the end of the pod and the pod is connected to the strut. The strut is attached under a vessel. An azimuthing podded system is designed to be able to rotate the whole system through 360 degrees by a gear box within a vessel. In Figure 2-1, a full-scale podded propulsion system which is used in a Russian ice-going tanker (Double

Acting Tanker), *Norilskiy Nickel*, navigating in ice covered water and conceptual sketch

are shown.
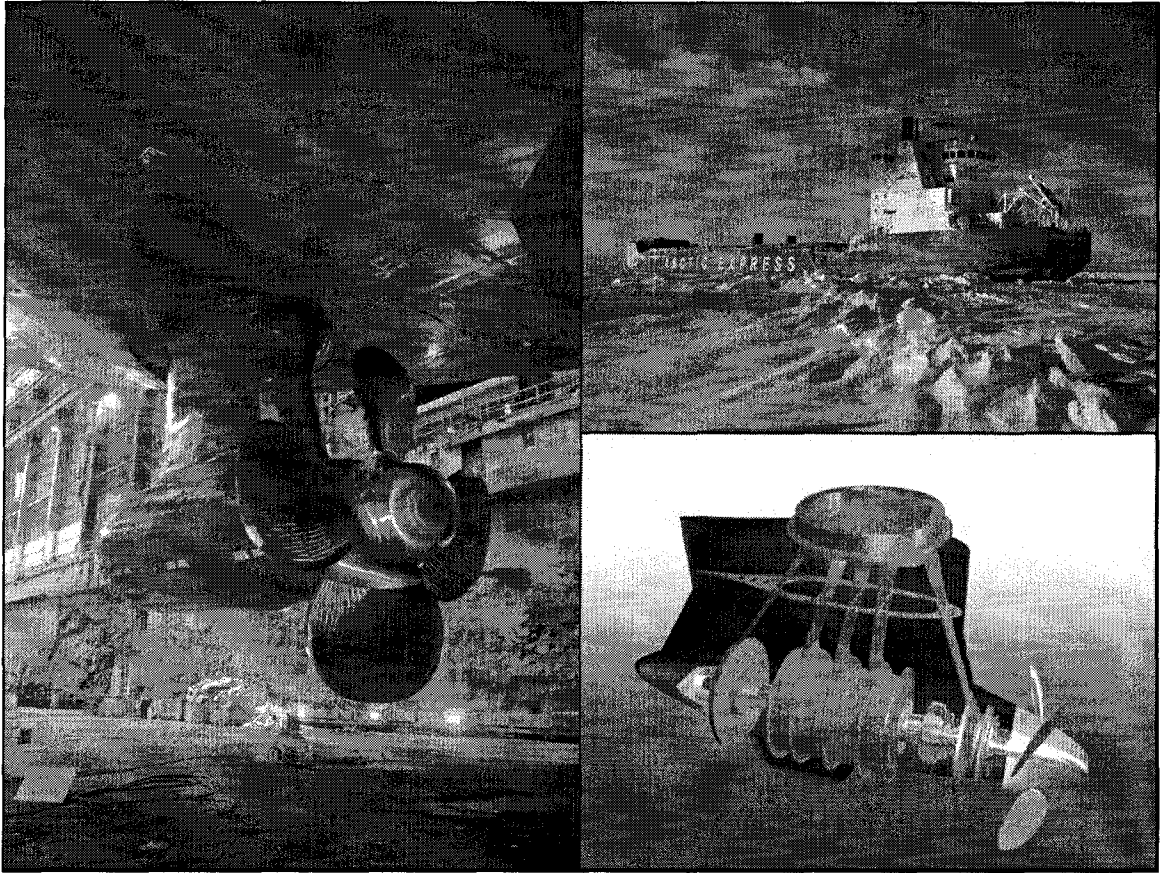
Figure 2-1: Full-scale podded propulsion system, sea trial and conceptual design (after ABB, personal communication)

The azimuthing podded propulsion system is a fully assembled propulsion unit and is also

a steering unit without a general rudder. Inside the pod, there is an electric motor, which

receives power and signals from the ship through the strut. A vessel with a pod system

can be designed with more flexible machinery arrangement within the hull because it may

not need shaft units, rudders and assisting thrusters. The azimuthing podded system

provides outstanding maneuvering capability through the ability to deliver full thrust in any direction. Also, space saving is another benefit. In addition, the pod system provides reduced noise and vibration, because this system would be isolated somewhat from the vessel's hull. Operating costs (fuel, lubricate oil, maintenance and repair costs) of podded system have been compared with those of typical operating system for a chemical tanker. The results showed the reduction of podded system operating costs would be at least 5 % per annum; for maintenance costs, the reduction of podded system could be about 6 - 8 % because the podded system may not need many traditional components such as reduction gear, propeller pitch control system and auxiliary system for main engine. General benefits of azimuthing podded propulsion systems are as follows: high steering ability, low level of noise and vibrations, increased payloads, lower operating cost, and high ice going capability in astern direction (Niini, 1997; Muller, 1999; Kron and Holmstrom, 1999; Van Terwisga, 2001).

In terms of cavitation, full-scale propeller blade cavitation patterns of a podded propeller were observed by Pustoshny and Kaprantsev (2001). They provided photographs and results of the actual observations. They reported that the dominant pattern of cavitation for a podded propeller was a tip vortex while a vessel was accelerating, turning or performing a crash stop. The thickness of the cavitating vortex was significantly increased in proportion to the loading of the propeller. Several model tests for cavitation in ice were reviewed in Section 2.5.1

There are some restrictions regarding speed and power due to the capability and size of

the electric motor and high manufacturing costs. In 2001, the maximum installable power

and speed was 21 MW and 26 Knots, respectively. In the future, it is likely to be

increased to 32 MW and 30 Knots (Mewis, 2001).

One of the commercial pod systems is the Azipod® which was developed by ABB

Industry and Kvaerner Masa-Yards Inc. The Azipod® system is an azimuthing electric

propulsion drive where the propulsion motor is installed inside a submerged azimuthing

(unlimited 360 degrees) pod and coupled directly to an extremely short propeller shaft.

Niini (1995) and Laukia (1996) reported the performance of the Azipod® which was

installed in the product tanker, *M/T Uikku*, in 1993 and tested in ice regions in 1994.

Originally, this tanker had a controllable pitch propeller and rudder. These propulsion

units, main engines, and shafting had been removed and the Azipod® system including

new main propulsion machinery was installed. The reports showed the differences

between the previous propulsion units and the newly installed podded propulsion system.

The turning radius of the Azipod® system in open water was the same with an

azimuthing angle of 30 degrees when the previous controllable pitch propeller and rudder

units had the maximum rudder angle which was 35 degrees. When the azimuthing angle

was equal to 60 degrees, the turning radius was less than the L_{WL} (Length of waterline) of

the tanker.

As introduced in the previous chapter, a podded propulsion system was used for a DAT

(Double Acting Tanker), which was designed to run astern in ice covered water while

maintaining hydrodynamic efficiency for ahead propulsion in open water (Juurmaa et al., 2001; Sasaki et al, 2004). Representative commercial podded propulsion systems for ice-going vessels are Azipod® of ABB, SPP of Siemens-Schottel, Dolphin of STN ATLAS Marine Electronics, and Mermaid™ of Rolls-Royce.

2.2. Full-Scale Measurements for Propeller-Ice Interaction Study

Studies on the interaction between ice and propeller using full-scale measurements have been performed by many researchers (Lewis et al., 1982; Jussila, 1983; Laskow and Revill, 1986; Kannari, 1988; Jussila and Koskinen, 1989; Keinonen et al., 1990; Williams et al., 1992; Cowper, 1992; Cowper et al., 1992). None of these full-scale measurements provided sufficient information to evaluate ice loads acting on a propeller in terms of ice properties, operational and environmental conditions. Full-scale trials are also expensive.

In 1991, in order to establish the magnitude of the loading regime during propeller-ice interaction, with a goal of updating the Canadian Arctic Shipping Pollution Prevention Regulations and the Swedish-Finnish Rules for Baltic Navigation, the governments of Canada and Finland entered into a Joint Research Project Arrangement (JRPA #6). As a part of the JRPA #6, the interaction between ice and propeller was studied from both theoretical and experimental points of view (Keinonen et al., 1990; Jussila and Soininen, 1991; Newbury et al., 1993, 1994; Jones et al., 1997; Browne, 1997; Browne et al., 1998).

13

Browne (1997) reported the results of the re-analyzed propeller-ice interaction data

obtained from the original records of six selected full-scale trials; two of them used open

propellers with a diameter of 4.8 meters and the rest of them were ducted propellers with

various diameters between 3 and 4.5 meters. Browne used shaft torque, positive and

negative shaft thrust, and reported parametric trends on the propeller-ice interaction loads

with regard to the primary parameters, which are propeller rpm (revolution per minute),

propeller pitch angle and ship speed. The reported ice conditions were a mixture of first-

and multi-year ice including ice ridges. The range of ice thicknesses was from 0.6 to 8

meters, and the crushing strength was from 200 kPa to 2300 kPa. Ship speeds were up to

5.5 m/s, and the range of rpm was between 120 and 220. The pitch angles of the

propellers varied from negative 23 degrees to positive 27 degrees.

Generally, full-scale trials did not provide precise information for environmental

conditions and ice interaction conditions. Their conclusions, therefore, showed only

general trends: (1) for both open and ducted propellers, the ice loads increased with the

increase in ice thickness and strength, (2) for open propellers, if forward speeds increased

then the ice loads decreased, (3) for ducted propellers, the ice loads increased with the

increase in pitch angles and the ice thrust increased with the square of propeller diameters.

One year later, Browne et al. (1998) reported results from seven selected full-scale trials

(five trials were same as those from Browne, 1997) considering blade forces, parametric

analysis and long-term prediction. They explained that the differences between blade

loads and shaft loads are due to a shaft dynamic effect. They corrected the shaft loads for

the influence of shaft dynamics by using Duhamel's convolution theorem so that the corrected shaft loads can be compared with their unified load model or other directly measured blade load data. The reported ratios between propeller and shaft were 0.99 ~ 1.7, 0.4 ~ 0.65 and 0.49 ~ 0.63 for the maximum propeller torque over shaft torque, positive propeller thrust over shaft thrust, and negative propeller thrust over shaft thrust, respectively.

Generally for both open and ducted propellers, propeller torque increased with the increase in pitch angles, and the ice loads are most likely directly proportional to ice strength (Browne et al., 1998). For long term predictions, an operating time of 10,000 hours was assumed and three-parameter Weibull distributions were used. From the long term predictions, propeller thrust and torque varied approximately with the square and cube of propeller diameters for the ducted propellers during the propeller interaction with thick ice. The maximum negative and positive propeller thrust for the open propellers were approximately four and two times those of ducted propellers with similar diameters. From their parametric analysis, negative ice loads (negative thrust) were larger than positive ice loads (positive thrust) for open propellers, but positive ice loads (positive thrust) were larger than negative ice loads (negative thrust), for ducted propellers.

The design of ice class propellers was introduced by Bose et al. (1998). The proposed method takes into account four limit states for design loads: (1) non-ice loading, (2) contact and hydrodynamic ice loads, (3) ice loads from full-scale data (from Browne (1997)) and (4) exceptional load limit state. The first three states are combined in an

15

interaction equation but the forth is applied independently. This design method can

provide the position and magnitude of the maximum principal stresses in the blade of

conventional propellers (non-highly skewed propellers) and proposed the interaction

equation for the blade design. One year later, Doucet et al. (1999) reported this design

method for an ice class propeller for *MV IKALUK*. The detailed calculations for the

scantling of the propeller are presented in their report.

2.3. Model Tests in Laboratories for Propeller-Ice Interaction Study

As mentioned in the previous section, the drawback of full-scale measurements is the lack

operational and environmental information. The cost of carrying out full-scale

measurements for propeller-ice interaction is often prohibitive. In order to overcome these

difficulties and to provide controlled conditions, model tests in laboratories have been

designed and performed. Several model tests with both sea ice and artificial refrigerated

ice were carried out (Veitch, 1995; Jones et al., 1997; Tamura et al., 1997; Soininen,

1998; Searle, 1999; Varma, 2000; Mintchev et al., 2001; Moores, 2001; Akinturk et al.,

2003, 2004a, 2004b; Wang et al., 2004, 2005, 2006). Model tests provide more precise

information in terms of ice properties, the interaction conditions, and the data collected

compared with full-scale measurements.

In general, model tests in laboratories for propeller-ice interaction can be classified into two categories: (1) compressive/swing tests with simplified blade-like tools and (2) actual rotating tests with model propellers in ice covered water. Veitch (1995), Jones et al. (1997), Soininen (1998) and Varma (2000) did tests in the first category, and Tamura et al. (1997), Searle (1999), Mintchev et al. (2001), Moores (2001) and the present tests (Akinturk et al.,2003, 2004a, 2004b; Wang et al., 2004, 2005, 2006) did tests in the second category.

Veitch (1995) used a wedge shape indenter to simulate a propeller blade and performed high speed compressive tests which simulated propeller blades in contact with ice. Soininen (1998) used a full-scale blade-like model and carried out swing tests to simulate propeller-ice interaction. Both Veitch (1995) and Soininen (1998) established empirical ice load models from their results. Detailed explanations are given in the next section.

Searle (1999) tested both an R-Class icebreaker propeller and a highly skewed propeller in four quadrants. Model tests were carried out in the IOT ice tank with EG/AD/S model ice. Searle measured the shaft thrust, shaft torque, rps, carriage speed, and ice properties. Sampling rate for the thrust and torque measurements was 5000 Hz. Searle reported that the increase in the depths of cut (penetrated distances of a blade into ice) resulted in an increase in the propeller thrust and torque and the propeller loads due to ice were strongly dependent on the propeller's operating conditions. As the advance coefficient increased, the thrust and torque increased until the advance coefficient was reached at certain values ($J = 0.3 \sim 0.4$) then they started to reduce above this range ($J > 0.4$). From the

17

comparisons of four quadrants tests, quadrants two and three experienced larger ice loads than those in quadrant one. In the quadrants two and three, the propeller blade may experience exceptional out-of-plane bending moments as off-design conditions. The effect of variation of compressive strength did not play a major role in the thrust values (for example, in the first quadrant a 27 % change in compressive strength resulted in a 3 % change in mean thrust values) but the torque values were sensitive to the variation of compressive strength (for example, in the first quadrant a 38 % change in compressive strength resulted in a 32 % change in mean torque values). Searle observed oscillatory ice loads, which varied approximately equal magnitude of maximum and minimum from mean value.

Moores (2001) tested a highly skewed propeller and measured the forces and moments due to ice acting on a propeller blade. Moores did the first successful tests to accurately measure blade loads during ice milling using a dynamometer at the root of one of the blades. The dynamometer was designed to distinguish the blade load in six components. The model tests were carried out with different pitch angles, depths of cut, ice strength, and advance coefficients. As results, Moores presented the maximum thrust and torque on the blade, and in plane and out of plane bending moments were also shown. The general trends from the results are:

1. As the pitch angles decreased, the shaft/blade thrust and torque coefficients decreased;

2. As the depth of cut and ice strength increased, the shaft/blade thrust and torque coefficients increased.

In plane bending moment and out of plane bending moment in ice conditions were approximately 2 to 4 times larger than the open water results. The results from Moores are similar to those from Searle; the thrust and torque values increased at a certain value of advance coefficient ($J = 0.3 \sim 0.4$) then started to decrease. Some of Moores' studies regarding compressive tests with high strain rate are presented in Section 2.5.2.

Both Searle and Moores did their work as master degrees, and some papers of their results have been published in the public domain (Searle et al., 1999, 2001; Moores et al., 2001a, 2001b, 2002).

2.4. Propeller-Ice Interaction Models

In the early 1990s, two literature reviews discussed the work done in the field of interaction between ice and propellers, Jussila and Soininen (1991) and Veitch (1992). These reviews described previous theoretical studies (Jagodkin, 1963; Ignatjev, 1964; Ignatjev, 1966; Wind, 1983; Belyashov and Shpakov, 1983; Kotras et al., 1985; Chernuka et al., 1989).

In the following years, Veitch (1995) and Soininen (1998) developed more precise and elaborate models than existed before. Veitch (1995) considered the dynamics between the ice block and the propeller, and simulated the process of contact based on the model test. Soininen (1998) carried out laboratory tests with a full-scale blade-like tool attached to a

19

pendulum at high speed. Based on these results and failure modes of the ice, a prediction

model was developed. In this chapter, three previous propeller-ice interaction models are

reviewed.

2.4.1. Prediction with the Model of Kotras et al.

Kotras et al. (1985) studied the prediction of ice milling loads from a simple wedge

shaped tool. They considered blade shadowing and four quadrant operating conditions

(Figure 2-2). Blade shadowing is caused by the interference between each blade path. The

blade shadowing is when the propeller blade interacts with part of the path generated by

the previous blades. Consequently, the consecutive blade does not fully contact with ice.
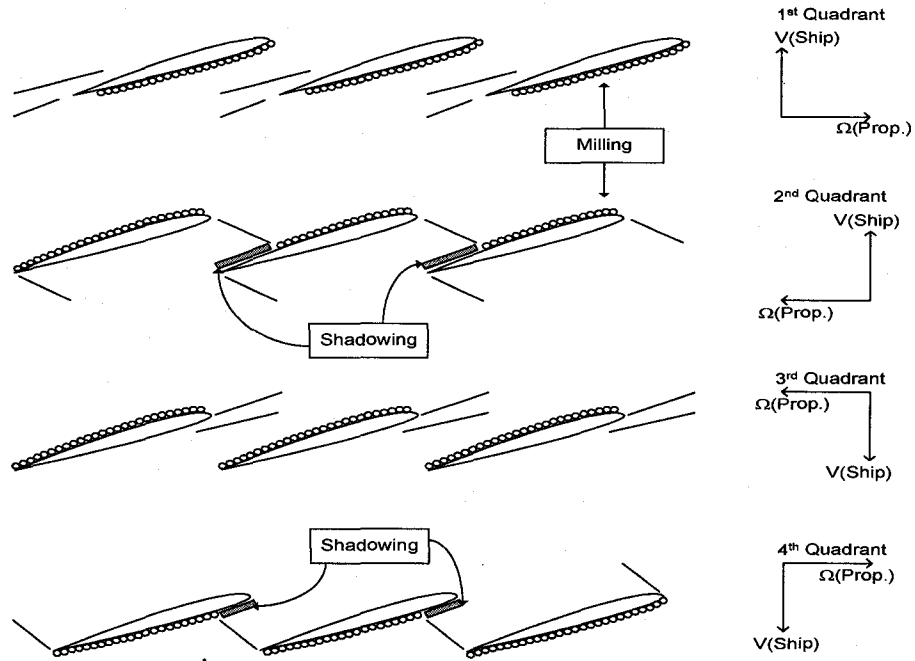
Figure 2-2: Four quadrants operating condition and blade shadowing phenomena (after Kotras et al., 1985)

In order to calculate the intersection (x, y) between ice and tool, Equation (2-1) is used,

when the propeller contacts with continuous ice (Figure 2-3):

$$x = \frac{h_s - y_1}{y_2 - y_1}(x_2 - x_1) + x_1$$
$$y = h_s$$

(2-1)

where h_s is the depth of the blade shadowing.
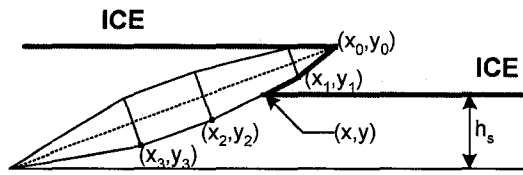
Figure 2-3: Intersection shape of the propeller blade (after Kotras et al., 1985)

The forces on each blade section are evaluated by volumetric crushing consideration
(Figure 2-4). The volume of the ice, V_o is a function of θ, L, Δt and Δx. Work done on
the deformation of the volume by crushing is equal to $\sigma_c V_o$, where σ_c is the crushing
stress of the ice. In other words, the work, W, done on the blade section consists of
normal forces and tangential forces:

$$W = (N \sin \theta + T \cos \theta) \Delta x .$$
(2-2)
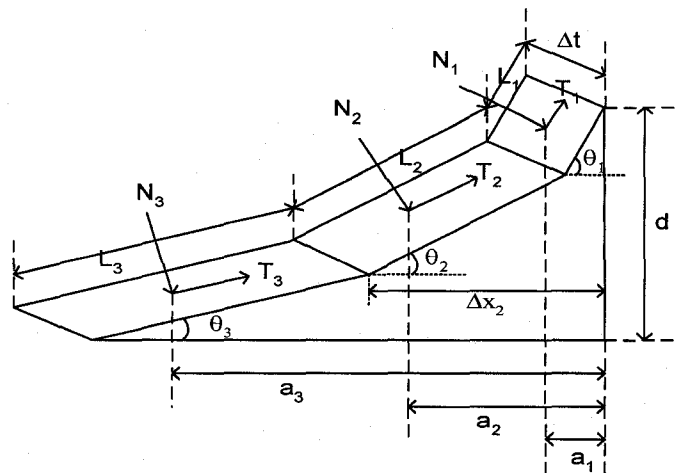
Figure 2-4: Acting stress calculation (after Kotras et al., 1985)

It is assumed that the tangential force (T) is due only to a friction that behaves in a simple Coulomb fashion:

$$T_i = \mu N_i,$$

(2-3)

where μ is the friction coefficient.

Finally, the normal force N_i is derived from Equation (2-4):

$$N_i = \frac{\sigma_c L_i \Delta t_i \sin \theta_i}{\sin \theta_i + \mu \cos \theta_i}.$$

(2-4)

The forces and moments acting on the blade can be estimated by integrating the sum of each blade strip component.

2.4.2. Prediction with Veitch's Model

A contact model was developed following a test series with a two-dimensional blade shaped cutting tool and a numerical calculation. The basic concept of this model was based on the model of Belyashov and Shpakov (1983), which was extended by Veitch (1995). The ice load acting on the blade was predicted at each local cutting angle. The procedure for the prediction of the ice loads is as follows: (1) determine a blade-ice intersection, (2) calculate a local cutting angle, (3) find a contact length of the tool, (4) evaluate an ice pressure, and (5) calculate a force and moment.
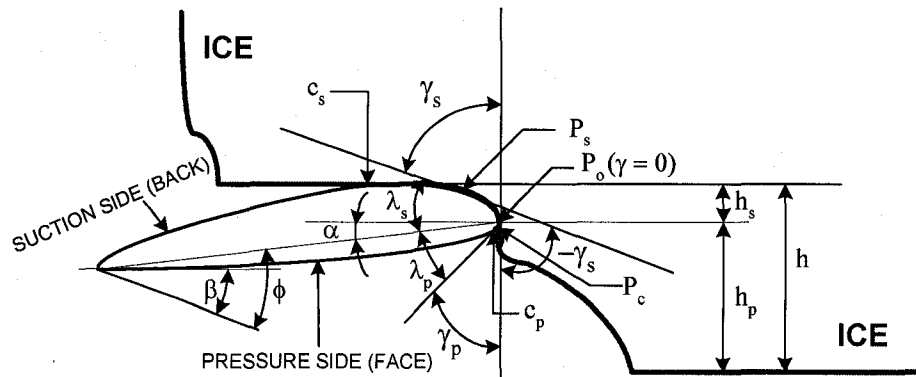
Figure 2-5: Cutting geometry (after Veitch, 1995)

Table 2-1: List of symbols for Veitch's method

α : Angle of attack, also cutting tool's clearance angle

ϕ : Geometric pitch angle

β : Hydrodynamic pitch angle

γ : Local cutting angle

λ : Local blade section angle from the pitch datum line to the tangent line at the point

of interest on the section

h : Thickness of the ice to be removed by cutting

c : Last contact point on the section

P : Point of interest on the section

s : Subscript denotes suction side of blade section

p : Subscript denotes pressure side of blade section

Figure 2-5 shows the cutting geometry, which provides the intersection shape, local cutting angle and contact length. The local cutting angle can be found from Equations (2-5) and (2-6):

$$\gamma_p = \frac{\pi}{2} - \lambda_p - \alpha, \tag{2-5}$$

$$\gamma_s = -\frac{\pi}{2} + \lambda_s - \alpha, \tag{2-6}$$

where $\alpha = \phi - \beta$.

When the γ values are known, pressure at each point can be calculated from Equations (2-7) and (2-8):

$$p = p_{max} \sqrt{1 - \left(\frac{s_p}{l_p}\right)^2} \cdot \frac{1}{2}(1 - \sin m(\gamma - k)) \; ; \; 0 \leq \gamma \leq \frac{\pi}{2}, \tag{2-7}$$

$$p = p_{max} \sqrt{1 - \left(\frac{s_s}{l_s}\right)^2} \cdot \frac{1}{2}(1 - \sin m(\gamma - k)) \; ; \; -\frac{\pi}{2} \leq \gamma \leq 0, \tag{2-8}$$

where coefficients m and k can be determined, which are geometric parameters of blade and ice, symbols l_p and l_s are the length of contact between P_o and c at each side.

Equations (2-7) and (2-8) originated from Hertzian pressure distributions and were modified for the propeller. Finally, forces at each point are evaluated from Equation (2-9):

$$\Delta F = -p \cdot \Delta A \cdot \vec{n} , \qquad\qquad (2\text{-}9)$$

where the symbol of ΔA indicates the incremental area of the blade.

Equations (2-10) and (2-11) give the total forces and moments acting on the blade of two-dimensional shape:

$$F = \sum \sum \Delta F , \qquad\qquad (2\text{-}10)$$

$$M = \sum \sum (r \times \Delta F) , \qquad\qquad (2\text{-}11)$$

where the symbol of r indicates the moment arm of interest.

In Veitch's works, numerical simulation including motion equation of submerged ice was developed. Simplified hydrodynamic loads were also added. Veitch emphasized the ice failure during propeller-ice interaction: ice chipping process with maximum pressure at leading edge and coalescence of small cracks at back side of the propeller. Although Veitch assumed an appropriate propeller-ice interaction scenario, blade dynamics including effect of interaction between propeller blades was ignored; only spherical shape of ice was considered; and changes of ice shape and mass during propeller-ice interaction were neglected.

2.4.3. Prediction with Soininen's Model

Soininen (1998) carried out experiments with a full-scale blade-like tool which represented the propeller of *MS Gudingen*. The tool was attached to a pendulum and impacted with ice sheets at a maximum tangential speed of about 8.3 m/s (Figure 2-6). Ice pressures were measured at different positions over the tool; 21 pressure sensors were used to measure the pressure distributions along the center line and leading edge of the tool. Global loads were measured from the top of the tool. The ice failure process observed from the experiments was a cyclic failure by cracking and extrusion of the ice. In order to evaluate the failure of solid ice, the Mohr-Coulomb failure criterion with slip-line theory was studied. The pressure distributions due to the extrusion of crushed ice were considered using both viscous and granular models. A model for effective load was developed and validated.
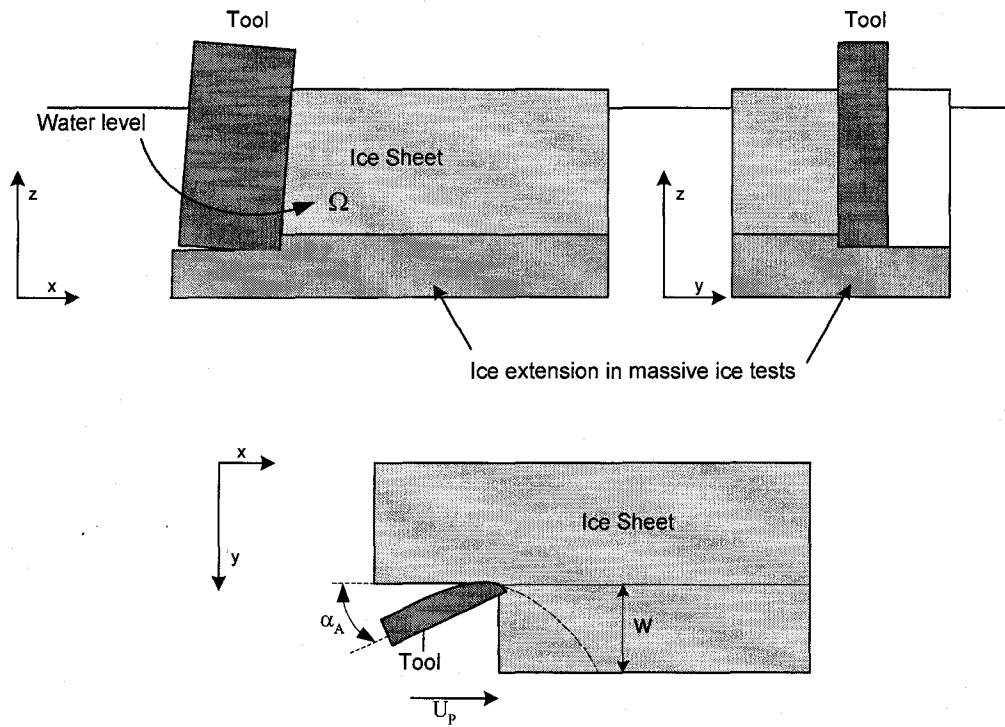
Figure 2-6: Test concept (after Soininen, 1998)

When the blade is in contact with the ice sheet, the flaking of the ice on the face side is

formed by a tensile crack with transversal direction in which the blade is proceeding

(Figure 2-7). The face side, therefore, does not experience significant contact loads with

the ice. The spalling is formed in the back side of the blade and crushing is generated

within the spall, while the leading edge is proceeding into the ice (Figure 2-8).
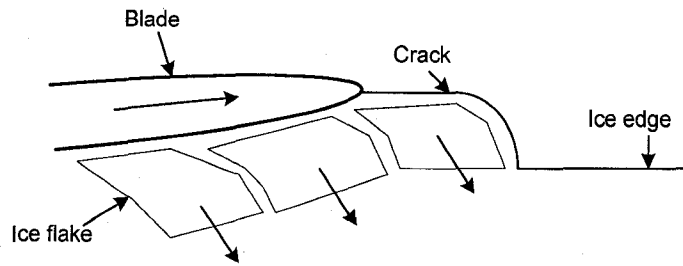
Figure 2-7: Ice flake on face side (after Soininen, 1998)
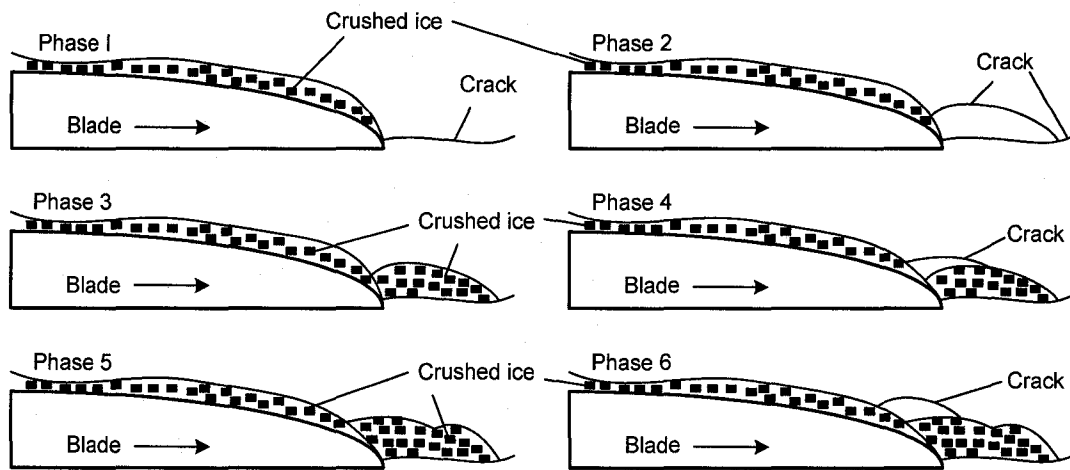
Figure 2-8: Ice crushing on back side (after Soininen, 1998)

Figure 2-9 shows a combination of the granular model at the leading edge extrusion and a viscous model for the compact crushed ice extrusion towards the trailing edge. Soininen's model is based upon a series of spalls in the profile direction, crushing within the spalls, and the extrusion process.
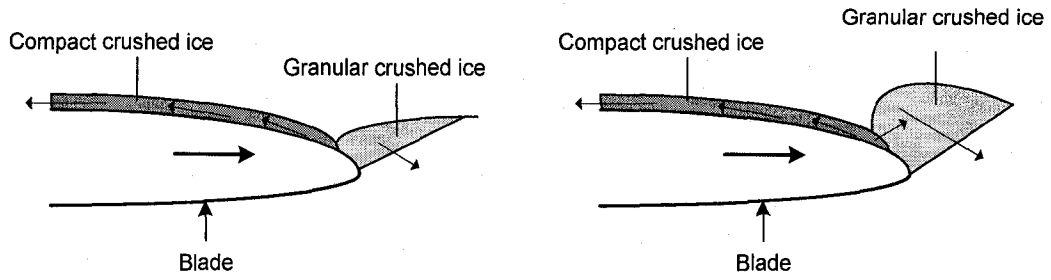
Figure 2-9: Crushed ice (after Soininen, 1998)

Figure 2-10 shows the pressure distribution on the blade. In this figure, pressure at each point can be calculated from Equations (2-12) to (2-18), which are based on the test results and the numerical considerations. The value of P_L was measured from the profile pressure distribution tests.
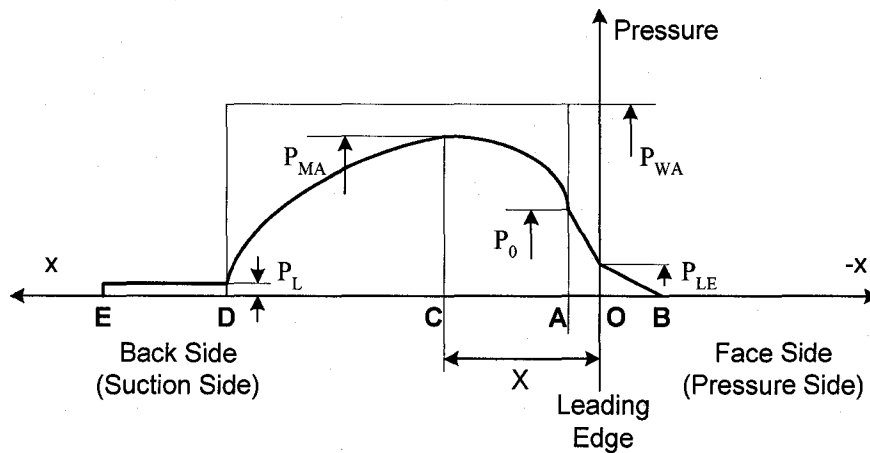
Figure 2-10: Pressure distributions (after Soininen, 1998)

$$P_{LE} = 4.5 + 26w,$$ (2-12)

$$P_{MA} = 10\sigma^{0.3},$$ (2-13)

30

where σ is the uniaxial compressive strength of the solid ice, w is the cut width (m), P_{LE} is the mean pressure (MPa), and P_{MA} is the maximum value of average pressure distribution along a section (MPa).

$$P_{WA} = 11.1\sigma^{0.3} \text{ or } P_{WA} = 2.866(P_{MAX})^{1/2}, \tag{2-14}$$

where P_{WA} is the average pressure at a wedge tip (MPa), and P_{MAX} is the maximum pressure (MPa).

$$P_0 = 0.54P_{WA} + 0.33P_{LE}. \tag{2-15}$$

From A to C,

$$P = P_{MA} - \left(\frac{P_{MA} - P_0}{(X - AO)^2}\right)(X - x)^2. \tag{2-16}$$

From C to D,

$$P = P_{MA} - \left(\frac{P_{MA} - P_L}{(AD + AO - X)^2}\right)(x - X)^2. \tag{2-17}$$

In the tip radius area,

$$\begin{aligned} P &= 0.6\frac{\alpha_A}{5}\left(\frac{2c\cos\phi}{1-\sin\phi}\right), when \ \alpha_A < 5^o \\ P &= 0.6\left(\frac{2c\cos\phi}{1-\sin\phi}\right), \quad when \ \alpha_A > 5^o \end{aligned} \tag{2-18}$$

31

where α_A is the angle of attack of a section (degrees), c is the cohesion, and ϕ is the internal friction angle.

The total load acting on the blade was calculated from the integration of the effective load at each section. From Soininen's work, detailed ice failures were studied by using both theoretic and experimental methods. Soininen used the full-scale blade-like tool, so that there was no scale effect. However, hydrodynamic loads and dynamic effect between the blades and ice were not considered and only milling type contacts on the leading edge were taken into account.

2.5. Theoretical Consideration for Propeller-ice Interaction Study

As introduced in the first chapter, three types of loads may act on the propeller blade during propeller-ice interaction: separable hydrodynamic loads, inseparable hydrodynamic loads, and ice contact loads. The inseparable hydrodynamic loads occur mainly due to the disturbance of the inflow of ice blocks and result in a blockage effect, a proximity effect, and cavitation. Ice contact loads are caused by the physical contact of ice. The ice contact loads are significantly varied depending on the ice properties, interaction conditions, and ship operating conditions and they can be much higher than

separable hydrodynamic loads. In this chapter, inseparable hydrodynamic loads and ice contact loads are reviewed.

2.5.1. Inseparable Hydrodynamic Loads

Inseparable hydrodynamic loads are the loads from a blockage effect, proximity effect or cavitation due to the presence of ice. The blockage and proximity effect are explained as follows. The blockage effect is mainly due to the wake from the ice and reduced inflow. When ice blocks interrupt the inflow of a propeller, this simulates low advance coefficient conditions. Based on a typical thrust-torque versus advance coefficient curve, the thrust and torque coefficients are expected to increase. This is called the "blockage effect." The "proximity effect" is mainly due to the presence of ice (in other words, a boundary effect). This effect influences the propeller loads by means of increased gap flow and the effect on unsteady loads between a propeller blade and ice block. In blocked flow, cavitation can occur even at atmospheric pressure because high local flow speeds and hence low pressures are generated, which affect the thrust and torque.

Regarding non-contact hydrodynamic loads, the effects of blockage and proximity in blocked flow have been studied (Shih and Zheng, 1992, 1993; Yamaguchi, 1993; Bose, 1996; Robbins et al, 1998; Liu et al., 2000). Shih and Zheng (1992) calculated propeller performance in blocked flow by using a two-dimensional boundary element method. The calculated maximum lift and drag coefficients of the blade in the blocked conditions were 5.78 times that in open water conditions. One year later, they extended from a two-

33

dimensional to a three-dimensional boundary element method in order to simulate more realistic propeller blades (Shih and Zheng, 1993). They reported that the calculated maximum thrust/torque in the blocked conditions were 1.6 times higher than open water conditions; which showed that the results were significantly lower than those predicted by their two-dimensional method. However, the local loadings at certain blade section were sometimes more than 5 times higher than open water results.

Yamaguchi (1993) developed a lifting surface method for the numerical prediction of propeller performance in blockage conditions and the numerical results were compared with the experimental results from an ice tank and cavitation tunnel. The effect of blocked flow was considered as two components: a flow separation effect and potential wake /displacement effect. The flow separation effect behind an ice block was considered in the calculation by using a zero axial velocity. However, the displacement effect (proximity effect), which was caused by the increased flow velocity between the propeller blade and ice block, was not considered due to the limitation of the lifting surface method. The experimental results showed that the thrust and torque in blocked conditions were much larger than those in open water conditions. For example, when the advance coefficient was 0.4, the loads in the blocked conditions were approximately 100 percent higher than those in the open water conditions. The comparison of thrust and torque between the experimental and numerical results showed a discrepancy because the effect of displacement had been ignored.

34

Bose (1996) used a three-dimensional unsteady panel method to predict propeller performance in blocked flow and the numerical results were compared with experimental results provided by Luznik et al. (1995). The numerical calculations used two conditions to simulate an ice block: a simplified inflow which represented the wake behind an ice block and the same inflow condition (simplified inflow) with the ice block geometry upstream of the propeller. The velocities of the freestream and the ice wake behind the blockage were 1.0 (one) and 0.01 respectively. The target advance coefficient was 0.4 with an axial wake velocity for the propeller, which was 1.46 times that of the freestream. The numerical results showed the sensitivity of the gap between the propeller and ice block. If the gap was more than 5 mm, then the prediction with only simplified inflow showed a good agreement with experimental results. If the gap was less than 5 mm, then the prediction using the block face with a simplified inflow gave more realistic trends for the thrust quantitatively than that with only simplified inflow. The torque prediction, however, showed opposite trends when the gap was less than 5 mm. Also the study emphasized a significant variation in the thrust during the blockage, and consequently suggested that the strength and fatigue of the blade should be taken into account.

Later, Liu et al. (2000) used panel method package, called PROPELLA, with three different ice shapes to simulate blocked flow conditions: ice with a blade milling contour, a wedge and a sphere shape. The numerical results showed the high blade loads during the blockage and similar performance trends to those of experimental results in terms of mean values.

The cavitation of an ice class propeller has been studied (Walker, 1994a, 1994b, 1994c and 1996; Doucet, 1996; Mintchev et al., 2001; Atlar et al., 2003). Walker (1996) conducted model tests with an open and ducted propeller in both a general towing tank and cavitation tunnel to investigate hydrodynamic loads and cavitation due to a blockage. The main conclusions derived from Walker's work were:

1. In blocked flow, cavitation could occur even at atmospheric pressure;

2. The blocked flow increased the propeller thrust and decreased total system thrust/efficiency due to the drag load imposed by the blockage;

3. The cavitation reduced the mean of both thrust and torque values;

4. In blocked flow, cavitation started as stable sheet/vortex cavitation and developed as cloud cavitation. Extensive cloud cavitation results in significantly increased vibration;

5. As the cavitation number was decreased, an unstable load feature was found (e.g. increase in noise, vibration and oscillation).

Mintchev et al. (2001) and Atlar et al. (2003) carried out model tests with Styrofoam model ice (compressive strength reported was 170 kPa) in a cavitation tunnel for an R-Class propeller and podded propeller, respectively. Atlar et al. (2003) simulated both milling and blockage conditions, and measured axial induced velocities and loads including thrust and torque. In conclusion, they explained that cavitation during milling in the recess should provide additional thrust and torque whereas Walker (1996) proposed a decrease in thrust and torque because of the cavitation in blockage conditions. Doucet

(1996) conducted propeller erosion tests in a cavitation tunnel and reported that erosion could occur in blocked flow even at atmospheric pressure.

2.5.2. Ice Contact Loads

In addition to three ice loads models described in Section 2.4, Veitch's model had been extended to be incorporated with the calculations of hydrodynamic loads using panel methods (Veitch et al., 1997; Doucet et al., 1998). Doucet et al. (1998) used the panel code, PROPELLA, to predict the hydrodynamic loads including blockage effect and ice contact loads. Their attempt was the first numerical prediction for propeller-ice interaction taking into account the hydrodynamic loads and ice contact loads simultaneously.

Studies on the ice loads acting on structures have been performed extensively. In this section, several structure-ice interaction studies, which take into account crushing failure in a brittle regime with relatively high strain rates (generally more than 10^{-3}/s), are reviewed (Tuhkuri, 1995; Sodhi, 1998; Sodhi et al., 1998; Sodhi, 2001; Sodhi and Haehnel, 2003). Sodhi (1998) performed indentation tests at different contact speeds (from 0.002 to 0.5 m/s). The results showed that an effective pressure, which was affected by the different failure modes (ductile and brittle), was mainly caused by the contact speed: at a low speed, simultaneous crushing failure occurred with a ductile behavior. Simultaneous crushing failure with a ductile behavior was reported at a low speed, whereas random or non-simultaneous failure due to a brittle flaking was reported at a high

speed. From the tests, the effective pressure of failure at a low speed was higher than that at a high speed of indentation; for example, the peak effective pressures for the indentation speeds of 8 mm/s and 409 mm/s were approximately 5.5 MPa and 1.8 MPa, respectively. The estimated strain rates for these two speeds, 8mm/s and 409 mm/s, are 8×10^{-3} /s and 4×10^{-1} /s, respectively.

Especially, at a high strain rate such as a propeller blade/ice impact, the ice failure mode is most likely brittle and may include a non-simultaneous crushing. Several experiments with high strain rate have been carried out in laboratories (Jones, 1997; Moores et al., 2001a; Dutta et al., 2004). Jones (1997) conducted high-speed uniaxial compression tests at different strain rates (from 10^{-1} to 10^{1} /s) with freshwater ice and Baltic Sea ice. The strain rate was calculated by the speed of an actuator divided by the original length of the specimen ice. Most of the previous results of compressive tests were carried out until the strain rate reached about 10^{-1} /s, and a typical stress-strain rate curve has convex shape which has maximum strength at the strain rate of approximately $10^{-2} \sim 10^{-3}$ /s. In the range of the strain rate between 10^{-2} /s and 10^{-1} /s, strength decreased as the strain rate increased. Jones found that if the strain rate was higher than 10^{-1} /s, then the strength increased as the strain rate increased up to 10^{1} /s, although there were significant data variations. The effect of strain rate is discussed in Section 3.7.

Moores et al. (2001a) showed similar results to the work done by Jones (1997). The compressive tests with a high speed Material Testing System (MTS) were carried out with EG/AD/S model ice at different strain rates (from 4.6×10^{-8} to 4.6×10^{0}/s). The

effect of temperature was taken into account: -2, -5 and -8 °C. The results showed that the low temperature ices (-8 °C) were about 17 % stronger than those at a high temperature (-2 °C). In conclusion, three different failure modes were found: a ductile creep failure at low strain rates (about $4.6 \times 10^{-8} \sim 4.6 \times 10^{-4}$ /s), a failure through the shear plane at an angle between 30° and 60° at intermediate strain rates (about $4.6 \times 10^{-3} \sim 4.6 \times 10^{-2}$ /s) and brittle failure at high strain rates (about $4.6 \times 10^{-1} \sim 4.6 \times 10^{0}$ /s). The compressive strength had been compared with previous test results (Jones, 1982; Jones 1997; Meglis et al., 1998), and results showed similar trends: results with the Baltic Sea ice had good agreement of those with EG/AD/S CD (Correct Density) model ice; results with polycrystalline ice had two to five times those of EG/AD/S model ice. At high strain rates (about $4.6 \times 10^{-1} \sim 4.6 \times 10^{0}$ /s) the strength increased as the strain rate increased. Significant variation of the strength was also found; the compressive strength at the highest strain rate (4.6×10^{0} /s) varied from 1.5 to 8.0 MPa.

The friction of ice was considered through experimental tests with various strain rates (Gagnon and Molgaard, 1991). The tests were carried out by using a steel wheel which drove up to 40 rpm, and a fixed frame to support an ice specimen. The results showed that friction coefficients decreased as the increase in the sliding speeds (0.06 to 0.82 m/s) and temperatures (from -19 to -5 °C). At high sliding speeds, e.g. more than 0.4 m/s, the friction coefficients appeared to asymptotically approach constant values, between 0.02 and 0.04.

Chapter 3 Experiments

The objective of this chapter is to introduce test facilities, experimental models, and

methodology of data analysis and to provide test results and comparisons with similar

studies. Experiments were carried out in the Ice Tank at the Institute for Ocean

Technology (IOT) of the National Research Council Canada (NRC). A model podded

propulsion system was manufactured and fitted with several dynamometers at various

positions by Akinturk et al. (2003, 2004a, and 2004b). The aim of the present tests was to

evaluate the performance of the propeller on a podded system in ice, and to investigate

the effect of ice properties and interaction conditions (depth of cut, rps, carriage speed

and azimuthing angle) on the ice loads experienced by the pod system, shaft and propeller.

3.1. Overviews of Test Facilities and Model Ice

3.1.1. Ice tank

The useable area of the tank for ice testing is 76 m long, 12 m wide and 3 m deep. In

addition, a 15 m long setup area is separated from the ice sheet by a thermal door to allow

40

equipment preparation while the test ice sheet is prepared, as shown in Figure 3-1 (Jones, 1987). The towing carriage is an 80 tonne steel structure and the range of operating speed is from 0.0002 to 4.0 m/s. The test frame of the carriage can move transversely and vertically in order to control the test position. The service carriage is an independent hydraulically operated unit and it is useful for ice control and sampling.
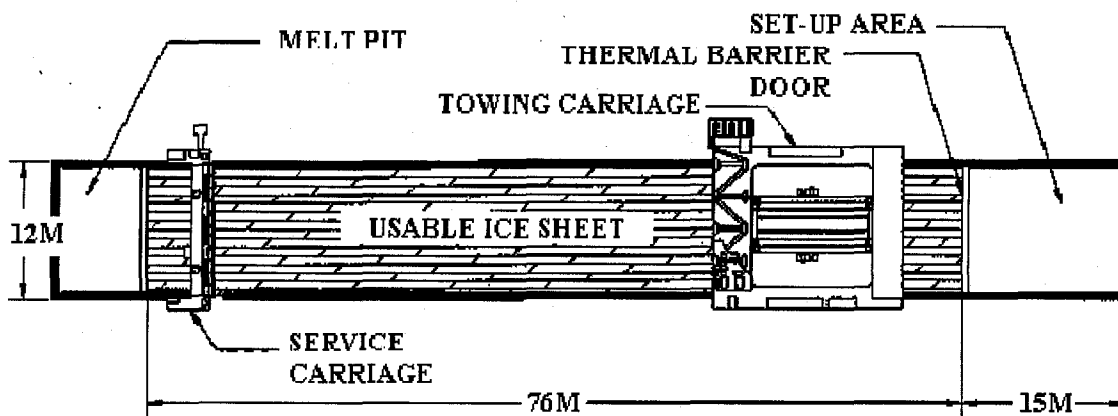
ICE TANK
3.0 METRES DEEP

Figure 3-1: Schematic diagram of the ice tank (after Jones, 1987)

3.1.2. Model ice

For model ice, a diluted aqueous solution of ethylene glycol (EG), aliphatic detergent (AD), and sugar (S), which is called EG/AD/S ice, was used in the present experiments. EG/AD/S ice is specifically designed to provide the scaled flexural strengths of columnar

sea ice (Timco, 1986; Spencer and Timco, 1990). It is The procedure to produce an ice sheet is:

- First, the ice sheet is grown by cooling the tank water and room to approximately 0 and -20 °C, respectively (this process is called cooling);

- Second, the tank is seeded by spraying warm water into the cold air in a thin mist, allowing it to form ice crystals with uniform grain size (this process is called seeding);

- Third, the ice is allowed to grow at approximately -20 °C until it has reached the desired thickness (this process is called growing);

- Fourth, the temperature of the tank is raised to above freezing and the ice is allowed to warm up and soften, until the target ice strength is reached (this process is called tempering).

In order to provide uniform properties of the model ice, micro-bubbles for the corrected density were not included in the ice sheets, although they are normally used in ship/ice interaction tests. Table 3-1 shows the average values of the modulus of the elasticity (E), density (ρ_i) and thicknesses (h_i) of the model ice for the 35 and 15 mm depths of cut (the depth of cut is amount of the blade penetration into ice and this refers different test conditions). Figure 3-2 and Figure 3-3 show the variation of the compressive strength, flexural strength and shear strength against the passing time.

Table 3-1: The properties of the model ice and their standard deviations (STDs)

Depth of Cut	E / STD	ρ_i / STD	h_i / STD

	(MPa)	(kg/m^3)	(mm)
35 mm	181.5/ 5.52	928.8/ 3.53	53.2/ 2.3
15mm	129.9/ 5.97	930.4/ NA	47.4/ 3.4
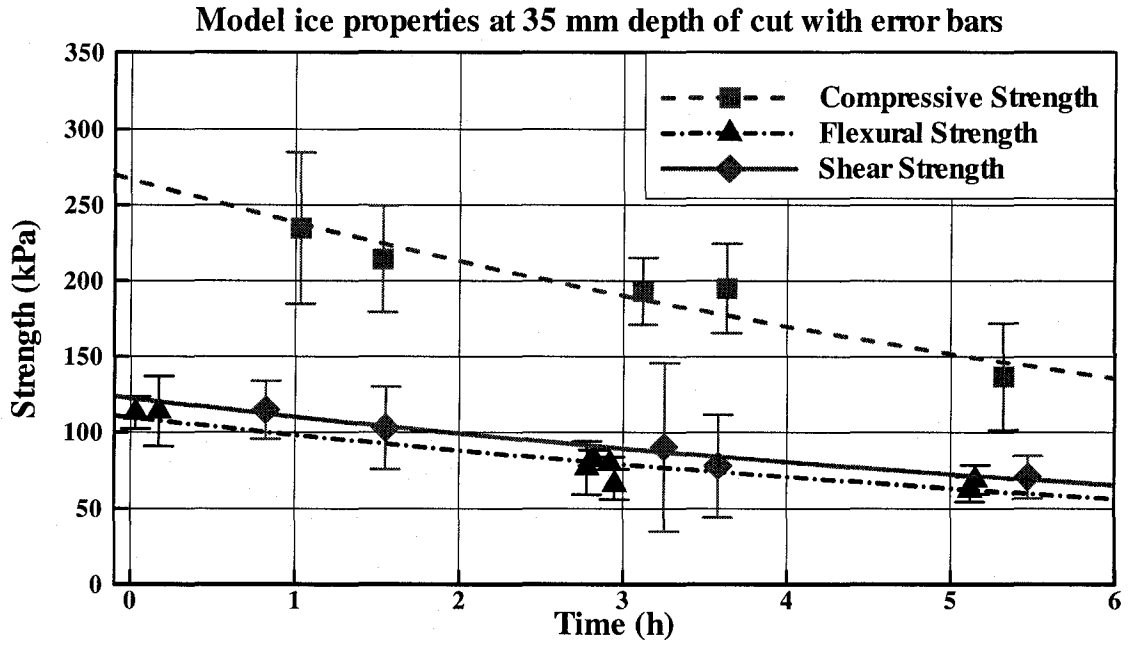
Figure 3-2: Model ice properties at the depth of cut of 35 mm with error bars ($\pm$ 2 times standard deviations)
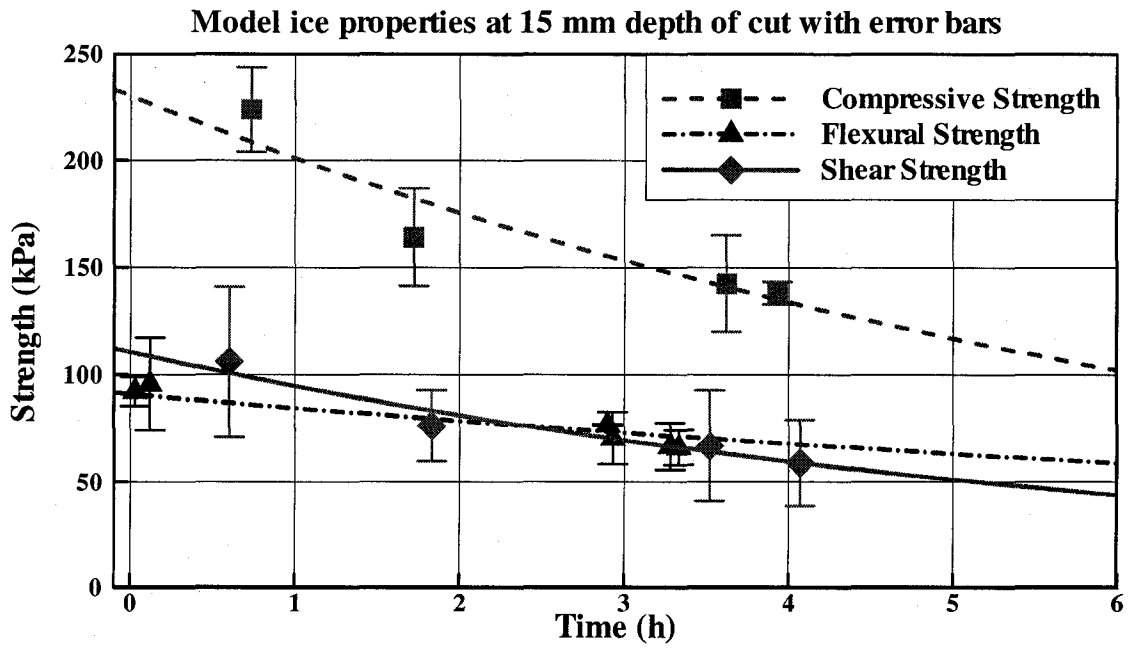
Figure 3-3: Model ice properties at the depth of cut of 15 mm with error bars ($\pm$ 2 times standard deviations)

The early trials for the present tests used level ice, as shown in Figure 3-4. The ice loads

acting on the strut, however, exceeded the maximum capacity of the dynamometers, thus

the ice sheets were pre-cut to reduce the breaking loads on the strut, which was called

pre-sawn ice. Although the ice sheets were pre-sawn, the ice segments were in place, thus

the ice conditions were assumed uniform (providing constant depth of cut), as shown in

Figure 3-5. Figure 3-6 shows the trajectory of the blades passing in the ice block from

underwater milling tests.

Figure 3-4: Picture of level ice
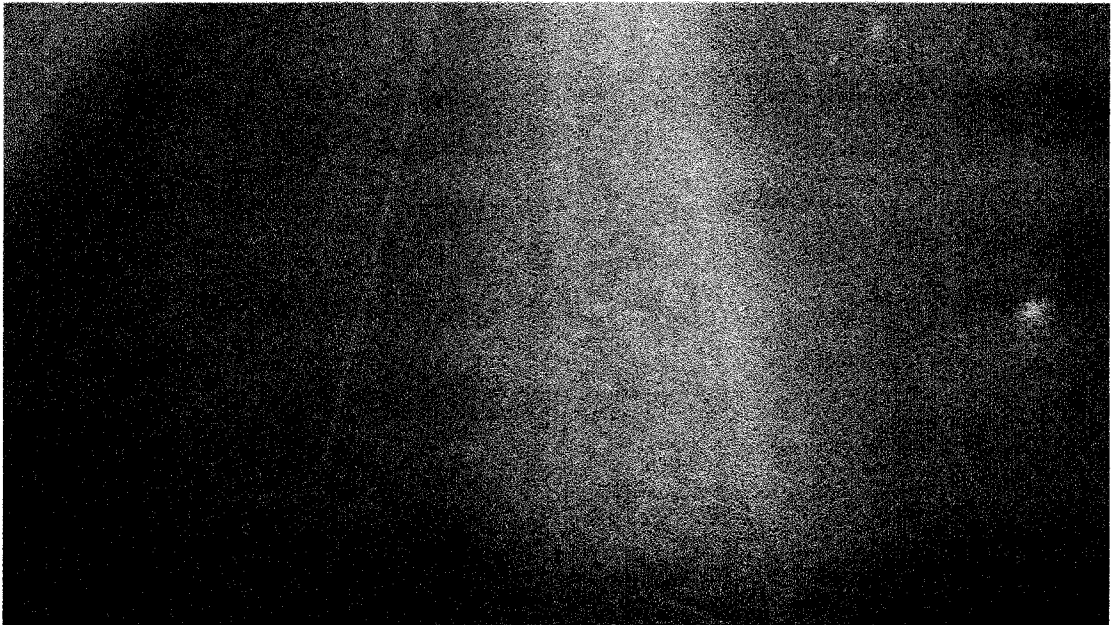
Figure 3-5: Picture of pre-sawn ice

Figure 3-6: Ice sample after underwater milling tests

3.2. Overview of Model Podded Propulsor

The general arrangement of the model podded propulsor with model stern is shown in

Figure 3-7.
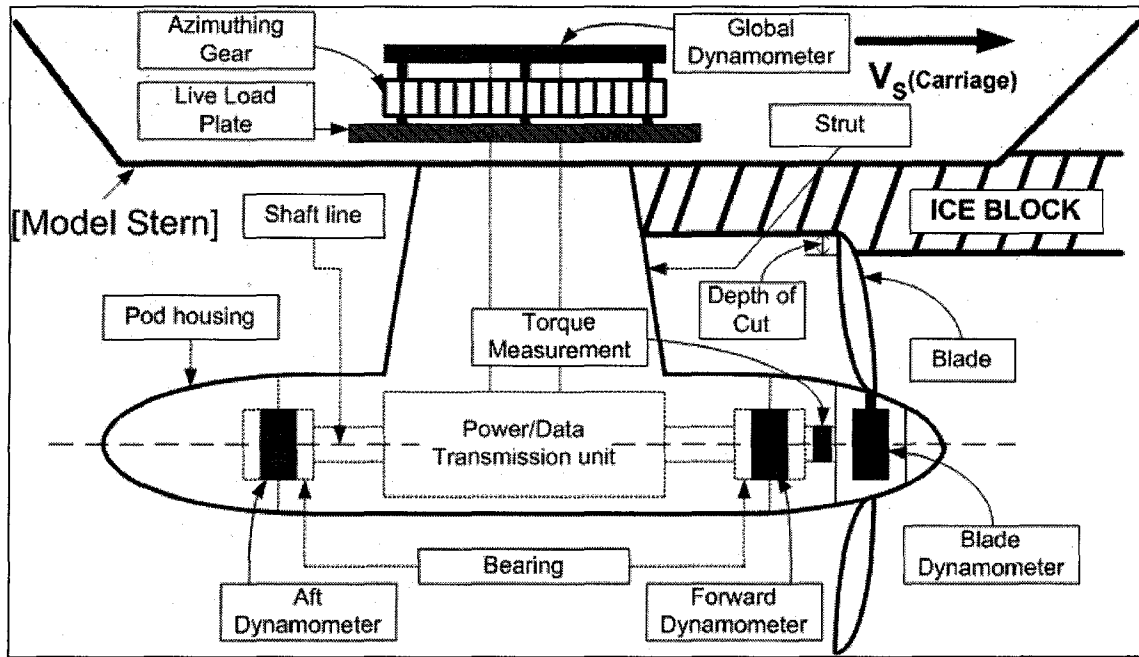
Figure 3-7: Sketch for the model podded propulsor system with measurement devices

The model stern was supported independently of the podded propulsor system. A lubricated slip joint was fitted where the strut passed through the model stern, thus loads from the model stern did not affect the global dynamometer. This also allowed adjustments to the distance between the propeller and the model stern in order to change the depth of cut. The live load plate supported the pod housing, strut and propulsion unit inside the pod and strut. The live load plate was fitted with a rotary bearing to facilitate the change of azimuthing angle. The azimuthing angle could vary from zero to 180 degrees. A vertically mounted motor provided the power (3.3 kW) for the propeller. In Figure 3-8, the live load plate, azimuthing gear, lubricated slip joint and some of the global dynamometers are shown.
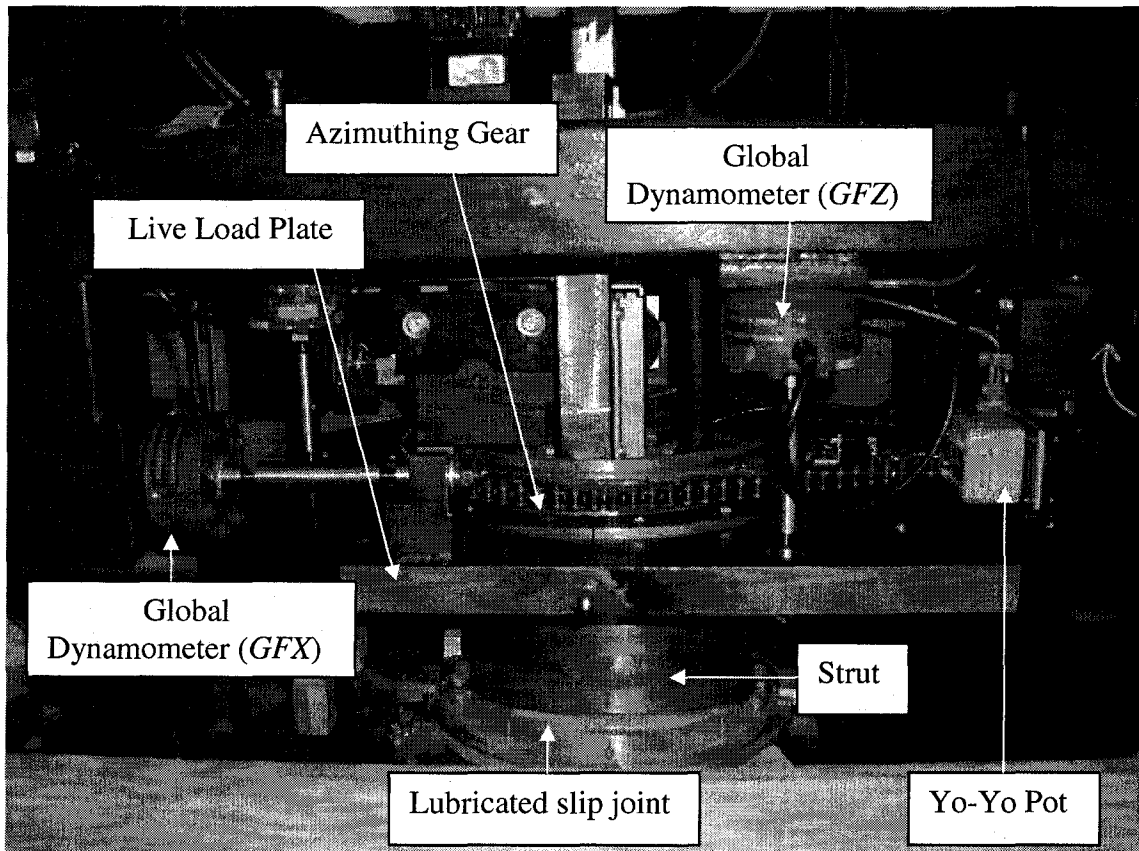
Figure 3-8: Apparatus of global dynamometer and azimuthing gear

The global dynamometers measured the loads on the whole unit including pod and strut. As shown in Figure 3-8, the global dynamometer used is a pancake style and tension/ compression unit with single axis, manufactured by Interface Advanced Force Measurement. A total of six global dynamometers were used: three of them were installed vertically and the rest of them were installed horizontally. Two of the horizontal dynamometers measured drag forces at each side from the centerline and one horizontal dynamometer measured side forces. The maximum capacity of each global dynamometer was 8896 N.

The model podded propulsor had three six-component dynamometers installed to measure

blade loads and shaft-bearing loads. The blade dynamometer was attached to one of the

blades inside the hub, and aft and forward dynamometers were mounted on the shaft

bearings, as shown in Figure 3-9. These three dynamometers were identical, as shown in

Figure 3-10. Shaft thrust was calculated by using the information obtained from the aft

and forward dynamometers. They were manufactured by Advanced Mechanical

Technology Inc. (AMTI) and were capable of measuring forces/moments in six degrees

of freedom. They could measure forces up to 2224 N in x- and y- directions, 4448 N in

the z- direction, and moments up to 56.5 Nm about all three axes. The AMTI load cell

model number for all three dynamometers was MC2.5-6-1000. The axis for the blade

dynamometer is shown in Figure 3-11.
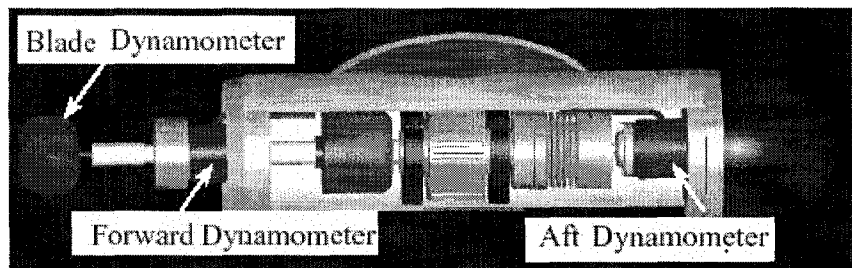
Figure 3-9: Dynamometers on the blade and shaft inside the pod
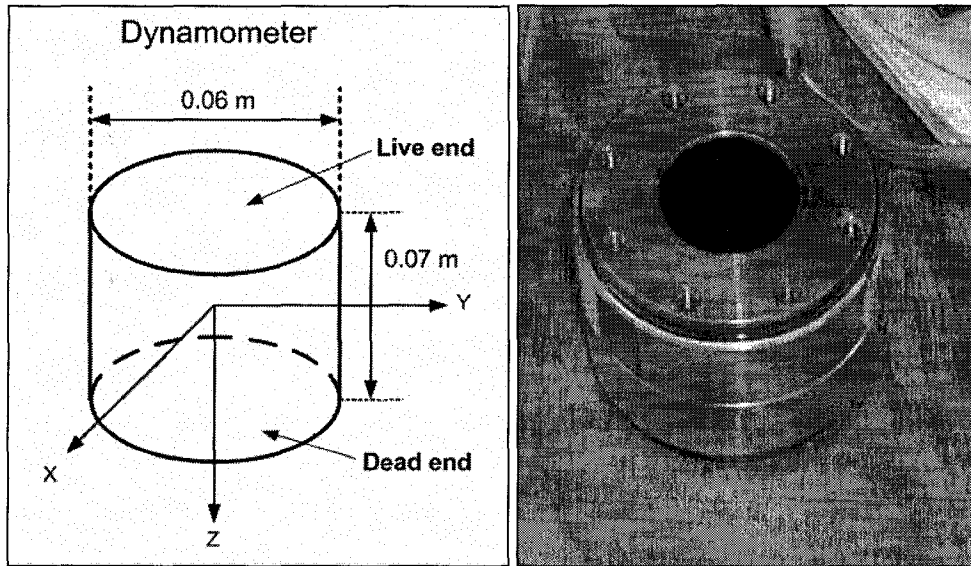
Figure 3-10: Dimension of AMTI dynamometer
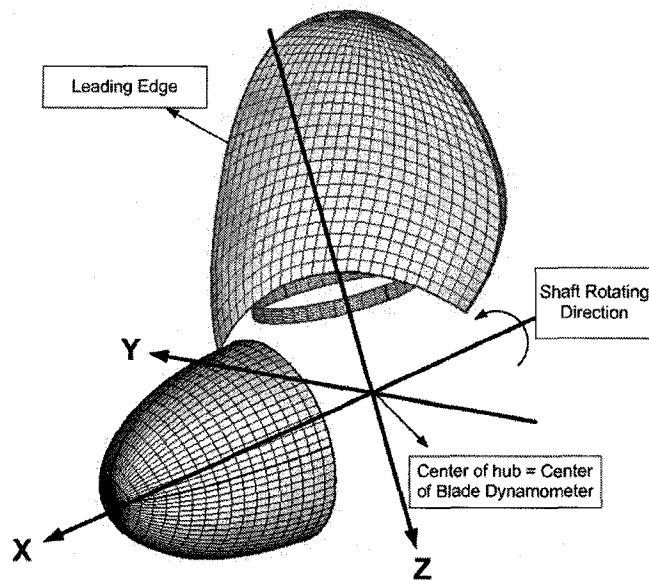
Figure 3-11: Axes for blade dynamometer

Figure 3-12 shows the model podded propulsor with wooden model stern as installed to

the carriage frame during the tests. The picture shows the port side of the experimental

model, which was in the tractor mode. Additionally, strain gauges were mounted on the

shaft for shaft torque measurement (model number was BLH FAED-07-35-6SE-P). Blade

angular position was measured by a rotary position transducer, Waters WPM Model 18-

09.
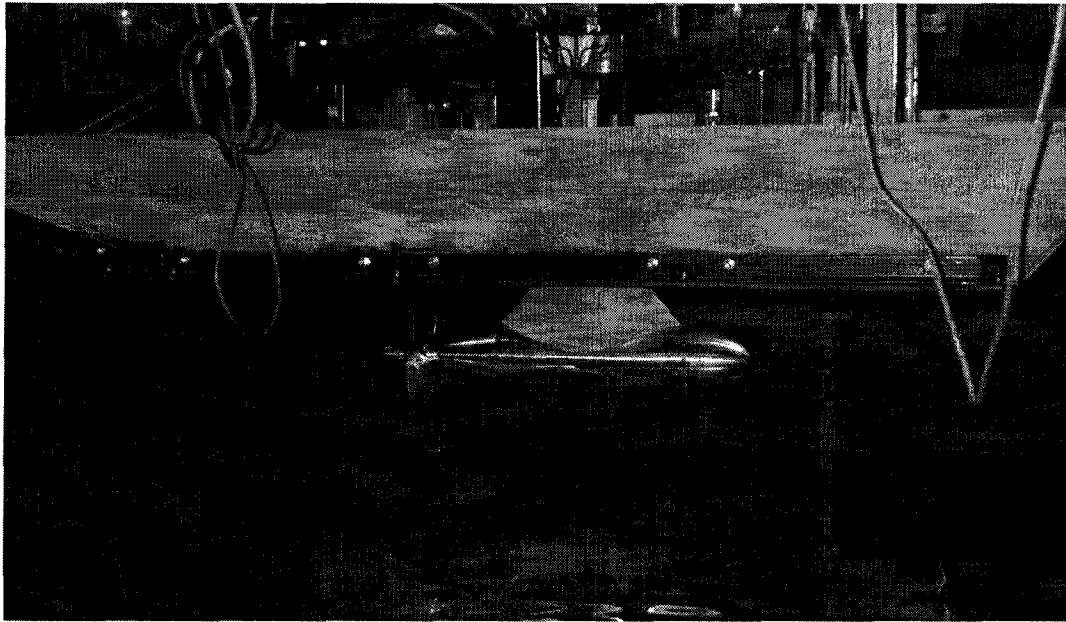
Figure 3-12: Experimental model

The present propeller design chosen was the propeller for the Canadian Coast Guard

Gulf/River Class Medium Icebreaker, R-Class propeller, as shown in Figure 3-13. The

model propeller was scaled to 13.7 and it had a diameter of 0.3 m and four blades. Mean-

pitch/diameter ratio (P/D) was 0.76 and expanded blade area ratio (EAR) was 0.669. The

diameter of the hub was 0.11 m. The blade design was based on the Stone Marine

Meridian series, but with thickened blades for operation in ice (Emerson and Sinclair,

1978).
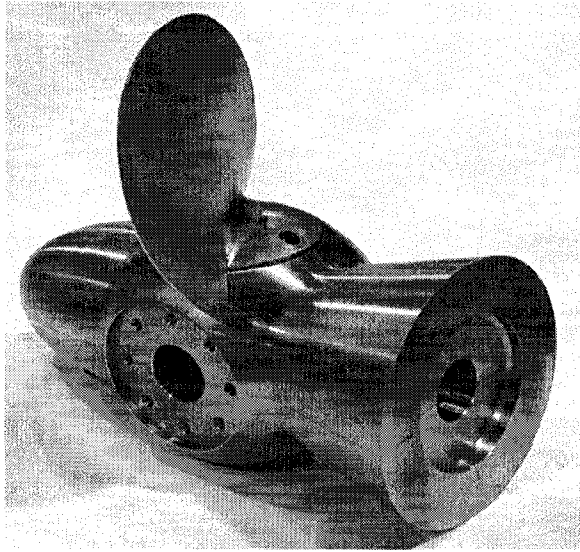
Figure 3-13: Hub with one of the blades mounted on

3.3. Test Procedure

The experiments were carried out in open water and ice covered water at the IOT ice tank.

Measurements were recorded through the Data Acquisition System (DAS) with 33

channels, which were time, forces and moments at various locations, shaft torque,

propeller rotational speed, propeller blade angular position, azimuthing angle, carriage

speed, carriage position, test frame height and motor current. The sampling rate was 5000

Hz for most channels, but some of the channels, e.g. azimuthing angle, carriage speed,

carriage position, test frame height and motor current, used 50 Hz.

Table 3-2 shows the test matrix for the present experimental tests. The tests were

performed with two different modes of the pod system, tractor and pusher mode. Each

group of tests had three different propeller rotational speeds (5, 7 and 10 rps), three

different carriage speeds (0.2, 0.5 and 0.8 m/s), two different depths of cut (15mm and 35

mm), and different azimuthing angles from zero to 180 degrees in 30 degrees intervals.

The azimuthing angle of non-azimuth condition (normal condition) is zero and 180

degrees for the pusher and tractor mode, respectively.

Table 3-2: Test matrix

Pod Mode	Tractor Mode, Pusher mode
Carriage Speed	0, 0.2, 0.5, (0.8) m/s
Propeller Rotating Speed	5, 7, 10 Hz
Depth of Cut	15mm, 35mm
Azim. Angle (Pusher Mode)	0, 30, 60, 90, 120, 150 degrees
Azim. Angle (Tractor Mode)	180, 150, 120, 90, 60, 30 degrees
Ice Condition	Pre-sawn Ice, Pack Ice
Ice Thick. / Flex. Strength	60mm / 80kPa

The tractor mode has been mainly studied in this thesis, because it provides uniform ice conditions, e.g. depth of cut. The propeller in tractor mode is placed in front of the pod and strut, thus the propeller experiences undisturbed ice blocks. Whereas, the propeller in pusher mode is placed at the back of the pod and strut so the propeller may experience broken or damaged ice pieces. Therefore, the results shown here are from the tractor mode and pre-sawn ice condition. Open water tests were carried out in the same conditions as ice covered water tests. In the ice covered water tests, some of the runs at the carriage speed of 0.8 m/s had to be cancelled because several channels of the dynamometers exceeded their maximum capacities.

Most ice covered water tests were carried out in a pre-sawn ice. In order to prepare the pre-sawn ice, level ice sheets were cut in longitudinal and diagonal directions, as shown in Figure 3-14. This figure shows the azimuthing angle of 180 degrees for the tractor

mode in the pre-sawn ice. The target thickness and flexural strength of the model ice for the ice covered water tests were 60 mm and 80 KPa, respectively.
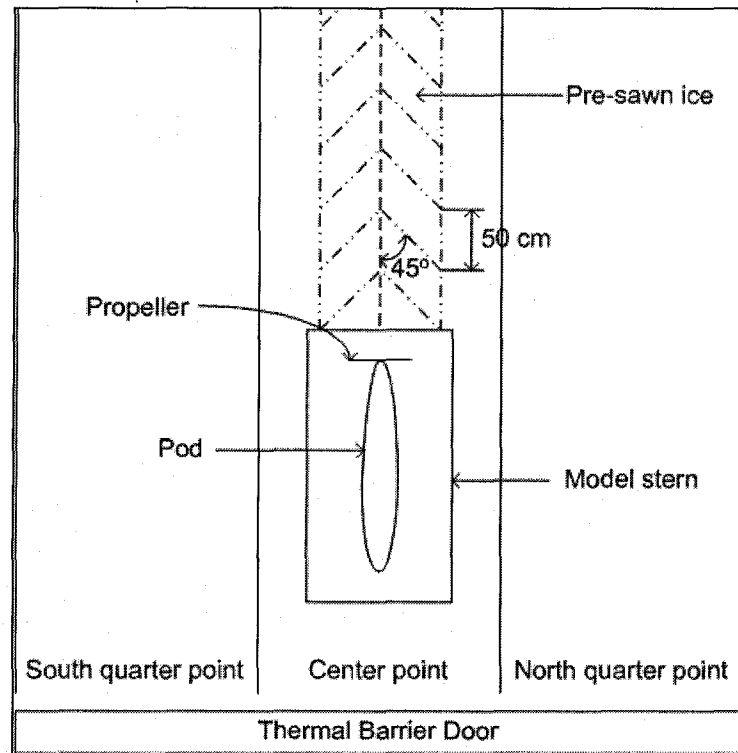
Figure 3-14: Sketch of pre-sawn ice sheet with 180 degrees tractor mode

3.4. Data Analysis

As introduced in the previous chapters, the author hypothesized that the ice loads acting on the model podded propeller blades in ice covered water have three components: separable hydrodynamic loads, inseparable hydrodynamic loads and ice contact loads. Total loads from the ice covered water tests are sum of the three components, and the ice related loads are the sum of the inseparable hydrodynamic loads and ice milling loads. In this thesis, the ice related loads are mainly focused and explained in detail, but the results of total loads and separable hydrodynamic loads are also shown and discussed.

The data were analyzed with regard to three different measured points, as shown in below:

(1) Global Loads: Global loads were measured by three horizontal dynamometers and three vertical dynamometers from the top of the model podded propulsor. Two horizontal dynamometers measured the longitudinal forces (GFX) and one horizontal dynamometer measured the transverse forces (GFY). Three vertical dynamometers measured the vertical forces (GFZ).

(2) Shaft Loads: Shaft thrust (T_{SHAFT}) was measured from the forward dynamometer and aft dynamometer on the shaft. Shaft torque (Q_{SHAFT}) was measured on the shaft very close to the hub by the torque transducer.

(3) Blade Loads: Blade thrust (T_{BLADE}) and torque (Q_{BLADE}) were measured inside the hub by the blade dynamometer, which was attached to the root of one of the blades.

3.4.1. Consideration of Separable Hydrodynamic Loads

Separable hydrodynamic loads are the hydrodynamic loads without any effect due to the presence of ice such as a blockage, proximity or cavitation and they can be obtained from open water tests. Once the data were acquired, they were analyzed by using a data analysis package, Generalized Experiment Control and Data Acquisition Package (GEDAP), for general statistical calculations including maximum, minimum, average, and standard deviation. The results in this thesis provide the thrust of the model podded propulsor (unit thrust), transverse/vertical forces acting on the model podded propulsor, shaft thrust/torque and blade thrust/torque at different azimuthing angles. Most results are presented with non-dimensional coefficients for thrust and torque against advance coefficients.

3.4.2. Consideration of Total Loads in Ice

The total loads in ice were obtained from the ice covered water tests. The data were acquired and analyzed using the same process as the separable hydrodynamic loads. In addition, propeller-ice interaction conditions and ice properties were measured and recorded. The results provide the thrust of the model podded propulsor (unit thrust), transverse/vertical forces acting on the model podded propulsor, shaft thrust/torque and blade thrust/torque at different azimuthing angles. Most results are presented with non-dimensional coefficients for thrust and torque against advance coefficients.

3.4.3. Consideration of the Ice Related Load (during milling period)

Ice related loads need additional calculations because they are considered only when the blades are in contact with ice, which is called the milling period. In order to find the appropriate milling period, the milling angle (α_m) that corresponded to the depth of cut was considered (Figure 3-15 and Table 3-3).
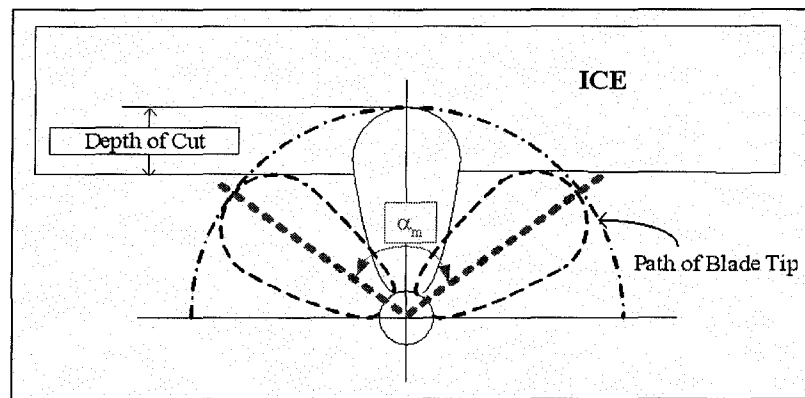
Figure 3-15: Depth of cut and milling angle

Table 3-3: Depth of cut vs. milling angle

Depth of cut	Milling angle (α_m)
15mm	63 degree (10 ~ -53 degrees)
35mm	105 degree (36 ~ -69 degrees)

Two FORTRAN programs (DANRA.F and DRSUM.F) were coded, in order to calculate the ice related loads from time series data of the experiments. Table 3-4 shows the summary of DANRA code. Once the DANRA code provides the ice related loads, DRSUM code uses them as the input data and carries out additional/optional calculations

58

including general statistical calculations (mean of maximum, mean of minimum, etc.),

uncertainty analysis and extreme probability calculations.

Table 3-4: Overview of DANRA.F (Data Analysis aNd Re-Arrangement)

Contents	Description
Aim	Ice related loads calculation during the milling period
Input	➢ The milling period is determined by the milling angle (α_m); ➢ Data ranges and other input data corresponding to the milling period are determined; ➢ All input data are stored at Data_range.xls [Appendix A].
Procedure	➢ All data point is read from time series data (ASCII file); ➢ Tare values from bollard condition are subtracted from the region for analysis (milling period); ➢ Another subtraction due to certain advance coefficient is applied; ➢ Statistical calculations (maximum, average and minimum) are performed.

Figure 3-16 shows the time series data obtained from the experiments as an example. The

blade thrust, carriage speed and rps against time are shown. From a time of 48 to 58

seconds, the test condition shows the bollard condition (5 rps and zero carriage speed). In

the tractor mode, the propeller rotated counter-clockwise, thus the rps was shown as a

negative value.
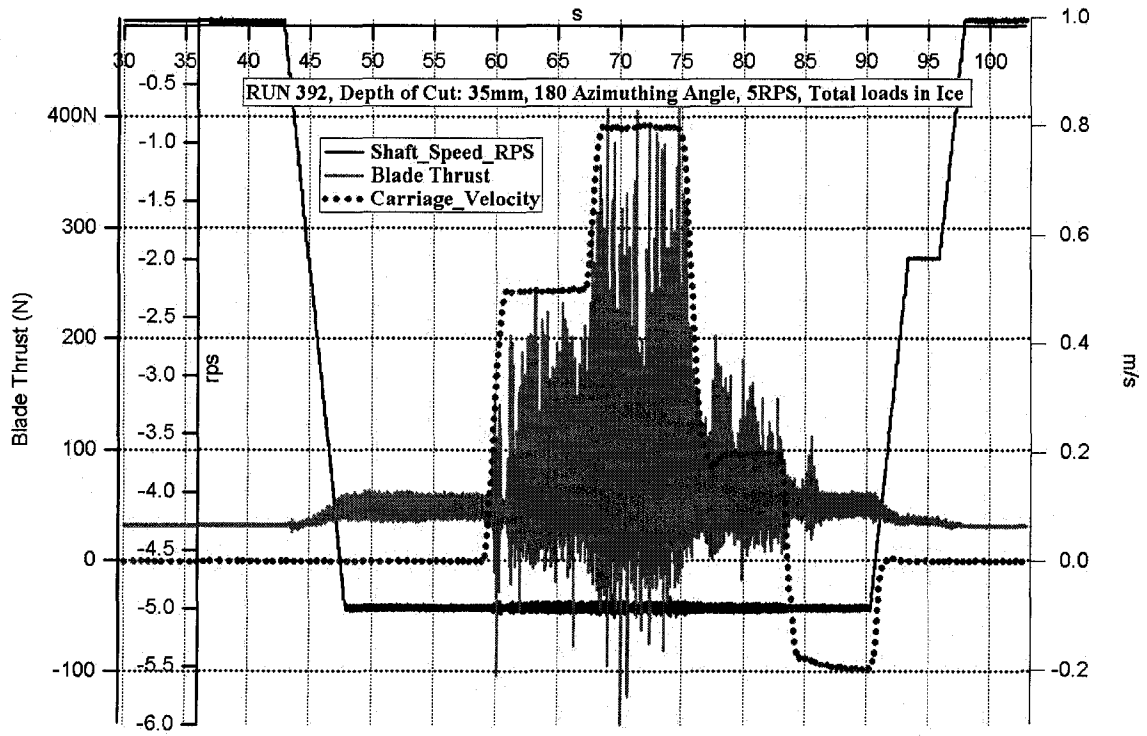
Figure 3-16: Time series data for blade thrust vs. rps & carriage speed

If Figure 3-16 is zoomed in, for example at the 65th second segment, then the enlarged

segment is given in Figure 3-17. In the graph shown in Figure 3-17, the separable

hydrodynamic loads have already been removed and the ice-related loads are shown by

open triangles. The separable hydrodynamic loads were the values from the open water

tests corresponding test conditions. As explained in Section 1.3, the separable

hydrodynamic loads used during the milling period were only approximated due to ice.

The figure shows that the blade enters the ice block at the blade angular position of 36

degrees and exits at negative 69 degrees. This period is defined as the milling period.
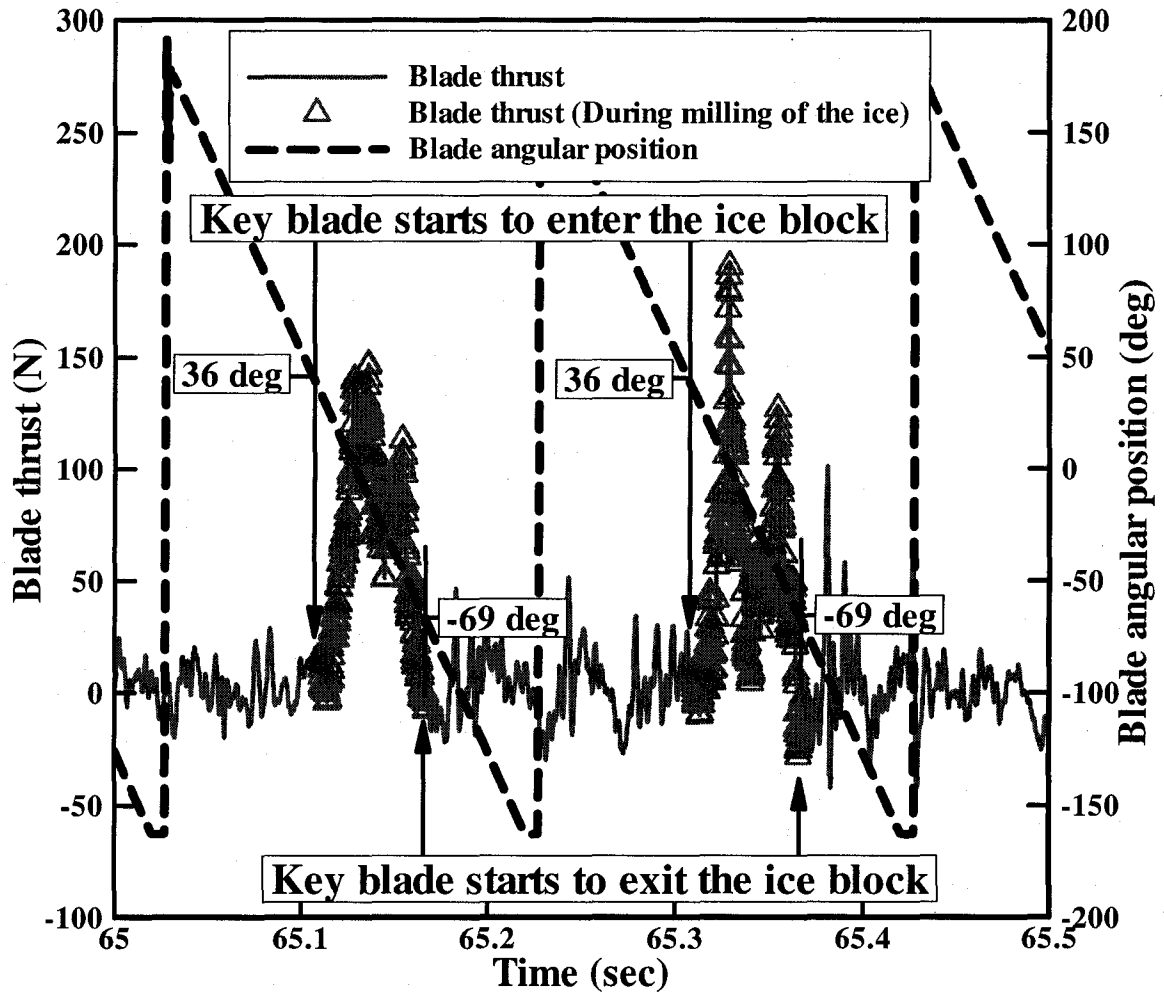
Figure 3-17: Blade thrust during ice milling periods based on the ice milling angle (α_m: from 36 degrees to -69 degrees, 35mm depth of cut and 5 rps)

It is noted that the blade angular position was measured up to positive and negative 180 degrees. From approximately - 160 degrees to - 180 degrees, the blade angular positions could not be measured because of limitations of the sensor.

3.5. Test Results:

3.5.1. Sign Conventions for Global/Shaft Forces and Azimuthing Angles

Figure 3-18 and Figure 3-19 present the sign conventions for shaft thrust, blade thrust and global forces with two different azimuthing angles (ψ), which are 180 and 150 degrees. The figures show a tractor mode from the top. The reference frame for global loads (GFX and GFY) is fixed to the carriage, therefore its orientation does not change throughout the tests.
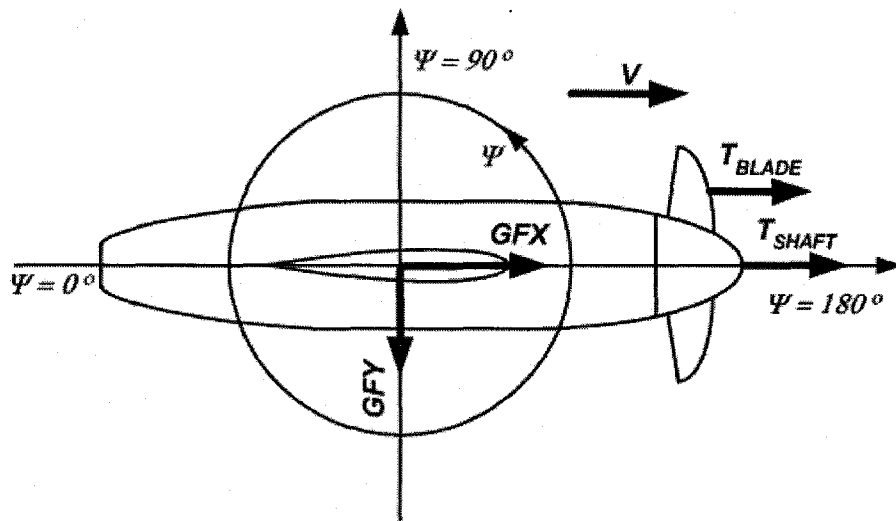
Figure 3-18: Tractor mode with an azimuthing angle of 180 degrees, V is the carriage speed, top view
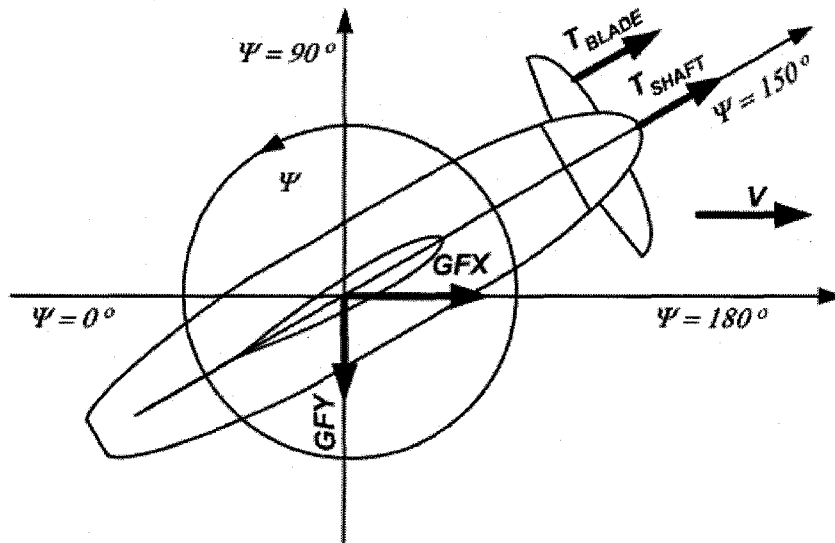
Figure 3-19: Tractor mode with an azimuthing angle of 150 degrees, V is the carriage speed, top view

3.5.2. Sign Conventions for Shaft/Blade Forces and Moments

Figure 3-20 shows the sign conventions for the forces and moments acting on the blade (measured from one of the blades): blade thrust, torque, in-plane bending moment, out-of plane bending moment and spindle torque. The shaft thrust and torque measured from the shaft are also shown for a reference. The positive shaft thrust and blade thrust have the same direction as the forward advance direction. The sign of the positive shaft torque and blade torque is opposite to the direction of the shaft rotating. The positive in-plane bending moment means the case when the leading edge is compressed and the trailing edge is tensed. The positive out-of plane bending moment means the tip of the blade bends backwards (backwards means the opposite direction of the thrust/advance). The positive spindle torque means the leading edge twists backwards. The direction of the positive moments is defined by the right hand rule.

63
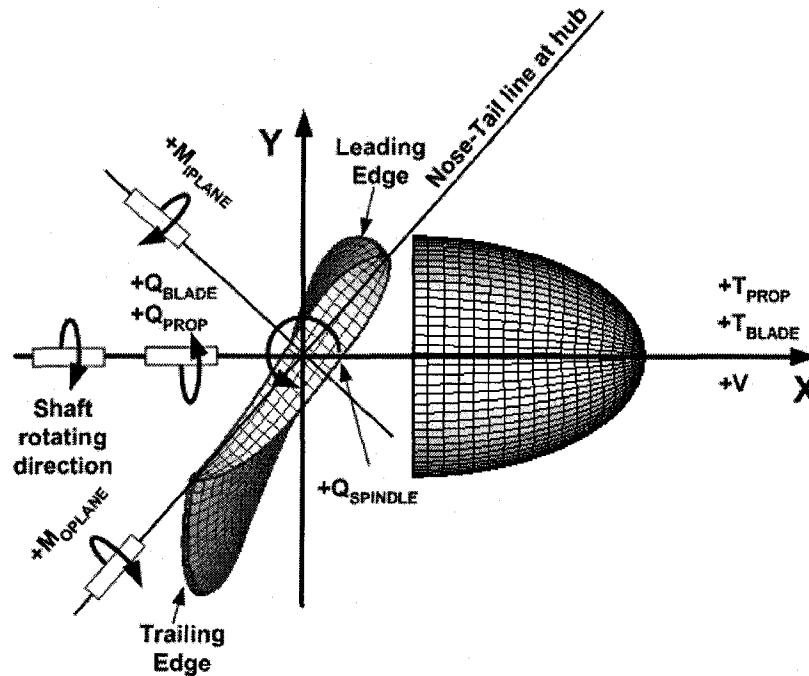
Figure 3-20: Sign conventions for the loads acting on the blade (look from the center of hub)

3.5.3. Separable Hydrodynamic Loads (Open Water Characteristics)

Figure 3-21 shows the open water characteristics in a tractor mode at an azimuthing angle of 180 degrees. Due to the increase in drag forces including other possibly associated effects (such as noise from the propeller) against a podded propulsor, the unit thrust coefficient (K_{T_UNIT}) is approximately 28% lower than that of shaft thrust coefficient (K_{T_SHAFT}) at the advance coefficient of 0.2.

Due to the limitation of an equipped motor, the maximum propeller rotating speeds was 10 rps (revolution per seconds). The range of the Reynolds number (R_e) for the present

experiments was from 1.2×10^5 to 2.4×10^5, whereas the R_e, recommended from ITTC, was over 1.0×10^6 (ITTC, 2002).

Open Water, Tractor Mode, 180 Azimuthing Angle
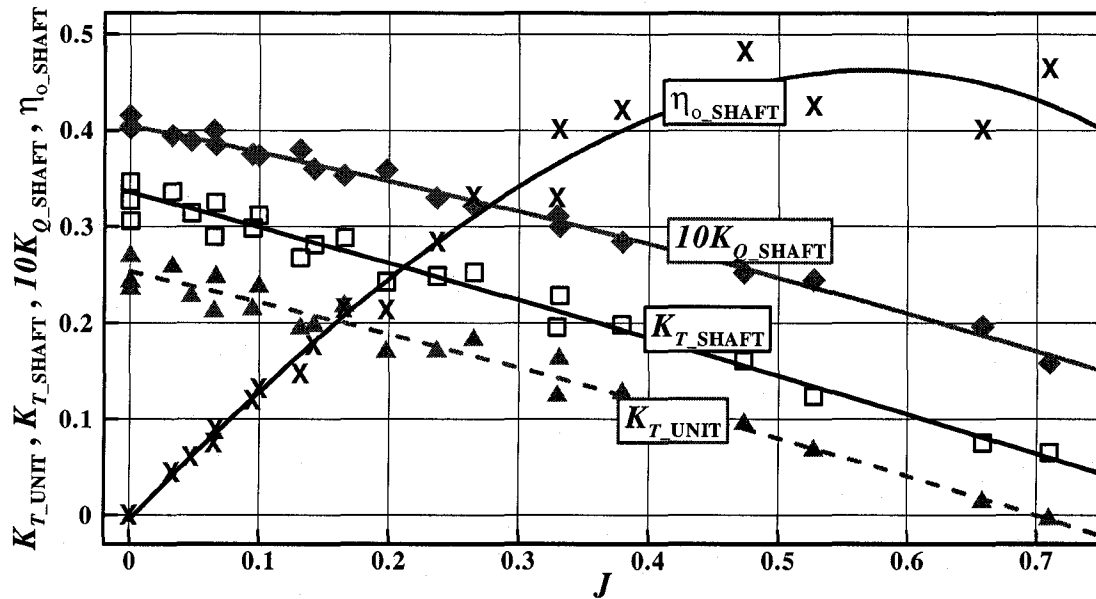
Figure 3-21: Open water characteristics of the model podded propulsor with a tractor mode

Figure 3-22 to Figure 3-24 show the effect of an azimuthing angle on the unit thrust, shaft thrust and shaft torque. As the azimuthing angle decreases (from 180 to 120 degrees), the unit thrust decreases because of two reasons: (1) the increase in the resistance forces against the pod and strut and (2) the decrease in the contribution from the shaft thrust to the unit thrust due to the azimuthing angles; the shaft thrust through the cosine of the angle between the azimuthing angle and center (180 degrees for a tractor mode) contributes to the unit thrust. The shaft thrust and shaft torque increase as the azimuthing angle decreases up to 120 degrees.

It is noted that the advance coefficients used in this study do not consider the effect of an azimuthing angle. When the azimuthing angles are taken into account (150 or 120 degrees), the axial velocity reduces with the cosine of the azimuthing angle from the centerline of the pod unit. Consequently, the propeller thrust and torque increase since the rps remains the same. The effective advance coefficient decreases due to the decrease in effective axial inflow speed.

In addition, a complex feature for the shaft thrust and shaft torque is observed when the azimuthing angle is less than 90 degrees because of the side force of the propeller blade, reversing wake, and unsteady axial inflow.

In Appendix B, results for the separable hydrodynamic loads are shown in detail including unit thrust, transverse/vertical force on unit, shaft thrust/torque and blade thrust/torque at the different azimuthing angles (from 180 to 30 degrees).
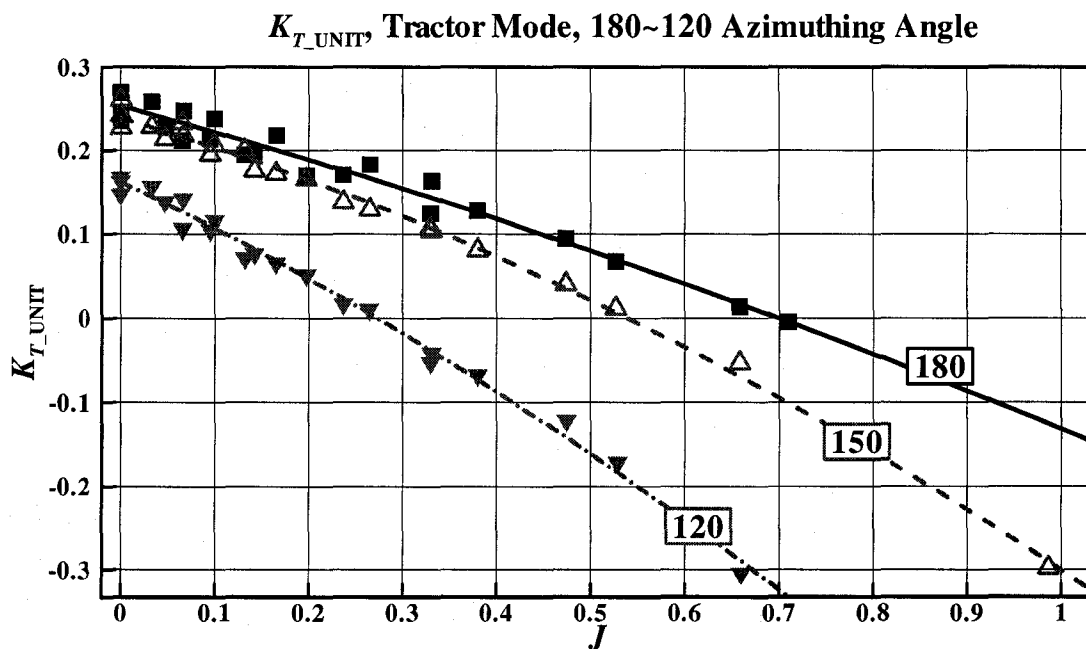
Figure 3-22: K_{T_UNIT} vs. J at different azimuthing angles (180-120 degrees)
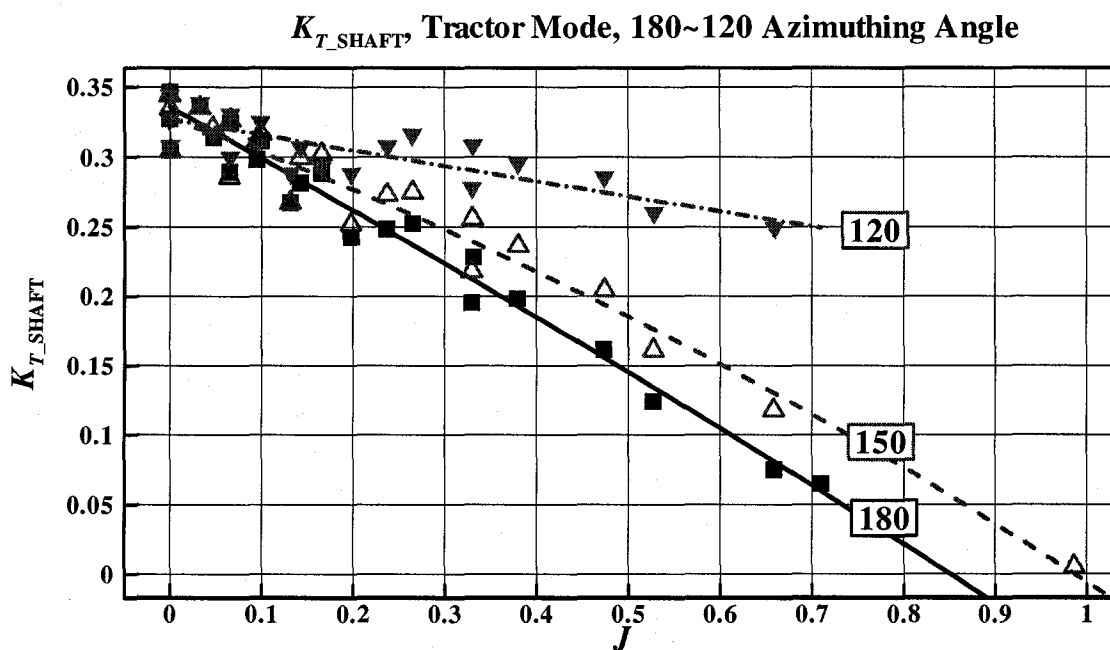
Figure 3-23: K_{T_SHAFT} vs. J at different azimuthing angles (180-120 degrees)
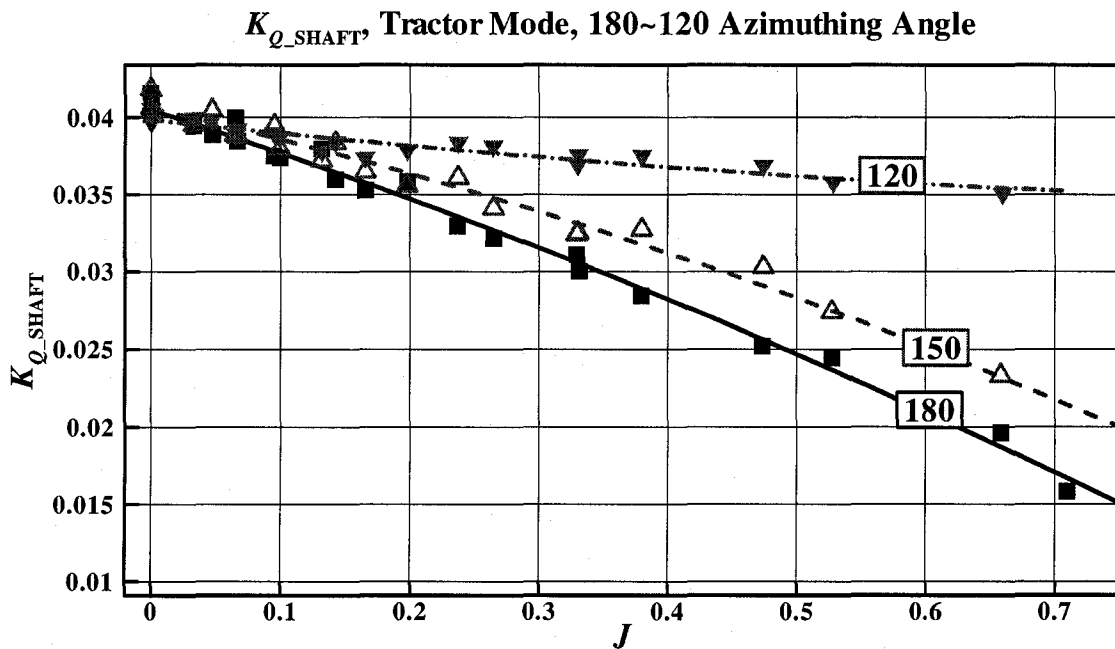
Figure 3-24: K_{Q_SHAFT} vs. J with different azimuthing angles (180-120 degrees)

3.5.4. Ice Related Loads (During Milling Period)

In this thesis, a propeller-ice interaction process is called a milling process. The failure modes of ice in this milling process are assumed to be composed of a crushing and shearing failure. As the propeller blade interacts with ice in the first quadrant operating conditions (positive ship speeds and positive propeller rotating speeds), pure crushing failure can be expected in the vicinity of the leading edge, where the region of the blade contacts with ice perpendicularly. Pure shearing failure, however, would occur at the pressure side of the propeller (if the angle of attack is positive and operating conditions are in the first quadrant), where the region of the blade contacts with ice in parallel. The propeller blades, interacting with ice, mainly experience a mixture of crushing and shearing failures during propeller-ice interaction.

The next set of figures, from Figure 3-25 to Figure 3-28, show the results for the 35 mm depth of cut in a tractor mode with an azimuthing angle of 180 degrees. Figure 3-25 and Figure 3-26 represent the shaft thrust and shaft torque coefficients versus the advance coefficient. Figure 3-27 and Figure 3-28 represent the blade thrust and torque coefficients measured from one of the blades versus the advance coefficient. In the figures, the open squares, open triangles and open deltas represent the maximum, average and minimum values respectively. The lines of fit through these points are 2nd order polynomials. Error bars at each symbol represent the range of the confidence level at 95 %. During propeller-ice interaction, large variations were observed with significantly increased magnitude of maximum and minimum values about the average values for both shaft and blade thrust/torque values. For example, the magnitudes of the maximum and minimum shaft thrust were approximately 400 % and 200 % larger than that of the average value at the advance coefficient of 0.4.

In the figures, the positive values mean that the additional thrust and torque, besides the separable hydrodynamic loads, are provided due to ice. The possible reasons are:

1. The pressure side of the blade interacts with ice physically;

2. Blockage effects occur (the blocked inflow simulates low advance coefficient conditions and hence the thrust and torque increase based on a typical thrust-torque-advance coefficient curve at the low advance coefficient);

3. Cavitation may increase the thrust and torque (Atlar et al., 2003).

With the increase in the advance coefficient, the maximum/average thrust and torque

coefficients increase. This phenomenon can be explained by the combination of effect of

advance coefficient, shadowing, depth of cut, and angle of attack. Detailed explanations

about these effects are given in the following sections.

It is also found that the ratio between average shaft thrust and average blade thrust is

approximately one during the milling period. The ratio between average shaft torque and

blade torque, however, is about 1.7 (average blade torque is 1.7 times of the averaged

shaft torque). The difference between shaft torque and blade torque may be influenced by

the effect of shaft dynamics in the present experimental model.
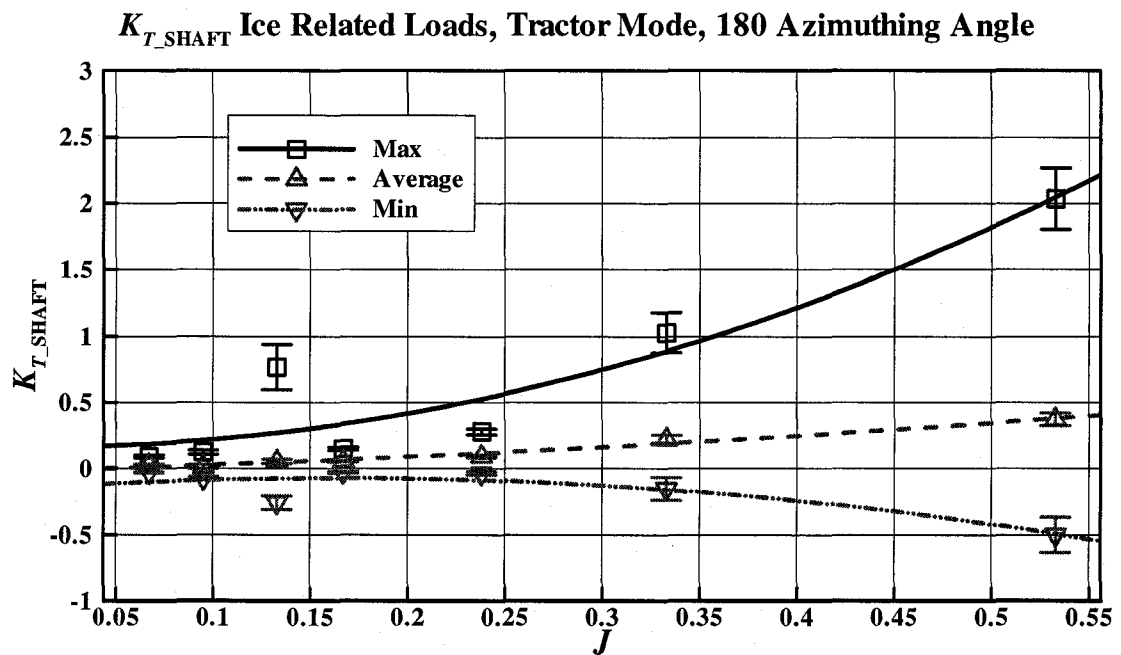
Figure 3-25: K_{T_SHAFT}, ice related loads at azimuthing angle of 180 degrees (tractor mode)
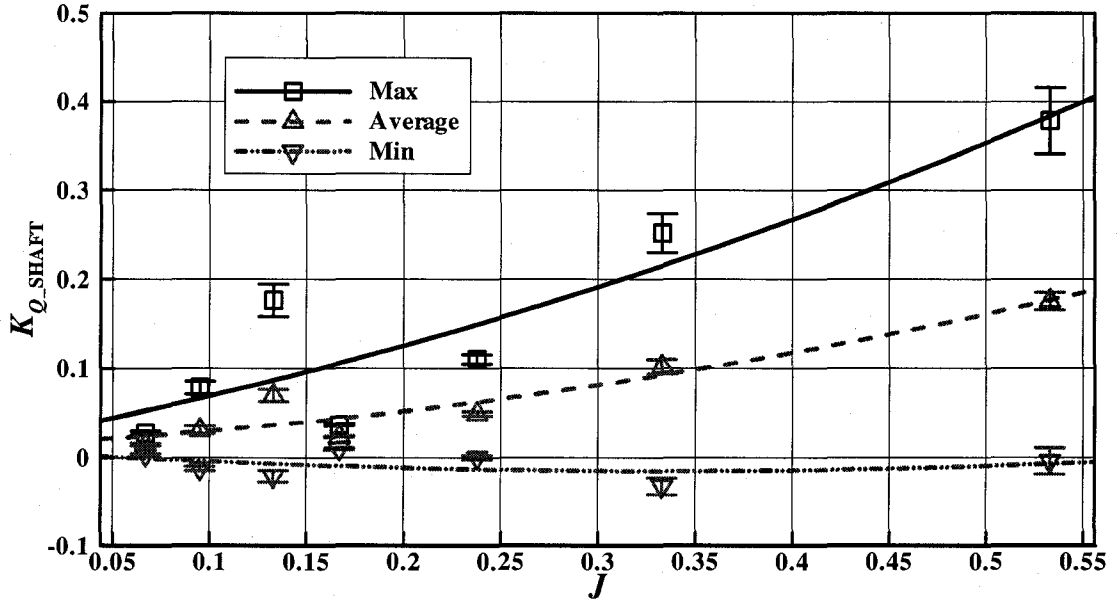
Figure 3-26: K_{Q_SHAFT}, ice related loads at an azimuthing angle of 180 degrees (tractor mode)
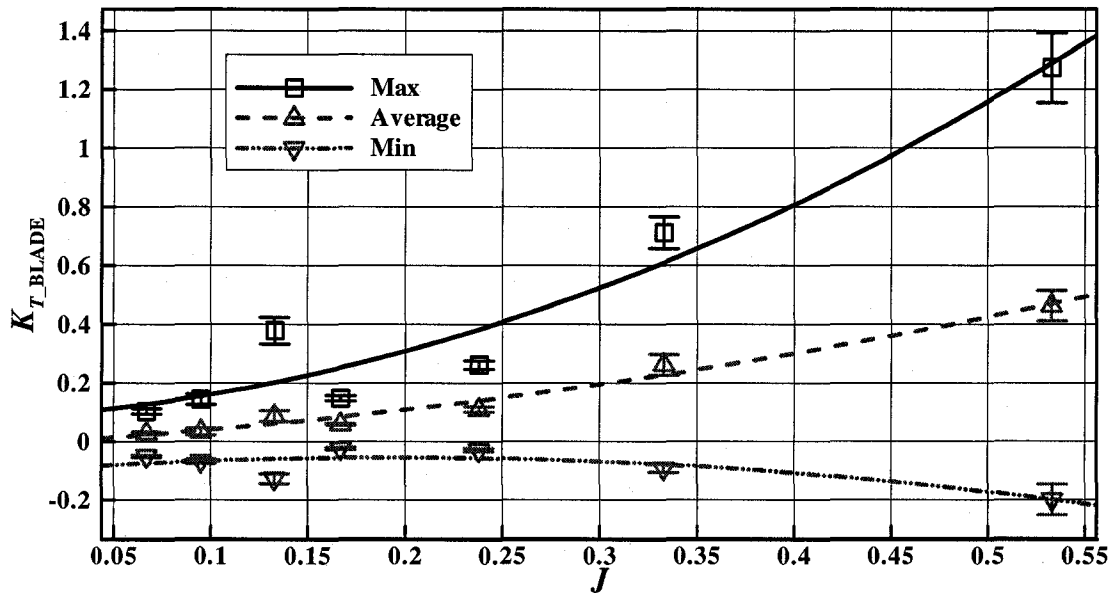
Figure 3-27: K_{T_BLADE}, ice related loads at an azimuthing angle of 180 degrees (tractor mode)
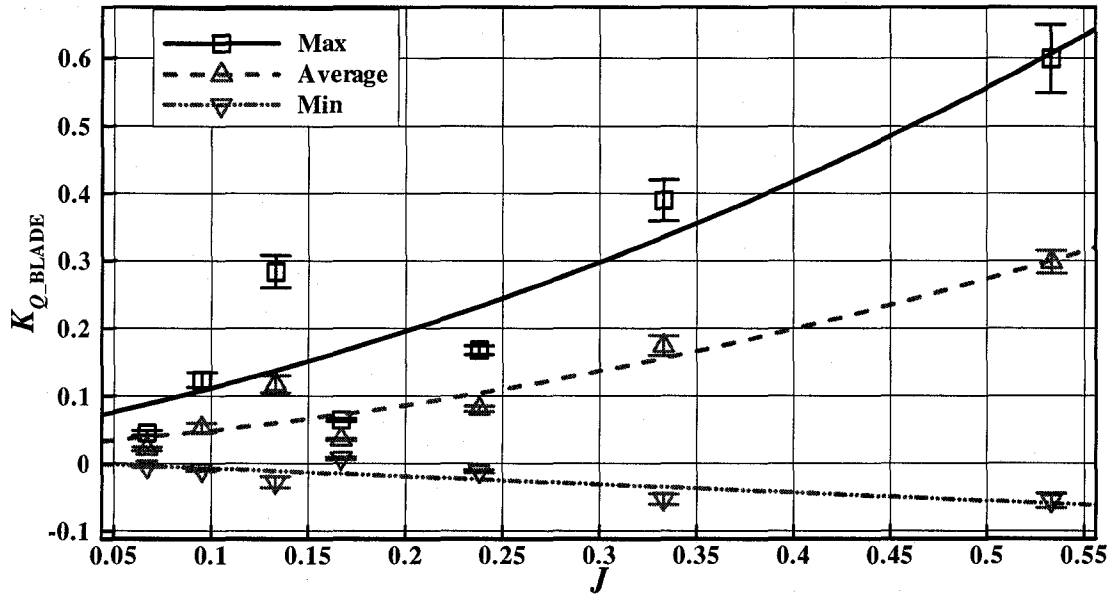
Figure 3-28: K_{Q_BLADE}, ice related loads at an azimuthing angle of 180 degrees (tractor mode)

3.5.4.1. Effect of Advance Coefficient/ Shadowing

As the advance coefficient increases, the average and maximum ice related loads increase. One of the possible reasons is a shadowing effect. When the propeller interacts with ice, the propeller blade experiences the part of the path generated by the previous blades and the consecutive blade does not fully contact with ice, as shown in Figure 3-29, which is called the shadowing effect. The figure is a top view, tractor mode and azimuthing angle of 180 degrees in ice covered water (the propeller mills the ice block from underwater). This figure shows one propeller at two time steps, which represent that the propeller rotates by 90 degrees. The colored area represents the ice block and the white area in the middle of the figure represents the milled area by the propeller blade. The propeller in the

72

right hand side (ice blocked is milled by the "Blade 2") is the previous time step, and the propeller in the left hand side (ice blocked is milled by the "Blade 3") is the present time step. As shown in the figure, the "Blade 3" in the present time step (left hand side) experiences white area (groove) created by the previous blade (the "Blade 2" in the previous time step, right hand side). The white area is called shadowing area. It is assumed that the "Blade 2" of the propeller in the right hand side contacts with the ice block for the first time (the propeller starts to rotate with "Blade 2"), so there is no shadowing area presented in the "Blade 2."
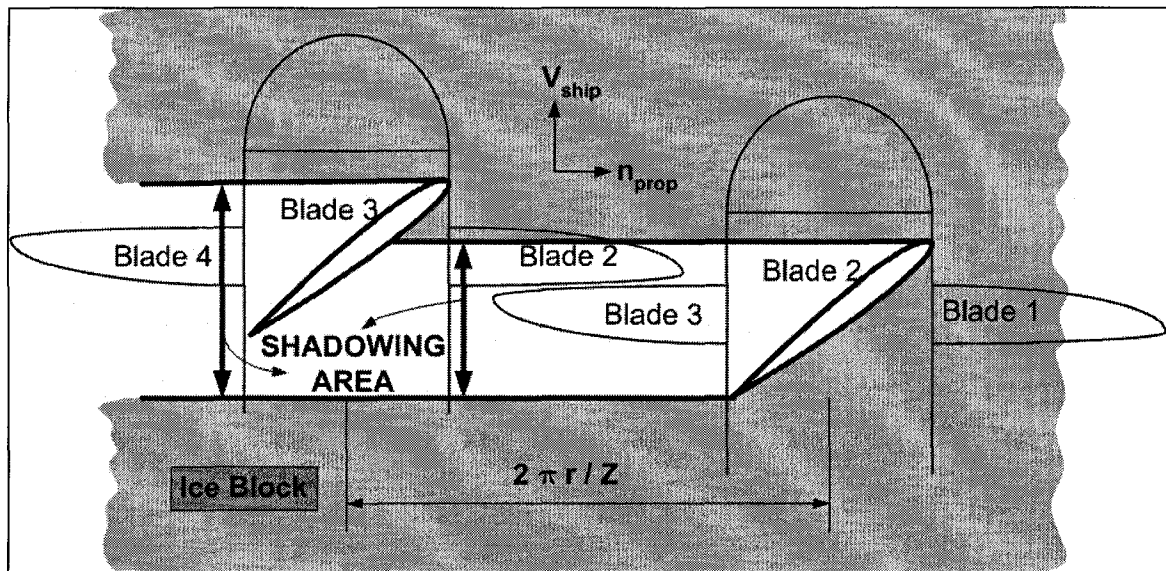
Figure 3-29: Shadowing area (Z is the number of the blades)

Figure 3-30 explains the effect of the advance coefficient using the shadowing and angle of advance. Three key blades demonstrate the blade's position at three different advance coefficients. $\beta_{i,j}$ is the angle of advance as defined in Equation (3-1) for each rps value.

$$\beta_{ij} = \text{arc tan} \left(\frac{V_A}{2\pi n_i r_j} \right) = \text{arc tan} \left(\frac{J_{ij}}{\pi(r_j / R)} \right), \tag{3-1}$$

where V_A is equal to V, n is rps, r is the radius of the propeller, J is the advance

coefficient, i is the index for rps (1,2 and 3 are for 10, 7 and 5 rps) and j is the index for

radial distance of each section. For simplicity, same blade section (same r_j values) is

considered in the next paragraph.

While the distance between two consecutive blades of the propeller are the same, the

axial ice contact length, $V /(Zn_i)$, between the two consecutive blade passes varies

because of the differences in the propeller rotational speeds for a given advance velocity.

As shown in Figure 3-30, the blade with the higher J (slower rps) experiences the larger

angle of advance, β, thus the longest axial ice contact length among the three and this

may be the reason for the largest torque measured in the highest J (slowest rps) case. As

this distance increases, the area of the blade in contact with ice increases and the

likelihood of encountering the groove made by the preceding blade pass decreases as

depicted in Figure 3-30.
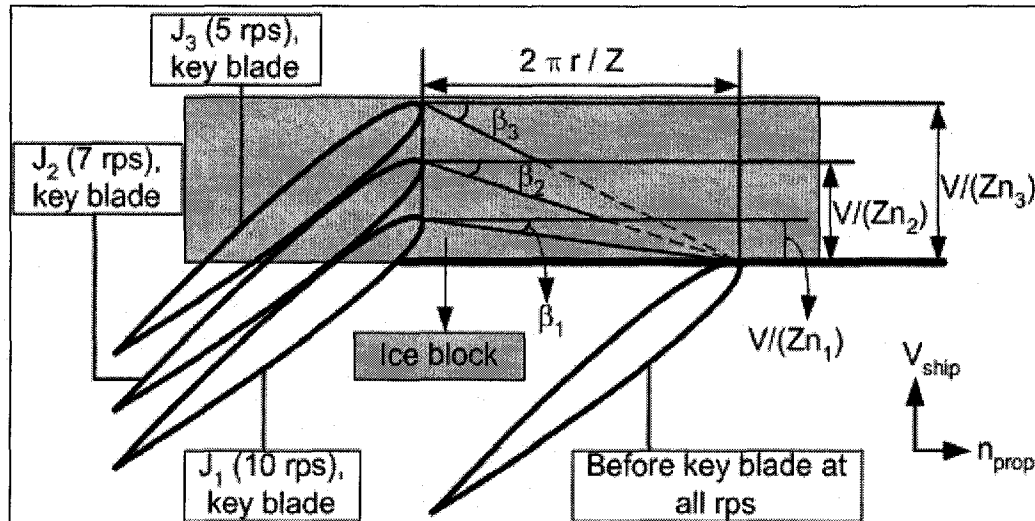
Figure 3-30: Conceptual sketch for propeller-ice interaction with top view, where β is the angle of advance, r is the radius of the propeller (0.15 m), Z is number of blades (4), V is carriage speed, n_1, n_2 and n_3 is 10, 7, and 5 rps respectively.

Therefore, the cases with higher J values result in higher torque values. Again other effects such as depth of cut or angle of attack need to be considered simultaneously to explain this trend. Once J passes the critical value at which the shadowing effect disappears, the blades are not affected by the shadowing effect. For example, when J is over 0.4 for 35 mm depth of cut, the shadowing effect is almost diminished. Detailed shadowing effect is explained the next paragraph.

The shadowing coefficient is defined by the ratio between shadowing area and blade area at the maximum blade section contacting with ice. When the depths of cut are 15 and 35 mm, the maximum blade section contacting with ice should be at 0.135 meter from the hub (0.9 R; R is radius of the propeller which is 0.15 meter) and at 0.115 meter from the hub (0.76 R), respectively.

The shadowing coefficient is estimated based on the chord length at the maximum blade section contacting with ice and the thickness of the section is ignored. The shadowing coefficients are calculated by Equation (3-2) and shown in Figure 3-31.

$$\text{Shadowing coefficient } (C_S) = \frac{Shadowing\ Area}{Blade\ Area}. \tag{3-2}$$

Figure 3-31 shows shadowing coefficients against the advance coefficient at two different depths of cut. For the depth of cut of 15 mm, the shadowing area disappears when the advance coefficient is 0.3 or more. Whereas, for the depth of cut of 35 mm, the shadowing area is still valid until $J = 0.4$.
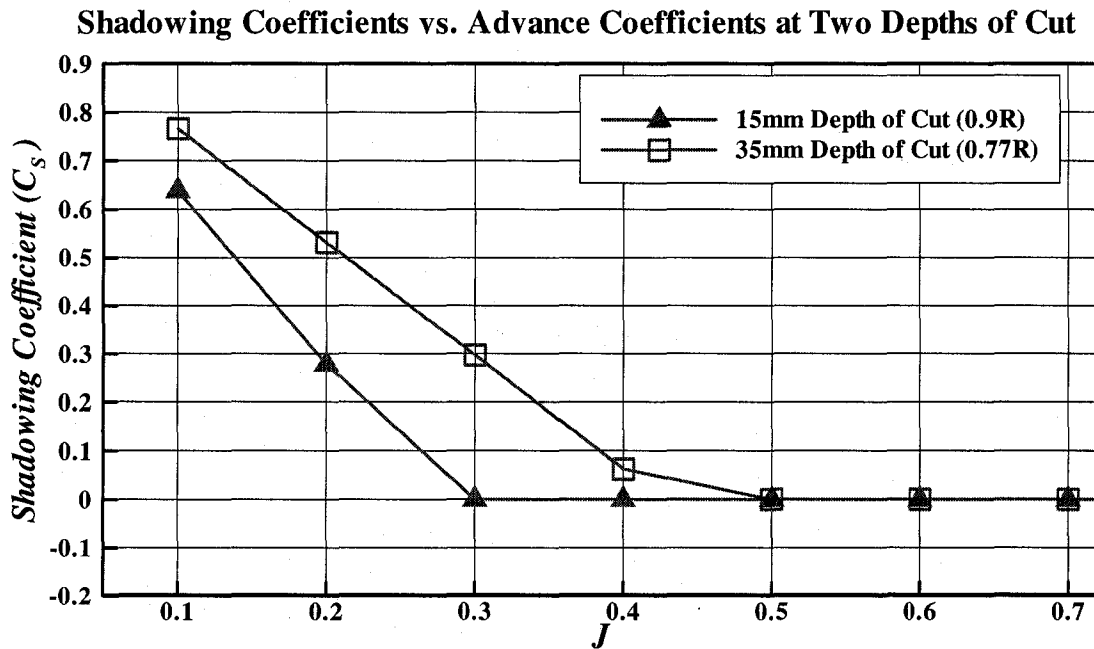
Figure 3-31: Shadowing coefficients vs. advance coefficients at two depths of cut

3.5.4.2. Effect of Depth of Cut

Figure 3-32 and Figure 3-33 show the blade thrust/torque coefficients from a depth of cut of 15 mm. The tests were repeated three times with identical test conditions (tractor mode and azimuthing angle of 180 degrees). The solid squares, solid triangles and solid deltas represent the maximum, average and minimum values respectively. The lines of fit through these data points are 2nd order polynomials. Again, in the ice related loads presented, the separable hydrodynamic loads have been removed.

When the advance coefficients increase from zero to about 0.33, the blade thrust and torque coefficients increase. This is because the shadowing effect decreases as described in the previous section (the shadowing effect can be diminished at $J = 0.3$ for a depth of cut of 15 mm case). When the advance coefficients are larger than 0.33, however, the thrust and torque values start to decrease. This can be explained by the angle of attack. For 15 mm depth of cut, the pitch angle is less than that of 35 mm depth of cut, consequently decreasing trends due to the less angle of attack occur at a lower advance coefficient (between the advance coefficients of 0.35 and 0.4) than that in 35 mm depth of cut (the advance coefficient that shows decreasing trends is not found from the present experimental tests). The effect of angle of attack is also discussed in the next section.
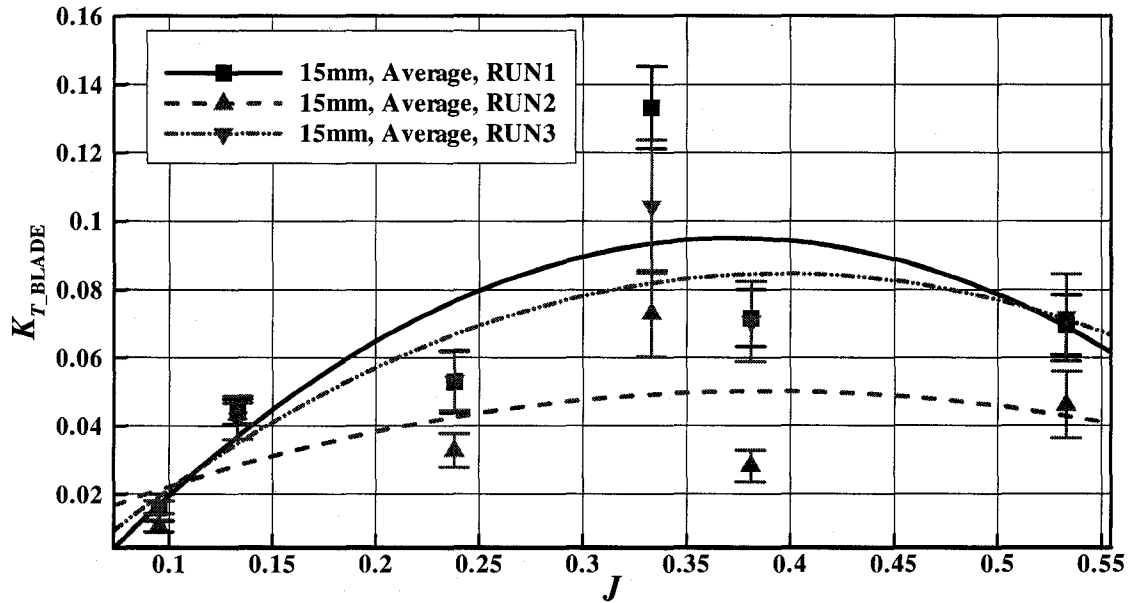
Figure 3-32: K_{T_BLADE}, average ice related loads, tractor mode, repeat runs (15mm)
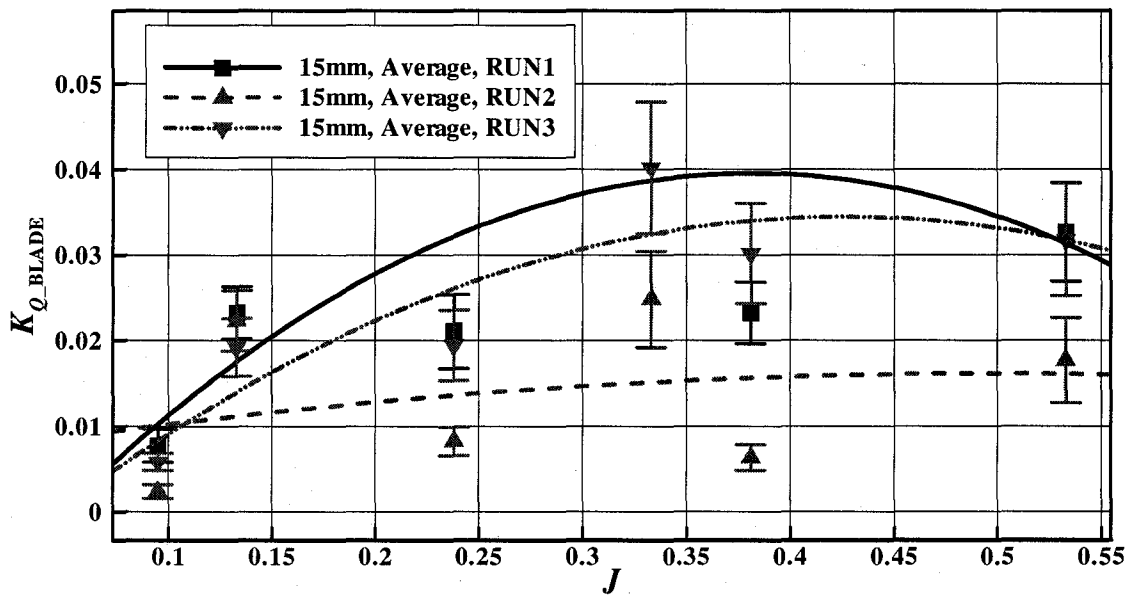
Figure 3-33: K_{Q_BLADE}, average ice related loads, tractor mode, repeat runs (15mm)

3.5.4.3. Effect of Geometric Angles of Attack

Since the ice sheets are assumed to be stationary, the induced velocities due to the propeller suction are assumed to be zero. Consequently, the geometric angle of attack can be used as an effective angle of attack. Based on the pitch angle at the maximum blade section contacting with ice, the geometric angles of attack are calculated and shown in Figure 3-34.

Geometric Angles of Attack vs. Advance Coefficients at Two Depths of cut
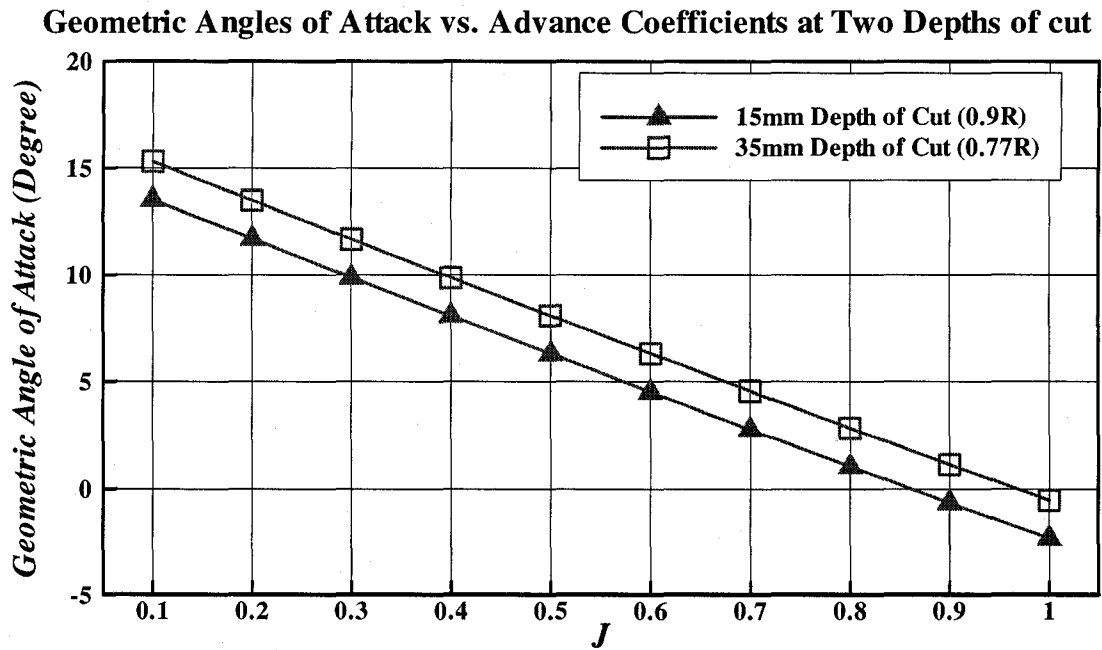
Figure 3-34: Geometric angles of attack vs. advance coefficients at two depths of cut

As J increases, the geometric angle of attack decreases. As the depth of cut increases from 15 to 35 mm, geometric pitch angle at the section contacting with ice increase and the geometric angle of attack decreases consequently. Therefore, the depth of cut of 15 mm shows decreased trend of blade thrust/torque coefficients due to the less angle of

attack occur at a lower advance coefficient (between the advance coefficients of 0.35 and 0.4) than that in 35 mm depth of cut.

In Appendix C, results for the ice related loads are shown in detail: shaft loads including thrust and torque measured from the shaft, and blade loads including thrust, torque, in-plane bending moment, out-of plane bending moment and spindle torque measured from one of the blades for various azimuthing angles (from 180 to 30 degrees). The results of the repeat runs for the tractor mode with 15 mm depth of cut are also given.

3.5.5. Total Loads in Ice (Ice Covered Water Characteristics)

The total loads consist of the separable hydrodynamic loads and ice related loads. Figure 3-35 through Figure 3-37 are some of the results for the total loads in ice covered water at a tractor mode with a 35 mm depth of cut. The solid squares, open triangles, solid deltas, open left triangles and solid diamonds represent the azimuthing angles of 180, 150, 120, 90 and 60 degrees, respectively. The curves fitted through these points are 2nd order polynomial lines of best fit.

Figure 3-35 shows the unit thrust coefficient versus the advance coefficient at five different azimuthing angles. As the azimuthing angle decreased from 180 to 120 degrees, the unit thrust decreased due to the similar reasons described in Section 3.5.3. The qualitative trends, however, are similar to those in separable hydrodynamic loads, but the magnitude in ice covered water is significantly higher. In addition to the separable

hydrodynamic loads, ice loads (resistance) acting on the strut play a major role in the increase of the magnitude at given azimuthing angles.

At the azimuthing angles of 90 and 60 degrees, the average unit thrust values are higher than those in any other azimuthing angles used in the experiments, i.e. 180, 150 and 120 degrees. This may be due to the reverse wake of the propeller; the reverse wake tends to push the ice blocks out of its direction and acts to reduce the ice contact forces on the strut.
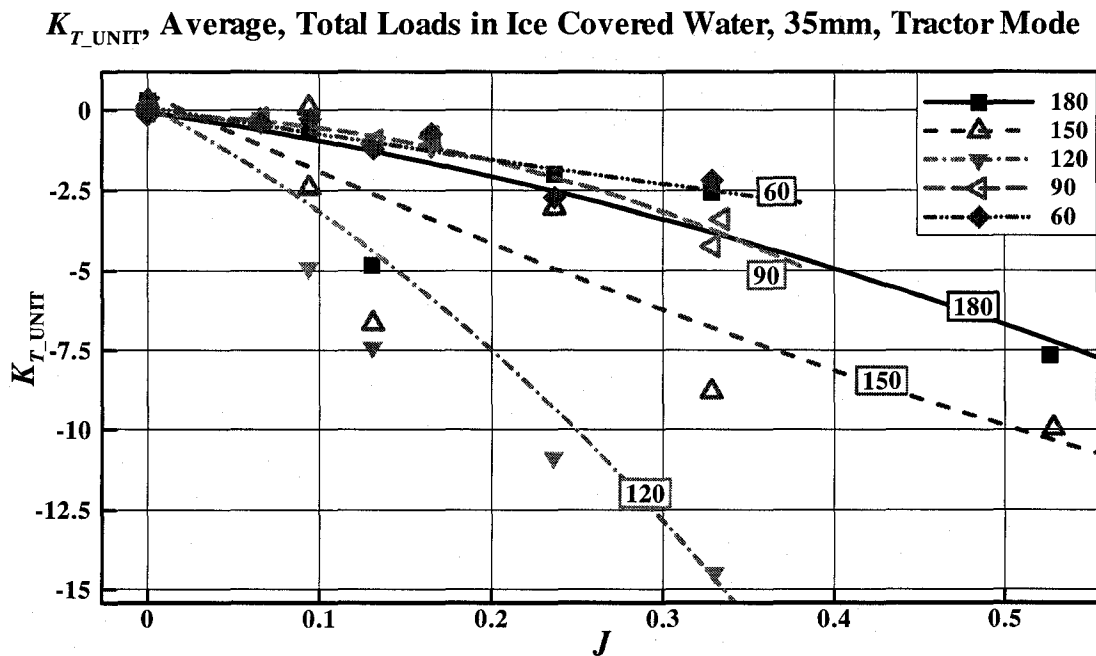
Figure 3-35: K_{T_UNIT}, total loads at various azimuthing angles in ice covered water

The next two figures, Figure 3-36 and Figure 3-37, show the average shaft thrust and torque coefficients against the advance coefficient at five different azimuthing angles.

The general trends of the total loads are similar to that of the ice related loads reported in Section 3.5.4. When the azimuthing angles are between 180 and 120 degrees, similar trends are shown. As the azimuthing angle decreases from 180 to 90 degrees, the geometric angle of attack increases. Accordingly, the failure mode of ice on the pressure side could change from a shearing failure to a crushing failure mode. The loads due to the crushing are generally two to four times higher than those due to the shearing, consequently this can explain the increased thrust at the decreased azimuthing angle until 90 degrees. In addition, the effect of shadowing area and oblique inflow could influence the results. Once the azimuthing angle is less than 90 degrees, e.g. 60 degrees, the reversing wake and unstable inflow may drop the shaft thrust and torque.

In Appendix D, results for the total loads in ice covered water are shown in detail: unit thrust, transverse/vertical force on unit, shaft thrust/torque and blade thrust/torque at the different azimuthing angles (from 180 to 60 degrees).

K_{T_SHAFT}, Average, Total Loads in Ice Covered Water 35mm, Tractor Mode
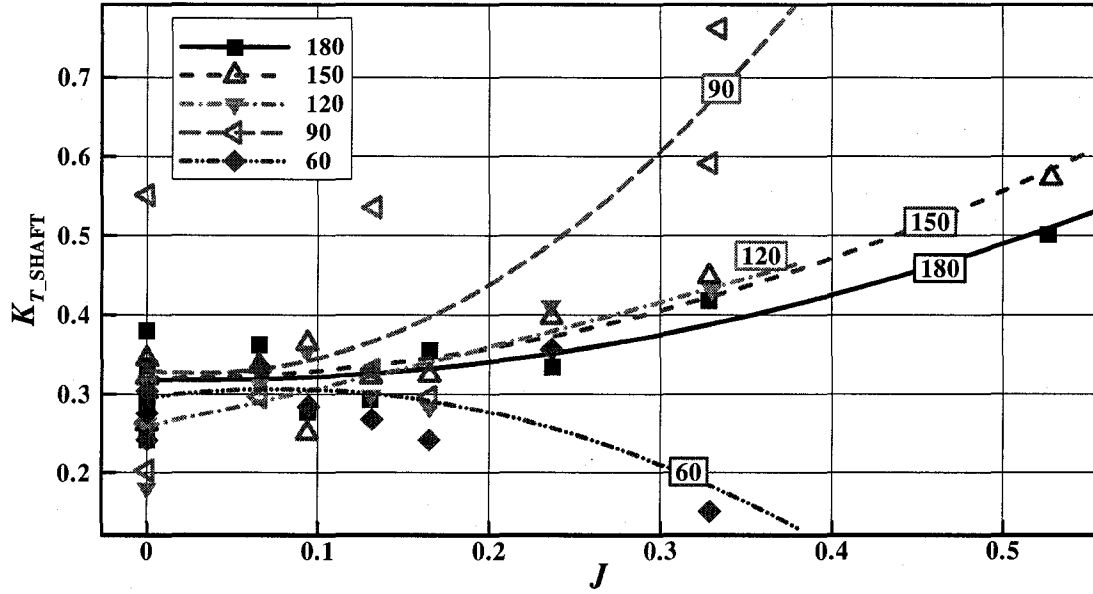
Figure 3-36: K_{T_SHAFT}, total loads at various azimuthing angles in ice covered water

K_{Q_SHAFT}, Total Loads in Ice Covered Water, Average, 35mm, Tractor Mode
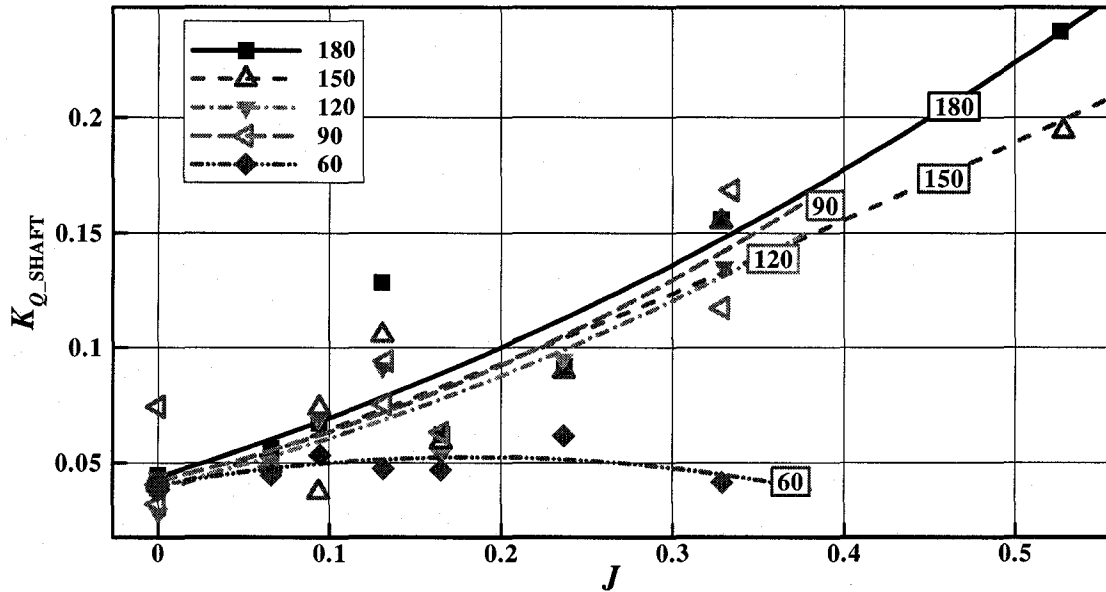
Figure 3-37:K_{Q_SHAFT}, total loads at various azimuthing angles in ice covered water

83

3.6. Comparisons with Previous Studies

In this section, results from the previous studies are compared with those from the present experiments. Two previous studies, Moores (2001) and Luznik et al. (1995), are presented for the ice related loads and blockage loads respectively.

As introduced in the previous chapter, Moores used a highly skewed propeller, which is significantly different shape from the present model. Data analysis methods employed were also different, because Moores' model did not have the capability to measure the angular position of the blade(s); the milling period was estimated based on the variations in the measured loads. Test conditions including model ice, however, are similar to those in the present tests.

In Figure 3-38, the results of the 15 mm and 35 mm depth of cut from the present tests are compared with the results of Moores with different depths of cut: 20.5 mm, 34 mm, and 43 mm. The figure illustrates that the average blade thrust coefficients (K_{T_BLADE}) increase with advance coefficients up to a certain value of advance coefficient (between 0.3 and 0.4), after which a decrease is observed. Moores' results also show that the magnitudes of the blade thrust increase with the increase in the depth of cut and their peak points corresponding to higher depths of cut are found at higher advance coefficients. In the case of the 35 mm depth of cut from the present experiments, however, the results do not seem to ever reach the peak value similar to the others for the advance coefficient range given in the figure.

K_{T_BLADE}, Average, Ice Related Loads
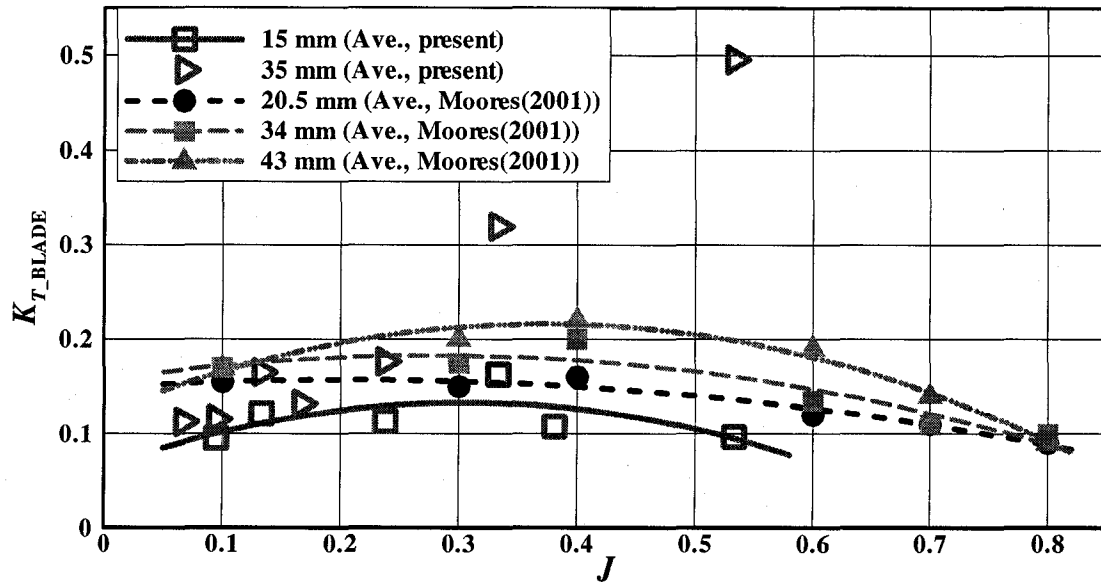
Figure 3-38: Comparison of average blade thrust coefficient (K_{T_BLADE}, one blade only) with previous test results (ice-related loads + separable hydrodynamic loads during a milling period). The lines are the 2nd order polynomial lines of best fit

With respect to a blockage effect, Luznik et al. (1995) presents the experimental results using very similar propeller geometry to the one used in the present study operating in the vicinity of an ice block. They reported an increase of 65-75 percent in the shaft thrust coefficient from the uniform flow performance. Figure 3-39 shows the comparison of the shaft thrust coefficients from open water, ice blockage and ice milling conditions. The solid line shows the thrust coefficient in open water conditions, and the dashed line shows the maximum possible thrust coefficient in blocked flow. Solid triangles and solid circles show the maximum total loads in ice for the 15 mm and 35 mm depths of cut, respectively. Generally, the maximum shaft thrust coefficients in ice covered water are higher than those in open water. For example, the maximum shaft thrust coefficients from

35mm, 15mm depths of cut, blockage are about 70%, 200%, and 700% higher than the

average open water results at the advance coefficient of 0.4.
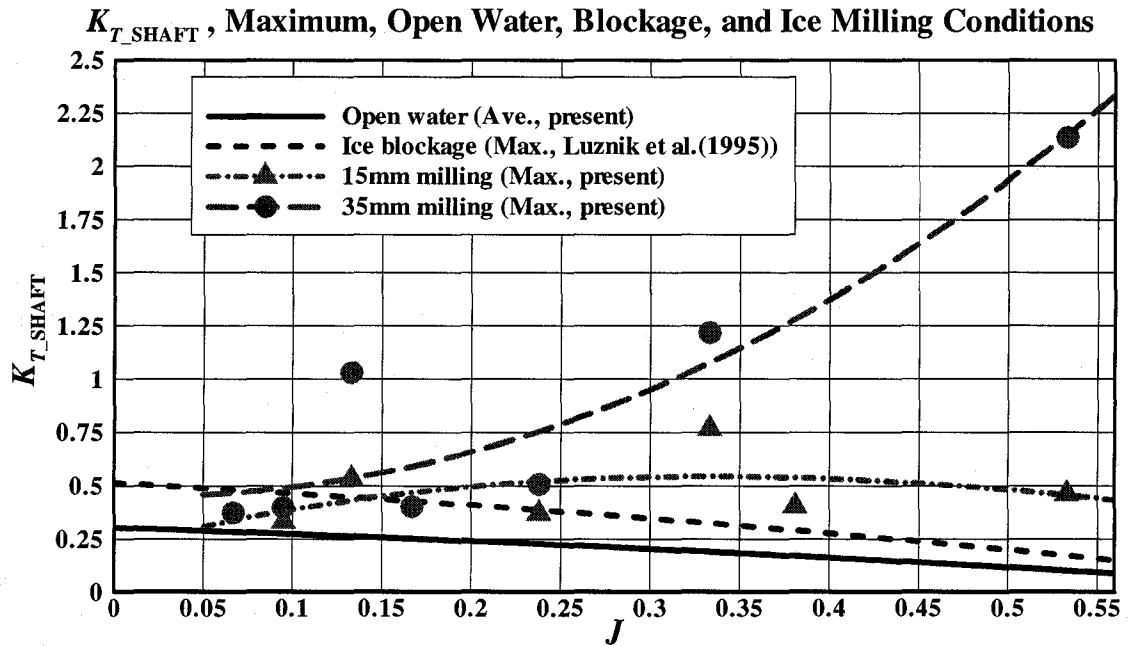
Figure 3-39: Thrust coefficient comparison among open water, ice blockage and ice milling conditions (for 15 and 35 mm depth of cut: ice-related loads + separable hydrodynamic loads during a milling period)

It is noted that the highest three values of the shaft thrust coefficients corresponding the

advance coefficients of 0.133, 0.33 and 0.53 are performed at 5 rps with the 35 mm depth

of cut tests (Figure 3-39). The effect of rps during propeller-ice interaction is discussed in

the next section.

3.7. Discussion of Experimental Results

3.7.1. Effect of RPS

3.7.1.1. Effect of Strain Rate

The effect of rps can be interpreted as the effect of strain rate. As mentioned in Section 2.5.2, Jones (1997) reported that the compressive strength increased as strain rate increased for the two types of ice. Later, Jones (2006) collected uniaxial compressive strength data from the various sources and compared various types of ice against strain rate (Figure 3-40). Although the present model ice (EG/AD/S) is not the same as any types of ice, its trends (compressive strength vs. strain rate) are similar (Moores et al., 2001a; see Section 2.5.2). For EG/AD/S model ice at high strain rate, $\dot{\varepsilon} > 0.5/s$, Moores et al. reported that the compressive strength showed increased trends with strain rate, though the results included a lot of scatter. Similar works were done by Varma (2000) with blade shaped indentation at various indentation speeds (from 0.5 to 1 m/s) using EG/AD/S model ice. Varma reported that there were not any particular trends of the effect of indentation speed but higher indentation speeds minimized the data variation.

Based on the results from Jones (2006) and Moores et al. (2001a), the ice compressive strength has generally increase trends as the strain rate increase at the high strain rate region such as $\dot{\varepsilon} > 0.5/s$.
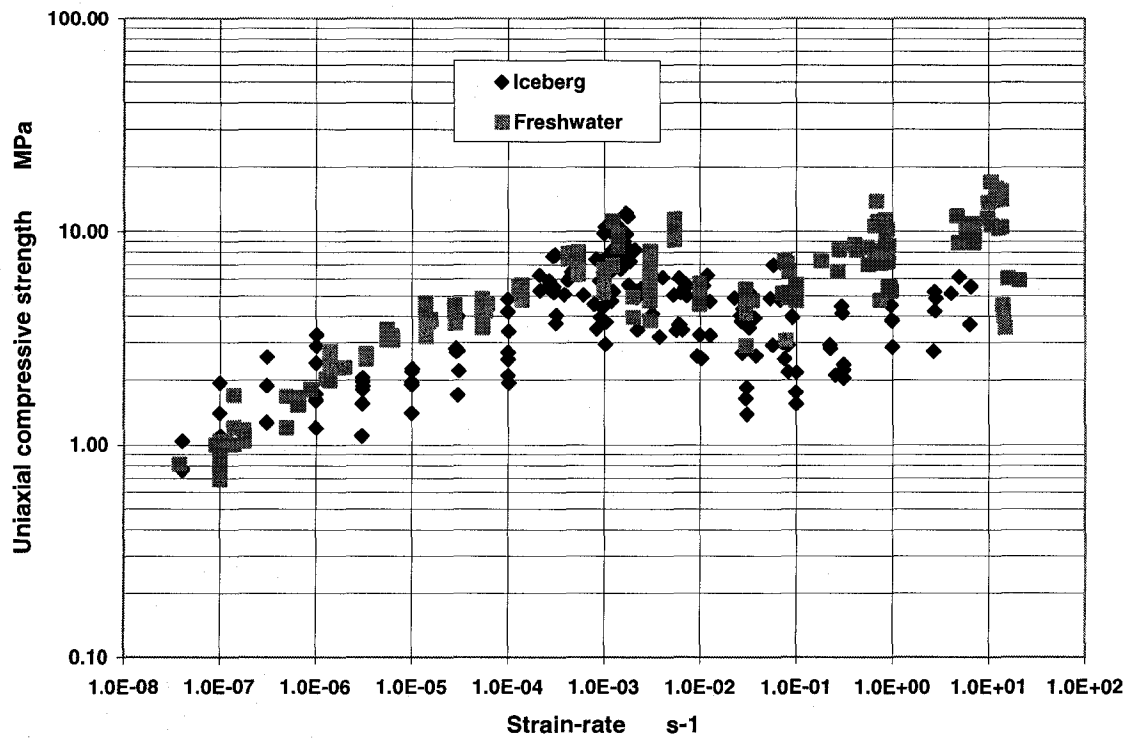
Figure 3-40: Uniaxial compressive strength vs. strain rate (after Jones, 2006)

The effect of the shaft speed on the maximum thrust and torque coefficients is

investigated in Figure 3-41 and Figure 3-42. Three different propeller speeds were used in

these tests: 5, 7 and 10 rps. Solid squares with solid line, solid squares with dotted line

and open squares with solid line denote the shaft torque coefficients based on the

maximum values measured during the ice milling periods for 5, 7 and 10 rps, respectively.

Solid line without symbols shows the average shaft values from open water tests. These

tests were carried out within an hour after the first test in this series in the same ice

channel. The range of measured compressive strength values for ice varied from 210 to

190 kPa. The results show that the case with lower rps requires a higher shaft torque. A

possible explanation is given below.

As explained in 3.5.4.1, the increase in the advance coefficient results in the increase in the ice related loads. Since the rps is in inverse proportion to the advance coefficient, the increase in the rps causes a decrease in the ice related loads. However, at the same advance coefficient value (for example, $J = 0.133$ at Figure 3-42), the rps seems relatively distinguished from each other ($10K_{Q\_SHAFT}$ are 2.06, 1.16 and 0.64 for 5, 7 and 10 rps). For the shaft thrust curve in Figure 3-41, the ice related loads at 5 rps are about three times higher than those at 7 or 10 rps. This is contrary to the general trend of compressive strength against strain rate as discussed in the beginning of this section. The present test results cannot be explained clearly, but they may include uncertainties associated with ice fracture, ice failure mechanism and ice crack propagation.
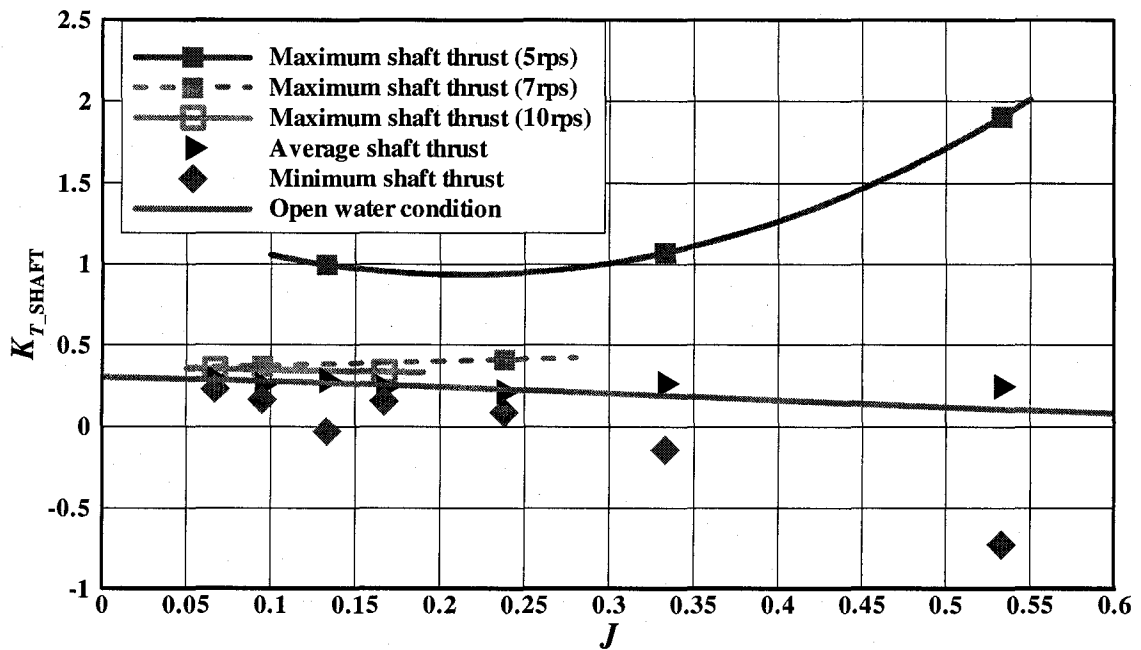
Figure 3-41: Maximum, minimum and average K_{T_SHAFT} for the 35mm depth of cut (ice-related loads + separable hydrodynamic loads during milling period) and open water
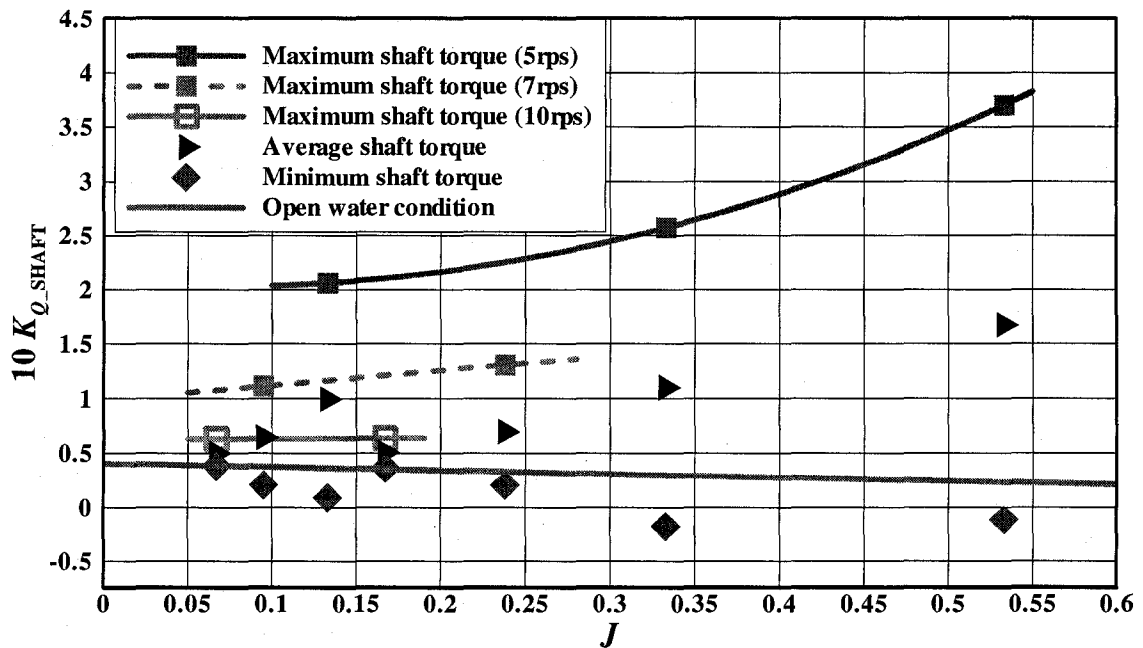
Figure 3-42: Maximum, minimum and average K_{Q_SHAFT} for the 35mm depth of cut (ice-related loads + separable hydrodynamic loads during milling period) and open water

3.7.1.2. Strain Rate vs. Propeller Rotating Speed

In this section, a relationship between strain rate and propeller rotating speed is discussed. For indentation tests (Jones, 1997 and Moores et al., 2001a), strain rate was defined as shown in Equation (3-3).

$$\varepsilon = \frac{\Delta l}{l_o}, \quad \dot{\varepsilon} = \frac{\varepsilon}{t} = \frac{\Delta l}{l_o t} = \frac{v}{l_o}, \tag{3-3}$$

where ε is strain, $\dot{\varepsilon}$ is strain rate, Δl is deformed length, l_o is undeformed length, t is total contacting time and v is indentation speed.

For the engineering points of view such as ship-ice or structure-ice interactions, various empirical formulae are widely used for their convenience. One of the typical empirical formulae is shown in Equation (3-4) (Cammaert and Muggeridge, 1988, p. 228).

$$\dot{\varepsilon} = \frac{V}{4D} \, , \qquad\qquad (3\text{-}4)$$

where V is the contact speed and D is the width of the indentor.

Since there are no formulae for high contact speed such as propeller rotating speed, Equations (3-3) and (3-4) were modified for propeller-ice interaction. For Equation (3-3), Δl and l_o are same as the length of blade traveling into ice at the maximum blade section contacting with ice and t is time of contacting with ice. For Equation (3-4), V is the propeller rotating speed ($V = 2\pi n r$ where r = radius of the propeller or $V = 2\pi n r_1$ where r_1 = distance between hub to center of the ice contact point and n = rps) and D is the diameter of the propeller or the thickness of the propeller blade at r_1. The expected strain rates with modified strain rate calculations for 35 mm depth of cut are shown in Table 3-5. Based on Table 3-5, the strain rate for propeller-ice interaction can be ranged from 4×10^0 to 1.6×10^2 /s.

Table 3-5: Estimated strain rate for propeller-ice interaction

RPS	Strain rate from Equation (3-3)	Strain rate from Equation (3-4)	
		D = diameter, r = radius	D = thickness, $r = r_1$
5	17/s	4/s	78/s
7	24/s	6/s	109/s
10	34/s	8/s	156/s

3.7.2. Effect of Compressive Strength of Model Ice

From the repeat tests at 15 mm depth of cut, the effect of the compressive strength was investigated, as shown in Figure 3-43. The symbols represent the maximum values observed during milling periods for each test, and the lines through these points represent 2nd order polynomial lines of the best fit. Each case in the figure, base case and the two repeats, consisted of three different carriage velocities (0.2, 0.5 and 0.8 m/s) conducted at two different rps values: 5 and 7. Since the time each case done and the section of the ice sheet used for each case were different, ice properties encountered during the tests were possibly different. This is because of the spatial and temporal variations of the model ice. The "Base case" and "Repeat 1" were tested consecutively in the Centre Channel of the same ice sheet, and "Repeat 2" was tested an hour later in the South Channel. The estimated compressive strengths for "Base case", "Repeat 1" and "Repeat 2" were 131.2, 129.0 and 107.4 kPa, respectively. The results show that the compressive strength of the ice over this range does not have significant effect on the magnitudes of the ice milling loads.

K_{T_BLADE}, Ice Related Loads, 15mm Depth of Cut, 180 Azimuthing Angle, Repeat Tests
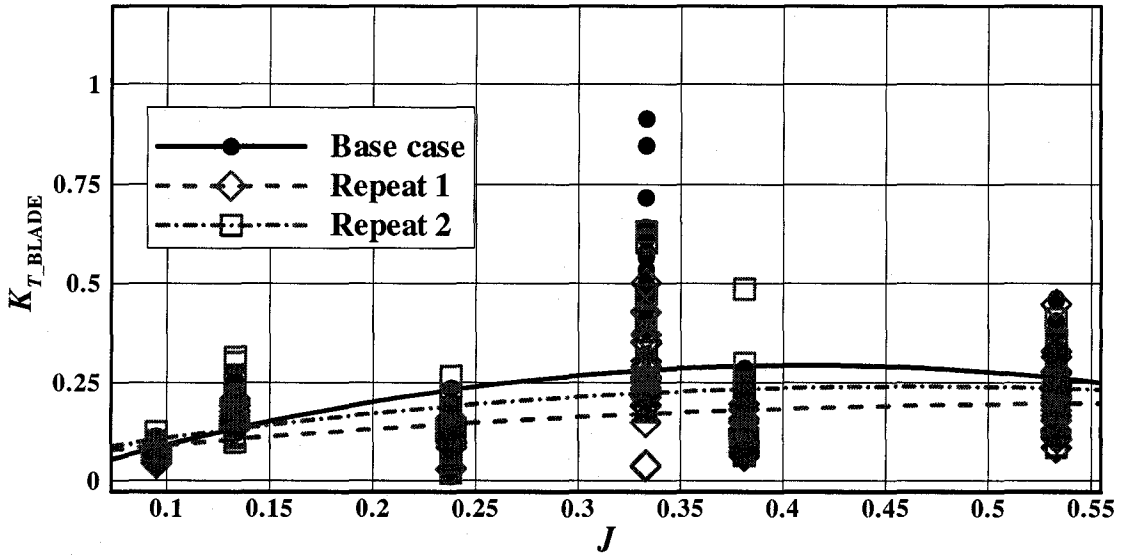
Figure 3-43: Maximum K_{T_BLADE} from the repeat tests (an azimuthing angle of 180 degrees, a depth of cut of 15 mm)

3.7.3. Variation of Experimental Results

Some results show their maximum and minimum as well as average values. It is easily found that the maximum or minimum values are sometimes significantly higher than the average values; for example, the maximum shaft thrust in ice related loads at $J = 0.4$ are approximately four times higher than the average values.

The large scatter in the measurements may have been caused by the way interaction with the ice occurred. It was observed during the experiments that some pre-sawn ice blocks accelerated and moved towards the propeller causing additional impact loads rather than

pure milling loads only. Note that the ice sheet was pre-sawn to reduce the crushing loads on the strut of the model propulsor.

The variation of the measurements also results in a spalling, cracking or damage of the ice sheets from the previous blade(s) as well as the nature of the ice loading. The other possible reasons are: (1) Ice properties may vary depending on location across the ice sheet, (2) The irregularity in the ice thickness along the path of the propeller may lead to a changing depth of cut. Generally, a large variation of the measurements is a typical feature for propeller-ice interaction tests (Searle, 1999 and Moores, 2002).

3.7.4. Deterministic Design Loads

In order to decide the design loads for the propeller that is operating in ice covered water, the maximum or minimum values (whichever, the bigger magnitude) from the present tests may be more important than average values. An extreme probability method might be useful for the deterministic ice design loads with appropriate reliability.

3.7.4.1. Extreme Probabilistic Methods

For extreme probability, there are three classical asymptotic models depending on the parent distribution. These are expressed as follows:

$$\text{Type 1: } F(x) = \exp[-\exp(-x)] \text{ for } -\infty < x < \infty , \qquad (3-5)$$

Type 2: $F(x) = \exp(-x^{-\alpha})$ with $\alpha > 0$ for $-\infty < x < \infty$, $\qquad$ (3-6)

Type 3: $F(x) = \exp[-(-x)^{\alpha}]$ with $\alpha > 0$ for $-\infty < x < \infty$. $\qquad$ (3-7)

Types 1, 2 and 3 are normally named as Gumbel, Frechet and Weibull distributions, respectively. For the maxima, the Type 1 distribution is the most useful because it is the natural extreme for most parent distributions (Jordaan, 2004).

3.7.4.2. Basic Concepts

At first, all events are assumed to have independent and identically distributed (*iid*) random quantities. The set of random quantities is, for example,

$$\{X_1, X_2, X_3, ..., X_i, ..., X_n\}. \qquad (3-8)$$

The extreme value Z can be defined as

$$Z = \max(X_1, X_2, X_3, ..., X_i, ..., X_n). \qquad (3-9)$$

The cumulative density function, $F_Z(z)$, can be written as

95

$$F_Z(z) = \Pr(all\ X_i \leq z) = F_X^{\ n}(z).$$

(3-10)

3.7.4.3. Application to Propeller-Ice Interaction

Propeller-ice interactions can be explained by the Poisson process because the events assumed to be *iid* and interaction would not occur continuously. For the extreme probability method, the only interesting region is the tail of the probability distribution and it may follow an exponential or double exponential form (Type 1, Gumbel distribution). In order to use the extreme statistics, the data set was ranked in descending order from order statistics (Castillo, 1988). The Weibull plotting position [*i/(n+1)*] was used for the exceedance probability and double exponential form was used for the tail distribution. Therefore, the exceedance probability was defined as a double logarithm. In the Weibull plotting, n is the total number of interactions and i is the sequence number. The one percent exceedance probability (for example "100 year" load case if the distribution is based on one year), can be written as

$$-\ln(-\ln(P_e')) = 4.6,$$

(3-11)

where $P_e' = 1 - P_e$, and $P_e = 0.01$.

When a propeller blade contacted ice, the ice-related loads were calculated, i.e. the total number of events was the same as the number of the ice contacts. The decision of a milling period was made by using blade angular position as shown in Section 3.4.3.

Although blade angular position is within the target range of α_m, a non-contact may

occur because of the shadowing of the blades or the irregularity of the ice feeding.

Therefore, the number of interactions (hits) is counted only when the ice-related loads are

larger than the maximum loads measured in open water tests (no ice case).

The Poisson distribution can be written as

$$P(n:\mu) = \frac{e^{-\mu}(\mu)^n}{n!}, \text{ n} = 0, 1, 2..., \tag{3-12}$$

where μ is the expected number of interactions (hits) per unit time for future estimation

($\mu = r\gamma$, where r is the proportion of hits and γ is the total expected number of events).

For most practical cases, the distribution of the tail can be represented by an exponential

or double exponential form (Jordaan et al., 1993), which is

$$1 - F_X(z) = \exp(-[az + b]). \tag{3-13}$$

A new Poisson process of tail for random quantities is:

$$\mu' = \mu(1 - F_X(z)), \tag{3-14}$$

$$P(n':\mu') = \frac{e^{-\mu'}(\mu')^{n'}}{n'!} \text{ n'} = 0, 1, 2... . \tag{3-15}$$

If *n'* is assumed to be equal to zero for the extreme case, then

$$F_Z(z) = \exp(-\mu') = \exp\{-\mu[1 - F_X(z)]\}$$

$$= \exp\{-\mu(\exp[-(az+b)])\}$$

$$= \exp\{-\exp(-[az+b] + \ln\mu)\}. \qquad (3\text{-}16)$$

Jordaan (2004, p. 501) shows the full derivation of equations with detailed explanation.

3.7.4.4. Test Matrix and Results

The present extreme probability analyses use the ice related loads from experimental results and test matrix is shown in Table 3-6. "Case 1" shows the results when the azimuthing angle is between 180 and 150 degrees. "Case 2" shows the results when the azimuthing angle is less than 150 degrees.

Table 3-6: Test conditions for extreme probability analysis

Tractor Mode	Azimuthing Angles (°)	Carriage Velocity	RPS	Ice Conditions
Case1	180 and 150	0.2, 0.5, and (0.8)	5, 7, and 10	Pre-sawn
Case2	120, 90, and 60	0.2, 0.5, and (0.8)	5, 7, and 10	Pre-sawn

In the calculations, the following assumptions are used as below:

- All events are independent and identically distributed (*iid*);

- Same contacting area (for a given test run, i.e. constant propeller rotational and advance velocities, the area of the blade contacting the ice during milling is assumed to be the same for each rotation of the propeller. Though, this area might vary during a test run);

Figure 3-44 shows the shaft thrust distribution in time series acting on the propeller blade in pre-sawn ice with 35 mm depth of cut. In order to use the extreme probability method, an appropriate return period must be defined. For simplicity, it is assumed that the return period is the time it took for the test run under consideration. This is called a unit time for the sake of argument. For the purpose of illustrating the concept, number of hits is then projected to a time scale equal to the 100 times of this unit time. This return period, however, can be controlled using a proper interaction scenario.

Figure 3-45 shows the total force on the blade, presented in Figure 3-44, against exceedance probability. If the "100 unit times" loads of the total force were considered, the exceedance probability value would be 4.6 from Equation (3-11). If the exceedance probability is determined, the design loads can be chosen.
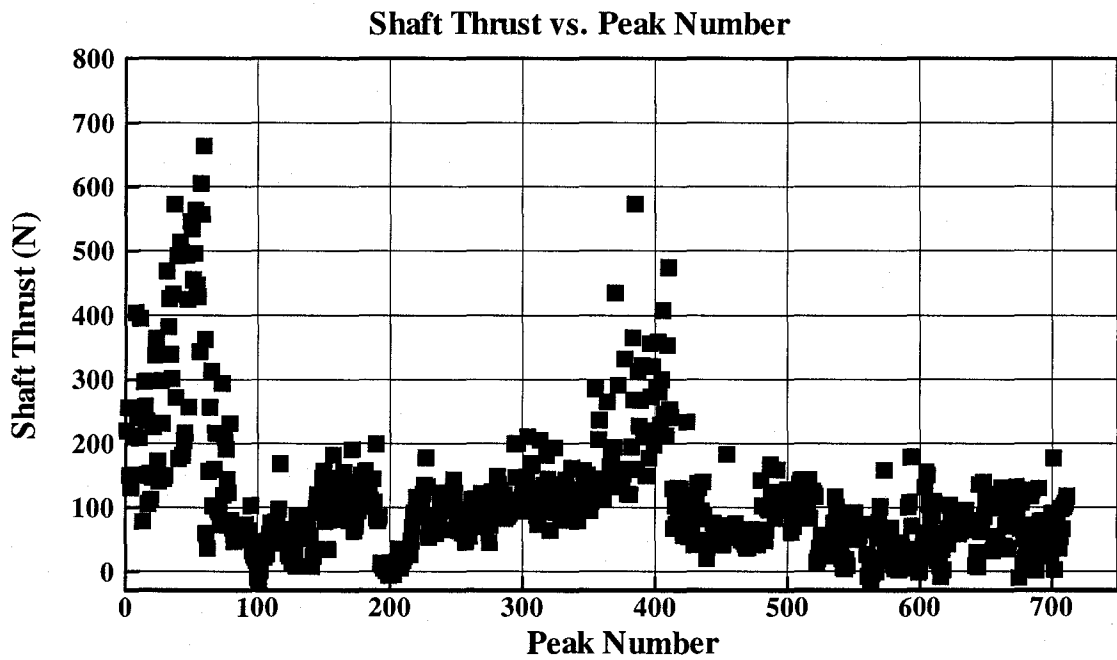
Figure 3-44: Measured maximum total force values for the assumed ice interaction segments in the time series for the selected test run (Case 1)
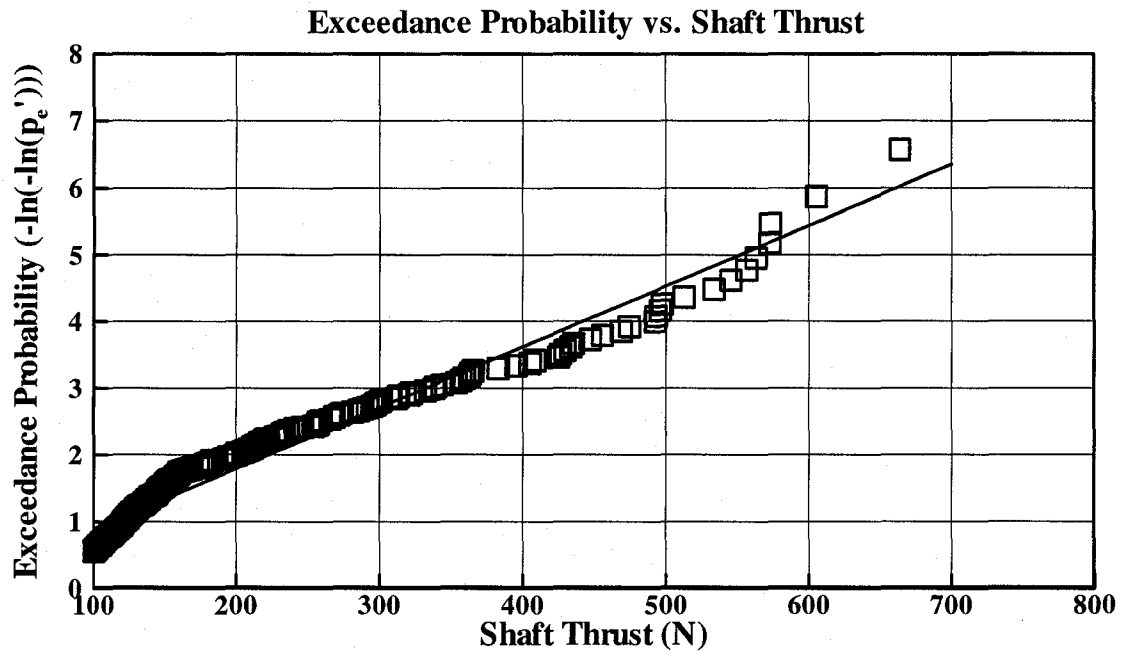
Figure 3-45: Data in Figure 3-44 ranked and plotted with exceedance probability (Gumbel plot)

100

In Figure 3-46, shaft thrust coefficients (K_{T_SHAFT}) are plotted for azimuthing angles of

150° and 180°. If we consider the "100 unit time" loads, the maximum K_{T_SHAFT} for 35

mm and 15 mm depths of cut are 2.56 and 1.4, respectively. It is noted that trend lines

are started from thrust coefficient of 1 (one) in order to consider extreme values more

accurately.

Exceedance Probability against K_{T_SHAFT} from Two Different Depths of Cut
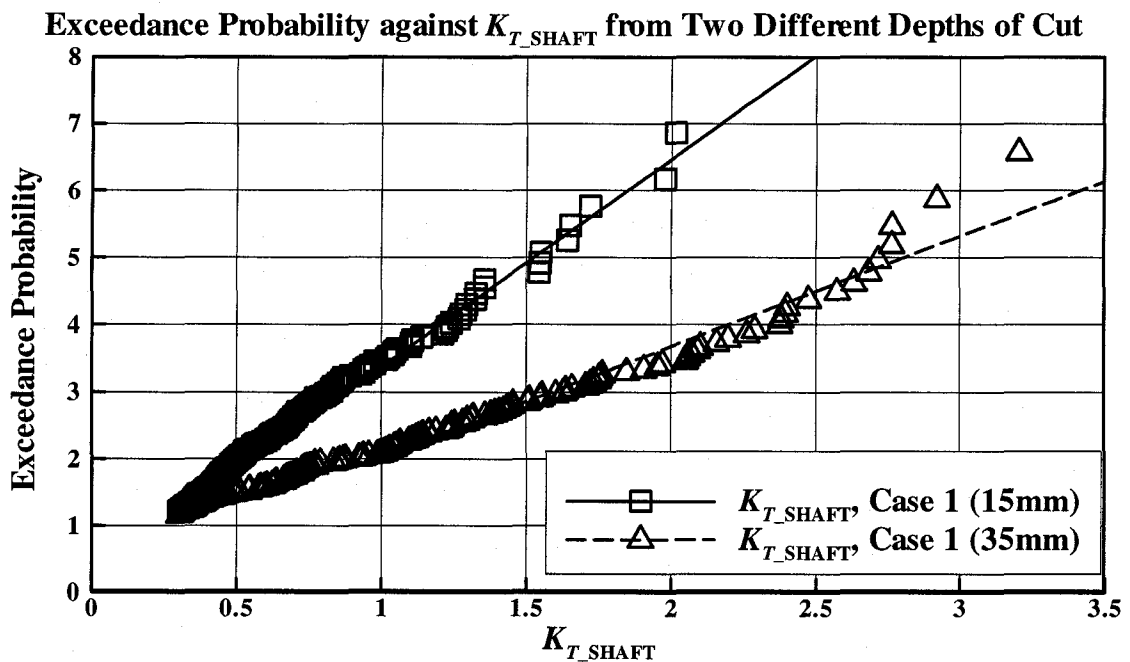
Figure 3-46: Exceedance probability against shaft thrust coefficients at two different
depths of cut in "Case 1"

Figure 3-47 shows the relationship between the shaft thrust and blade thrust coefficients

at 35 mm depth of cut in "Case 1." As shown in Figure 3-25 and Figure 3-27, the

maximum values of shaft thrust coefficients are generally higher than those of blade

thrust coefficients. Consequently, deterministic maximum values of shaft thrust

coefficient are higher than those of blade thrust coefficients. For example, the maximum K_{T_SHAFT} for and K_{T_BLADE} are 2.56 and 1.53, respectively at the "100 unit time" loads (exceedance probability = 4.6).
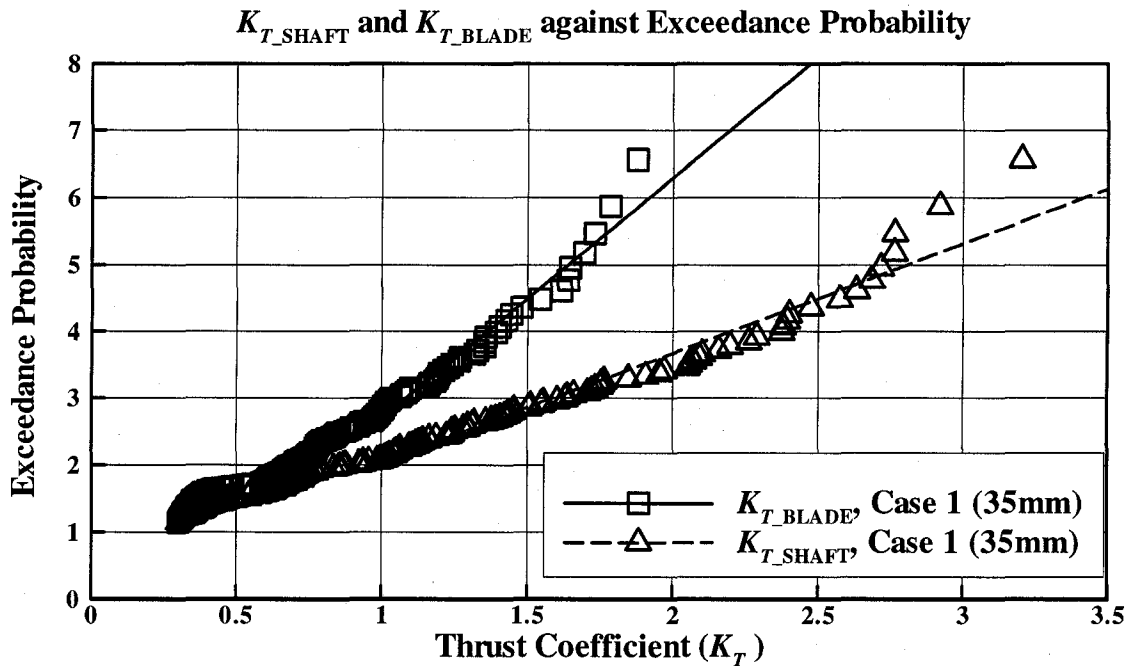
Figure 3-47: Comparison between shaft thrust and blade thrust coefficients with exceedance probability in "Case 1"

In Figure 3-48, shaft torque coefficients are plotted with the exceedance probability for 35 mm depth of cut. Comparisons are made with "Case 1" and "Case 2." It is concluded that "Case 2", which is sort of off-design condition, shows the less torque coefficients before the exceedance probability reaches between 5 and 6. Once the exceedance probability is over 6, shaft torque coefficient from "Case 2" is slightly bigger than those from "Case 1."

102

Exceedance Probability against K_{Q_SHAFT} from Two Different Depths of Cut
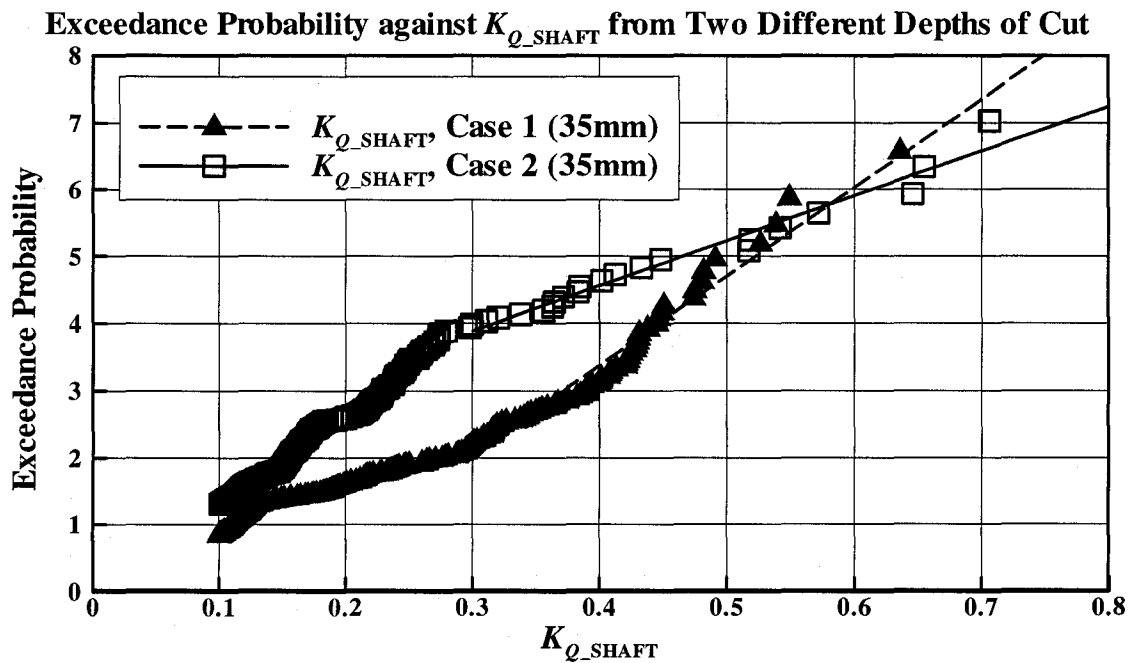
Figure 3-48: Exceedance probability against shaft torque coefficients at two Cases

The extreme probability method is important to evaluate the maximum ice loads in terms of their frequencies and variations. From this method, the maximum values can be predicted statistically. This extreme probability method is also useful for the decision of the ice loads in ice-class propeller design. The same method can be applied to any other parameter, such as total forces/moments on the propeller blade or shaft to assess the design loads. Based on an appropriate propeller-ice interaction scenario and corresponding return period, the extreme probability method could be one of the useful tools to evaluate the propeller-ice interaction loads.

Chapter 4 Numerical Predictions

In this chapter, the methodology for the numerical prediction of propeller performance in ice covered water is presented; in particular, the prediction of ice related loads is mainly described. Special attention has been given to the effect of shadowing and azimuthing angle. Hydrodynamic loads, including separable and inseparable hydrodynamic loads, are calculated by a three-dimensional unsteady panel method. The process for the ice milling loads calculations is implemented in the panel method, and that is incorporated with both separable and inseparable hydrodynamic loads in ice covered water conditions.

4.1. Overview of the Panel Method (Code Name: PROPICE)

The general explanation of the panel method is not provided in this thesis. The code used in this study was originally developed at the NASA Ames, and was called PMARC. Bose (1996) modified this code for propeller performance in blocked flow. This modified code was called PROPS. In this study, the PROPS code was used as the basic frame and some

parts were modified and developed to include the ice milling loads calculations; this modified code is called PROPICE. The basic features of this code are:

- Unsteady code with time stepping calculation,
- Calculations were made over three revolutions of the propeller with 10 degree angular intervals, and the mean values for thrust and torque were calculated from the values obtained in the third full cycle,
- Influence coefficients were calculated by using constant doublet distributions over hyperboloidal shaped panel elements,
- A rigid wake model was used,
- Morino's Kutta condition was used (Morino et al., 1975),
- The hydrodynamic friction force was estimated using the friction coefficient values of 0.005,
- Process for the ice milling loads calculation was implemented,
- The Bi-Conjugate Gradient Stability (BICGSTAB) matrix solver was used (Van der Vorst, 1992; Subroutine from Liu, 1996).

The flowchart for the hydrodynamic calculation is shown in Figure 4-1 and Figure 4-2. The process for the ice related loads calculation was implemented into one of the subroutines, called AERODAT.F., and a detailed explanation is presented in Section 4.4.
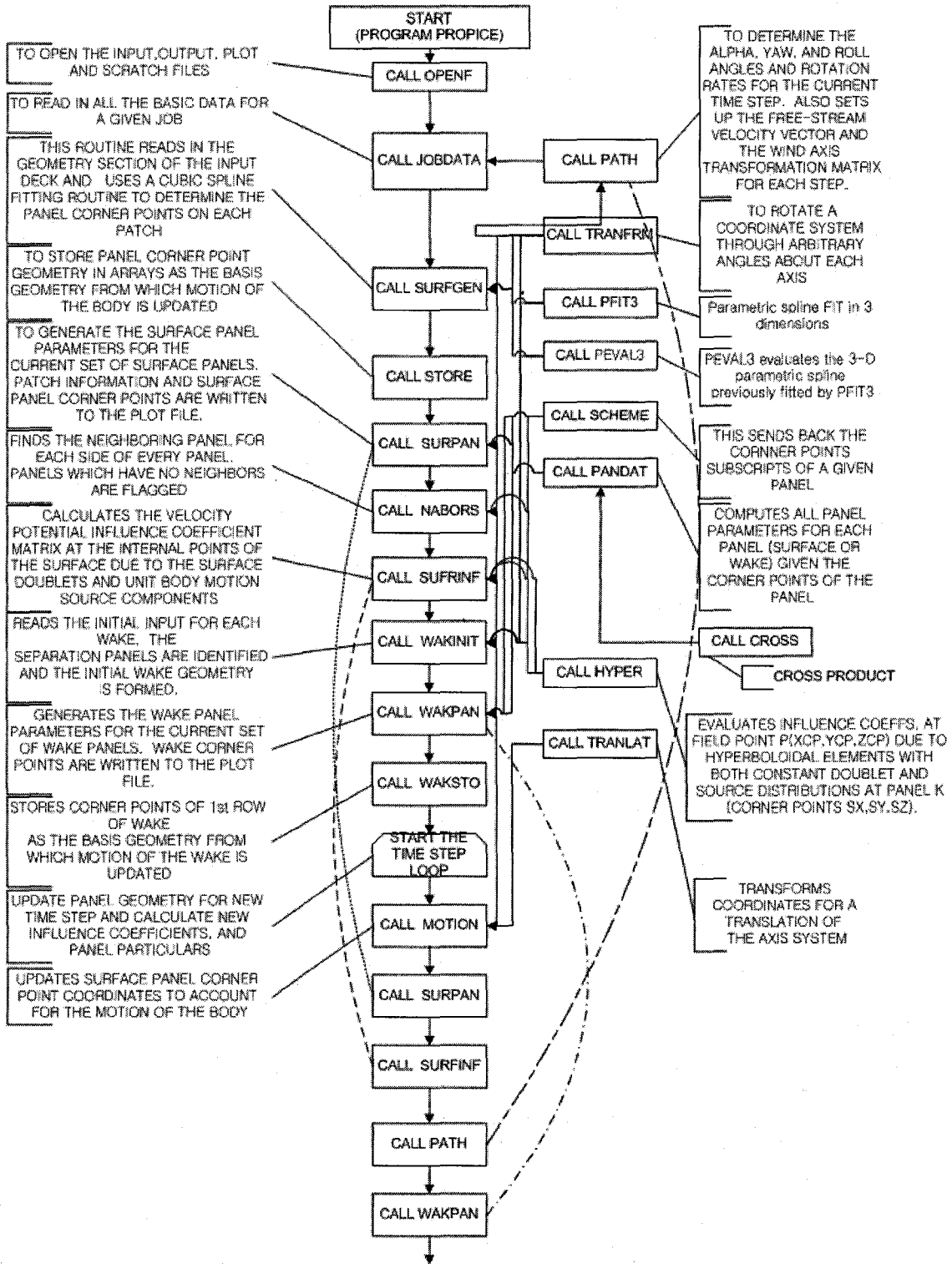
Figure 4-1: Flowchart for PROPICE

106
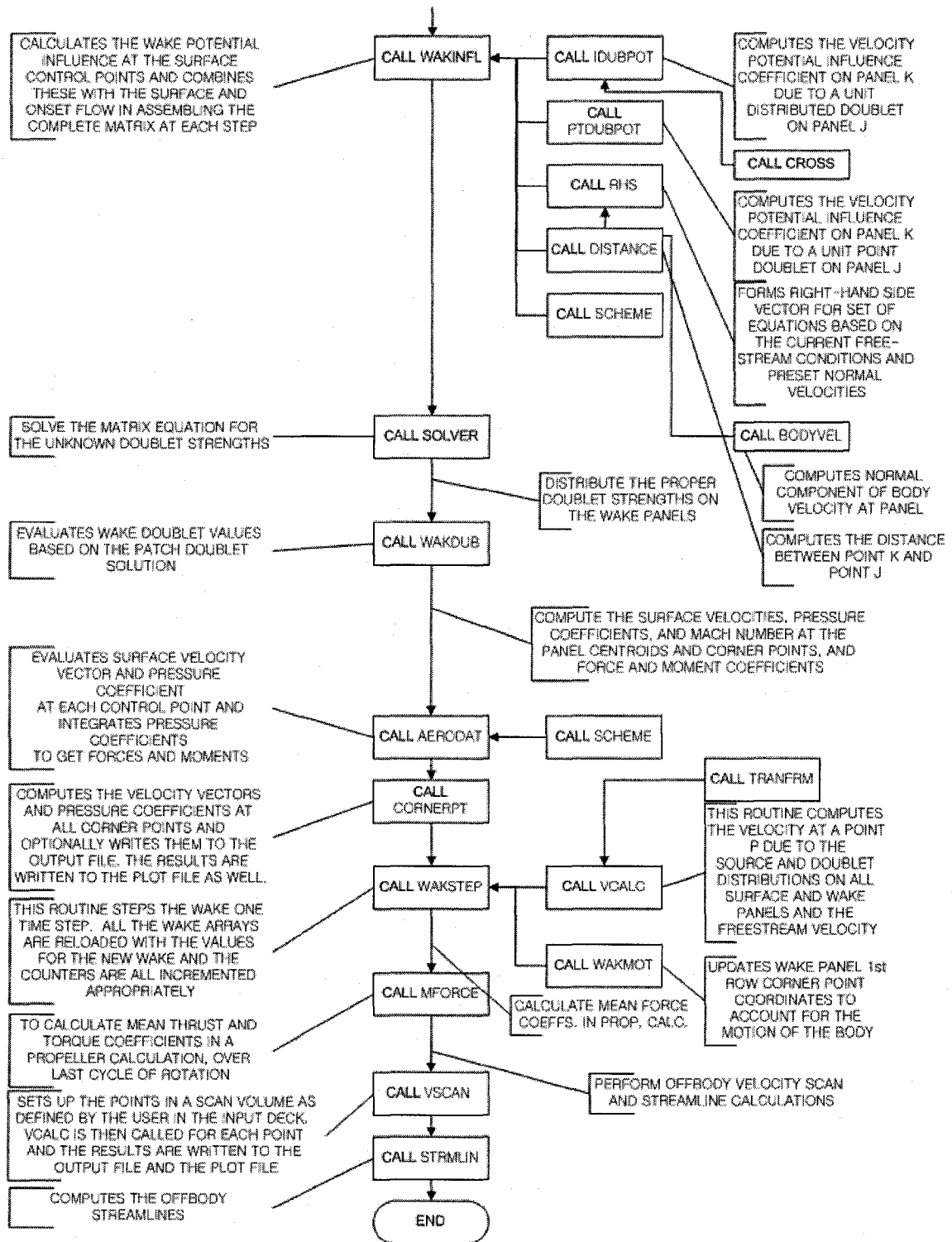
Figure 4-2: Flowchart for PROPICE, -continued

4.2. Consideration of Separable Hydrodynamic Loads

The aim of the separable hydrodynamic load calculations are: first, to access the effectiveness of the code; second, to predict the separable and inseparable hydrodynamic loads. For the separable hydrodynamic loads, the process for the ice related loads was not activated. In the PROPICE code, propeller blades only were modeled by using 44 chordwise and 18 spanwise panels, as shown in Figure 4-3.
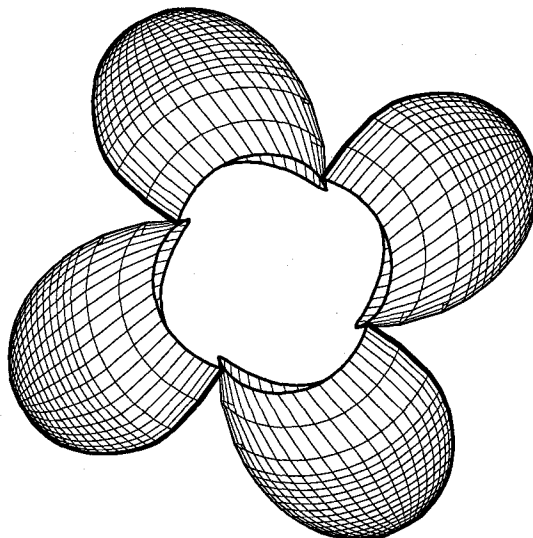
Figure 4-3: Geometry and paneling of the propeller

The numerical results from the PROPICE code in open water conditions, i.e. the separable hydrodynamic loads, are compared with the experimental results in Figure 4-4. The thrust and torque coefficients from PROPICE are somewhat higher than the experimental results. For the present experimental set up, the propeller rotational speeds

108

were up to 10 rps and the highest R_e was 2.4×10^5; as discussed in previous chapters. It is noted that the propeller performance at low Reynolds numbers can show underestimated thrust and torque coefficient values (ITTC, 2002). In addition, when the tip of the blade was approaching towards the bottom of the model stern, the distance between the blade tip and model stern was not far enough away to ignore the blockage effects on the propeller and this may cause some of the variations between the two results. For example, the closest distance between the blade tip and model stern was approximately 25 mm, which is the condition for 35mm of depth of cut.

Tuning a panel method for the hydrodynamic calculations is an extensive task and it was not the aim here to do that, but to focus on the ice related components which are at a much higher level. With regard to a panel method, no hub and cone may affect significant effect on the results as well as wake panel geometry, first wake panel, panel size and discretization.

K_{T_SHAFT} & $10K_{Q\_SHAFT}$, Average Separable Hydrodynamic Loads, Tractor Mode, 180 Azimuthing Angle, Open Water
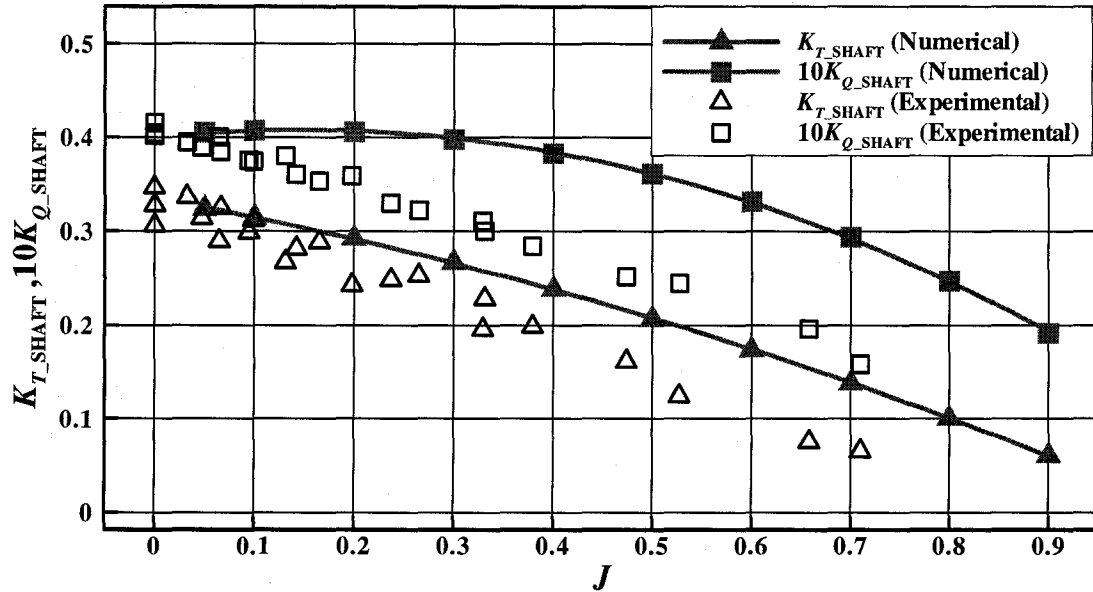
Figure 4-4: Comparison of results from panel method with those from the experiments in open water conditions

4.3. Consideration of Blockage/Proximity & Shadowing

Effects

When the blade contacts with ice, the process for the ice related loads calculation is activated. The panels of the blade within the ice block experience either inseparable hydrodynamic loads or ice milling loads and they should be identified; this identification procedure is addressed in the next section. In this section, numerical considerations of the inseparable hydrodynamic loads are mainly discussed. As mentioned in the previous

chapters, the inseparable hydrodynamic loads are generated due to the presence of ice without any physical contact; for example, blockage, proximity and cavitation.

For the numerical calculation in blocked flow, a simplified ice wake model was used in this study. The ice block itself did not need to be modeled physically in the code, but it was considered conceptually. The blockage model was assumed that the propeller was rotating in a simplified wake behind the ice; the simplified ice wake was defined such that the downstream velocity of the wake was 0.01 times that of the free stream (similarly to that done by Bose (1996)).

When the propeller is in contact with the ice block, the shadowing effect must be considered, particularly at low advance coefficients. Again, the shadowing effect refers to the situation when a blade encounters part of the path created by the previous blade, as described in Section 3.5.4.1. For example, if the propeller operates in the first quadrant (positive ship speed and positive propeller rotating speed), the blockage and the shadowing effect can be found on the suction and pressure side of the blade, respectively (Figure 4-5). The shadowing area is treated as the blockage condition.
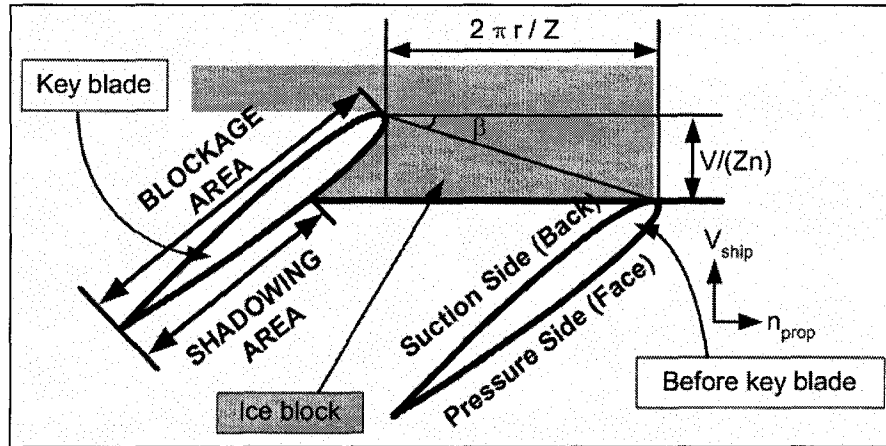
Figure 4-5: Conceptual sketch of the blockage and shadowing area (β is the angle of advance, V is the carriage speed, and Z is the number of blade)

In the blockage condition, the effect of the gap between the blade surface and ice block is not considered, even though the blockage loads vary depending on the size of the gap (Bose, 1996). The effect of proximity and cavitation is not considered in this thesis.

4.4. Consideration of Ice Milling Loads (Including Implementation Procedure into a Panel Method)

The numerical procedure for the ice related load calculation is presented in this section. When the propeller blades contact with the ice, the process for the ice related load calculations is activated and the ice related loads are calculated at the blade panels which are in contact with ice. The compressive strength of the model ice measured during the experiments is taken into account as the ice reference pressure for the numerical calculation. The procedure of the ice milling loads calculation is addressed below.

[Step.1] Determination of a depth of cut, an ice reference pressure ($P_{REF(ICE)}$) and an azimuthing angle (ψ) of the system as input data. In order to provide the uniform interaction conditions between the propeller and ice, the calculations were performed in the tractor mode only; for the pusher mode, the pod and strut interact with the ice block before the propeller, so ice blocks can be disturbed. The azimuthing angles used in this calculation are 180, 150, 120 and 90 degrees in the tractor mode. Two different depths of cut, 15 and 35 mm, were considered. The ice reference pressure of the calculation for the 15 mm and 35 mm depths of cut were 120 kPa and 195 kPa respectively.

[Step.2] Determination of the panels which are in contact with the ice block. Once the coordinate of the bottom of the conceptual ice block is defined, the blade panels can be identified with their radial components; if the radial component of the blade is larger than the bottom line of the conceptual ice block, then the panel is assumed to be in contact with the ice block. The positive direction of the radial component of the blade is from the root to the tip of the blade.

[Step.3] Determination of the geometric angle of attack (α_G) and the angle of advance (β). The ice block is assumed stationary and the induced velocities are ignored (Figure 4-6).

$$\alpha_G = \tan^{-1}\left(\frac{P}{2\pi r}\right) - \tan^{-1}\left(\frac{V}{2\pi n r}\right), \quad \beta = \tan^{-1}\left(\frac{V}{2\pi n r}\right). \tag{4-1}$$
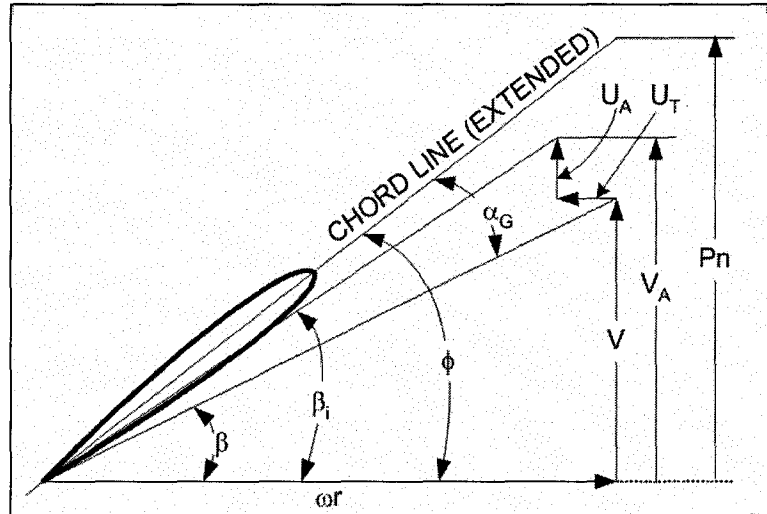
Figure 4-6: Velocity diagram for a propeller blade section, β is the angle of advance, β_i is the hydrodynamic pitch angle, ϕ is the geometric pitch angle, α_G is the geometric angle of attack, V is the carriage speed, V_A is the advance speed, U_T and U_A are the tangential and axial induced velocities, and P is the pitch at 0.7R

[Step.4] Choice between the milling and blockage area at each panel which contacts with ice. Depending on the angle of advance, panels can be identified as either the milling or blockage area (including shadowing), as shown in Figure 4-7. If the interacting angle (Θ), which is the angle between the normal vector of the panel and the directional vector of the angle of advance, is greater than 0 degrees and less than 90 degrees, then this panel is involved in the milling area; if this interacting angle (Θ) is more than 90 degrees or less than 0 degrees, then this panel is involved in the blockage area.

114
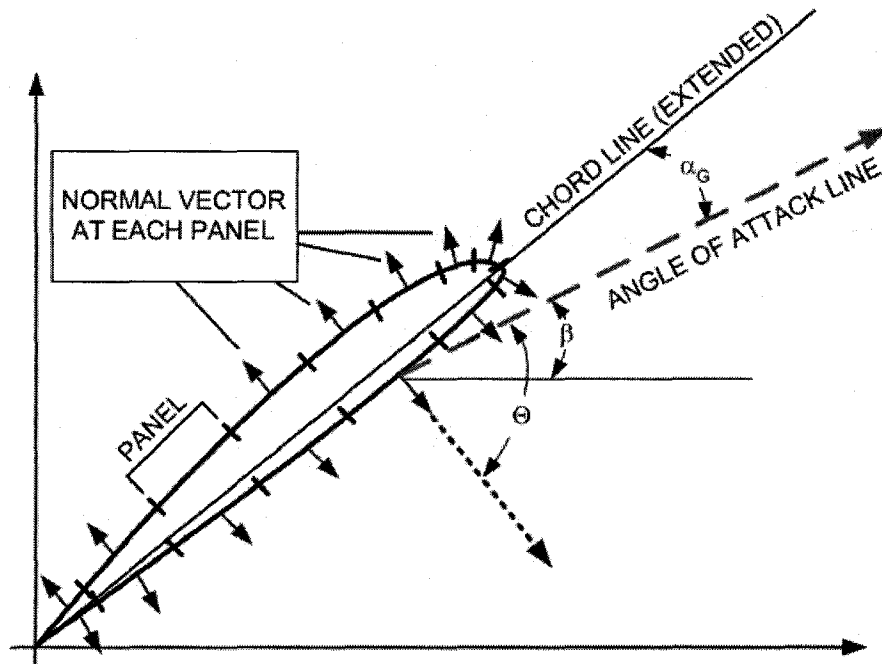
Figure 4-7: Geometrical consideration for the ice contact area (Θ : the interacting angle)

[Step.5] Correction of the shadowing area. Once the panel is identified as the milling

area, the shadowing area should be checked. If the panel is within the shadowing area,

then the panel must be considered as blockage area (shadowing and blockage in Figure

4-5). When a certain azimuthing angle, which is less than 180 degrees and more than 90

degrees, is given, additional kinematic considerations are made, as shown in Figure 4-8.

In particular, Figure 4-9 shows the shadowing area when the azimuthing angle is equal to

90 degrees. Once the shadowing area is determined, the calculation is performed in the

same manner as the blockage area.

The principle to calculate the shadowing area is:

1. Relative motion between the propeller and carriage (ship) is taken into account

    with two directions, which are axial (perpendicular to the propeller rotating

    direction) and radial directions (same as propeller rotating direction, $n = n_{PROP}$);

2. The advance distance at each blade is to be $\dfrac{V(=V_{ship})}{Zn}$ based on the angle of

    advance (β);

3. Once the azimuthing angle is less than 180 degrees (tractor mode), contribution

    of the azimuthing angle (ψ) on the axial and radial direction must be

    considered; i.e. the advance and radial distances are $\dfrac{V\sin(\psi)}{Zn}$ and $\dfrac{V\cos(\psi)}{Zn}$,

    respectively;

4. If the panels are placed out of the advance or radial distances then the panels are

    finally identified as the shadowing area, even though the panels belong to the

    milling area, as shown in [Step.4]
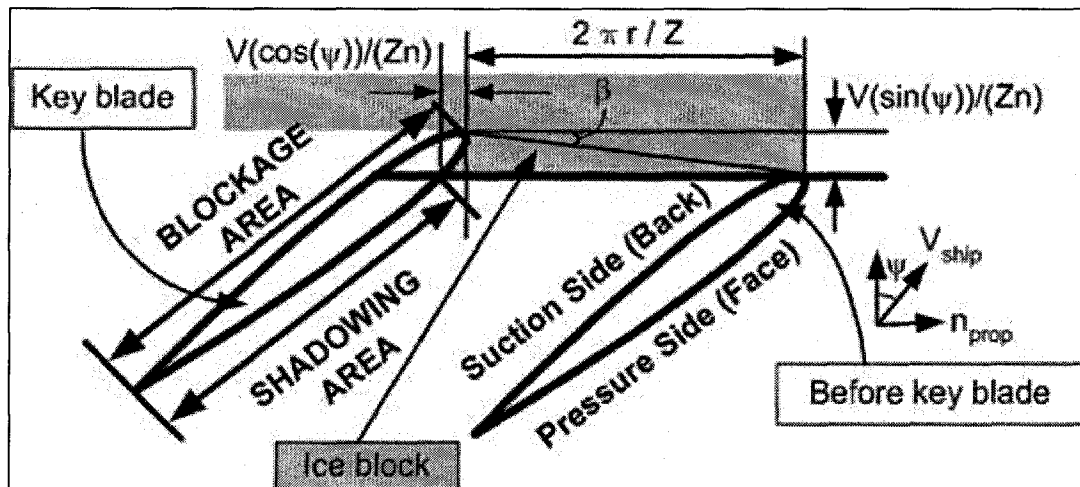
Figure 4-8: Shadowing area at various azimuthing angles

116
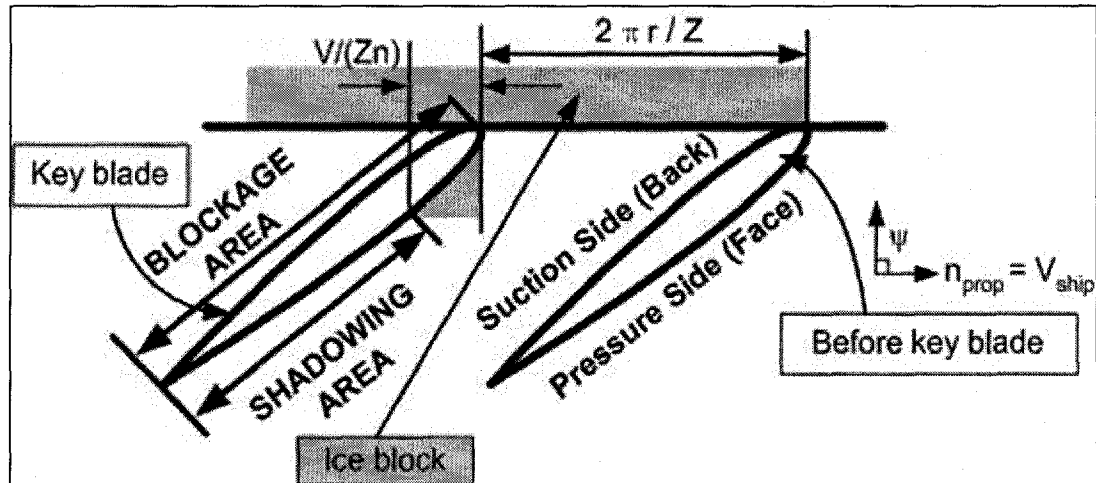
Figure 4-9: Shadowing area at an azimuthing angle of 90 degrees

[Step.6] Determination of the pressure coefficient at each panel. The total pressure

coefficient ($C_{P(TOTAL)}$) is sum of the hydrodynamic pressure and ice crushing pressure

coefficients, as shown in Equation (4-2):

$$C_{P(TOTAL)} = C_{P(HYDRODYNAMIC)} + C_{P(CRUSHING)}.$$ (4-2)

The hydrodynamic pressure values can be calculated by using the panel method and the

ice crushing pressure coefficient can be evaluated by empirical formulae based on

geometric and kinematic considerations. If the interacting angle (Θ) is 0 degrees, then

the panel interacts with the ice perpendicularly, which is called pure crushing. On the

other hand, if the interacting angle (Θ) is 90 degrees, then the panel interacts with the ice

in parallel, which is called pure shearing. The crushing pressure is calculated based upon

the ice reference pressure and the interacting angle (Θ).The empirical factor for the

117

crushing (*EFC*), four, is multiplied by the ice reference pressure, which may represent

effect of high strain rate. For the maximum values, a weight factor (W) is used: $W = 1$ for

average value and $W = 6$ for the maximum value of the propeller thrust and torque. It is

assumed that the crushing pressure is distributed with a cosine distribution regarding the

interacting angle (Θ). The ice crushing pressure coefficient can be calculated by

$$C_{P(CRUSHING)} = \left(W \times EFC \times P_{REF(ICE)} \times COS(\Theta)\right) / \left(\frac{1}{2}\rho_I V_{ref}^{2}\right), \qquad (4\text{-}3)$$

where $P_{REF(ICE)}$ is the ice reference pressure, Θ is the interacting angle, ρ_I is the ice

density, W is the weight factor, *EFC* is the empirical factor for crushing, and V_{ref} is the

local inflow velocity (inflow velocity (V) + propeller rotational velocity ($\Omega \times r$)).

Shearing forces are considered independently, because they cannot be presented in the

pressure term. Constant shearing forces are applied to the milling area, which are the ice

reference pressure divided an empirical factor for shearing (*EFS*), four. From the ice

samplings during the tests, the compressive strength was two to four times shear strength.

Equation (4-4) shows the shearing force:

$$F_{(SHEARING)} = \frac{P_{REF(ICE)}}{EFS} \times AREA, \qquad (4\text{-}4)$$

where *EFS* is the empirical factor for shearing and *AREA* is an area of the panel.

118

The discussions of these empirical factors are presented in Section 5.5. It is noted that the frictional force in ice is not considered because the shearing force can include the friction; the ice frictional coefficient is as small as 0.02 (Gagnon and Molgaard, 1991).

[Step.7] Calculation of the total forces from the hydrodynamic loads and the ice related loads. Thrust and torque coefficients are calculated from the total forces.

Chapter 5 Comparisons

The objective of this chapter is to compare the results from the numerical code

(PROPICE) with the experimental data, in order to validate PROPICE. All numerical

results were obtained from the average values from the last full cycle of a total of three

rotations; one full cycle consists of 36 time steps corresponding to 10 degrees angular

intervals and a total of 108 time steps for three rotations were performed for each

calculation. The ice related loads and total loads in ice covered water are mainly

considered.

5.1. Comparison of Ice Related Loads on Propeller

Blade

5.1.1. Time Series Comparison

In order to verify the numerical calculation, time series data of the ice related loads from

the PROPICE are compared with those from the experiments in Figure 5-1 through

Figure 5-4. The ice related loads in the experiments were rearranged and superimposed relative to the blade angular positions. The number of data points at the same blade angular position from the experiments is mainly more than a hundred, so basic statistics is applied to find an average value. The uncertainty levels in the experimental results represent the 95 % confidence levels and are shown as error bars on the figures.

In these comparisons, the depth of cut was 35 mm and the azimuthing angle was 180 degrees. The propeller rotated counter-clockwise and the milling angle was from 36 degrees to -69 degrees. For convenience, the origin of the blade angular positions was shifted by 180 degrees so that the propeller blade entered the ice block at the blade angular position of 216 degrees and exited at 111 degrees. In the figures, the inner part of the box shows the milling period.

In Figure 5-1, blade thrust coefficients in time series from the experiments and PROPICE are plotted against the blade angular position. The comparison for the numerical blade thrust coefficients presents a good agreement both quantitatively and qualitatively. In the experimental results, a trough between the two peaks during the milling period is found. This may be caused by the pre-sawn ice; i.e. the ice sheet was cut in center, as shown in Figure 3-5.

Figure 5-2 shows the x-direction moment of the blade (Blade M_X), which represent the negative blade torque (Q_{BLADE}). The sign conventions are given in Section 3.5.2. Because of the effect of the shaft dynamics observed in the experiments, the numerical

121

results were multiplied by 1.7; as mentioned in Section 3.5.4, the blade torque is 1.7 times the shaft torque during the milling period. In Figure 5-2 the comparison is generally encouraging, even though the numerical results show at most 50 percent lower values than the experimental results during the milling period.

For the blade M_Y and M_Z, comparisons are presented in Figure 5-3 and Figure 5-4, respectively. The numerical results for the blade M_Y show slightly higher values than the experimental results, but the trends are similar. The blade M_Z represents a positive spindle torque. In Figure 5-4 the trends of the numerical results are slightly different from those in the experiments, but the magnitude of these values is relatively small compared to other components (M_X and M_Y).

In general, ice loads experienced by the blade are well predicted by the PROPICE code in terms of overall trends. It is noted that the experimental results shown in the figures are ice related loads, thus the separable hydrodynamic loads are removed. For the numerical calculations, separable hydrodynamic loads are set to be zero, but the inseparable hydrodynamic loads are calculated and included in the results.

Blade F$_X$ (K_{T_BLADE}), Time Series Comparison (Ice Related Loads on the Blade)
J = 0.238, 35mm Depth Of Cut, Tractor Mode, 180 Azimuthing Angle
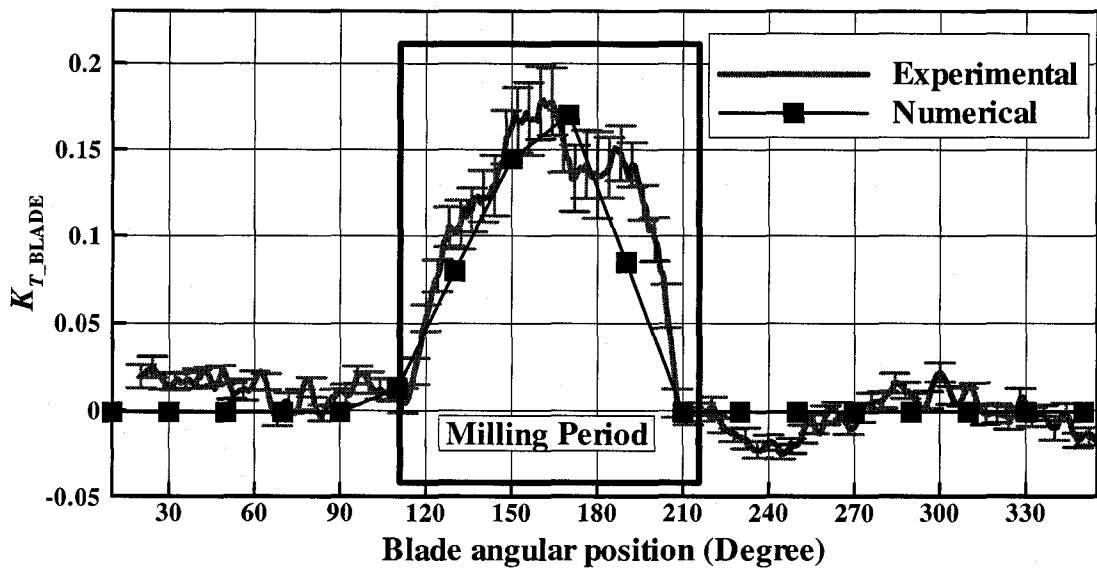
Figure 5-1: Time series comparison for K_{T_BLADE} (ice related loads, J= 0.238, 35mm)

Blade Mx (K_{M_MX}), Time Series Comparison (Ice Related Loads on the Blade)
J = 0.238, 35mm Depth Of Cut, Tractor Mode, 180 Azimuthing Angle
After Multiply 1.7 for Blade Torque
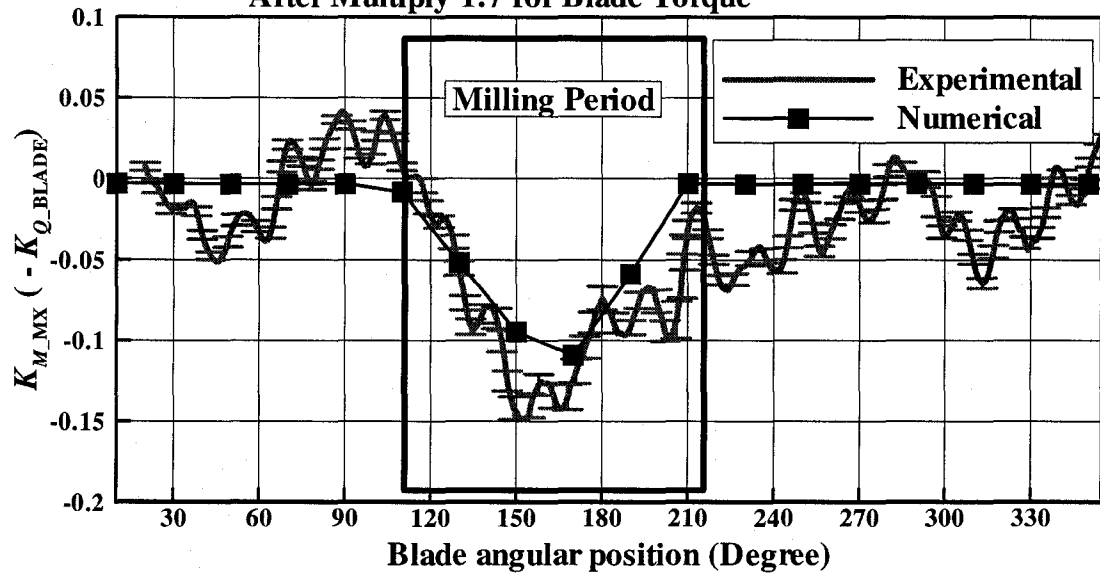
Figure 5-2: Time series comparison for K_{M_MX} after multiplying 1.7 for the blade torque
(ice related loads, J= 0.238, 35mm)

Blade M_Y (K_{M_MY}), Time Series Comparison (Ice Related Loads on the Blade)
J = 0.238, 35mm Depth Of Cut, Tractor Mode, 180 Azimuthing Angle
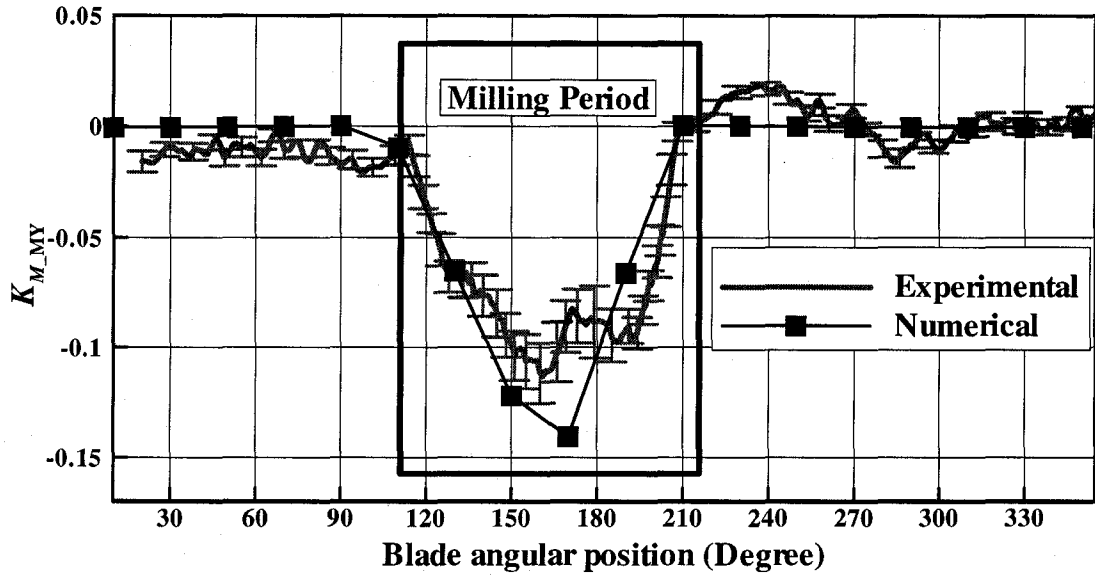
Figure 5-3: Time series comparison for K_{M_MY} (ice related loads, J= 0.238, 35mm)

Blade M_Z (K_{M_MZ}), Time Series Comparison (Ice Related Loads on the Blade)
J = 0.238, 35mm Depth Of Cut, Tractor Mode, 180 Azimuthing Angle
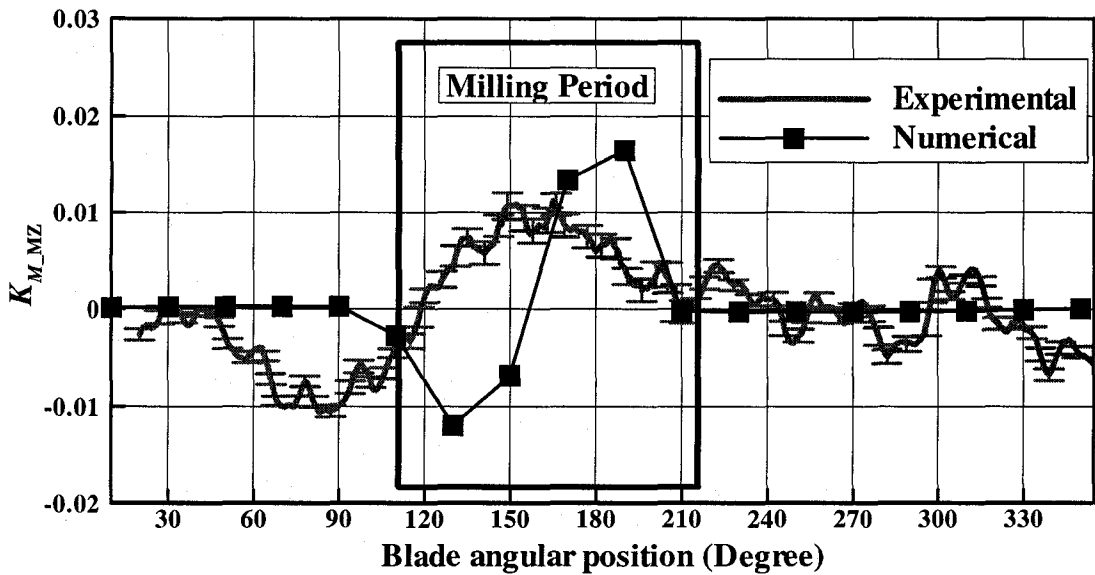
Figure 5-4: Time series comparison for K_{M_MZ} (ice related loads, J= 0.238, 35mm)

124

5.2. Comparison of Ice Related Loads in Ice Covered Water

5.2.1. Ice Related Loads on the Blade

The experimental results measured from the blade dynamometer are compared with the numerical results, in which only the key blade loads have been calculated. From Figure 5-5 to Figure 5-9, coefficients of blade thrust, blade torque, in plane bending moment, out of plane bending moment and spindle torque against the advance coefficient are presented. The test conditions are: tractor mode, an azimuthing angle of 180 degrees, and a 35 mm depth of cut. The solid circles represent experimental results, and the open squares represent numerical results.

The detailed explanations for the trend of the blade thrust are addressed here. Most trends in the figures are similar to those from the shaft loads. From the numerical calculations, the shadowing effect occurred at low advance coefficient ($J < 0.4$). For example, at an advance coefficient of 0.1, approximately 23 % of the pressure side panels of the blade within the ice block experience the ice contact loads due to the shadowing effect (see Sections 3.5.4.3 and 4.4); most of the suction side of the blade experiences the blockage effect (Figure 4-5). When the advance coefficient is 0.4, approximately 94 % of the pressure side experience the ice milling loads.

As the advance coefficient increases to 0.4, the thrust coefficients show the increased trends. This is caused by the combinative effect of the angle of attack and shadowing. Generally, as the angle of attack is decreased, the thrust coefficients decrease; as the shadowing effect is decreased, the thrust coefficients increase. When the advance coefficient is 0.4, the shadowing effect is almost negligible. As the advance coefficient increases over 0.4, the angle of attack decreases, thus the thrust coefficient starts to decrease.

In the figures, the numerical results are fairly well predicted, particularly at lower advance coefficients ($J < 0.4$). As the increase in advance coefficients over 0.4, blade thrust, out of plane bending moment and spindle torque coefficients are underestimated in terms of the absolute magnitude. This may be explained by the variation of the depth of cut. As the model stern slightly pushes down the ice sheet, depths of cut may be changed due to the inertia, especially at the high carriage velocities. It was also found that ice pieces sometimes cumulated in front of model stern, thus the depth of cut could be changed.

It is noted that the blade torque coefficients from the PROPICE are multiplied by 1.7, which represent the effect of shaft dynamics.

K_{T_BLADE}, Ice Related Loads, Tractor Mode, 180 Azimuthing Angle
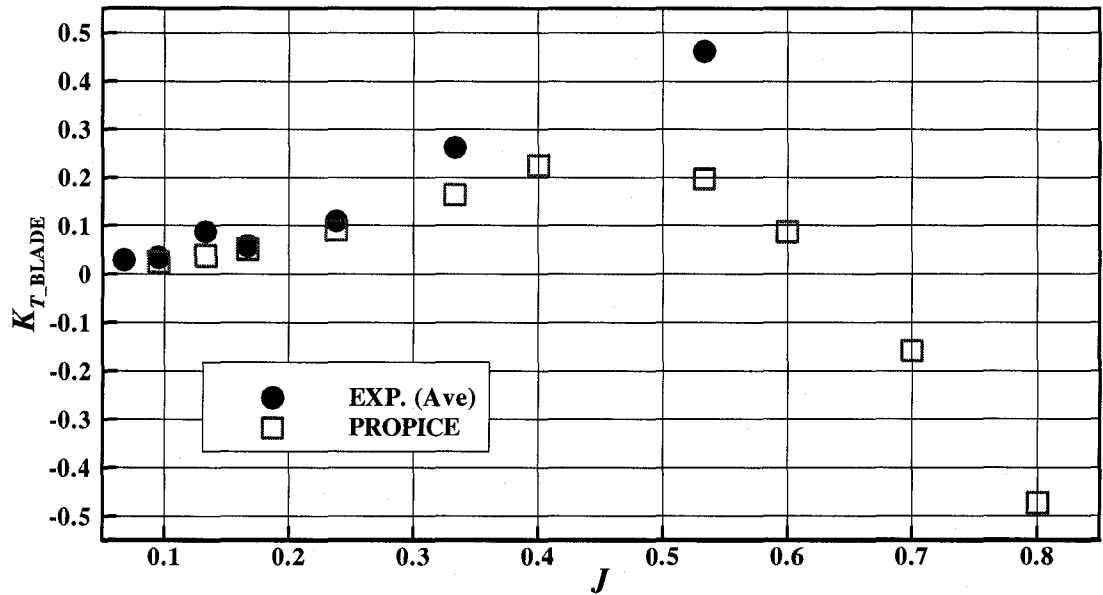
Figure 5-5: K_{T_BLADE} comparison (ice related loads, azimuthing angle of 180 degrees, 35 mm depth of cut, key blade only)

K_{Q_BLADE}, Ice Related Loads, Tractor Mode, 180 Azimuthing Angle
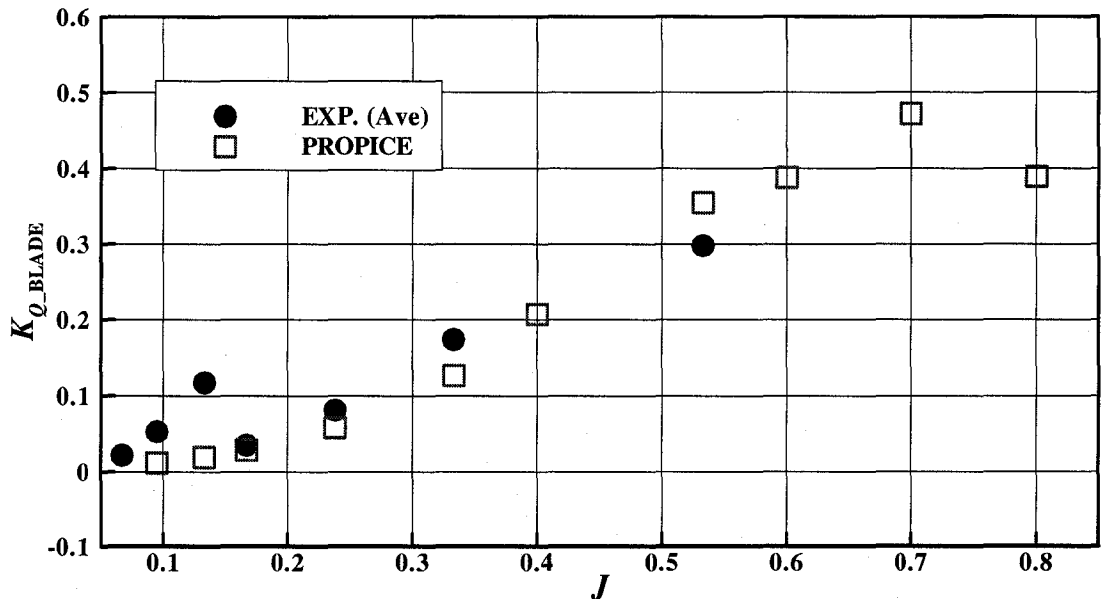
Figure 5-6: K_{Q_BLADE} comparison (ice related loads, azimuthing angle of 180 degrees, 35 mm depth of cut, key blade only)

127
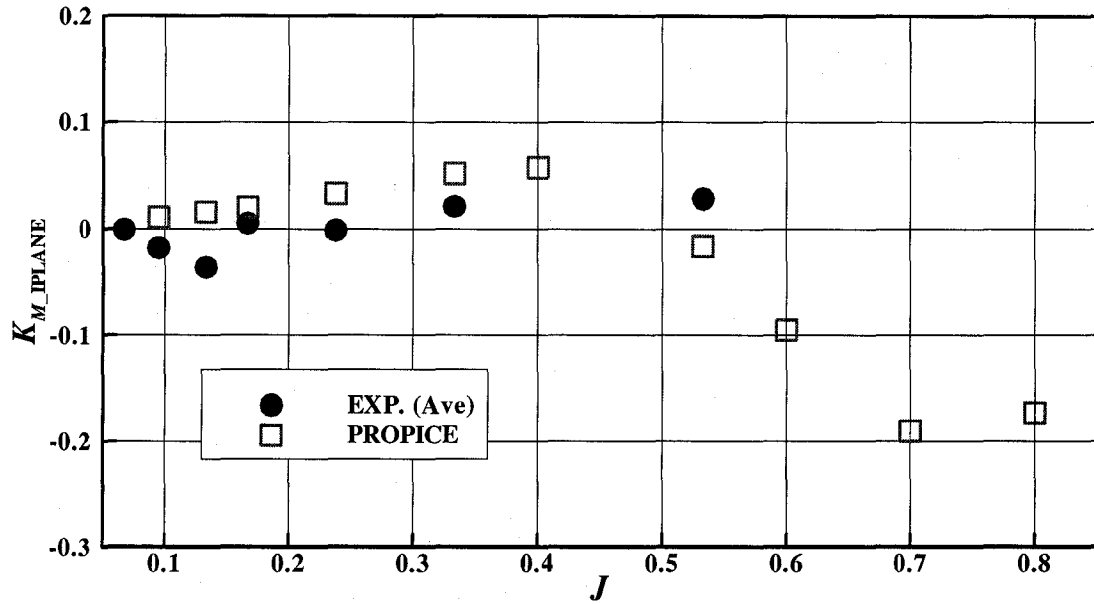
Figure 5-7: K_{M_IPLANE} comparison (ice related loads, azimuthing angle of 180 degrees, 35 mm depth of cut, key blade only)
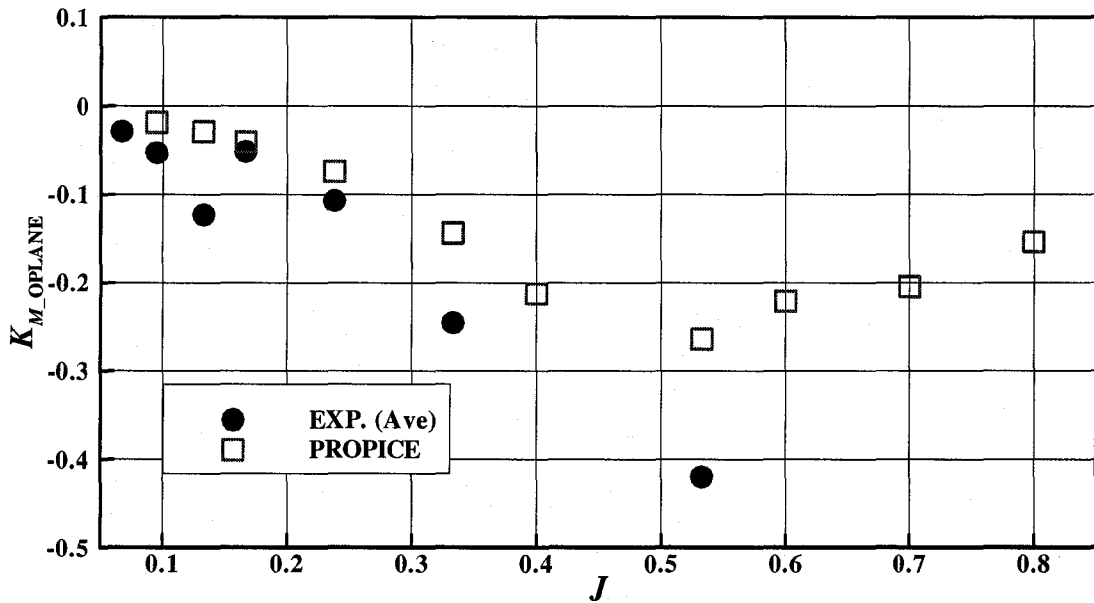
Figure 5-8: K_{M_OPLANE} comparison (ice related loads, azimuthing angle of 180 degrees, 35 mm depth of cut, key blade only)

128
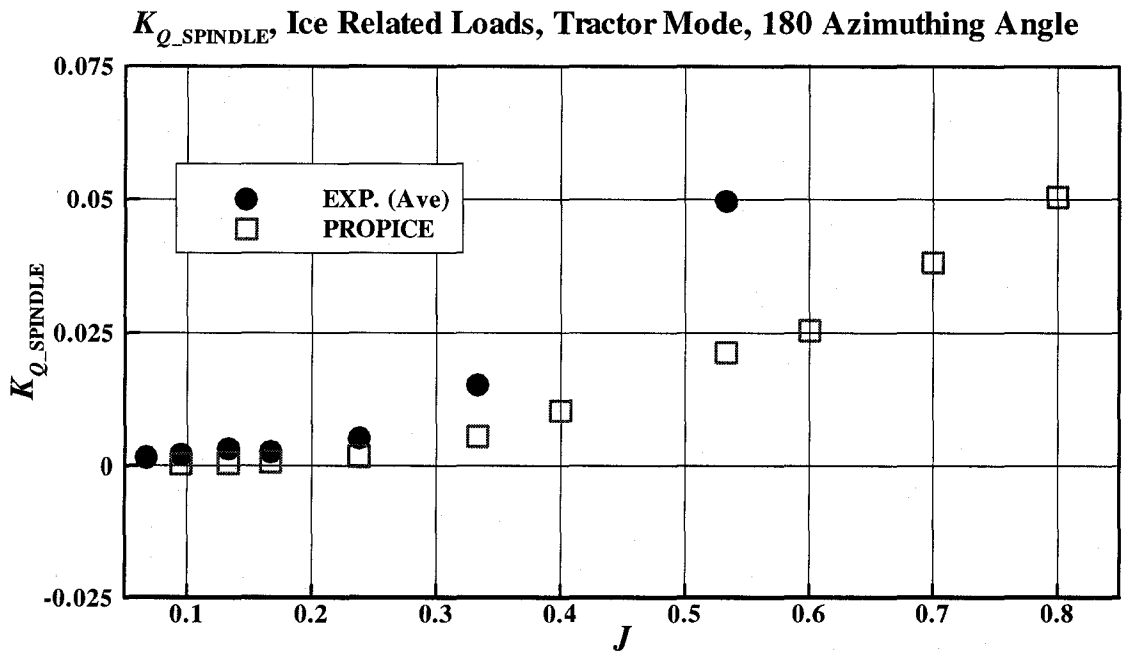
Figure 5-9: $K_{Q\_SPINDLE}$ comparison (ice related loads, azimuthing angle of 180 degrees, 35 mm depth of cut, key blade only)

5.2.2. Ice Related Loads on the Shaft at Various Azimuthing Angles

From Figure 5-10 to Figure 5-17, comparisons between numerical results from the PROPICE and experimental results are made regarding average shaft thrust coefficients and average shaft torque coefficients against the advance coefficient at various azimuthing angles. Inseparable hydrodynamic loads and ice milling loads are considered. A total of four different azimuthing angles (180, 150, 120 and 90 degrees) are presented. For the azimuthing angle of 120 and 90 degrees, the experiments were limited until the advance coefficient was 0.33. The maximum shaft thrust and torque coefficients from the PROPICE are presented in Appendix E.

For the average shaft thrust coefficients (from Figure 5-10 through to Figure 5-13), most numerical results have a good agreement with experimental results at the lower advance coefficients ($J < 0.4$); at the azimuthing angle of 90 degrees (in Figure 5-13), one extraordinary point is found at $J = 0.33$. When the advance coefficients are over 0.4, qualitative trends are similar, whereas the magnitudes are slightly different. It can be explained by the variation of the depth of cut, as described in the previous section.

With respect to the average shaft torque coefficients (from Figure 5-14 to Figure 5-17), numerical results are corresponding well with the experimental results at the low advance coefficients ($J < 0.4$). When the advance coefficients are over 0.4, discrepancies between numerical and experimental results are also found.
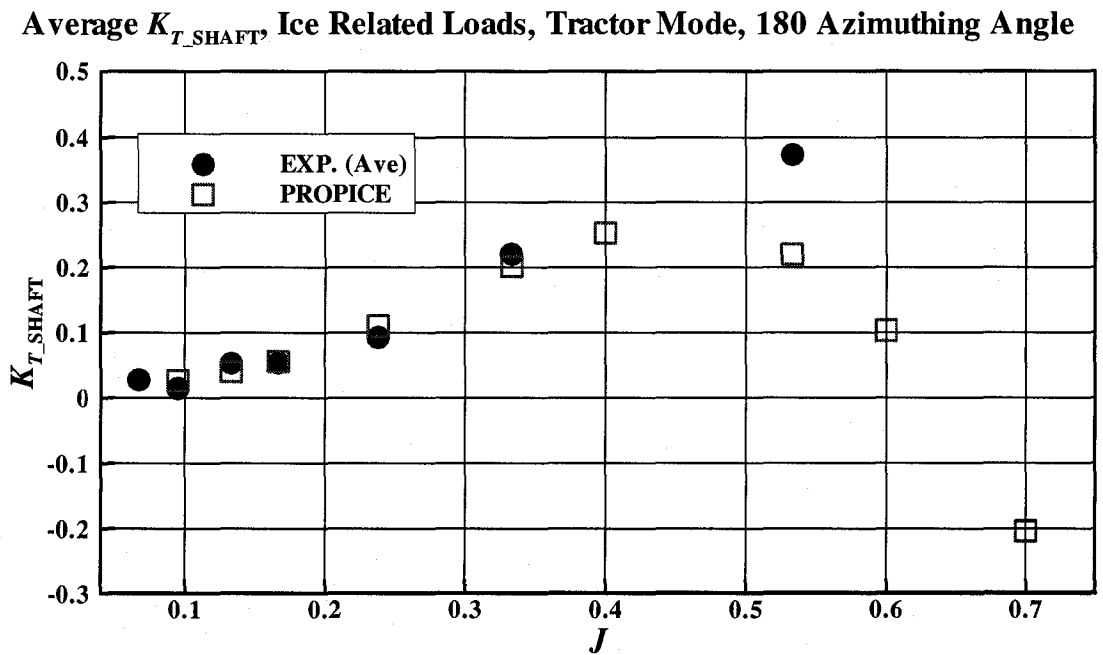
Figure 5-10: K_{T_SHAFT} comparison (ice related loads, azimuthing angle of 180 degrees, 35 mm depth of cut)

Average K_{T_SHAFT}, Ice Related Loads, Tractor Mode, 150 Azimuthing Angle
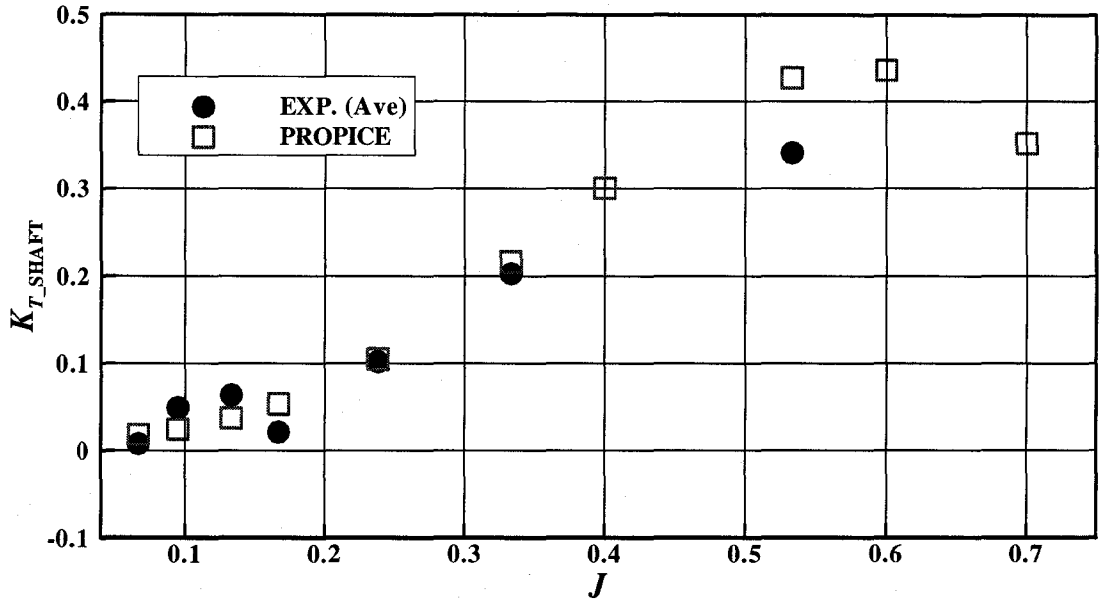
Figure 5-11: K_{T_SHAFT} comparison (ice related loads, azimuthing angle of 150 degrees, 35 mm depth of cut)

Average K_{T_SHAFT}, Ice Related Loads, Tractor Mode, 120 Azimuthing Angle
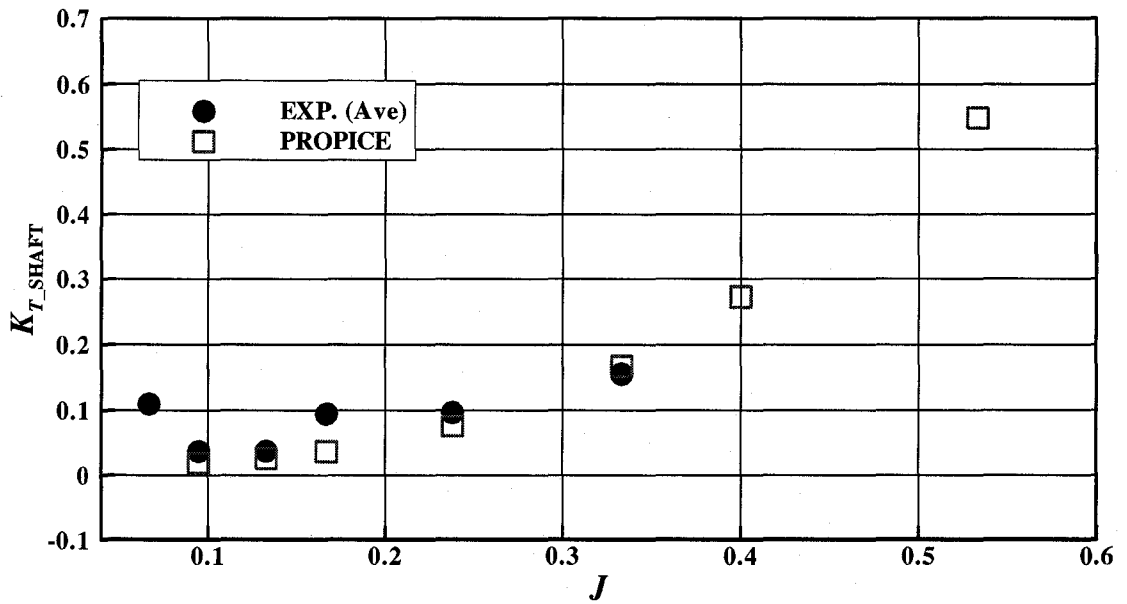
Figure 5-12: K_{T_SHAFT} comparison (ice related loads, azimuthing angle of 120 degrees, 35 mm depth of cut)

131

Average K_{T_SHAFT}, Ice Related Loads, Tractor Mode, 90 Azimuthing Angle
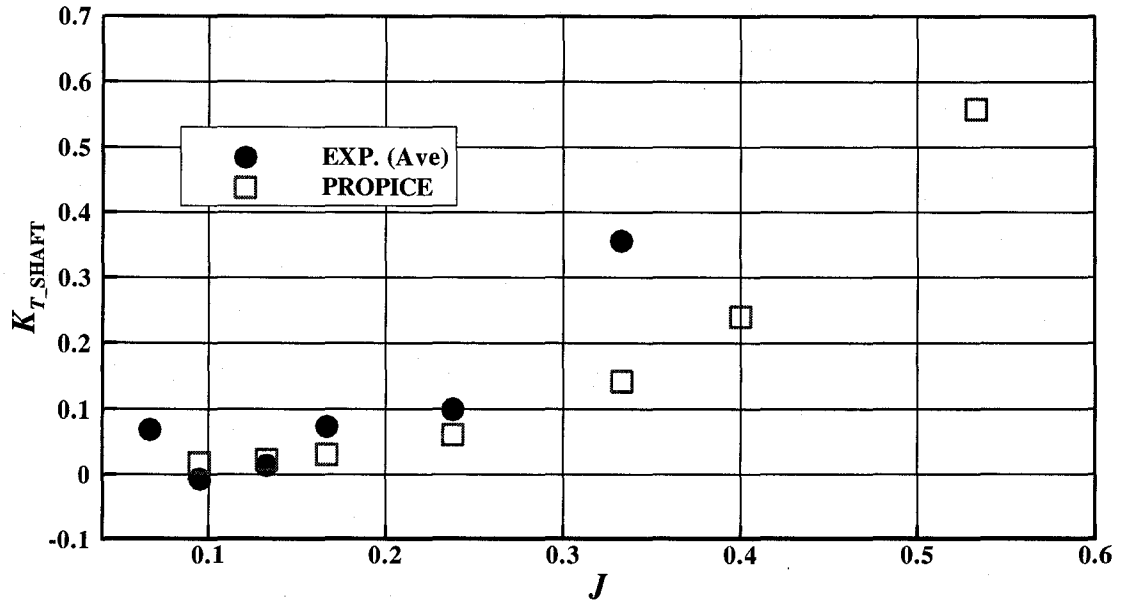
Figure 5-13: K_{T_SHAFT} comparison (ice related loads, azimuthing angle of 90 degrees, 35 mm depth of cut)

Average $10K_{Q\_SHAFT}$, Ice Related Loads, Tractor Mode, 180 Azimuthing Angle
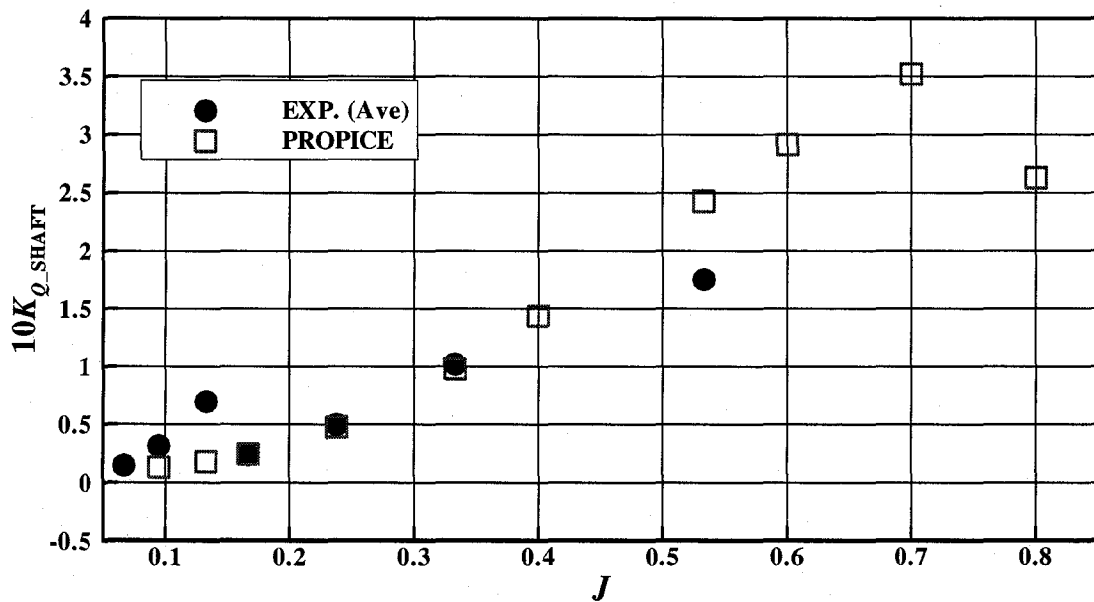
Figure 5-14: $10K_{Q\_SHAFT}$ comparison (ice related loads, azimuthing angle of 180 degrees, 35 mm depth of cut)

Average $10K_{Q\_SHAFT}$, Ice Related Loads, Tractor Mode, 150 Azimuthing Angle
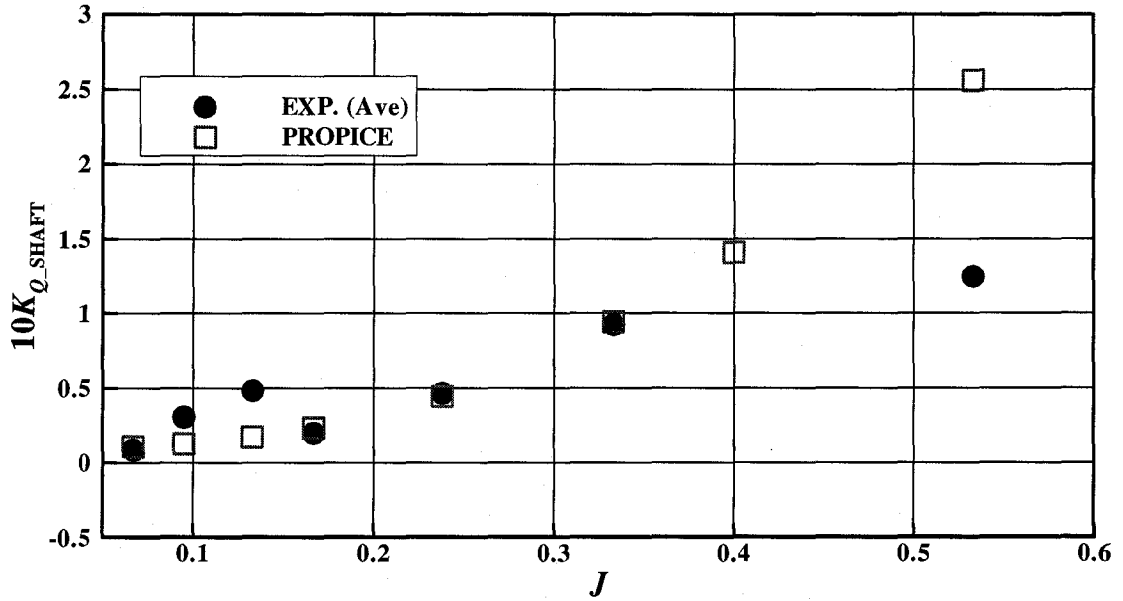
Figure 5-15: $10K_{Q\_SHAFT}$ comparison (ice related loads, azimuthing angle of 150 degrees, 35 mm depth of cut)

Average $10K_{Q\_SHAFT}$, Ice Related Loads, Tractor Mode, 120 Azimuthing Angle
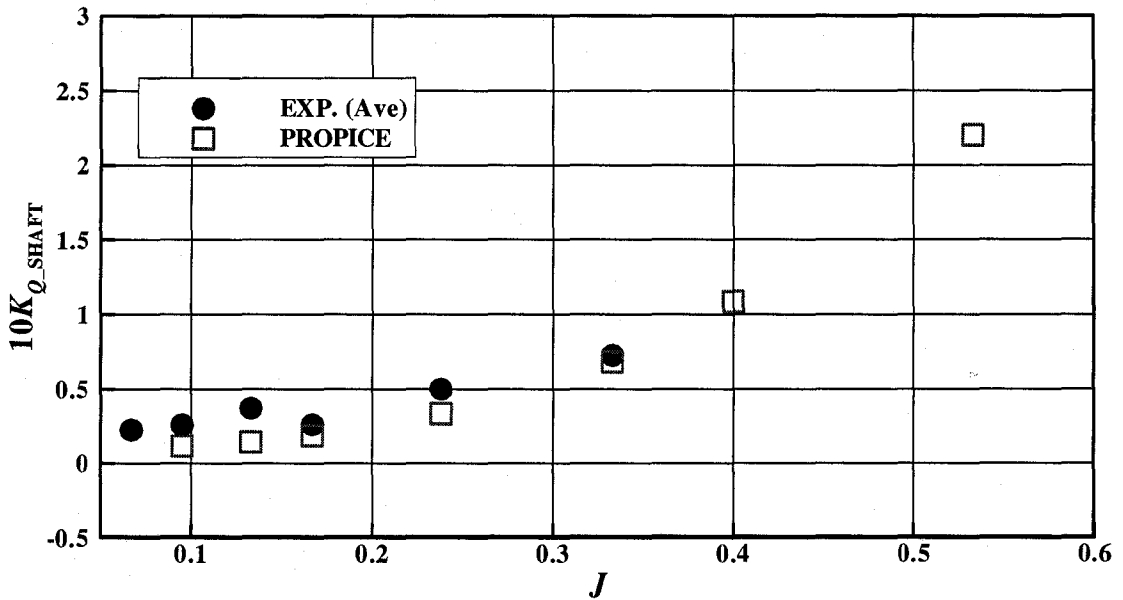
Figure 5-16: $10K_{Q\_SHAFT}$ comparison (ice related loads, azimuthing angle of 120 degrees, 35 mm depth of cut)
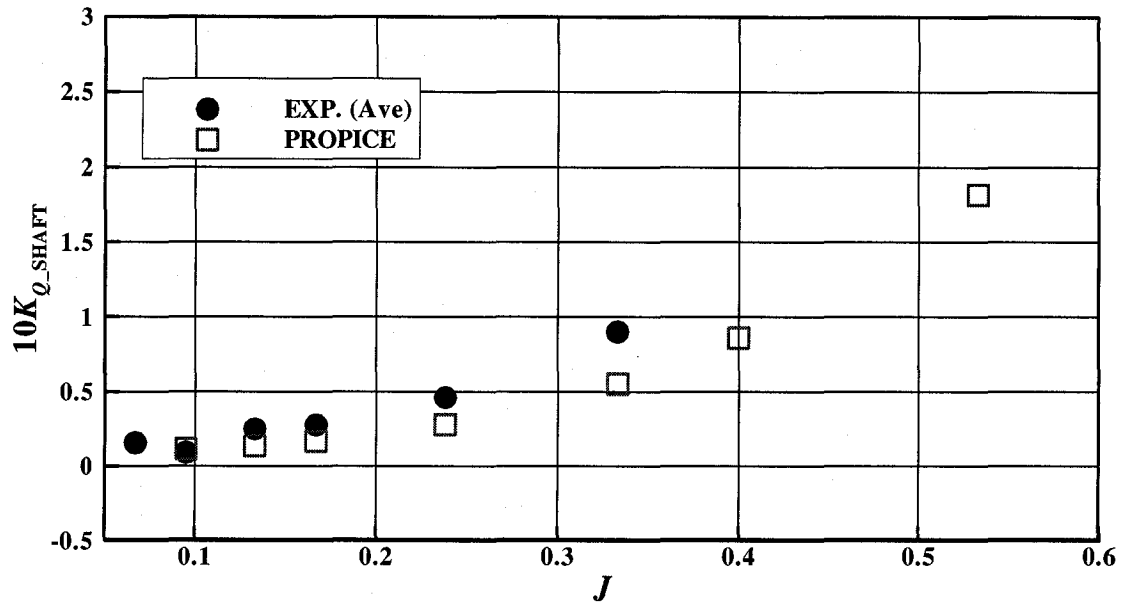
Figure 5-17: $10K_{Q\_SHAFT}$ comparison (ice related loads, azimuthing angle of 90 degrees, 35 mm depth of cut)

5.3. Comparison of Total Loads in Ice Covered Water

Figure 5-18 and Figure 5-19 present the average shaft thrust and torque coefficients versus the advance coefficient from the experiments and the PROPICE in ice covered water. The total loads present here consist of separable hydrodynamic loads and ice related loads. The comparisons are made under the following test conditions: an azimuthing angle of 180 degrees, a tractor mode and depth of cut of 35 mm. The solid circles represent the experimental results and the open squares represent the numerical results.

The experimental results for the average thrust coefficient, K_{T_SHAFT}, correspond closely with the numerical results (PROPICE), as shown in Figure 5-18. The trends are similar to those for the ice related loads on the blade, as described in 5.2.1

In Figure 5-19, the average shaft torque coefficients, 10 K_{Q_SHAFT}, from the PROPICE present a good agreement with those from the experiments. In the numerical results, as the advance coefficients increase until $J = 0.7$, the torque coefficients show the increased trends. Due to the limitation of the model tests, comparisons are made until $J = 0.53$.

Total Loads in Ice, Average K_{T_SHAFT}, 180 Azimuthing Angle, Tractor Mode
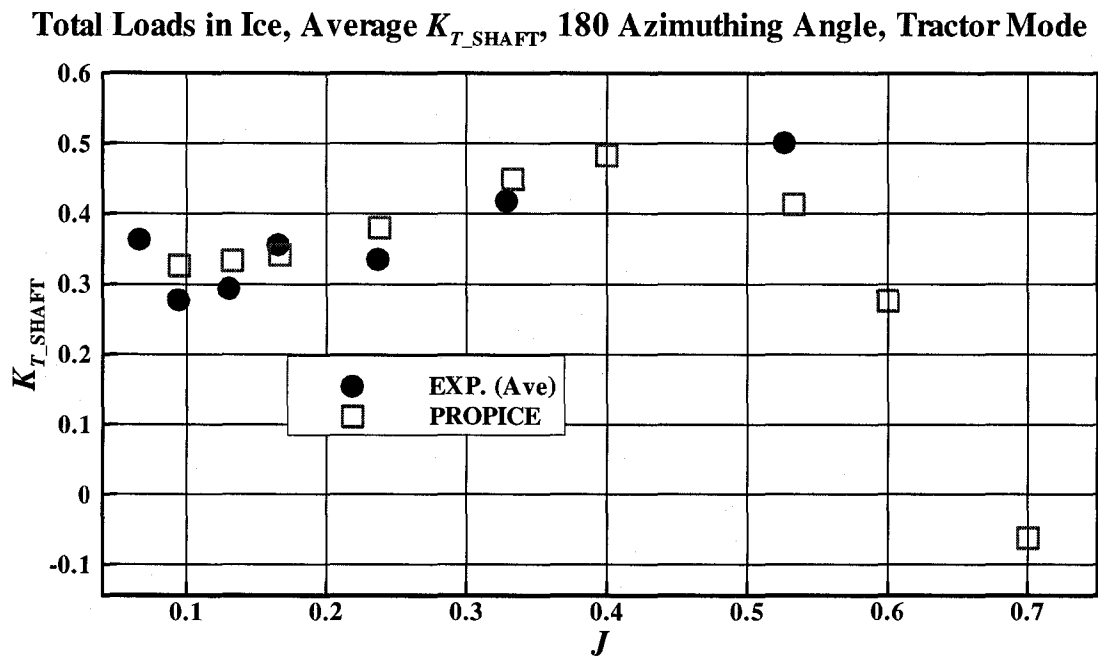
Figure 5-18: K_{T_SHAFT} comparison (Total loads, azimuthing angle of 180 degrees, 35 mm depth of cut)

Total Loads in ice, Average $10K_{Q\_SHAFT}$, 180 Azimuthing Angle, Tractor Mode
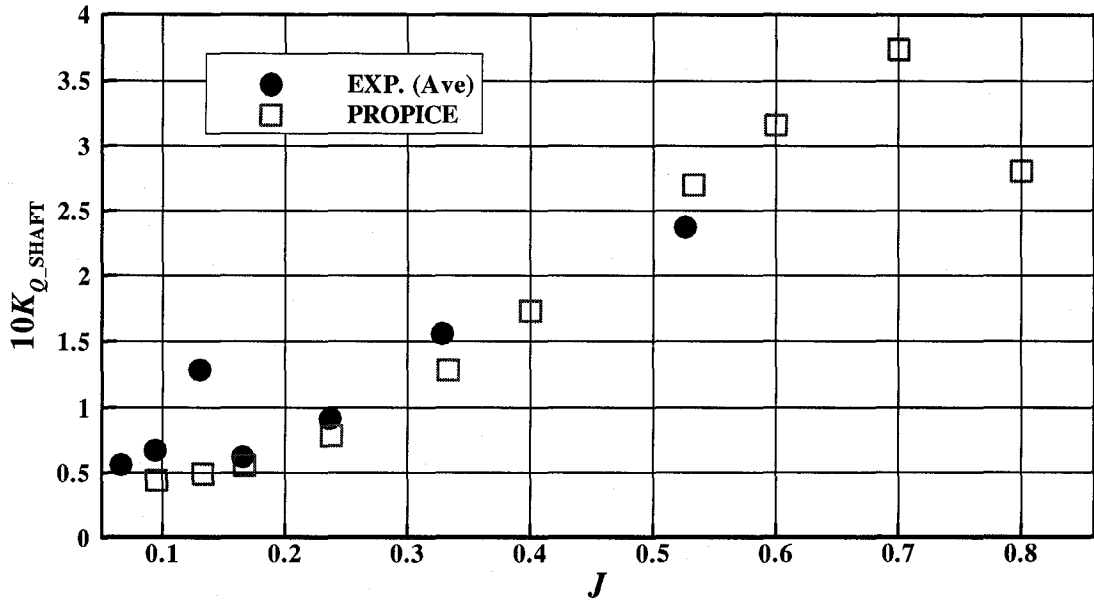
Figure 5-19: $10K_{Q\_SHAFT}$ comparison (Total loads, azimuthing angle of 180 degrees, 35 mm depth of cut)

At the depth of cut of 15 mm, the average shaft thrust and torque coefficients from both numerical calculations and experiments are shown in Figure 5-20. For the ice load calculations, 120 kPa, measured from the experiments, was used for the ice reference pressure for the PROPICE. In the experiments, repeat runs were carried out three times at 15 mm depth of cut. Although the test condition was identical, variation in the loads was observed, particularly in the shaft torque coefficients. Detailed explanations regarding experimental results are shown in Section 3.5.4. The overall trends for the calculated shaft thrust and shaft torque values have a good agreement with those of the experiments.

136
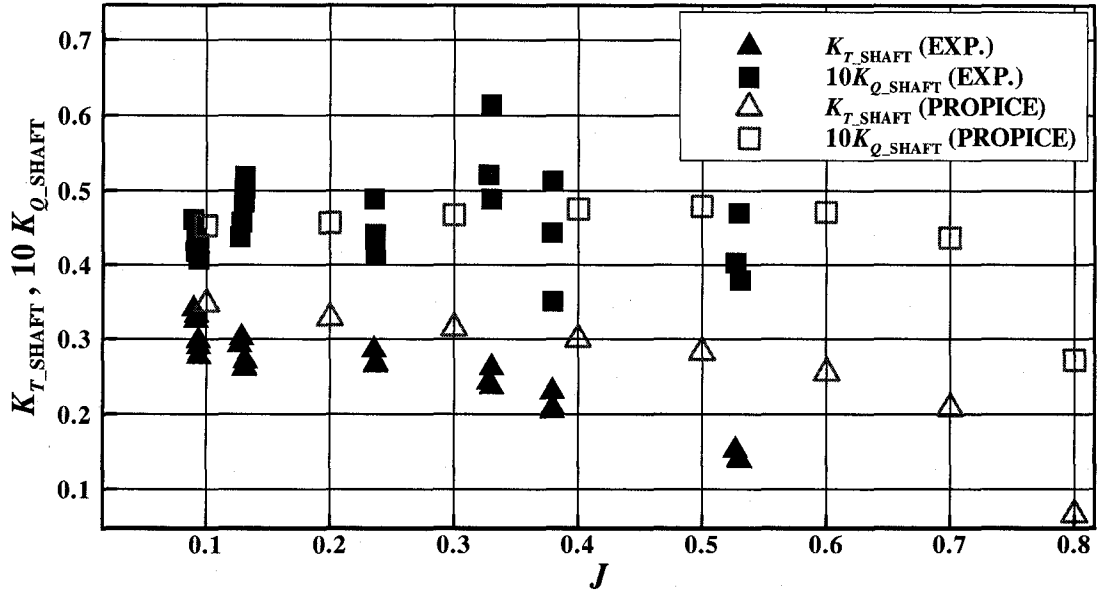
Figure 5-20: K_{T_SHAFT} and $10K_{Q\_SHAFT}$ comparison (Total loads, azimuthing angle of 180 degrees, 15 mm depth of cut)

Figure 5-21 shows the distribution of the calculated pressure coefficient on both the pressure and suction sides of the propeller blade for 35 mm depth of cut. In the two pictures at the top, the advance coefficient is 0.133 and 0.238, and the shadowing areas are clearly visible. In the two pictures in the middle, the advance coefficient is 0.4 and 0.533, and the shadowing areas have almost disappeared. The geometric angle of attack is still positive up to advance coefficients of 0.7. In the two pictures at the bottom, the advance coefficient is 0.7 and 0.8, and the ice loads gradually move from the pressure side to the suction side of the propeller due to the negative geometric angle of attack. At the advance coefficient of 0.7, even most pressure side is in contact with the ice, the interacting angle (Θ) is closed to the 90 degrees, so the crushing forces contribute to the blade or shaft thrust are minimized.

137
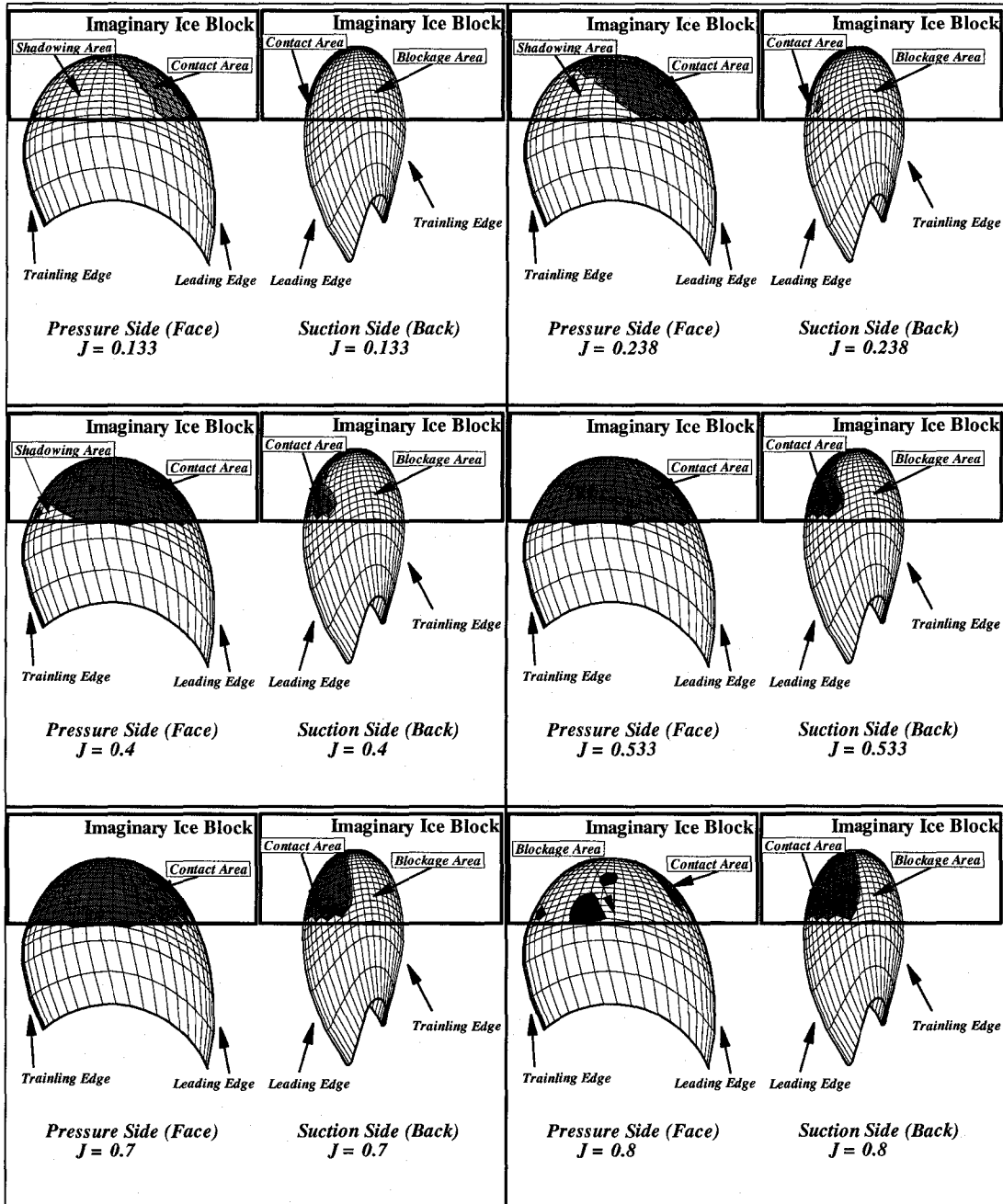
Figure 5-21: Calculated pressure distribution on the pressure and suction side of the blade
(from top left, J = 0.133, 0.238, 0.4, 0.533, 0.7 and 0.8)

138

5.4. Comparison with Available Ice Loads Formulae

In this section, two ice load models are introduced. The objective of this section is to provide comparisons between experimental results and existing ice load models. The experimental results are scaled up to full-scale by using Froude scaling law with a scale factor of 13.733. Certain conditions for the ice load models are addressed. The symbols for the JRPA #6 and IACS model are shown in Table 5-1.

Table 5-1: List of symbols for the JRPA #6 and IACS ice load models

JRPA #6	IACS
F_{bl} : maximum blade force [kN]	F_b : maximum backward blade force [kN]
J : advance coefficient	F_f : maximum forward blade force [kN]
Q_{av} : average shaft torque [kNm]	Q_{max} : maximum propeller torque [kNm]
Q_{max} : maximum shaft torque [kNm]	S_{ice} : ice strength index for blade ice force
α : angle of attack [degrees]	(for PC7, $S_{ice} = 1$.)
σ : uniaxial compressive strength of ice [MPa]	S_{qice} : ice strength index for blade ice torque
	(for PC7, $S_{qice} = 1$.)
d - hub diameter [m]; D - propeller diameter [m]; EAR - expanded area ratio; H_i - Ice block thickness [m]; n - propeller rotating speed [rps]; $P/D = P_{0.7}/D$ - pitch ratio at 0.7 R; $t/D = t_{0.7}/D$ - blade thickness ratio at 0.7 R; Z - number of blades	

5.4.1. JRPA #6 Design Loads

As a part of the JRPA #6 project, a simulation model for propeller-ice interaction loads was developed. After parametric studies with the simulation model, a simple regression type dimensioning model was presented (Koskinen et al., 1996; Jones et al., 1997). The limitations of this model are:

1. Valid for open propellers such as fixed pitch and controllable pitch propellers (ducted propellers can be calculated, but the formulae are not shown in this thesis);

2. Valid for the first quadrant operating condition and limited use of negative angles of attack.

In this thesis, only shaft thrust and torque calculations are shown. The ice block thickness for the JRPA # 6 model used the depth of cut of 35 mm multiplied by scale ratio (13.733).

Minimum blade force (F_{bl}), which represent backward bending, is

$$F_{bl} = -92.9717 \times \left(\sigma \times \frac{EAR}{Z} \right)^{0.2866} \times \left(\frac{H_i}{D} \right) \times e^{(-0.1830\alpha)} \times (nD)^{0.7126} \times D^{2.0235} . \qquad (5\text{-}1)$$

Maximum blade force (F_{bl}), which represent forward bending, is

$$F_{bl} = 400 \times (EAR/Z) \times \pi (D/2)^2 . \qquad (5\text{-}2)$$

Shaft thrust is

$$T = 1.1304 \times F_{bl}. \qquad (5\text{-}3)$$

Maximum shaft torque is

$$Q_{\max} = -234.3560 \times (1 - d/D) \times \sigma^{0.1948} \times \left(\frac{H_i}{D}\right)^{1.0741} \times (-0.9026 \times J^2 + J + 0.4384)$$
$$\times (P/D)^{0.1620} \times (t/D)^{0.6047} \times (nD)^{0.1728} \times D^{3.0421} \qquad (5\text{-}4)$$

Average shaft torque is

$$Q_{av} = -152.0408 \times (1 - d/D) \times \sigma^{0.1825} \times \left(\frac{H_i}{D}\right)^{1.1987} \times (-0.8811 \times J^2 + J + 0.5198)$$
$$\times (P/D)^{0.2747} \times (t/D)^{0.5624} \times (nD)^{0.2009} \times D^{3.0413} \qquad (5\text{-}5)$$

5.4.2. IACS Design Loads

The International Association of Classification Societies (IACS) design loads are addressed in this section (IACS, 2006). The IACS requirements are composed of seven different ice classes: PC1 to PC7; for which increasing number indicates that the ice properties including thickness and strength become thinner and weaker. For the present comparison, the PC7 ice class (ice thickness is 1.5 meter) is considered.

The formulae provided here are suitable for the present experimental model only because IACS formulae can be different depending on interaction conditions. The rps used for the IACS model was 1.35, which is equivalent to 5 rps case in the model tests based on Froude scaling law. The effect of shaft dynamics is not considered.

141

Maximum backward blade force is

$$F_b = -27 \times S_{ice} [nD]^{0.7} \left[\frac{EAR}{Z} \right]^{0.3} [D]^2 \text{ kN}. \qquad (5\text{-}6)$$

Maximum forward blade force is

$$F_f = 250 \times \left[\frac{EAR}{Z} \right] [D]^2 \text{ kN}. \qquad (5\text{-}7)$$

Maximum propeller torque is

$$Q_{max} = 105 \times (1 - d/D) \times S_{qice} \times (P_{0.7}/D)^{0.16} \times (t_{0.7}/D)^{0.6} \times (nD)^{0.17} \times D^3 \text{ kNm}. \qquad (5\text{-}8)$$

Finally, maximum forward and backward thrust values (T_f and T_b) on the shaft during propeller-ice interaction are

$$T_f = 1.1 \times F_f \text{ kN and} \qquad (5\text{-}9)$$

$$T_b = 1.1 \times F_b \text{ kN}. \qquad (5\text{-}10)$$

5.4.3. Comparisons of Experimental Results with Ice Loads Formulae

With respect to the present test results, non dimensional shaft thrust and torque coefficients were calculated from the total loads (sum of the ice related loads and separable hydrodynamic loads) during the milling period. Both JRPA #6 and IACS

models consider the effect of rps; as the rps increases, the magnitudes of the thrust/torque coefficients decrease. As the ice class number in the IACS model decreases, the maximum thrust values remain constant (only minimum thrust values vary). The effects of angle of attack and advance coefficient are taken into account for the thrust and torque calculations in the JRPA #6 model except for the maximum thrust value.

In Figure 5-22, the gray area shows the range of the JRPA #6 model. For most values of advance coefficient, our measurements fall within the JRPA #6 range. At the advance coefficient of 0.53, both the maximum and minimum shaft thrust magnitudes from the JRPA #6 are slightly lower than those from the measurements. The IACS model shows somewhat underestimated maximum and overestimated minimum shaft thrust values in terms of the magnitude.
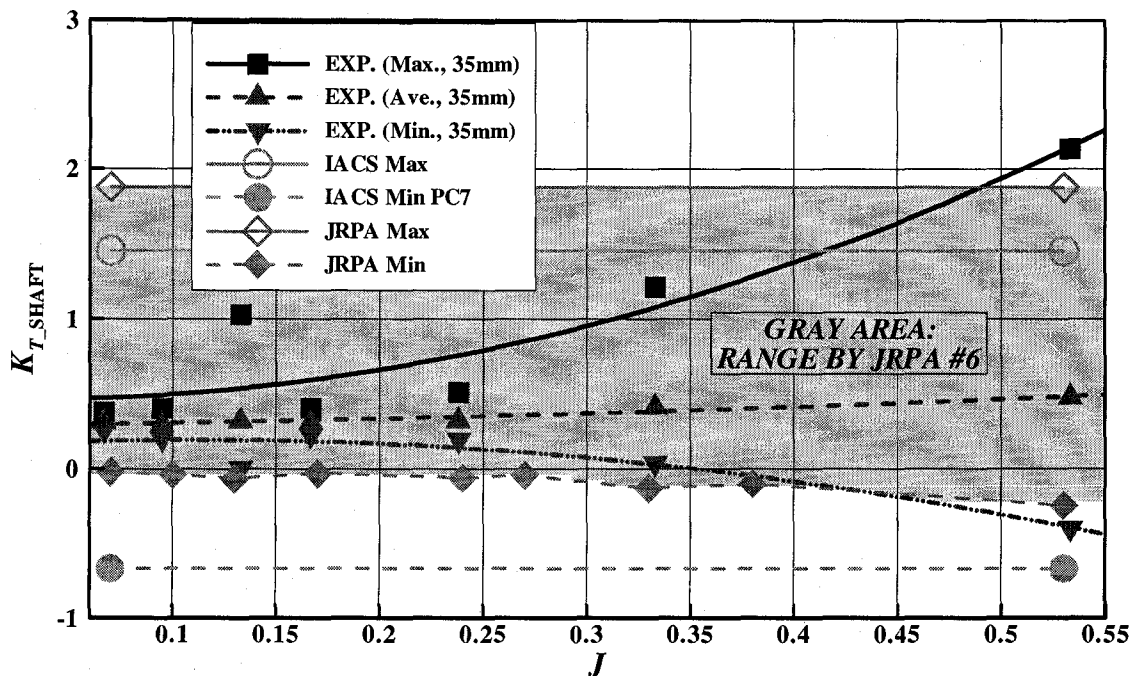
Figure 5-22: K_{T_SHAFT} comparison among the present tests (maximum, minimum and average values), the JRPA #6 (maximum and minimum), and the IACS (maximum and minimum for the PC7)

In Figure 5-23, the maximum torque values from the IACS shown are slightly lower than those from the present measurements at the advance coefficient of 0.53, but the average or maximum torque values from the JRPA #6 are lower than the most average torque values from the present measurements. Although the JRPA #6 model gives underestimated torque coefficient values, the trends of lower rps causing higher torque values are similar as the findings of this study.
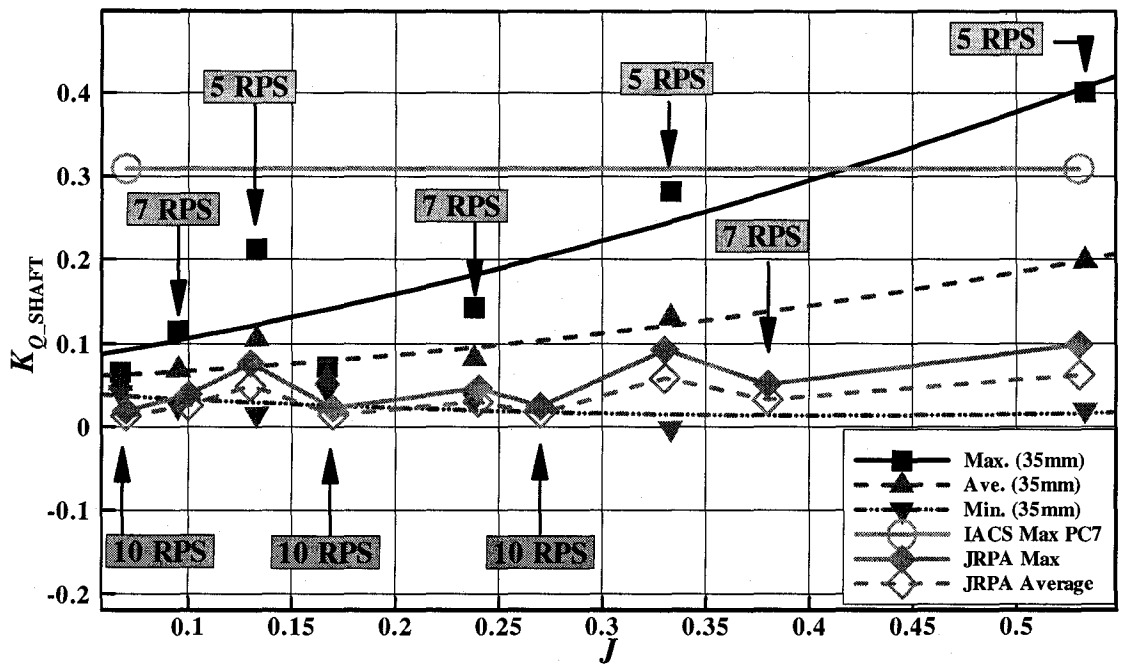
Figure 5-23: K_{Q_SHAFT} comparison among the present tests (maximum, minimum and average values), the JRPA #6 (maximum and average), and the IACS (maximum for the PC7)

5.5. Discussion of Numerical Results

5.5.1. Sensitivity Analysis

In order to verify the sensitivity of the empirical factors to affect the results, various empirical factors were used. As explained at [Step.6] in Section 4.4, for ice crushing pressure, an empirical factor (*EFC*) of 4 was used. For ice shearing force, ice reference pressure was divided by an empirical factor (*EFS*) of 4 was used. In this section, determination of these empirical factors is explained and the effects of these empirical factors on the numerical results are assessed by using sensitivity analyses.

5.5.1.1. Empirical Factor for Ice Crushing Pressure (*EFC*)

For the present numerical study, the *EFC* was estimated from Moores (2002) results because Moores used EG/AD/S model ice same as present model ice. The compressive strength of EG/AD/S model ice was measured from in-situ test which used the compression speed of 0.004 m/s and strain rate is approximately 4×10^{-3}. At this strain rate, compressive strength is about 2 - 3 MPa. When the strain rates are from 1 to 10, compressive strength is about 4.5 - 8 MPa without error bar. As discussed in Section 3.7.1.2, expected strain rate for present tests would be up to 10^2 /s range, so the compressive strength at this strain rate could be reached at 4 times of that of strain rate of 4×10^{-3}.
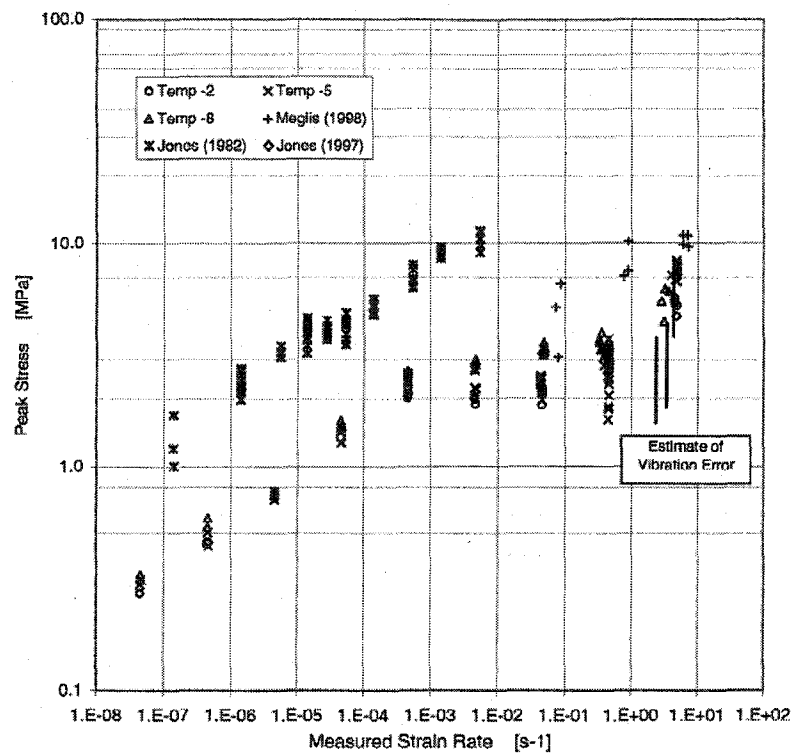
Figure 5-24: EG/AD/S compressive strength with three different temperatures and other types of ice from literatures against strain rate (after Moores, 2002)

5.5.1.2. Empirical Factor for Ice Shearing Force (*EFS*)

Since there were no references for shearing strength against strain rate, *EFS* was estimated from in-situ measurements. During the present model tests, model ice properties were measured and shown in Figure 3-2 and Figure 3-3. From the figures, the shearing strength was about 25 % to 50 % of the compressive strength. If the strain rate increases, shearing strength may be changed. In this thesis, *EFS* of 1/4 (25 %) was used.

5.5.1.3. Sensitivity of Empirical Factors

Sensitivity analyses are carried out with various empirical factors in this section. Three different empirical factors for crushing pressure (*EFC*): 3, 4, and 5 and three different those for shearing force (*EFS*): 1/2, 1/4, and 1/8 are combined. Numerical results are compared with experimental results at 35 mm depth of cut. From Figure 5-25 to Figure 5-29 and from Figure 5-30 to Figure 5-34, differences of shaft thrust and shaft torque coefficients between experimental and numerical results are compared respectively. ΔK_{T_SHAFT} and ΔK_{Q_SHAFT} are defined as Equations (5-11) and (5-12).

$$\Delta K_{T\_SHAFT} = K_{T\_SHAFT} \text{ from experiments} - K_{T\_SHAFT} \text{ from numerical calculations.} \quad (5\text{-}11)$$

$$\Delta K_{Q\_SHAFT} = K_{Q\_SHAFT} \text{ from experiments} - K_{Q\_SHAFT} \text{ from numerical calculations.} \quad (5\text{-}12)$$

From Figure 5-25 to Figure 5-28, ΔK_{T_SHAFT} decreases when the *EFC* increases or *EFS* decreases. Once the *EFC* increases, numerical K_{T_SHAFT} increases because most crushing pressure will be acting on the pressure side of the propeller blade if *J* is less than about

0.8 as shown in Figure 5-21 and Figure 3-34. Once the *EFS* increases, numerical K_{T_SHAFT} decreases because drag on the pressure side increases.

Figure 5-29 shows ΔK_{T_SHAFT} for 15 mm depth of cut with 180 degrees of azimuthing angle. Effect of various empirical factors is not obvious because ice loads may not significantly affect the total shaft thrust coefficient due to small ice contact area in 15 mm depth of cut case.
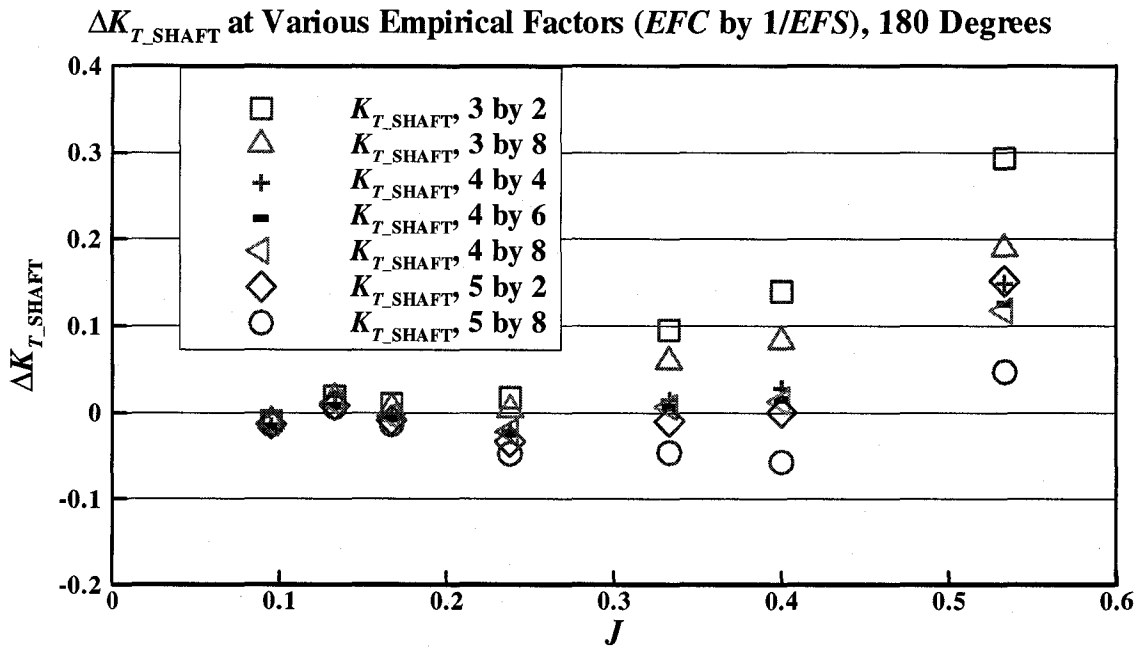
Figure 5-25: ΔK_{T_SHAFT} at various empirical factors (*EFC* by 1/*EFS*) with 180 degrees and 35 mm depth of cut
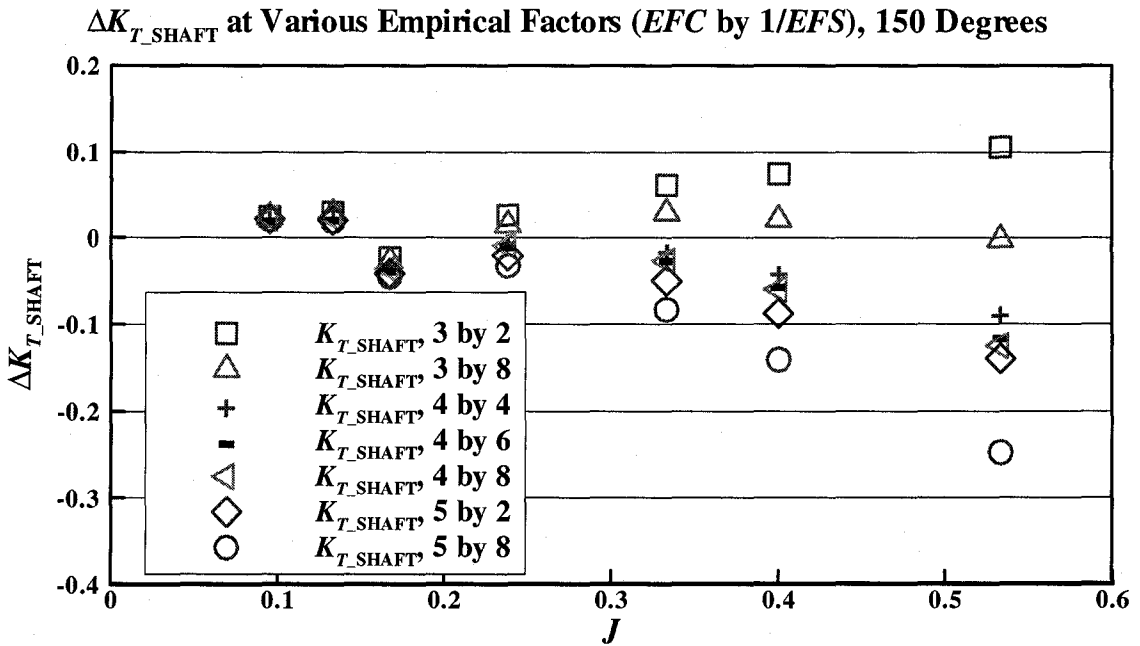
Figure 5-26: ΔK_{T_SHAFT} at various empirical factors (*EFC* by 1/*EFS*) with 150 degrees and 35 mm depth of cut
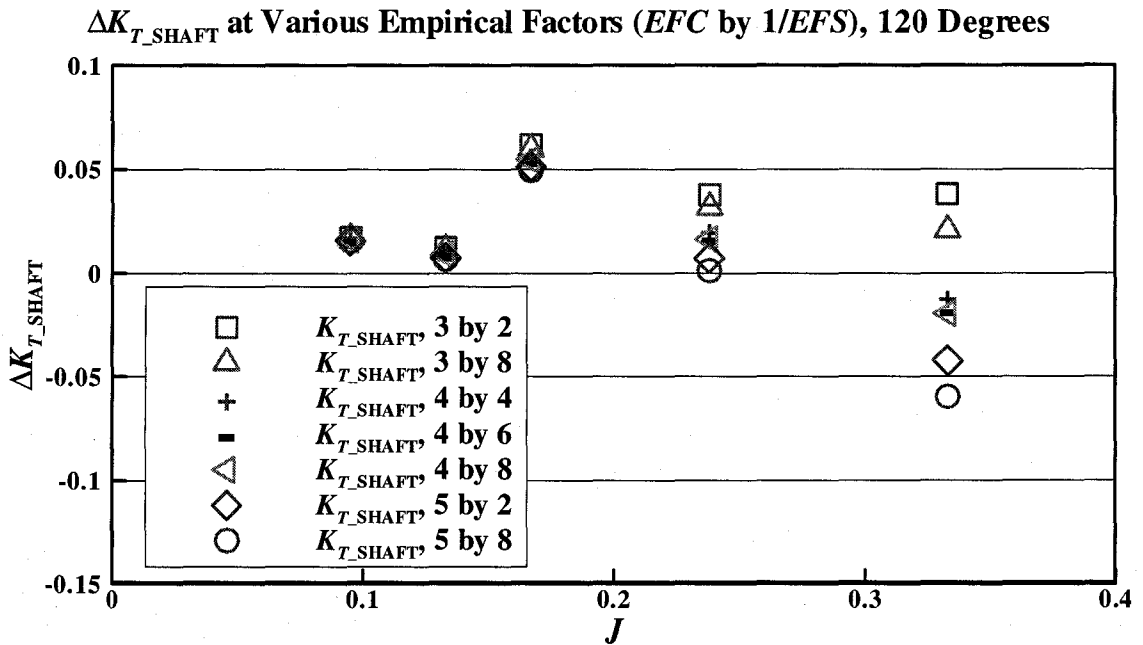
Figure 5-27: ΔK_{T_SHAFT} at various empirical factors (*EFC* by 1/*EFS*) with 120 degrees and 35 mm depth of cut
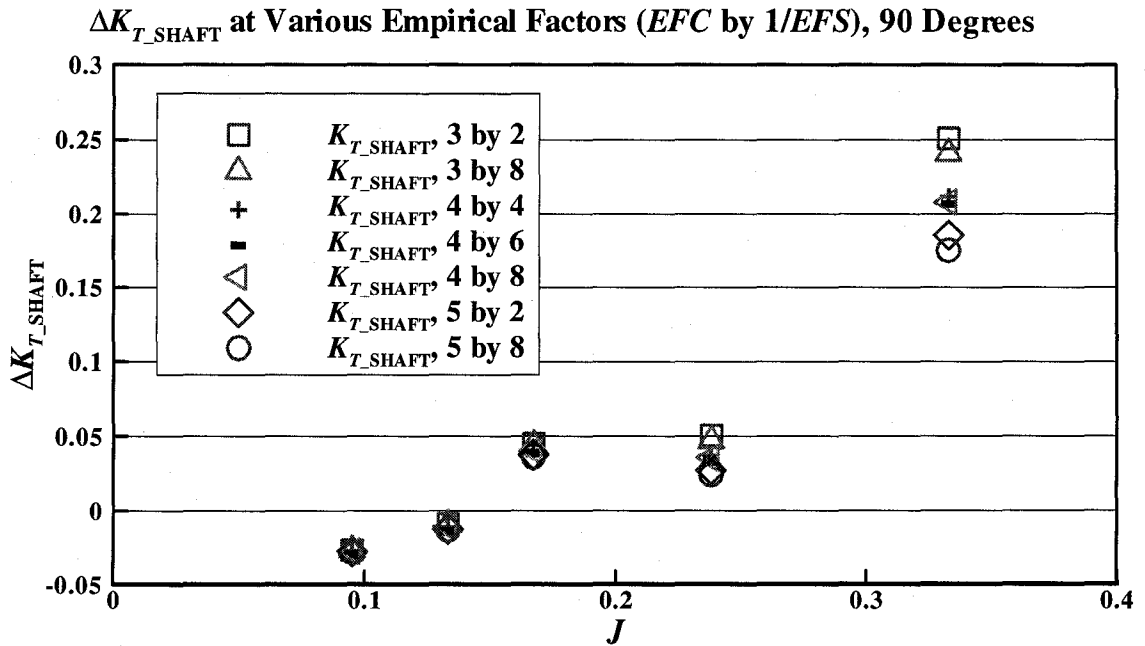
Figure 5-28: ΔK_{T_SHAFT} at various empirical factors (*EFC* by 1/*EFS*) with 90 degrees and 35 mm depth of cut
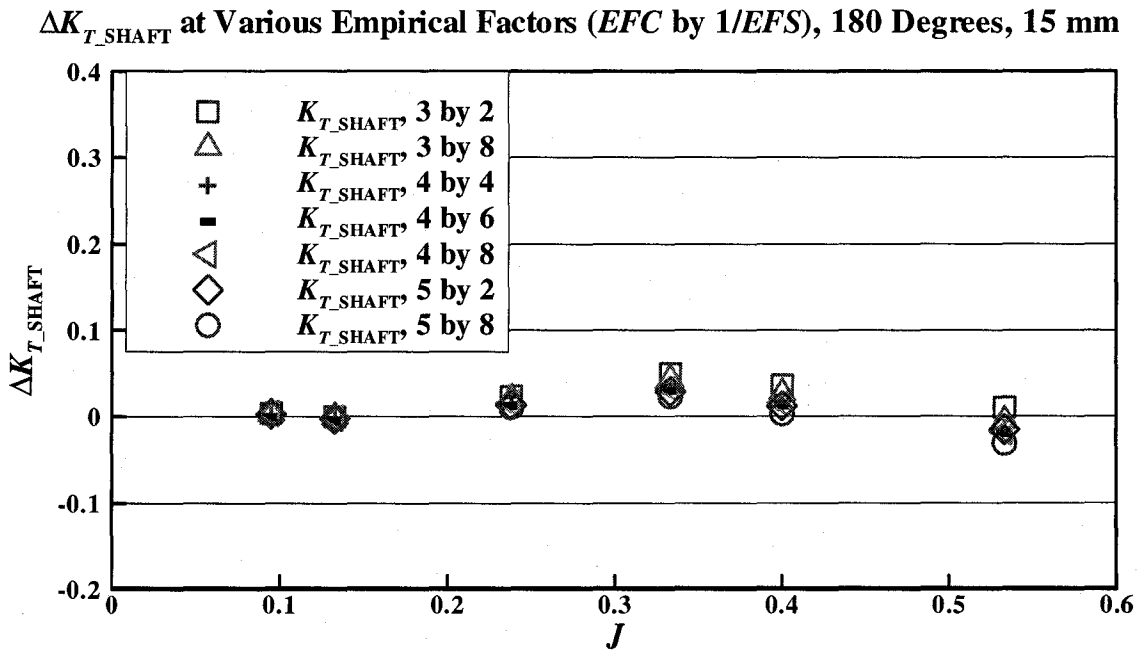
Figure 5-29: ΔK_{T_SHAFT} at various empirical factors (*EFC* by 1/*EFS*) with 180 degrees and 15 mm depth of cut

From Figure 5-30 to Figure 5-33, ΔK_{Q_SHAFT} decreases when the *EFC* increases or *EFS*

increases. Once the *EFC* increases, numerical K_{Q_SHAFT} slightly increases as compared

values for 3 by 2 with 5 by 2. Once the *EFS* increases, numerical K_{T_SHAFT} sensitively

increases because shearing forces are directly corresponding to shaft torque. Again,

values of ΔK_{Q_SHAFT} for 15 mm depth of cut with 180 degrees of azimuthing angle do not

show the effect of various empirical factors clearly because of small ice contact area

(Figure 5-34).

Figure 5-30: ΔK_{Q_SHAFT} at various empirical factors (*EFC* by 1/*EFS*) with 180 degrees
and 35 mm depth of cut

Figure 5-31: ΔK_{Q_SHAFT} at various empirical factors (*EFC* by 1/*EFS*) with 150 degrees and 35 mm depth of cut

Figure 5-32: ΔK_{Q_SHAFT} at various empirical factors (*EFC* by 1/*EFS*) with 120 degrees and 35 mm depth of cut

ΔK_{Q_SHAFT} at Various Empirical Factors (*EFC* by 1/*EFS*), 90 Degrees

0.08

0.06

0.04

0.02

0

-0.02

ΔK_{Q_SHAFT}

□	K_{Q_SHAFT}, **3 by 2**
△	K_{Q_SHAFT}, **3 by 8**
+	K_{Q_SHAFT}, **4 by 4**
■	K_{Q_SHAFT}, **4 by 6**
◁	K_{Q_SHAFT}, **4 by 8**
◇	K_{Q_SHAFT}, **5 by 2**
○	K_{Q_SHAFT}, **5 by 8**

0   0.1   0.2   0.3   0.4

J

Figure 5-33: ΔK_{Q_SHAFT} at various empirical factors (*EFC* by 1/*EFS*) with 90 degrees and 35 mm depth of cut

ΔK_{Q_SHAFT} at Various Empirical Factors (*EFC* by 1/*EFS*), 180 Degrees, 15mm

0.02

0

-0.02

-0.04

-0.06

ΔK_{Q_SHAFT}

□	K_{Q_SHAFT}, **3 by 2**
△	K_{Q_SHAFT}, **3 by 8**
+	K_{Q_SHAFT}, **4 by 4**
■	K_{Q_SHAFT}, **4 by 6**
◁	K_{Q_SHAFT}, **4 by 8**
◇	K_{Q_SHAFT}, **5 by 2**
○	K_{Q_SHAFT}, **5 by 8**

0   0.1   0.2   0.3   0.4   0.5   0.6

J

Figure 5-34: ΔK_{Q_SHAFT} at various empirical factors (*EFC* by 1/*EFS*) with 180 degrees and 15 mm depth of cut

153
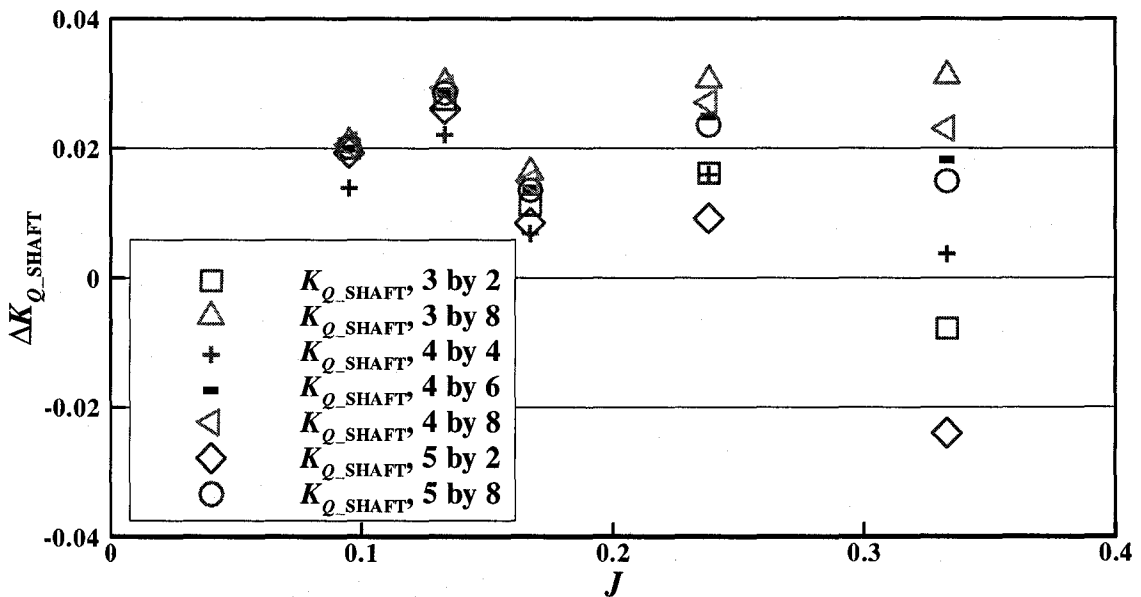
Figure 5-35 shows Root Mean Square (RMS) of ΔK_{T_SHAFT} and ΔK_{Q_SHAFT} for four

azimuthing angles at 35 mm depth of cut and for 180 of azimuthing angles at 15 mm

depth of cut with various empirical factors (Equations (5-13) and (5-14)).

$$\text{RMS of } \Delta K_{T\_SHAFT} = \sqrt{\frac{1}{N}\sum_{i}^{N} \Delta K_{T\_SHAFT}{}^{2}{}_{i}} , \tag{5-13}$$

$$\text{RMS of } \Delta K_{Q\_SHAFT} = \sqrt{\frac{1}{N}\sum_{i}^{N} \Delta K_{Q\_SHAFT}{}^{2}{}_{i}} , \tag{5-14}$$

where N is the number of conditions (30).

For ΔK_{T_SHAFT}, *EFC* of 4 seems appropriate. At *EFC* of 4, 1/*EFS* of 8 can reach the

minimum RMS of ΔK_{T_SHAFT}. For ΔK_{Q_SHAFT}, 1/*EFS* of 8 shows minimum RMS of
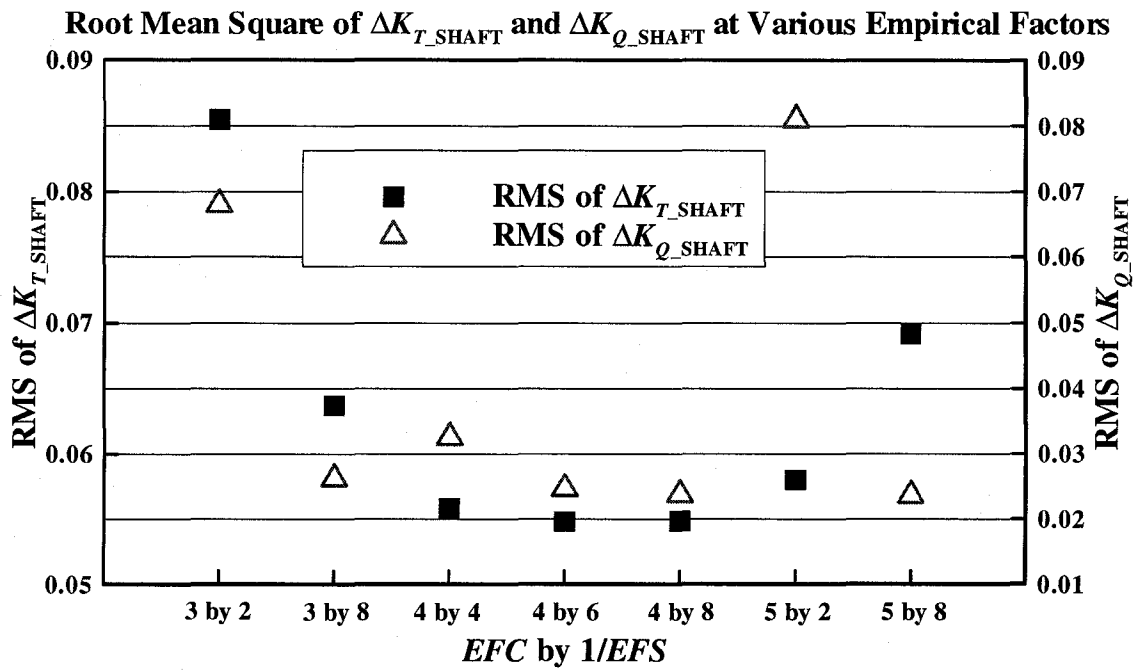
ΔK_{Q_SHAFT}.

Figure 5-35: RMS of $\Delta K_{T\_\text{SHAFT}}$ and $\Delta K_{Q\_\text{SHAFT}}$ at Various Empirical Factors (*EFC* by 1/*EFS*)

As shown in Figure 5-35, the empirical factors used in this thesis may not the best combination, but RMS differences for shaft thrust and shaft torque coefficients between "4 by 4" and "4 by 8" cases are as small as 0.001 and 0.009, respectively. It is also expected that the shearing strength of the model ice at high strain rate such as propeller rotating speed can be as small as 13% (1/8 of *EFS*) of compressive strength measured from in-situ tests.

Chapter 6 Conclusions

This thesis provides the results of an investigation for the propeller-ice interaction

phenomenon through model tests in an ice tank with a model podded propulsor. A

numerical model has been developed to predict ice loads acting on a propeller during

propeller-ice interaction and this has been validated with experimental results. For the

numerical model, a pod, strut, and hub were not considered. In this chapter, some major

findings from this work are summarized.

6.1. Conclusions

In the first chapter, the author hypothesized that the ice loads acting on the propeller

during propeller-ice interaction consist of separable hydrodynamic loads, inseparable

hydrodynamic loads, and ice milling loads; ice related loads are the sum of the

inseparable hydrodynamic loads and ice milling loads. This hypothesis is useful to assess

individual load components, but this includes several assumptions: 1. Three components

can be calculated by linear superposition; 2. Separable hydrodynamic loads experienced

partially on the blade during the milling period are the same as separable hydrodynamic loads from open water condition; 3. Inseparable hydrodynamic loads are calculated by using only simplified blockage condition (cavitation or proximity effects are not taken into account). Inseparable hydrodynamic loads did not measured separately by using such as cavitation tunnel or physical blockage model but these loads were estimated from previous results and numerical calculations. Calculated ice related loads and total loads have a good agreement with experimental results at lower J ($J < 0.4$). Inseparable hydrodynamic loads from ice blockage (Luznik et al., 1995) also showed reasonable values (about 170 % of separable hydrodynamic loads). This hypothesis is important especially for the milling period because three load components are acting on the blade simultaneously. From this hypothesis, it is concluded that the ice milling loads are much higher than inseparable hydrodynamic loads or approximated separable hydrodynamic loads as shown in Figure 3-39. The ice related loads during the milling period are useful to present and understand the propeller-ice interaction loads because the position of the propeller blade contacted with ice can be identified.

6.1.1. Ice Related Loads during Milling Period

Ice related loads on the blade and shaft were investigated during the milling period. The major findings from the ice related loads in the present model tests and numerical model are:

1. Propeller-ice interaction loads are strongly dependent on the advance coefficient (J), pitch angle (ϕ), and their combinations and they can be determined by using kinematic and geometric considerations, as explained in Sections 4.3 and 4.4. As the advance coefficient increases, propeller-ice interaction can be explained with three periods as below:

- First period ($0 < J \leq 0.4$ for a 35 mm depth of cut)- the shadowing area starts to decrease and the ice milling area on pressure side increases due to the increase in the angle of advance, β;

- Second period ($0.4 < J \leq 0.7$ for a 35 mm depth of cut)- the ice milling area on suction side increases and ice milling loads on the pressure side decrease (the ice failure mode partially changes from crushing to shearing on the pressure side) due to the decrease in the angle of attack;

- Third period ($J > 0.7$ for a 35 mm depth of cut) - the milling area on the suction side increases and the milling area on the pressure side almost disappears.

As a result, it is concluded that the performance of the propeller during the milling period is:

- Non dimensional coefficients of the ice related loads acting on the shaft and blade increase as the advance coefficient (J) increase until J reaches certain value, which can be determined by the shadowing effect and the angle of attack. Once the J goes over the certain value, the shaft and blade thrust start to decrease.

- As the depth of cut increases, the ice related loads increase. This is because of the increase in the contacting area and higher pitch angle at lower blade radii. Deeper depth of cut leads to a higher pitch angle, consequently the angle of attack increases positively as shown in Figure 3-34.

- At lower advance coefficient regions (J < 0.1 ~ 0.2), the ice milling loads are not as significant as at higher advance coefficient regions because the shadowing effect mainly occurs at low advance coefficient.

2. From the numerical model, it is assumed that the crushing force during propeller-ice interaction is approximately four times the compressive strength from in-situ tests (EFC = 4), while a shearing force is 25 % of the compressive strength from in-situ tests (EFS = 1/4) as discussed in Section 5.5. Based on the sensitivity analyses for empirical factors in Section 5.5, these empirical factors are well matched with experimental results in terms of shaft thrust and shaft torque coefficients. For the maximum loads, the crushing force is multiplied by weight factor of 6. Effect of azimuthing angle (ψ) is also taken into account by using geometric and kinematic considerations, as explained in Section 4.4. For example, the shadowing criteria for the advance and radial distances are $\dfrac{V \sin(\psi)}{Z\,n}$ and $\dfrac{V \cos(\psi)}{Z\,n}$ respectively. Most numerical results for non-dimensional force/moment coefficients show a good agreement with experimental results.

3. For the present experimental tests, the average shaft thrust values are almost equal to the average blade thrust values, while the average blade torque values are 1.7 times higher than the average shaft torque values. A possible reason is the shaft dynamic effects due to the ice torque excitation.

4. At the advance coefficient of 0.4, which may be a maximum value when a ship navigates in ice covered water, the maximum shaft thrust values (separable hydrodynamic loads + ice related loads during the milling period) for 35mm and 15mm depths of cut are about 800% and 300%, respectively, of the average shaft thrust value in open water. At the same condition, the maximum shaft torque values for 35mm and 15mm depths of cut are 1100% and 400%, respectively, of the average shaft torque value in open water.

5. As the azimuthing angle decreases from 180 to 90 degrees, the shaft/blade thrust increase due to the increase in the angle of attack; which can increase the force acting on the pressure side of the blade because the ice failure mode can be changed from shearing to crushing modes.

6. For ice related loads during a milling period, the maximum and minimum loads with large magnitude from average loads are observed from the experimental results, as shown in Table 6-1. For both thrust coefficients, the average values are similar (the shaft thrust coefficient is 83 % of blade thrust coefficient) but the maximum shaft thrust coefficients can be varied about two times of the variation of the maximum blade thrust coefficients. This is because the shaft thrust coefficients can be affected by the ice loads acting on the

160

other blades except the key blade even though ice related loads are considered during the

milling period. For torque coefficients, though blade torque coefficients are 1.7 times of

shaft torque coefficients, the variations of the magnitude for maximum and minimum are

similar. It is noted that the values in Table 6-1 were calculated from ice related loads

during the milling period; at each milling event, statistics (maximum, minimum and

average) were compiled and took an average over the total milling events for each

maximum, minimum and average.

Table 6-1: Variations of the maximum and minimum about average values at $J = 0.4$.

	K_{T_SHAFT}	K_{Q_SHAFT}	K_{T_BLADE}	K_{Q_BLADE}
Maximum (%)	489	228	269	210
Minimum (%)	-98	-12	-36	-22

6.1.2. Total Loads in Ice Covered Water

For the experimental results, total loads in ice covered water have been calculated by

general statistics to present the maximum, minimum, and average values. This procedure

does not take into account the milling period, so the results show a general trend of the

propeller-ice interaction loads. The major findings are:

1. Overall trends are similar to those for ice related loads; the magnitudes of most average

values are similar to those of ice related loads; maximum values for the blade loads are

slightly different. For the shaft thrust case, the maximum K_{T_SHAFT} from the total loads is

over 6, while the value from the ice related loads is approximately 2. It cannot be explained clearly, but the uncertainty related problems may result in.

2. As the azimuthing angle decreases from 180 to 120 degrees, the unit thrust decreases due to the increase in the resistance. When the azimuthing angle is less than 120 degrees, the unit thrust increases again, because the reversing wake can push the ice away from the pod and strut.

6.2. Recommendations

6.2.1. Model test in ice

1. The model tests were designed for constant milling conditions in pre-sawn ice. Tests in level ice would provide more accurate values than those from pre-sawn ice. In order to do so, the unit system including strut and sensors should be designed to withstand the level ice loads.

2. In order to distinguish inseparable hydrodynamic loads and ice milling loads, air milling tests (with the propeller rotating above the ice, i.e. in the air, and milling the ice at the same depth of cut as those of underwater milling) were carried out. The air milling test results, however, were not useful because the extensive vibration seemed to disturb the sensors when the blade contacted with the ice in air.

3. Furthermore, unsteady propeller ice interaction tests need to be designed and tested based on the present experimental set up. Propeller interaction with moving ice pieces with given size, mass, and shape would be necessary in order to simulate "real" propeller ice interaction phenomena.

4. The shaft dynamic effects need to be studied. From the present experiments, the ratio between blade torque and shaft torque is 1.7. It needs to be identified more precisely by using shaft dynamic analysis or dynamic calibration. It is noted that the static calibration had been carried out and applied to the sensors prior to the tests.

6.2.2. Numerical prediction of propeller ice interaction loads

1. For more accurate hydrodynamic load prediction, the present panel method needs to be improved. In addition, the hub and cone should be modeled.

2. If the ice block is modeled, the blockage effect can be more precisely predicted because the blockage effect is varied depending on the gap between the ice and propeller.

3. Consideration of cavitation would be important since cavitation in blocked flow can occur even at atmospheric pressure.

4. In order to avoid using empirical factors or weight factors, the mechanics of damage and fracture of ice needs to be studied and implemented especially at high strain rate.

163

References

ABB homepage, Retrieved August 15, 2006, from http://www.abb.com/.

Akinturk, A., Jones, S., Moores, C., and Bell, J. (2003). Measuring ice loading on podded propellers system. *Proceedings of the 22nd International Conference on Offshore Mechanics and Arctic Engineering*, Cancun, Mexico.

Akinturk A., Jones, S., Duffy, D., and Rowell, B. (2004a). Ice Loads on azimuthing podded propulsors. *Proceedings of the 23rd International Conference on Offshore Mechanics and Arctic Engineering, (OMAE'04)*, New York (CD-ROM, no page numbers).

Akinturk, A., Jones, S., Duffy, D., and Rowell, B. (2004b). Measuring Podded Propulsor Performance in Ice. *Proceedings of the 1st International Conference on Technological Advances in Podded Propulsion*, School of Marine Science and Technology, University of Newcastle Upon Tyne, UK, pp. 187-198.

Atlar, M., Prasetyawan, I., Aryawan W. D., and Wang, D. (2003). Cavitation in Ice-Milling with a Podded Propulsor. *Proc. ASME FEDSM'03 4th ASME_JSME Joint Fluids Engineering Conference*, Honolulu, Hawaii, USA.

Belyashov, V. and Shpakov, V. (1983). On Mechanics of Ice Crushing by Propeller Blade. *Ice Mechanics and Physics*, Nauka, Academy of Sciences of the USSR, Moscow. (Translation by the ECTC, No.T-830-03, New York).

Bose, N. (1996). Ice Blocked Propeller Performance Prediction Using a Panel Method. *Transaction of the Royal Institution of Naval Architects*, Vol. 138.

Bose, N., Veitch, B., and Doucet, J. (1998). A Design Approach for Ice Class Propellers. *Transactions of the Society of Naval Architects and Marine Engineers*, Vol. 106, pp.185-211.

Browne, R. P. (1997). Analysis of Canadian Full Scale Propeller and Ice Interaction Trials Data for Correlation with Empirical Models. *Report No. CR-1997-12*, Institute for Ocean Technology, National Research Council of Canada.

Browne, R. P., Revill, C. R., Ritch, A. R., and Keinonen, A. J. (1998). Propeller Design Load Model. *Report No. TP 13243E*, Institute for Ocean Technology, National Research Council of Canada.

Cammaert, A. B. and Muggeridge, D. B. (1988). *Ice Interaction with Offshore Structures*, New York: Van Nostrand Reinhold.

Castillo, E. (1988). Extreme Value Theory in Engineering, Academic Press Inc., Harcourt Brace Jovanovich Publishers, Boston, 389 pages

Chernuka, M., Jategaonkar, R., Norwood, M., and Warner, J. (1989). Development of a Procedure for Predicting Propeller-Ice Interaction Forces. Transport Canada Publication TP 9850E.

Cowper, B. (1992). Review of Full-Scale Trial Propulsion System R&D., Volume I and Volume II (Appendices). *Transportation Development Centre Report, TP 11260E*.

Cowper, B., Browne, R., Glen, I, and Ritch, R. (1992). Resistance and Propulsive Performance Trials of the MV Terry Fox and MV Ikaluk in Level Ice. *Transactions of the Society of Naval Architects and Marine Engineers*, Vol. 100, pp.315-343.

Doucet, J. (1996). Cavitation Erosion Experiments in Blocked Flow with Two Ice-Class Propeller Models. Master of Engineering Thesis, Memorial University of Newfoundland, St. John's, Newfoundland.

Doucet, J., Liu, P., Bose, N. and Veitch, B. (1998). Numerical Prediction of Ice-Induced Loads on Ice-Class Screw Propellers using a Synthesized

Contact/Hydrodynamic Code. *Report No. OERC-1998-004*, Ocean Engineering Research Centre, Memorial University of Newfoundland, Canada.

Doucet, J. M., Bose, N., and Veitch, B. (1999). Selection of Scantlings for an Ice Class Propeller: A Case Study for the *MV IKALUK*. *Proc. 18th International Conference on Offshore Mechanics and Arctic Engineering, (OMAE'99)*, St.John's, Newfoundland, Canada.

Dutta, P., Cole, D., Schulson, E., and Sodhi, D. (2004). A Fracture Study of Ice under High Strain Rate Loading. *Journal of Offshore and Polar Engineering*, **14**(3), pp.182-188.

Emerson, A. and Sinclair, L. (1978). Propeller Design and Model Experiments. *Trans. North East Coast Institution of Engineers and Shipbuilders*, **94**, pp. 199-234 and D31-34.

Gagnon, R. and Molgaard, J. (1991). Crushing Friction Experiments on Freshwater Ice. *Proc. IUTAM-IAHR Symposium*, S. Jones et al., ed., Springer, Berlin, pp.405-421.

IACS (International Association of Classification Societies) (2006). I3 Machinery Requirement for Polar Class Ships. http://www.iacs.org.uk/ureqs/URI.PDF.

Ignatjev, M. (1964). Determination of Ice Loads Encountered by Ship Propeller Blades. (trans.), *Problems of the Arctic and Antarctic*, No. 15, pp.41-51.

Ignatjev, M. (1966). Screw Propellers for Ships Navigating in Ice. (trans.), *Sudostroenie.*

ITTC (2002). The Propulsion Committee: Final Report and Recommendations to the 23rd ITTC. *23rd Intl. Towing Tank Conf.*, **1**, pp. 89-151, 671-683.

Jagodkin, V. (1963). Analytical Determination of the Resistance Moment of a Propeller during Its Interaction with Ice. (Trans.) *Problems of the Arctic and Antarctic*, Vol. 12, pp.78-88.

Jones, S. J. (1982). The Confined Compressive Strength of Polycrystalline Ice. *Journal of Glaciol.*, Vol. 28, No. 98, pp.171-177.

Jones, S. (1987). Ice Tank Test Procedure at the Institute for Marine Dynamics. *Report No. LM-AVR-20*, Institute for Ocean Technology, National Research Council of Canada.

Jones, S.J, (1997). High Strain-Rate Compression Tests on Ice. *Journal of Physical Chemistry B*, **101**(32), pp. 6099-6101.

Jones, S., Soininen, H., Jussila, M., Koskinen, P., Newbury, S. and Browne, R. (1997). Propeller-Ice Interaction. *Transactions of the Society of Naval Architects and Marine Engineers*, Vol. 105, pp.399-425.

Jones, S. J. (2006). Comparison of the Strength of Iceberg and Other Freshwater Ice and the Effect of Temperature. *Report Number TR-2006-07*, Institute for Ocean Technology, National Research Council of Canada.

Jordaan, I., Maes, M., Brown, P., and Hermans, I. (1993). Probabilistic analysis of local ice pressures, *Journal of Offshore Mechanics and Arctic Engineering*, Vol. 115, No. 1, pp. 83-89.

Jordaan, I. (2004). Decisions under Uncertainty –Probabilistic Analysis for Engineering Decisions, Cambridge University Press, 672 pages.

Jussila, M. (1983). Ice Loads on the Propulsion System of an Ice Breaking Tug, *7th International Conference on Port and Ocean Engineering under Arctic Conditions (POAC'83)*, Vol. 2, Helsinki, Finland.

Jussila, M. and Koskinen P. (1989). Ice Loads on CP-Propeller and Propeller Shaft of Small Ferry and Their Statistical Distributions during Winter '87. *8th International Conference on Offshore Mechanics and Arctic Engineering (OMAE'89/ASME)*, Vol. 4, Netherlands, New York.

Jussila, M. and Soininen, H. (1991). Interaction between Ice and Propeller. *Research Reports 1281*, Technical Research of Finland, Espoo.

Juurmaa, K., Mattson, T. and Wilkman G. (2001). The Development of the New Double Acting Ships for Ice Operation. *16th International Conference on Port and Ocean Engineering under Arctic Conditions (POAC'01)*, Ottawa.

Kannari, P. (1988). Full Scale and Model Tests Performed with a Nozzle and Open Propeller Simultaneously. *Proceedings IAHR Symposium*, Sapporo, pp.772-781.

Keinonen, A., Browne, R. and Jacobsen, C. (1990). Ice propeller interaction forces. *Transportation Development Centre Report, TP 10401E*.

Koskinen, P., Jussila, M. and Soininen, H. (1996). Propeller Ice Load Models. *Research Reports 1739*, Technical Research of Finland, Espoo.

Kotras, T., Humphreys, D., Baird, A., Morris, G. and Morley, G. (1985). Determination of Propeller-Ice Milling Loads. *Proceedings of the Fourth International Offshore Mechanics and Arctic Engineering Symposium*, Vol. 2, pp.336-343, Dallas.

Kron, P. and Holmstrom, L. (1999). Hydrodynamic Aspects of Mermaid Propulsion System. *21st Century Cruise Ship, London/IMARE conferences and symposia*, Vol. 111, No.3.

Laskow, V. and Revill, C. (1986). Engineering Analysis of Ice/Propeller Interaction Data. *Transportation Development Centre Report, TP 8450E*.

Laukia, K. (1996). The Azipod System – Operational Experience and Designs for the Future. *Redundancy vs. Reliability the motor ship 18th annual marine propulsion conference*, Hamburg.

Lewis, J., DeBord, F. and Bulat, V. (1982). Resistance and Propulsion of Ice-Worthy Ships. *Transactions of the Society of Naval Architects and Marine Engineers*, Vol. 90, pp.249-276.

Liu, P. (1996). A Time-Domain Panel Method for Oscillating Propulsors with Both Chordwise and Spanwise Flexibility. Ph. D. Thesis, Memorial University of Newfoundland, St. John's, Newfoundland.

Liu, P., Doucet, M., Veitch, B., Robbins, I. and Bose, N. (2000). Numerical Prediction of Ice Induced Hydrodynamic Loads on Propellers due to Blockage. *Oceanic Engineering International*, Vol. 4, No.1, pp. 31-38.

Luznik, L., Walker, D., Bose, N., and Jones, S.J. (1995). Effects of Ice Blockage Size and Proximity on Propeller Performance During Non-Contact Propeller Ice Interaction. *Proc. 14th International Conference on Offshore Mechanics and Arctic Engineering, (OMAE'95)*, Copenhagen, **4**, pp. 35-39.

Meglis, I., Melanson, P., and Jordaan, I. (1998). High Speed Testing of Freshwater Granular Ice. *Report No. CR-1998-02*, Institute for Ocean Technology, National Research Council of Canada.

Mintchev, D., Bose, N., Veitch, B., Atlar, M. and Paterson, I. (2001). Some Analysis of Propeller Ice Milling Experiments. *Canadian Marine Hydromechanics and Structures Conference '01*.

Mewis, F. (2001). The Efficiency of Pod Propulsion. *Proceedings of the 22nd International Conference on Hydrodynamics and Aerodynamics in Marine Engineering*, Bulgaria.

Moores, C. (2001). Shaft and Blade Load Measurements on a Highly Skewed Propeller Model in Ice. Master of Engineering Thesis, Memorial University of Newfoundland, St. John's, Newfoundland.

Moores, C., Veitch, B., Bose, N., Jones, S. J., and Bugden, A. (2001a). Effects of Strain Rate and Temperature on the Uniaxial Compressive Strength of Model Ice. *Proc. Port and Ocean Engineering under Arctic Conditions '01.*

Moores, C., Veitch, B., Bose, N., Jones, S. J., Bell, J., and Carlton, J. (2001b). Preliminary Blade Load Measurements on a Model Propeller in Ice. *Proc. International Conference on Offshore Mechanics and Arctic Engineering '01*, Paper No. OMAE-01-6102.

Moores, C., Veitch, B., Bose, N., Jones, S. J., and Carlton, J. (2002). Multi-Component Blade Load Measurements on a Propeller in Ice. *Trans. Society of Naval Architects and Marine Engineers*, **110**, pp. 169-188.

Morino, L., Chen, L. and Suciu, E. (1975). Steady and Oscillatory Subsonic and Supersonic Aerodynamics around Complex Configurations. *AIAA Journal Vol.13 No.3, pp368-374.*

Muller, J. (1999). Podded Drives and Conventional Cargo Tonnage. *21st marine propulsion conference*, Athens.

Newbury, S., Shih, L., Browne, R., Revill, C., Kenny, S. and Zheng, Y. (1993). Experimental and Theoretical evaluation of Hydrodynamic Pressure during Non-Contact Propeller/Ice Interaction. *Proceedings of the 2nd Canadian Marine Dynamics Conference*, Vancouver.

Newbury, S., Browne, R. and Jones, S. (1994). Experimental Determination of Hydrodynamic Non-Contact loads during Propeller-Ice Interaction. *Proceedings of ISOPE 94*, Osaka, Vol. 2, pp 596-601.

Niini, M. (1995). New Propulsion Technology for Arctic Tankers. *Shipbuilding Technology International.*

Niini, M. (1997). Azipod Propulsion Breakthrough for Large Cruise. *Cruise & Ferry*, London.

Pustoshny, A. V. and Kaprantsev, S.V. (2001) AZIPOD Propeller Blade Cavitation Observations during Ship Maneuvering. *CAV 2001: Fourth International Symposium on Cavitation*, Pasadena, USA.

Robbins, I., Doucet, J., Liu, P. and Bose, N. (1998). Numerical Prediction of Ice-Induced Loads on Ice-Class Screw Propellers. *Report No. OERC-1998-003*, Ocean Engineering Research Centre, Memorial University of Newfoundland, Canada.

Sasaki, N., Laapio, J., Fagerstrom, B., Juurmaa, K. and Wilkman, G. (2004). Full Scale Performance of Double Acting Tankers TEMPERA & MASTERA. *Proceedings of the 1st International Conference on Technological Advances in Podded Propulsion*, Newcastle, UK.

Searle, S. (1999). Ice Tank Test of a High Skewed Propeller and a Conventional Ice-Class Propeller in Four Quadrants. Master of Engineering Thesis, Memorial University of Newfoundland, St. John's, Newfoundland.

Searle, S., Veitch, B., and Bose, N., (1999). Ice-Class Propeller Performance in Extreme Conditions. *Trans. Society of Naval Architects and Marine Engineers*, **107**, pp. 127-152.

Searle, S., Veitch, B., and Bose, N. (2001). Experimental Investigation of a Highly Skewed Propeller in Ice. *Journal of Offshore Mechanics and Arctic Engineering, American Society of Mechanical Engineers*, Vol.123, p.191-197.

Shih, L. and Zheng, Y. (1992). Constricted Hydrodynamic Flow due to Proximate Ice Blockage over a Blade Profile in Two Dimensions. *Proceedings of the 2nd International Symposium on Propellers and Cavitation*, China.

Shih, L. and Zheng, Y. (1993). Application of 3-D BEM to Time Dependent Potential Flow around a Propeller Blade Profile during Ice Contact. *Proceedings International Shipbuilding Conference*, Russia.

Sodhi, D. (1998). Nonsimultaneous Crushing during Edge Indentation of Freshwater Ice Sheets. *Cold Regions Science and Technology*, **27**, pp. 179-195.

Sodhi, D., Takeuchi, T., Nakazawa, N., Akagawa, S., and Saeki, H. (1998) Medium-Scale Indentation Tests on Sea Ice at Various Speeds. *Cold Regions Science and Technology*, **28**, pp. 161-182.

Sodhi, D. (2001). Crushing Failure during Ice-Structure Interaction. *Journal of Engineering Fracture Mechanics*, **68**, pp. 1889-1921.

Sodhi, D. and Haehnel, R. (2003). Crushing Ice Forces on Structures. *Journal of Cold Regions Engineering*, **17**(4), pp. 153-170.

Soininen, H. (1998). A Propeller-Ice Contact Model. Dissertation for the degree of Doctor of Technology, Helsinki University of Technology, Espoo, 116p.

Spencer, D.S., and Timco, G.W. (1990). CD Model Ice: a Process to Produce Correct Density (CD) Model Ice. *Proc. 10th IAHR Symposium on Ice*, Espoo, Finland, **2**, pp. 745-755.

Tamura, K., Kato, H. and Yamaguchi, H. (1997). Experimental Approach to the Interaction between Nozzle-Propeller and Ice Block. *Proceedings of 16th International Conference on Offshore Mechanics and Arctic Engineering / 14th International Conference on Port and Ocean Engineering under Arctic Conditions (Joint OMAE/POAC Conference)*, Yokohama, Vol. IV, pp. 109-118.

Timco, G. (1986). EG/AD/S: A New Type of Model Ice for Refrigerated Towing Tanks. *Cold Science and Technology*, Vol. 12, pp. 175-195.

Tuhkuri, J. (1995). Experimental Observations of the Brittle Failure Process of Ice and Ice-Structure Contact. *Cold Regions Science and Technology*, **23**, pp. 265-278.

Van der Vorst, H. (1992). Bi-CGSTAB: A Fast and Smoothly Converging Variant of BI-CG for the Solution of Nonsymmetric Linear Systems. *SIAM J. Sci. Stat. Comput.*, **13**, pp. 631-644.

Van Terwisga, T., Quadvlieg, F. and Valkhof, H. (2001). Steerable Propulsion Units: Hydrodynamic issues and Design Consequences. *Occasion of the 80th anniversary of Schottel GmbH & Co.*

Varma, G. (2000). Ice Loads on Propellers under Extreme Operating Conditions. Master of Engineering Thesis, Memorial University of Newfoundland, St. John's, Newfoundland.

Veitch, B. (1992). Propeller-ice Interaction. *Licentiate of Technology Thesis*, Helsinki University of Technology, Espoo.

Veitch, B. (1995). Predictions of Ice Contact Forces on a Marine Screw Propeller during the Propeller-Ice Cutting Process. Acta Polytechnica Scandinavica, *Mechanical Engineering Series* No. 118, Helsinki.

Veitch, B., Bose, N., Meade, C., and Liu, P. (1997). Prediction of Hydrodynamic and Ice Contact Loads on Ice Class Screw Propellers. *Proceedings of the 16th International Conference on Offshore Mechanics and Arctic Engineering*, American Society of Mechanical Engineers, Vol. 4, pp. 119-125.

Walker, D., Bose, N., and Yamaguchi, H. (1994a). Hydrodynamic Performance and Cavitation of an Open Propeller in a Simulated Ice Blocked Flow. *Journal of OMAE*, Vol. 116.

Walker, D. and Bose, N. (1994b). Hydrodynamic Loads and Dynamic Effects of Cavitation on Ice Class Propellers in Simulated Ice Blocked Flow. *Proceedings of Propller/Shafting' 94*, Virginia beach, Virginia, No. 20, 19p.

Walker, D., Bose, N. and Casey S. (1994c). Ducted Propeller Cavitation in Blocked Flow. *2nd International Symposium on Cavitation*, Tokyo.

Walker, D. (1996). The Influence of Blockage and Cavitation on the Hydrodynamic Performance of Ice Class Propellers in Blocked Flow. Ph.D. Thesis, Memorial University of Newfoundland, St. John's, Newfoundland.

Wang, J., Akinturk, A., Foster, W., Jones, S. J., and Bose, N. (2004). An Experimental Model for Ice Performance of Podded Propellers. *Proc. of the 27th American Towing Tank Conference*, Institute for Ocean Technology, National Research Council of Canada. (CD-ROM, no page numbers).

Wang, J., Akinturk, A., Jones, S.J., and Bose, N. (2005). Ice Loads on a Model Podded Propeller Blade in Milling Conditions. *Proc. 24th International Conference on Offshore Mechanics and Arctic Engineering, (OMAE'05)*, Halkidiki, Greece, (CD-ROM, no page numbers).

Wang, J., Akinturk, A., Jones, S., Bose, N., Kim, M.C., and Chun, H.H. (2006). Ice Loads Acting on a Model Podded Propeller Blade. To be published in *ASME J. Offshore Mechanics and Arctic Engineering*.

Williams, F., Spencer, D., Mathews, S. and Bayly, I. (1992). Full Scale trials in Level Ice with Canadian R-Class Icebreaker. *Transactions of the Society of Naval Architects and Marine Engineers*, Vol. 100, pp. 293-313.

Wind, J. (1983). The Dimensioning of High Power Propeller System for Arctic Icebreaking Vessels. *Proceeding of the 5th Lips Propeller Symposium*, Drunen.

Yamaguchi, H. (1993). Investigation on Propeller Performance in Uniform and Blocked Flow for the Open Propellers used in IMD Ice Tank and Cavitation Tunnel Experiments: Investigation from Lifting Surface Calculation. *Report No. LM-1993-11*, Institute for Ocean Technology, National Research Council of Canada.

Appendix A   Example of Input Data for DANRA code

RUN number: 392 ~ 406: various azimuthing angles (180 ~ 60 degrees), tractor mode, presawn ice, depth of cut of 35 mm

RUN number: 410 ~ 424: various azimuthing angles (180 ~ 60 degrees), tractor mode, pack ice condition, depth of cut of 35 mm

RUN number: 435 ~ 445: various azimuthing angles (180 ~ 150 degrees), tractor mode, presawn ice, depth of cut of 15 mm, repeated in three times

Run Number				Tare for Blade Dynamometer (Bollard Condition)								
				F_X		F_Y		F_Z		M_X		M_Y
&R392	t0 =	392	,t1=	25.1	,t2=	48.9	,t3=	-12	,t4=	3.01	,t5=	-1.8
&R393	t0 =	393	,t1=	42.3	,t2=	67.4	,t3=	-99	,t4=	5	,t5=	-2.4
&R394	t0 =	394	,t1=	78.3	,t2=	106	,t3=	-278	,t4=	9.4	,t5=	-3.7
&R395	t0 =	395	,t1=	25.3	,t2=	50.3	,t3=	-8.4	,t4=	3.13	,t5=	-1.8
&R396	t0 =	396	,t1=	42.3	,t2=	68.8	,t3=	-101	,t4=	5.14	,t5=	-2.4
&R397	t0 =	397	,t1=	78.6	,t2=	108	,t3=	-279	,t4=	9.58	,t5=	-3.7
&R398	t0 =	398	,t1=	25.5	,t2=	51.5	,t3=	-9.9	,t4=	3.21	,t5=	-1.9
&R399	t0 =	399	,t1=	42.5	,t2=	69.6	,t3=	-95	,t4=	5.25	,t5=	-2.5
&R400	t0 =	400	,t1=	68.3	,t2=	72.2	,t3=	-272	,t4=	5.28	,t5=	-2.8
&R401	t0 =	401	,t1=	24.7	,t2=	50.4	,t3=	-9.6	,t4=	3.07	,t5=	-1.8
&R402	t0 =	402	,t1=	41.5	,t2=	68.6	,t3=	-91	,t4=	5.14	,t5=	-2.4
&R403	t0 =	403	,t1=	70.9	,t2=	77.9	,t3=	-271	,t4=	5.83	,t5=	-3
&R404	t0 =	404	,t1=	24.8	,t2=	50.2	,t3=	-8.2	,t4=	3.02	,t5=	-1.8
&R405	t0 =	405	,t1=	41.2	,t2=	68.5	,t3=	-96	,t4=	5.1	,t5=	-2.4
&R406	t0 =	406	,t1=	77.3	,t2=	98.2	,t3=	-273	,t4=	8.18	,t5=	-3.6
&R410	t0 =	410	,t1=	24.9	,t2=	50.4	,t3=	-8.7	,t4=	3.06	,t5=	-1.8
&R411	t0 =	411	,t1=	40.3	,t2=	60.7	,t3=	-97	,t4=	3.98	,t5=	-2.3
&R412	t0 =	412	,t1=	77.6	,t2=	107	,t3=	-277	,t4=	9.39	,t5=	-3.7
&R413	t0 =	413	,t1=	24.8	,t2=	51.6	,t3=	-14	,t4=	3.15	,t5=	-1.8
&R414	t0 =	414	,t1=	41.2	,t2=	64.1	,t3=	-97	,t4=	4.42	,t5=	-2.4
&R415	t0 =	415	,t1=	76	,t2=	92.1	,t3=	-273	,t4=	7.35	,t5=	-3.5
&R416	t0 =	416	,t1=	25	,t2=	51.6	,t3=	-13	,t4=	3.14	,t5=	-1.8
&R418	t0 =	418	,t1=	42	,t2=	69.1	,t3=	-99	,t4=	5.09	,t5=	-2.4
&R419	t0 =	419	,t1=	72.1	,t2=	81.7	,t3=	-273	,t4=	6.2	,t5=	-3.1
&R420	t0 =	420	,t1=	24.4	,t2=	49.8	,t3=	-5.4	,t4=	2.96	,t5=	-1.8
&R421	t0 =	421	,t1=	41.1	,t2=	68.5	,t3=	-99	,t4=	5.03	,t5=	-2.4
&R422	t0 =	422	,t1=	68.7	,t2=	74.6	,t3=	-272	,t4=	5.44	,t5=	-2.8
&R423	t0 =	423	,t1=	24.3	,t2=	51.2	,t3=	-14	,t4=	3.1	,t5=	-1.8
&R424	t0 =	424	,t1=	40.7	,t2=	65.1	,t3=	-98	,t4=	4.61	,t5=	-2.4
&R435	t0 =	435	,t1=	25.6	,t2=	50.2	,t3=	-0.6	,t4=	3.1	,t5=	-1.8
&R436	t0 =	436	,t1=	42.6	,t2=	68.1	,t3=	-88	,t4=	5.08	,t5=	-2.4
&R437	t0 =	437	,t1=	26	,t2=	50.8	,t3=	-3.2	,t4=	3.15	,t5=	-1.8
&R438	t0 =	438	,t1=	42.8	,t2=	68.1	,t3=	-89	,t4=	5.06	,t5=	-2.4
&R439	t0 =	439	,t1=	25.9	,t2=	50.7	,t3=	-4	,t4=	3.12	,t5=	-1.8
&R440	t0 =	440	,t1=	42.7	,t2=	68.8	,t3=	-89	,t4=	5.15	,t5=	-2.4
&R441	t0 =	441	,t1=	25.6	,t2=	50.4	,t3=	-5.6	,t4=	3.07	,t5=	-1.8
&R442	t0 =	442	,t1=	42.1	,t2=	64.4	,t3=	-92	,t4=	4.5	,t5=	-2.4
&R443	t0 =	443	,t1=	25.3	,t2=	51	,t3=	-10	,t4=	3.11	,t5=	-1.8
&R444	t0 =	444	,t1=	43	,t2=	68.7	,t3=	-92	,t4=	5.12	,t5=	-2.4
&R445	t0 =	445	,t1=	26.3	,t2=	50.6	,t3=	-4.5	,t4=	3.1	,t5=	-1.8

		M_Z	Total Time	sec	Tare for Shaft Thrust and Shaft torque (Bollard)	T		Q	RPS	rps	α_m start	angle
&R392	,t6=	1.12	,t7=	103	,t8=	500	,t9=	-2.2	,t10=	5	,t11=	216
&R393	,t6=	1.58	,t7=	79	,t8=	433	,t9=	-4.6	,t10=	7	,t11=	216
&R394	,t6=	2.54	,t7=	103	,t8=	281	,t9=	-9.7	,t10=	10	,t11=	216
&R395	,t6=	1.1	,t7=	71	,t8=	492	,t9=	-2.3	,t10=	5	,t11=	216
&R396	,t6=	1.6	,t7=	111	,t8=	425	,t9=	-4.7	,t10=	7	,t11=	216
&R397	,t6=	2.66	,t7=	79	,t8=	271	,t9=	-9.9	,t10=	10	,t11=	216
&R398	,t6=	1.18	,t7=	77	,t8=	488	,t9=	-2.4	,t10=	5	,t11=	216
&R399	,t6=	1.66	,t7=	103	,t8=	420	,t9=	-4.8	,t10=	7	,t11=	216
&R400	,t6=	2.17	,t7=	93	,t8=	399	,t9=	-6.8	,t10=	10	,t11=	216
&R401	,t6=	1.09	,t7=	82	,t8=	492	,t9=	-2.3	,t10=	5	,t11=	216
&R402	,t6=	1.65	,t7=	91	,t8=	427	,t9=	-4.6	,t10=	7	,t11=	216
&R403	,t6=	2.42	,t7=	88	,t8=	381	,t9=	-7.5	,t10=	10	,t11=	216
&R404	,t6=	1.12	,t7=	84	,t8=	492	,t9=	-2.2	,t10=	5	,t11=	216
&R405	,t6=	1.65	,t7=	81	,t8=	426	,t9=	-4.6	,t10=	7	,t11=	216
&R406	,t6=	2.82	,t7=	87	,t8=	310	,t9=	-9.4	,t10=	10	,t11=	216
&R410	,t6=	1.13	,t7=	64	,t8=	496	,t9=	-2.2	,t10=	5	,t11=	216
&R411	,t6=	1.63	,t7=	76	,t8=	462	,t9=	-4	,t10=	7	,t11=	216
&R412	,t6=	2.7	,t7=	74	,t8=	279	,t9=	-9.6	,t10=	10	,t11=	216
&R413	,t6=	1.16	,t7=	72	,t8=	489	,t9=	-2.3	,t10=	5	,t11=	216
&R414	,t6=	1.68	,t7=	73	,t8=	440	,t9=	-4.5	,t10=	7	,t11=	216
&R415	,t6=	2.73	,t7=	73	,t8=	320	,t9=	-9.5	,t10=	10	,t11=	216
&R416	,t6=	1.17	,t7=	69	,t8=	490	,t9=	-2.3	,t10=	5	,t11=	216
&R418	,t6=	1.67	,t7=	89	,t8=	427	,t9=	-4.6	,t10=	7	,t11=	216
&R419	,t6=	2.5	,t7=	71	,t8=	366	,t9=	-8	,t10=	10	,t11=	216
&R420	,t6=	1.19	,t7=	67	,t8=	495	,t9=	-2.2	,t10=	5	,t11=	216
&R421	,t6=	1.65	,t7=	69	,t8=	427	,t9=	-4.6	,t10=	7	,t11=	216
&R422	,t6=	2.3	,t7=	79	,t8=	400	,t9=	-6.6	,t10=	10	,t11=	216
&R423	,t6=	1.17	,t7=	72	,t8=	491	,t9=	-2.2	,t10=	5	,t11=	216
&R424	,t6=	1.69	,t7=	73	,t8=	438	,t9=	-4.4	,t10=	7	,t11=	216
&R435	,t6=	0.98	,t7=	66	,t8=	507	,t9=	-2.3	,t10=	5	,t11=	196
&R436	,t6=	1.5	,t7=	65	,t8=	441	,t9=	-4.6	,t10=	7	,t11=	196
&R437	,t6=	0.97	,t7=	69	,t8=	503	,t9=	-2.3	,t10=	5	,t11=	196
&R438	,t6=	1.51	,t7=	72	,t8=	440	,t9=	-4.6	,t10=	7	,t11=	196
&R439	,t6=	1	,t7=	62	,t8=	503	,t9=	-2.3	,t10=	5	,t11=	196
&R440	,t6=	1.53	,t7=	87	,t8=	437	,t9=	-4.7	,t10=	7	,t11=	196
&R441	,t6=	1.02	,t7=	68	,t8=	506	,t9=	-2.2	,t10=	5	,t11=	196
&R442	,t6=	1.55	,t7=	76	,t8=	456	,t9=	-4.3	,t10=	7	,t11=	196
&R443	,t6=	1.07	,t7=	81	,t8=	504	,t9=	-2.3	,t10=	5	,t11=	196
&R444	,t6=	1.58	,t7=	75	,t8=	438	,t9=	-4.6	,t10=	7	,t11=	196
&R445	,t6=	1	,t7=	69	,t8=	504	,t9=	-2.3	,t10=	5	,t11=	196

	α_m end		Azimuthing angle		Data Range (data point)				Carriage speed	
				degree	start data		finish data		(1st data set)	
&R392	,t12=	111	,t13=	180	,t14=	548	,t15=	840	,t16=	0.5
&R393	,t12=	111	,t13=	179	,t14=	254	,t15=	461	,t16=	0.2
&R394	,t12=	111	,t13=	179	,t14=	4	,t15=	150	,t16=	0.2
&R395	,t12=	111	,t13=	150	,t14=	640	,t15=	933	,t16=	0.5
&R396	,t12=	111	,t13=	150	,t14=	108	,t15=	317	,t16=	0.2
&R397	,t12=	111	,t13=	150	,t14=	257	,t15=	403	,t16=	0.2
&R398	,t12=	111	,t13=	120	,t14=	330	,t15=	622	,t16=	0.2
&R399	,t12=	111	,t13=	120	,t14=	583	,t15=	792	,t16=	0.2
&R400	,t12=	111	,t13=	120	,t14=	466	,t15=	761	,t16=	0.2
&R401	,t12=	111	,t13=	90	,t14=	487	,t15=	779	,t16=	0.2
&R402	,t12=	111	,t13=	89.4	,t14=	276	,t15=	485	,t16=	0.2
&R403	,t12=	111	,t13=	89.4	,t14=	326	,t15=	472	,t16=	0.2
&R404	,t12=	111	,t13=	60	,t14=	328	,t15=	621	,t16=	0.2
&R405	,t12=	111	,t13=	60.1	,t14=	573	,t15=	782	,t16=	0.2
&R406	,t12=	111	,t13=	60.6	,t14=	148	,t15=	294	,t16=	0.2
&R410	,t12=	111	,t13=	180	,t14=	679	,t15=	972	,t16=	0.5
&R411	,t12=	111	,t13=	180	,t14=	337	,t15=	546	,t16=	0.5
&R412	,t12=	111	,t13=	180	,t14=	30	,t15=	175	,t16=	0.5
&R413	,t12=	111	,t13=	150	,t14=	234	,t15=	527	,t16=	0.5
&R414	,t12=	111	,t13=	150	,t14=	450	,t15=	658	,t16=	0.2
&R415	,t12=	111	,t13=	150	,t14=	114	,t15=	260	,t16=	0.2
&R416	,t12=	111	,t13=	120	,t14=	84	,t15=	377	,t16=	0.2
&R418	,t12=	111	,t13=	120	,t14=	112	,t15=	320	,t16=	0.2
&R419	,t12=	111	,t13=	120	,t14=	484	,t15=	630	,t16=	0.2
&R420	,t12=	111	,t13=	90	,t14=	56	,t15=	348	,t16=	0.2
&R421	,t12=	111	,t13=	89.4	,t14=	700	,t15=	909	,t16=	0.2
&R422	,t12=	111	,t13=	89.4	,t14=	423	,t15=	569	,t16=	0.2
&R423	,t12=	111	,t13=	60	,t14=	559	,t15=	853	,t16=	0.2
&R424	,t12=	111	,t13=	60.4	,t14=	531	,t15=	740	,t16=	0.2
&R435	,t12=	127	,t13=	180	,t14=	637	,t15=	830	,t16=	0.5
&R436	,t12=	127	,t13=	180	,t14=	435	,t15=	572	,t16=	0.5
&R437	,t12=	127	,t13=	180	,t14=	236	,t15=	429	,t16=	0.5
&R438	,t12=	127	,t13=	180	,t14=	59	,t15=	195	,t16=	0.5
&R439	,t12=	127	,t13=	150	,t14=	519	,t15=	712	,t16=	0.5
&R440	,t12=	127	,t13=	151	,t14=	128	,t15=	264	,t16=	0.5
&R441	,t12=	127	,t13=	180	,t14=	275	,t15=	468	,t16=	0.5
&R442	,t12=	127	,t13=	180	,t14=	248	,t15=	385	,t16=	0.5
&R443	,t12=	127	,t13=	150	,t14=	109	,t15=	301	,t16=	0.5
&R444	,t12=	127	,t13=	150	,t14=	139	,t15=	276	,t16=	0.5
&R445	,t12=	127	,t13=	150	,t14=	937	,t15=	1129	,t16=	0.5

	1st data set (time)		Carriage speed	2nd data set (time)	
	start	end	(2nd data set)	start	end
&R392	,t17= 61	,t18= 67	,t19= 0.8	,t20= 69	,t21= 75
&R393	,t17= 36	,t18= 45	,t19= 0.5	,t20= 47	,t21= 54
&R394	,t17= 41	,t18= 51	,t19= 0.5	,t20= 55	,t21= 61
&R395	,t17= 28	,t18= 34	,t19= 0.8	,t20= 36	,t21= 42
&R396	,t17= 37	,t18= 43	,t19= 0.5	,t20= 45	,t21= 51
&R397	,t17= 32	,t18= 44	,t19= 0.5	,t20= 46	,t21= 53
&R398	,t17= 25	,t18= 37	,t19= 0.5	,t20= 39	,t21= 46
&R399	,t17= 34	,t18= 43	,t19= 0.5	,t20= 45	,t21= 52
&R400	,t17= 31	,t18= 42	,t19= 0.5	,t20= 45	,t21= 51
&R401	,t17= 25	,t18= 37	,t19= 0.5	,t20= 39	,t21= 46
&R402	,t17= 29	,t18= 40	,t19= 0.5	,t20= 42	,t21= 49
&R403	,t17= 28	,t18= 39	,t19= 0.5	,t20= 42	,t21= 48
&R404	,t17= 27	,t18= 38	,t19= 0.5	,t20= 41	,t21= 47
&R405	,t17= 29	,t18= 40	,t19= 0.5	,t20= 43	,t21= 49
&R406	,t17= 32	,t18= 42	,t19= 0.5	,t20= 45	,t21= 51
&R410	,t17= 25	,t18= 31	,t19= 0.8	,t20= 33	,t21= 39
&R411	,t17= 31	,t18= 36	,t19= 0.8	,t20= 39	,t21= 44
&R412	,t17= 29	,t18= 34	,t19= 0.2	,t20= 46	,t21= 50
&R413	,t17= 28	,t18= 33	,t19= 0.2	,t20= 45	,t21= 48
&R414	,t17= 36	,t18= 46	,t19= 0.5	,t20= 48	,t21= 54
&R415	,t17= 28	,t18= 39	,t19= 0.5	,t20= 42	,t21= 48
&R416	,t17= 28	,t18= 38	,t19= 0.5	,t20= 40	,t21= 47
&R418	,t17= 47	,t18= 56	,t19= 0.5	,t20= 59	,t21= 65
&R419	,t17= 30	,t18= 40	,t19= 0.5	,t20= 42	,t21= 49
&R420	,t17= 29	,t18= 41	,t19= 0.5	,t20= 43	,t21= 49
&R421	,t17= 32	,t18= 42	,t19= 0.5	,t20= 44	,t21= 50
&R422	,t17= 35	,t18= 45	,t19= 0.5	,t20= 48	,t21= 54
&R423	,t17= 28	,t18= 37	,t19= 0.5	,t20= 40	,t21= 45
&R424	,t17= 32	,t18= 41	,t19= 0.5	,t20= 44	,t21= 50
&R435	,t17= 26	,t18= 31	,t19= 0.8	,t20= 34	,t21= 39
&R436	,t17= 29	,t18= 34	,t19= 0.8	,t20= 37	,t21= 42
&R437	,t17= 32	,t18= 37	,t19= 0.8	,t20= 39	,t21= 44
&R438	,t17= 32	,t18= 36	,t19= 0.8	,t20= 40	,t21= 44
&R439	,t17= 27	,t18= 32	,t19= 0.8	,t20= 35	,t21= 40
&R440	,t17= 35	,t18= 40	,t19= 0.8	,t20= 30	,t21= 32
&R441	,t17= 33	,t18= 38	,t19= 0.8	,t20= 41	,t21= 46
&R442	,t17= 33	,t18= 38	,t19= 0.8	,t20= 41	,t21= 46
&R443	,t17= 37	,t18= 43	,t19= 0.8	,t20= 45	,t21= 50
&R444	,t17= 31	,t18= 37	,t19= 0.8	,t20= 39	,t21= 44
&R445	,t17= 34	,t18= 39	,t19= 0.8	,t20= 42	,t21= 47

	Carriage speed		3rd data set (time)			
	(3rd data set)		start		end	
&R392	,t22=	0.2	,t23=	79	,t24=	83	&end
&R393	,t22=	0	,t23=	0	,t24=	0	&end
&R394	,t22=	0	,t23=	0	,t24=	0	&end
&R395	,t22=	0.2	,t23=	45	,t24=	50	&end
&R396	,t22=	0	,t23=	0	,t24=	0	&end
&R397	,t22=	0	,t23=	0	,t24=	0	&end
&R398	,t22=	0	,t23=	0	,t24=	0	&end
&R399	,t22=	0	,t23=	0	,t24=	0	&end
&R400	,t22=	0	,t23=	0	,t24=	0	&end
&R401	,t22=	0	,t23=	0	,t24=	0	&end
&R402	,t22=	0	,t23=	0	,t24=	0	&end
&R403	,t22=	0	,t23=	0	,t24=	0	&end
&R404	,t22=	0	,t23=	0	,t24=	0	&end
&R405	,t22=	0	,t23=	0	,t24=	0	&end
&R406	,t22=	0	,t23=	0	,t24=	0	&end
&R410	,t22=	0.2	,t23=	43	,t24=	47	&end
&R411	,t22=	0.2	,t23=	48	,t24=	52	&end
&R412	,t22=	0	,t23=	0	,t24=	0	&end
&R413	,t22=	0	,t23=	0	,t24=	0	&end
&R414	,t22=	0	,t23=	0	,t24=	0	&end
&R415	,t22=	0	,t23=	0	,t24=	0	&end
&R416	,t22=	0	,t23=	0	,t24=	0	&end
&R418	,t22=	0	,t23=	0	,t24=	0	&end
&R419	,t22=	0	,t23=	0	,t24=	0	&end
&R420	,t22=	0	,t23=	0	,t24=	0	&end
&R421	,t22=	0	,t23=	0	,t24=	0	&end
&R422	,t22=	0	,t23=	0	,t24=	0	&end
&R423	,t22=	0	,t23=	0	,t24=	0	&end
&R424	,t22=	0	,t23=	0	,t24=	0	&end
&R435	,t22=	0.2	,t23=	43	,t24=	47	&end
&R436	,t22=	0.2	,t23=	46	,t24=	50	&end
&R437	,t22=	0.2	,t23=	49	,t24=	52	&end
&R438	,t22=	0.2	,t23=	49	,t24=	52	&end
&R439	,t22=	0.2	,t23=	44	,t24=	48	&end
&R440	,t22=	0.2	,t23=	43	,t24=	48	&end
&R441	,t22=	0.2	,t23=	50	,t24=	54	&end
&R442	,t22=	0.2	,t23=	50	,t24=	54	&end
&R443	,t22=	0.2	,t23=	55	,t24=	59	&end
&R444	,t22=	0.2	,t23=	49	,t24=	53	&end
&R445	,t22=	0.2	,t23=	51	,t24=	55	&end

Appendix B   Separable Hydrodynamic Loads (Experimental Results in Open Water)

Experimental results for the separable hydrodynamic loads are shown including unit thrust, transverse/vertical force on unit, shaft thrust/torque and blade thrust/torque with maximum, minimum, and average in tractor mode at the azimuthing angle of 180 degrees. The results are plotted with non-dimensional coefficients.
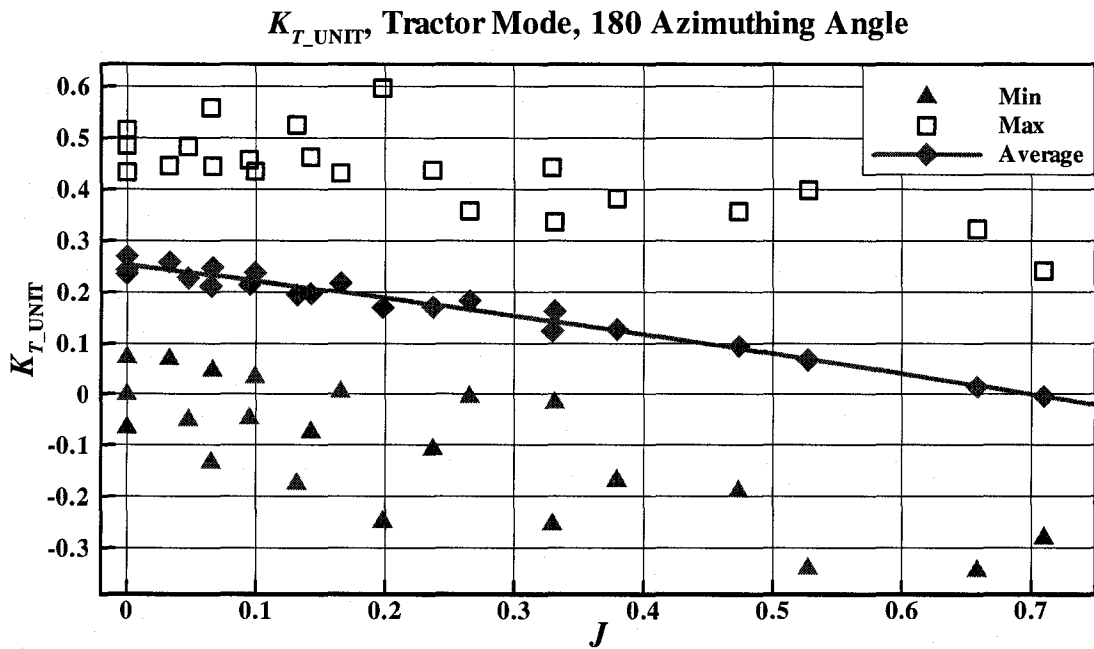
Figure B-1: K_{T_UNIT} vs. J at an azimuthing angle of 180 degrees in open water
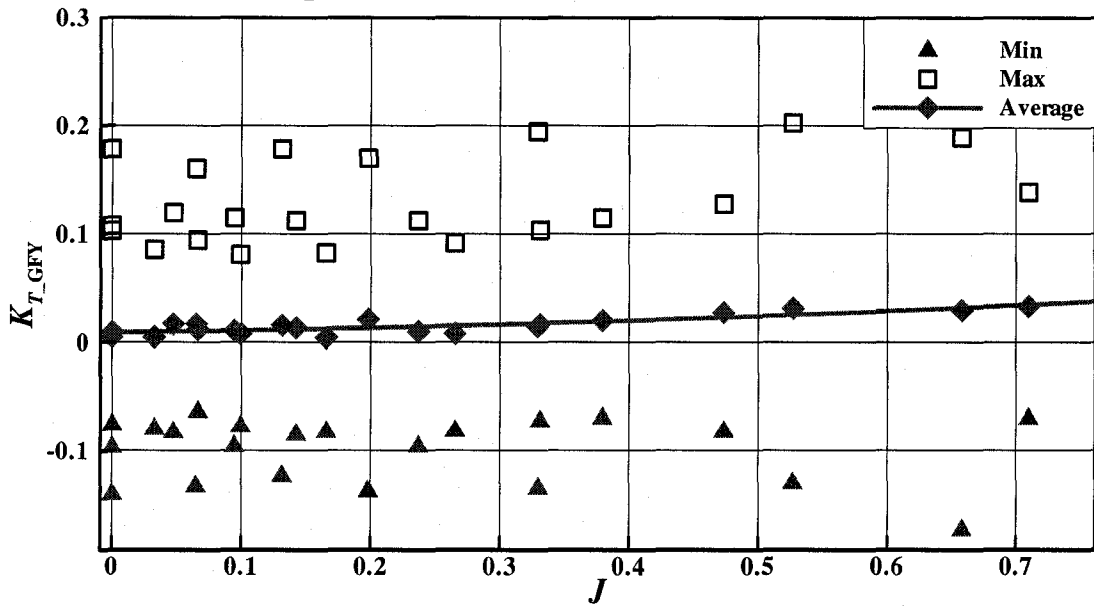
Figure B-2: K_{T_GFY} vs. J at an azimuthing angle of 180 degrees in open water
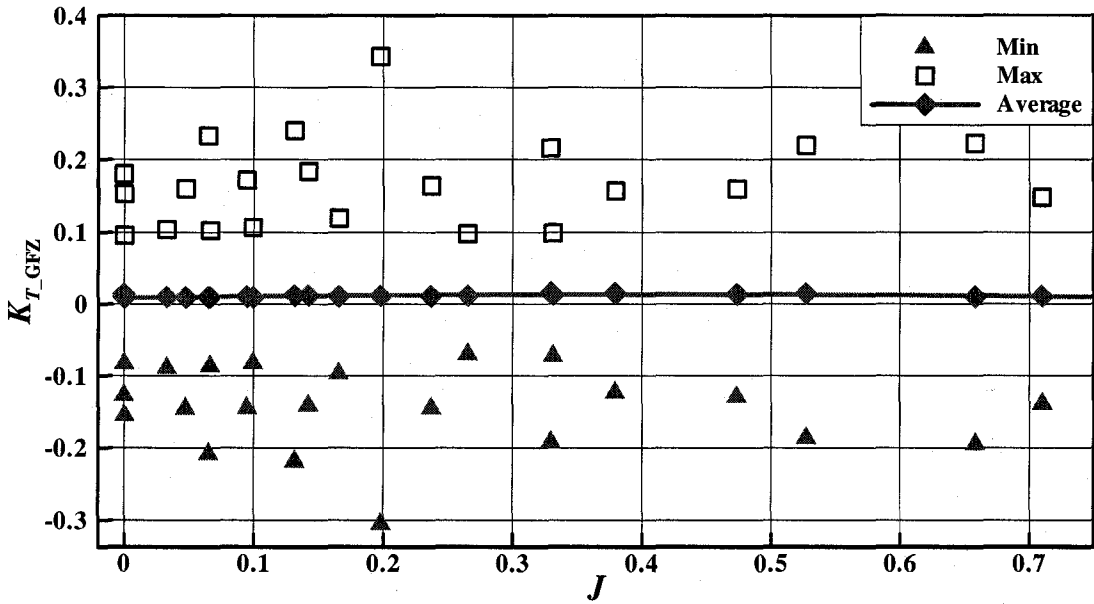
Figure B-3: K_{T_GFZ} vs. J at an azimuthing angle of 180 degrees in open water
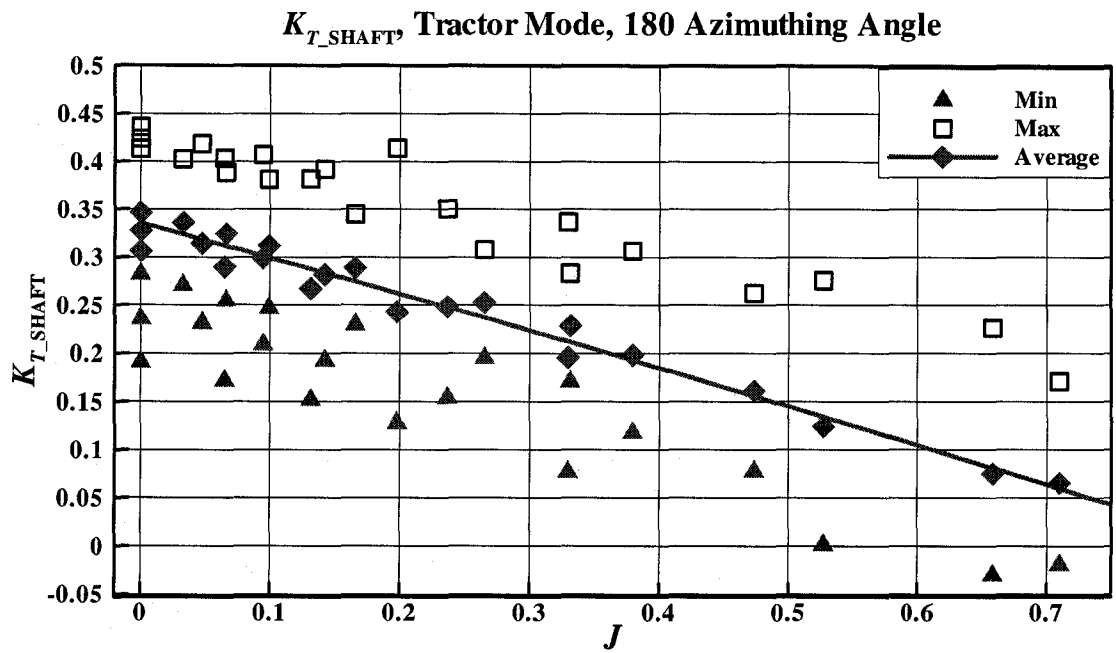
Figure B-4: K_{T_SHAFT} vs. J at an azimuthing angle of 180 degrees in open water
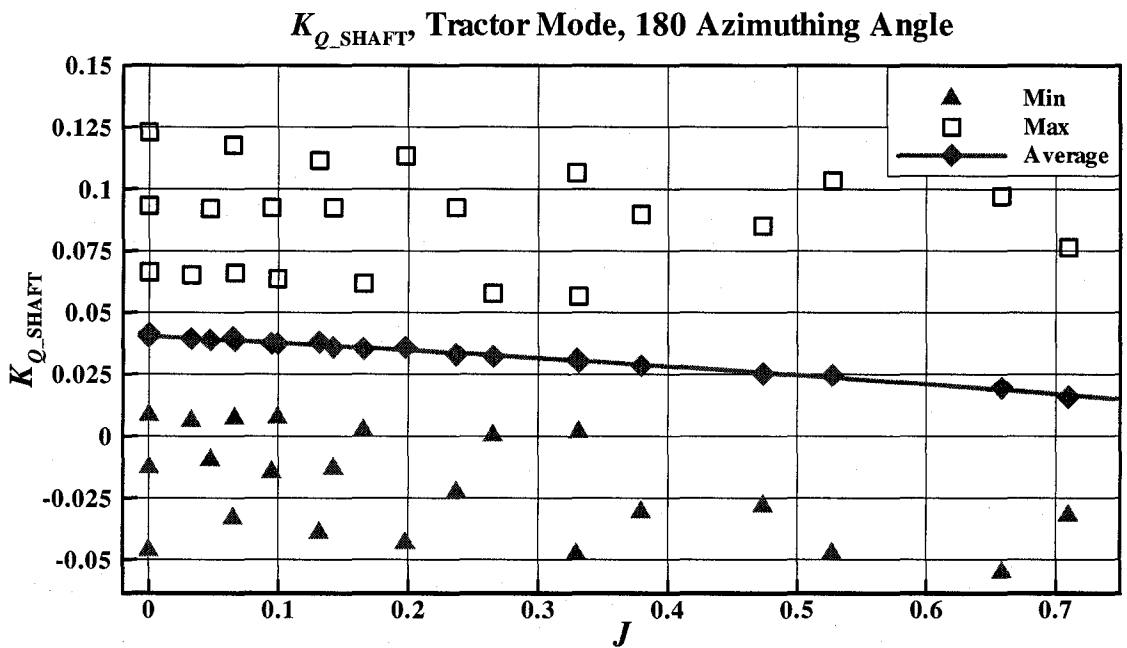
Figure B-5: K_{Q_SHAFT} vs. J at an azimuthing angle of 180 degrees in open water
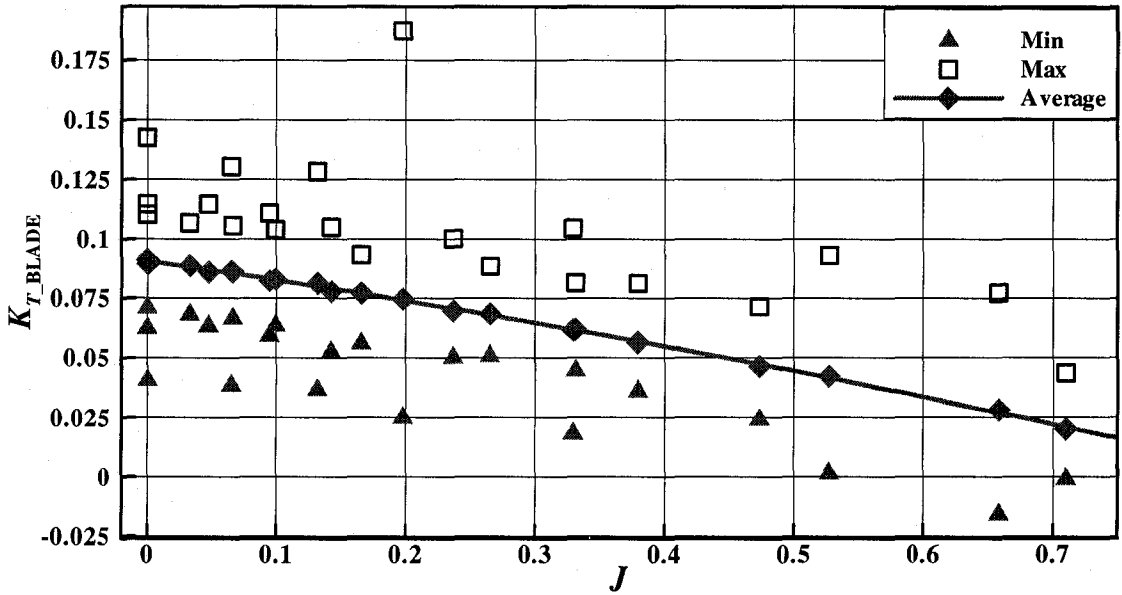
Figure B-6: K_{T_BLADE} vs. J at an azimuthing angle of 180 degrees in open water
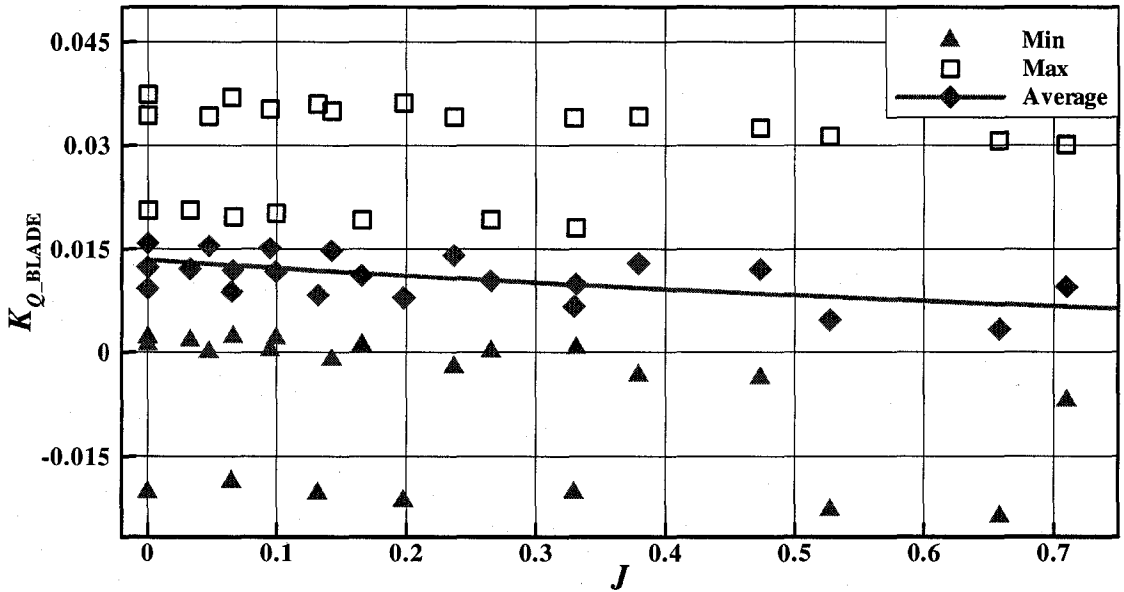
Figure B-7: K_{Q_BLADE} vs. J at an azimuthing angle of 180 degrees in open water

B.1. Separable Hydrodynamic Loads at Various Azimuthing Angles

Experimental results for the average separable hydrodynamic loads are shown including unit thrust, transverse/vertical force on unit, shaft thrust/torque and blade thrust/torque in tractor mode at various azimuthing angles (180 - 60 degrees). The results are plotted with non-dimensional coefficients.
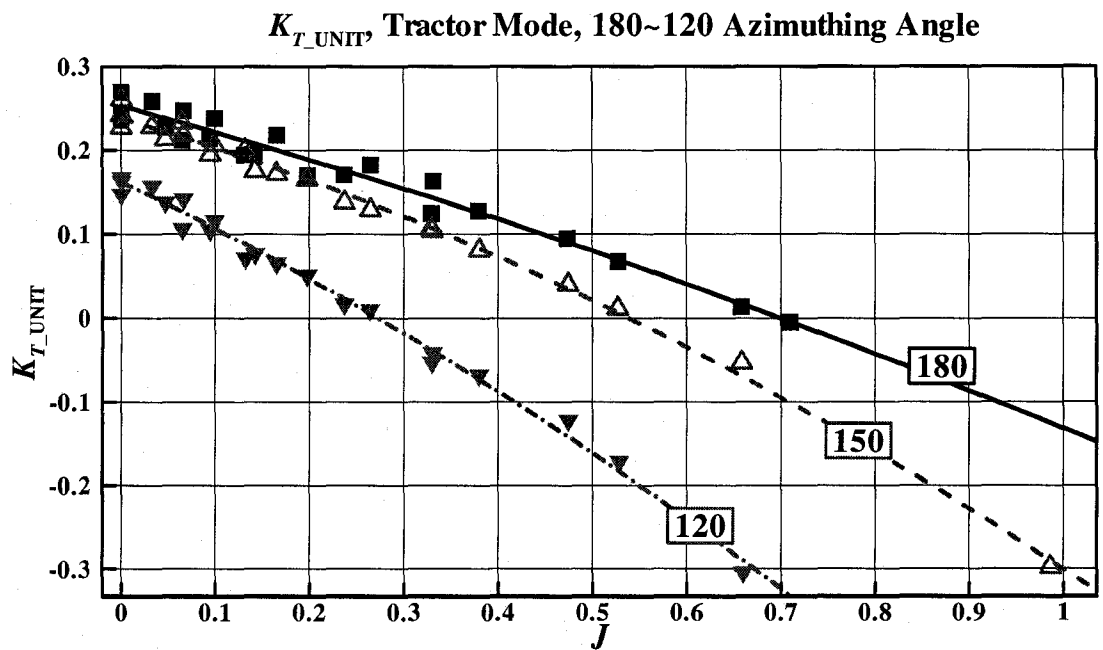
Figure B-8: K_{T_UNIT} vs. J at various azimuthing angles (180–120 degrees) in open water
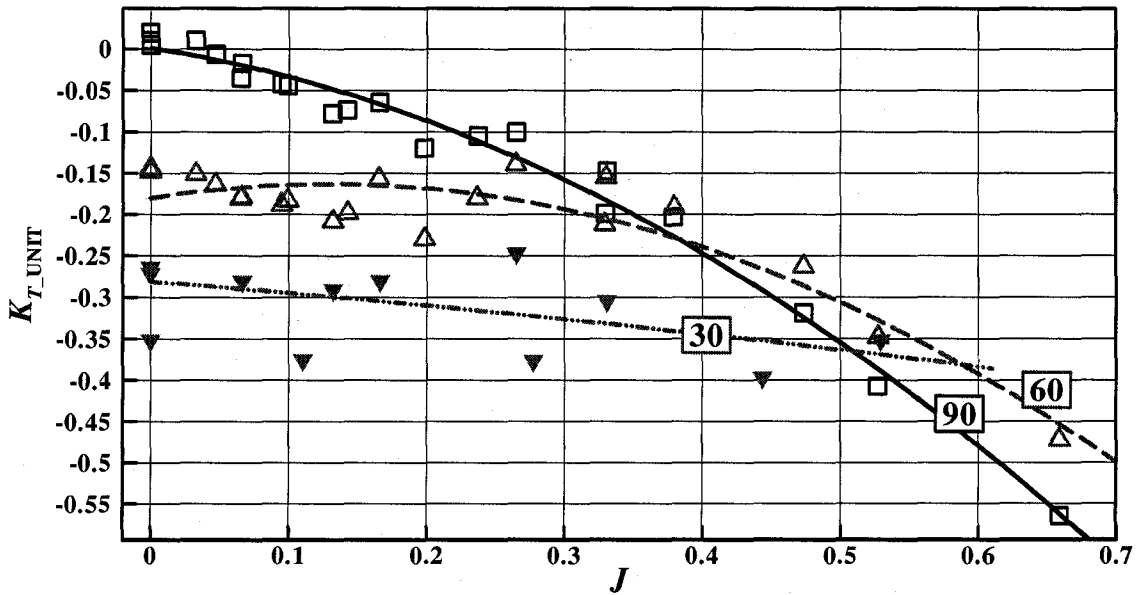
Figure B-9: K_{T_UNIT} vs. J at various azimuthing angles (90–30 degrees) in open water
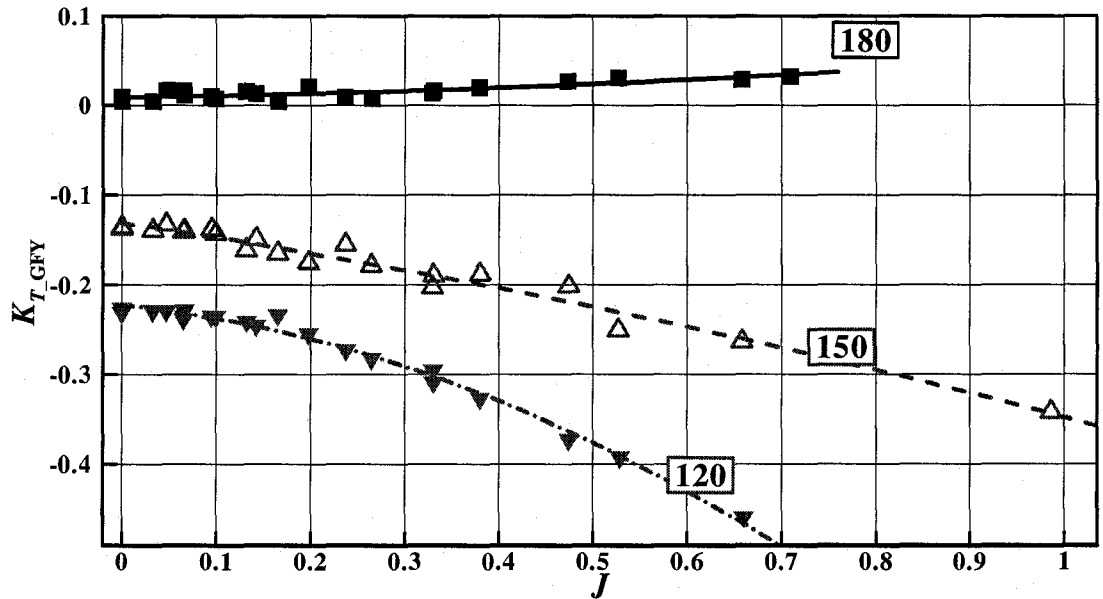
Figure B-10: K_{T_GFY} vs. J at various azimuthing angles (180–120 degrees) in open water
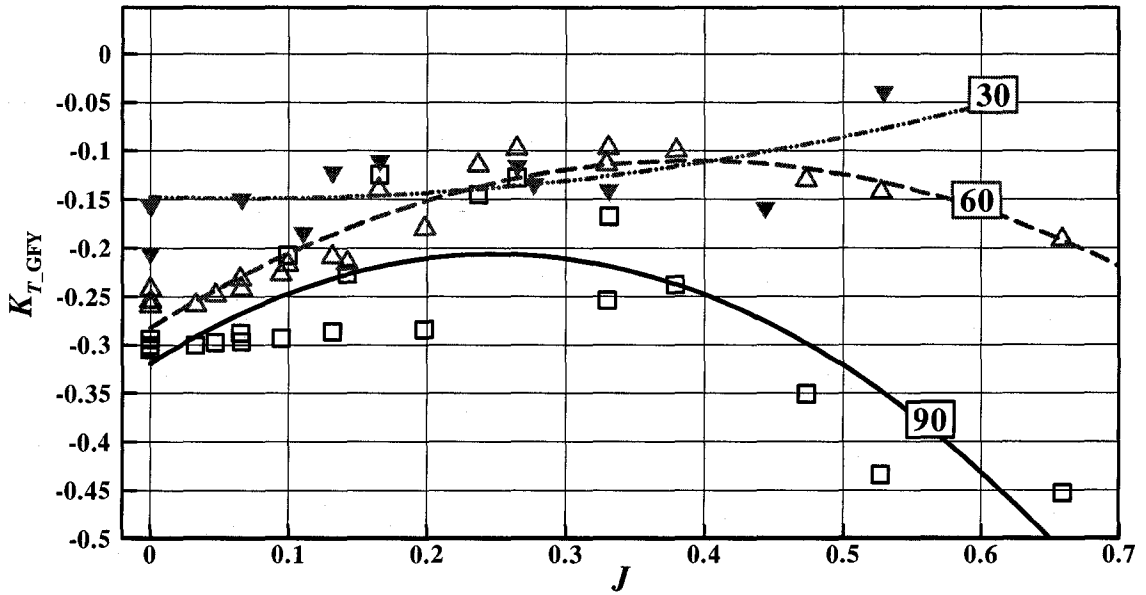
Figure B-11: K_{T_GFY} vs. J at various azimuthing angles (90–30 degrees) in open water
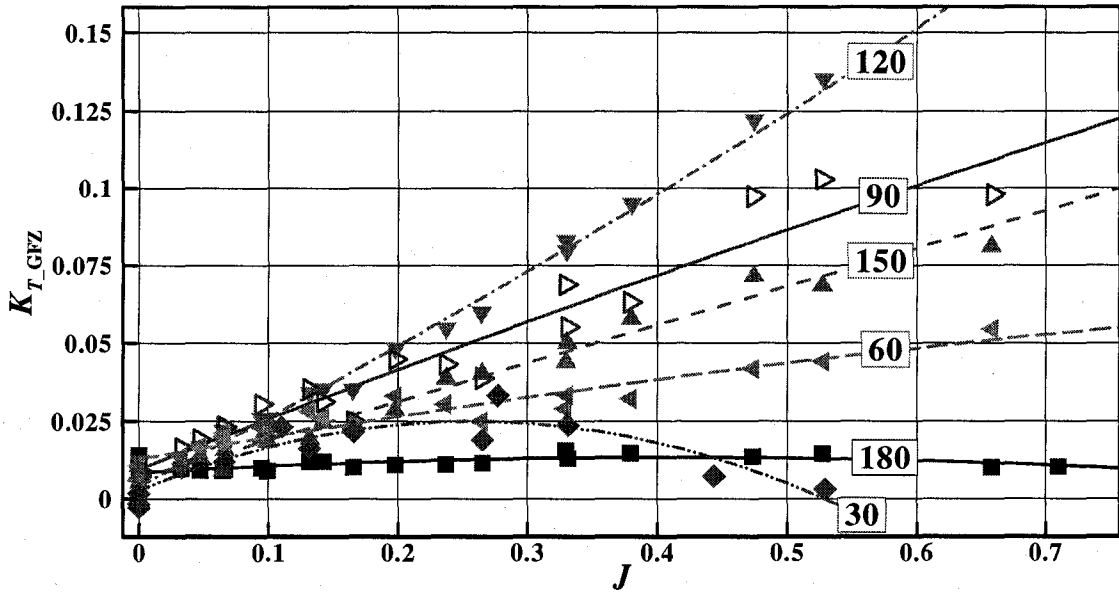
Figure B-12: K_{T_GFZ} vs. J at various azimuthing angles (180–30 degrees) in open water
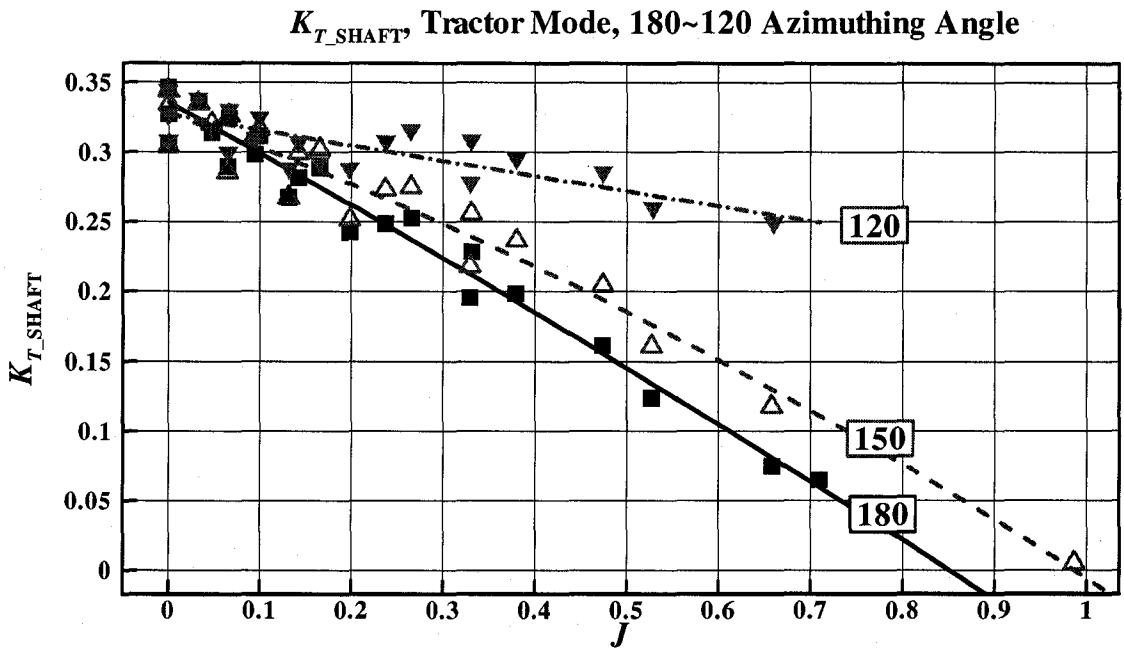
Figure B-13: K_{T_SHAFT} vs. J at various azimuthing angles (180–120 degrees) in open water
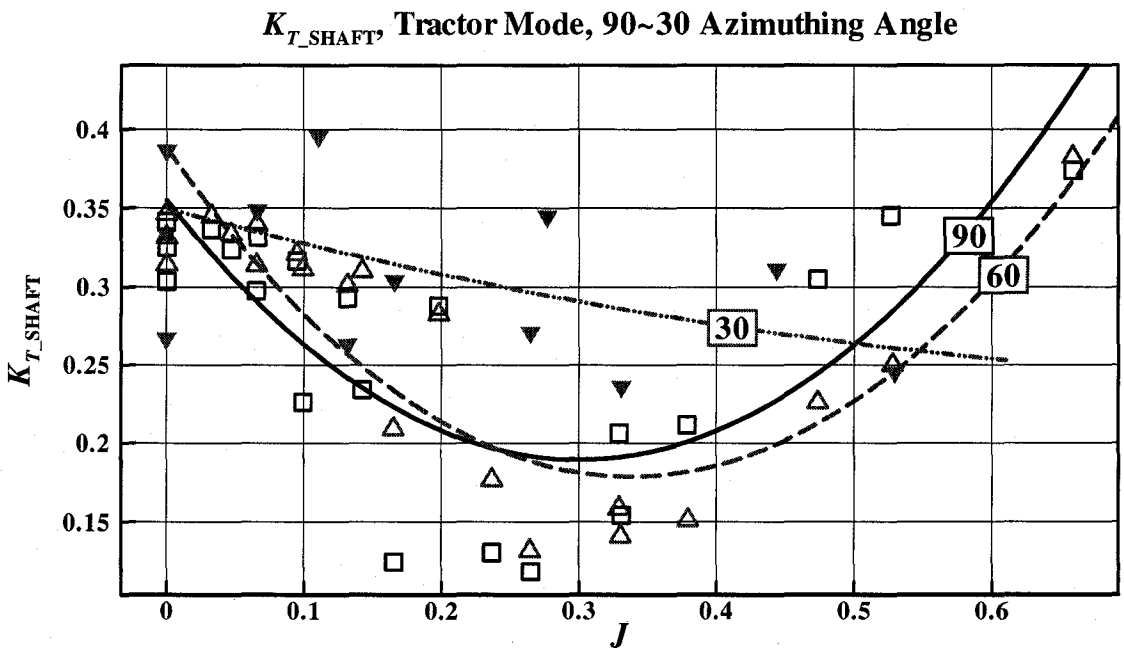
Figure B-14: K_{T_SHAFT} vs. J at various azimuthing angles (90–30 degrees) in open water

189
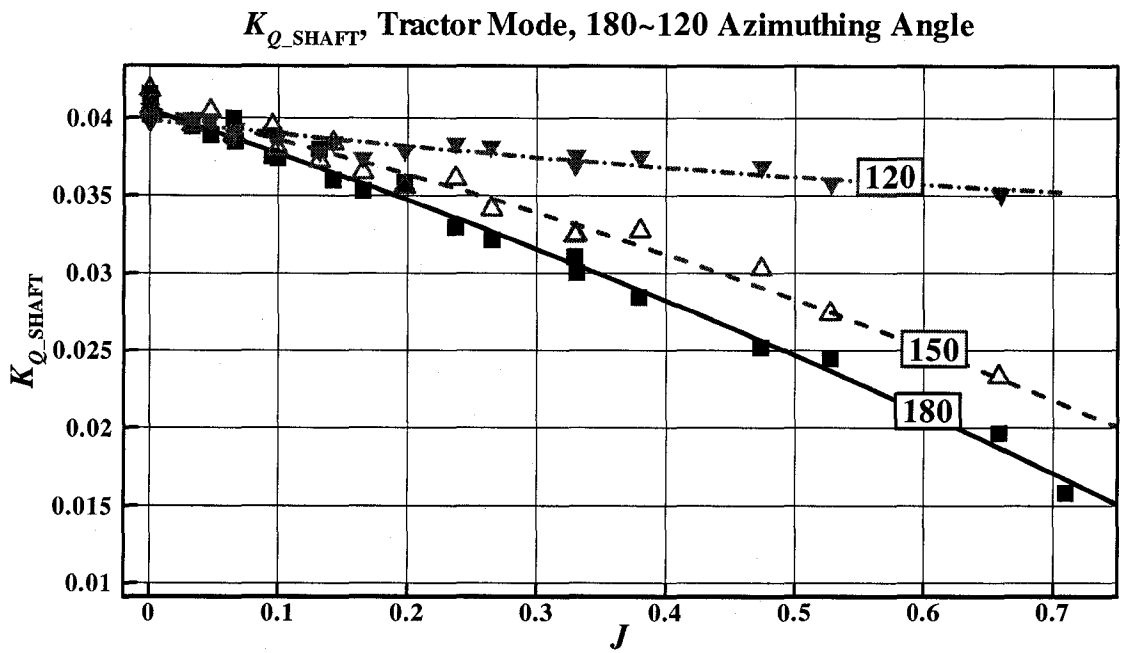
Figure B-15: K_{Q_SHAFT} vs. J at various azimuthing angles (180–120 degrees) in open water
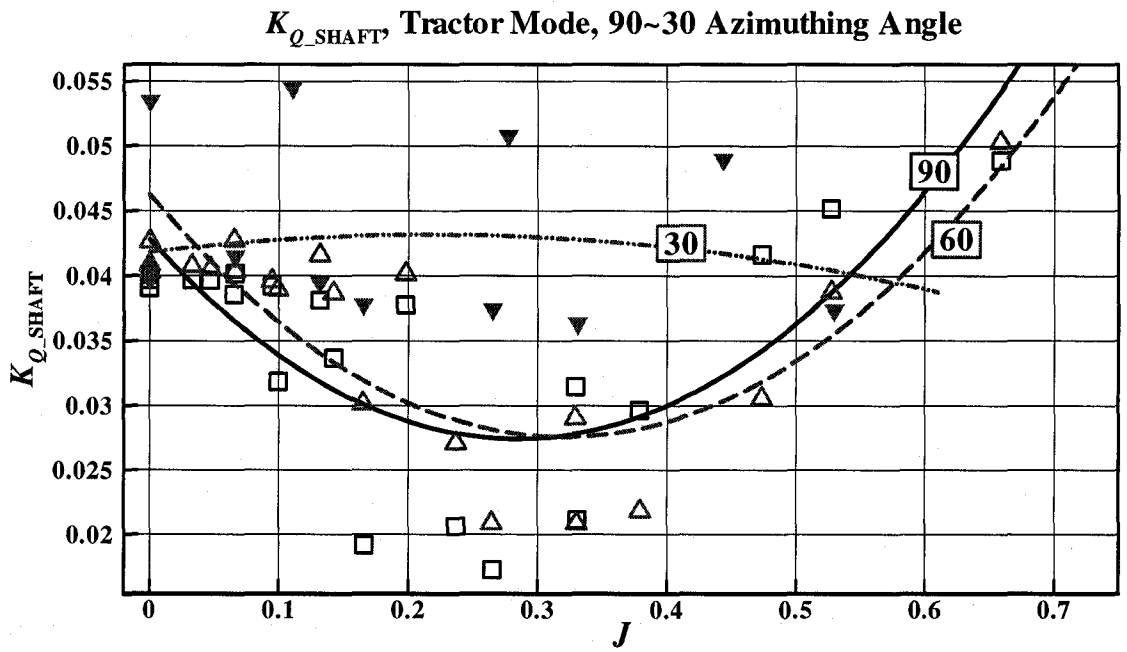
Figure B-16: K_{Q_SHAFT} vs. J at various azimuthing angles (90–30 degrees) in open water

190
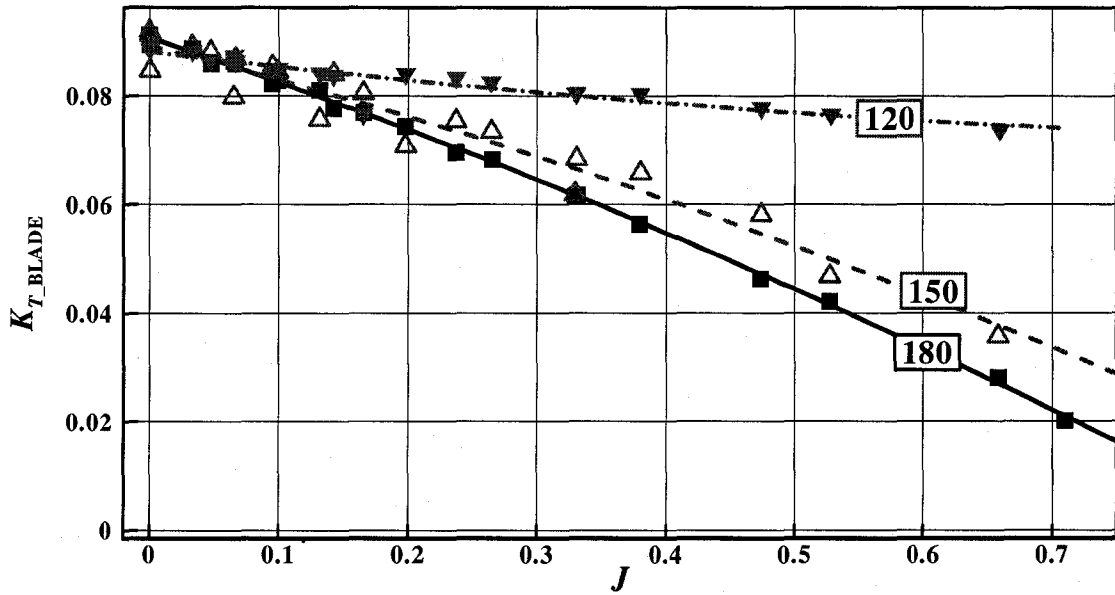
Figure B-17: K_{T_BLADE} vs. J at various azimuthing angles (180–120 degrees) in open water
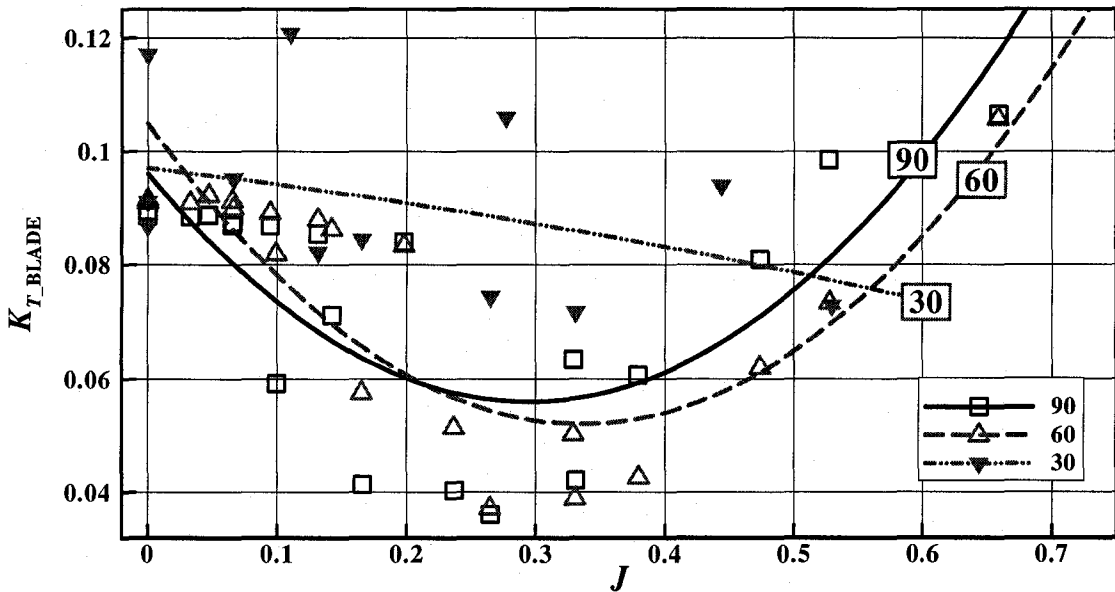
Figure B-18: K_{T_BLADE} vs. J at various azimuthing angles (90–30 degrees) in open water

191
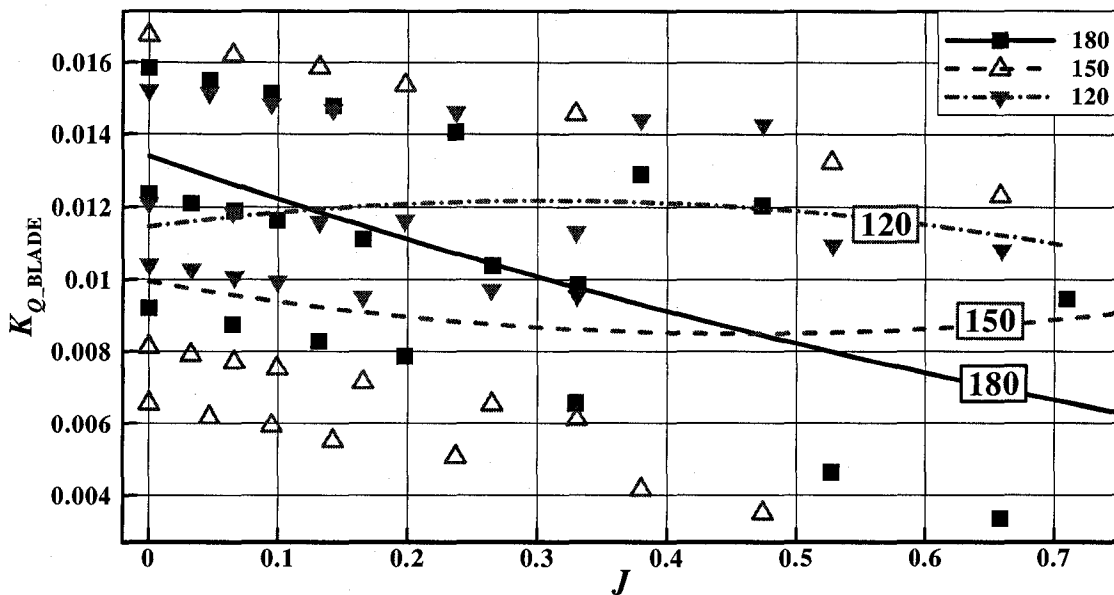
Figure B-19: K_{Q_BLADE} vs. J at various azimuthing angles (180–120 degrees) in open water
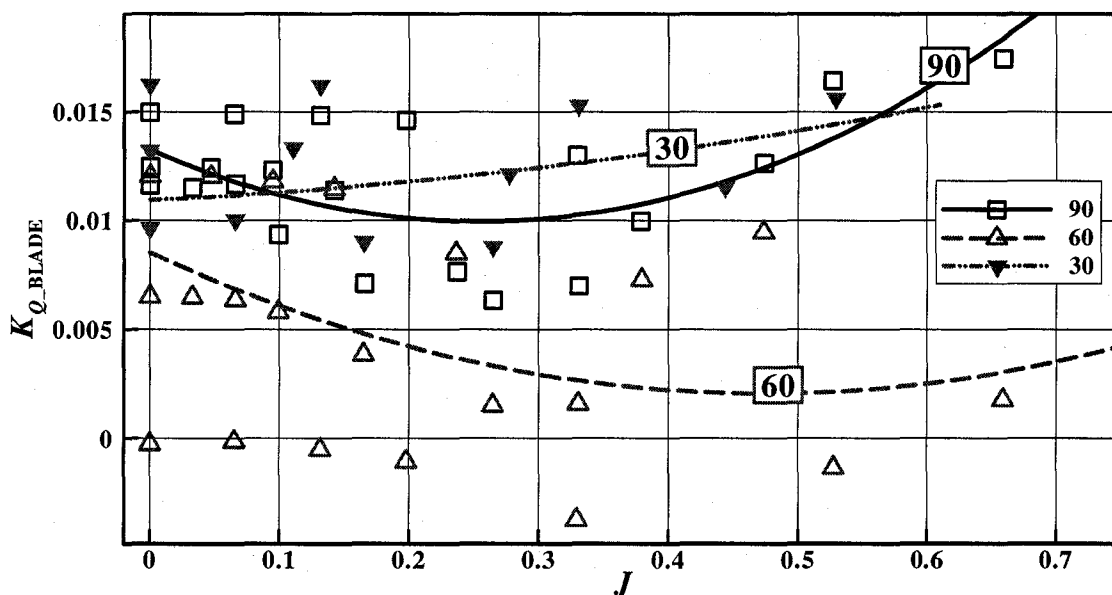
Figure B-20: K_{Q_BLADE} vs. J at various azimuthing angles (90–30 degrees) in open water

B.2. Performance Characteristics in Open Water at Various Azimuthing Angles

Experimental results for the average separable hydrodynamic loads are shown including unit thrust, shaft thrust/torque, and efficiency on the shaft in tractor mode at various azimuthing angles (180-60 degrees). The results are plotted with non-dimensional coefficients
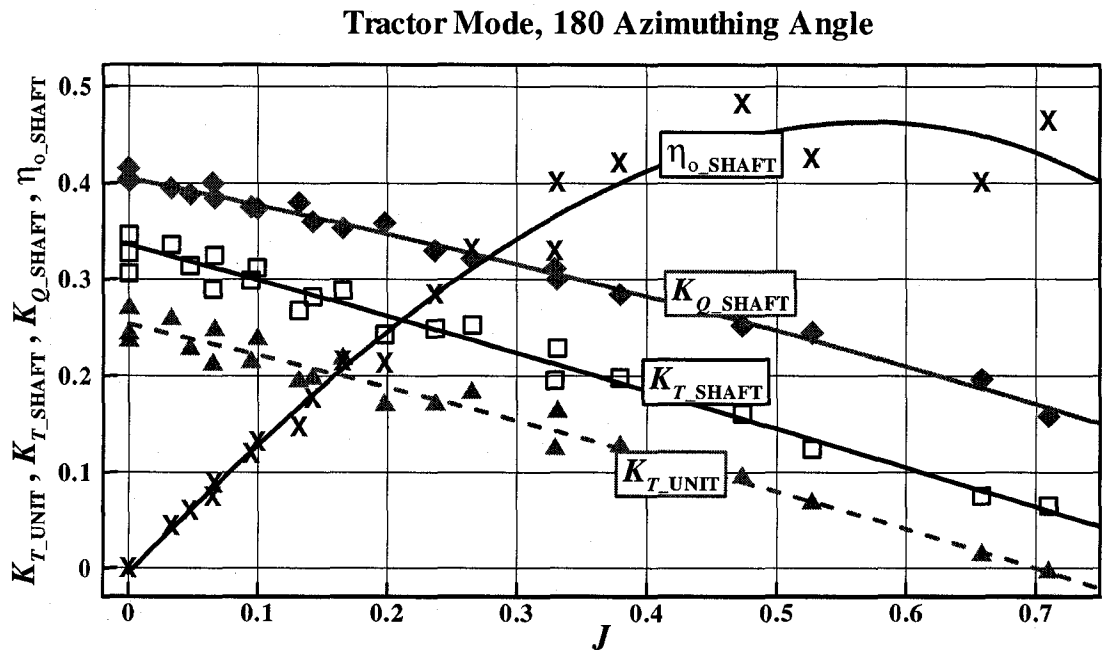
Figure B-21: Open water characteristics for tractor mode at 180° azimuthing angle

Tractor Mode, 150 Azimuthing Angle
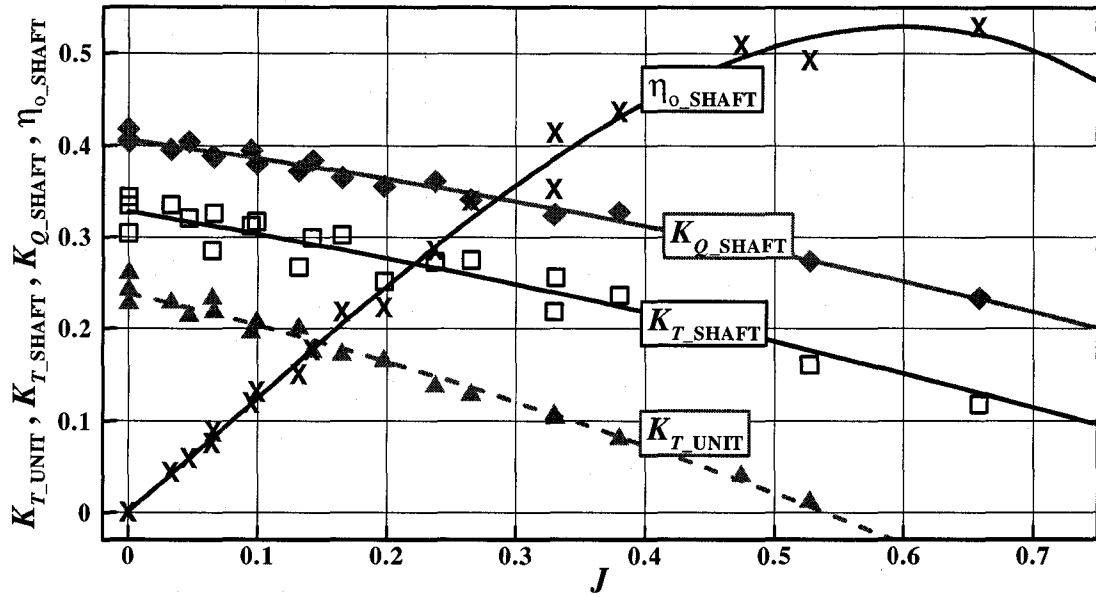
Figure B-22: Open water characteristics for tractor mode at 150° azimuthing angle

Tractor Mode, 120 Azimuthing Angle
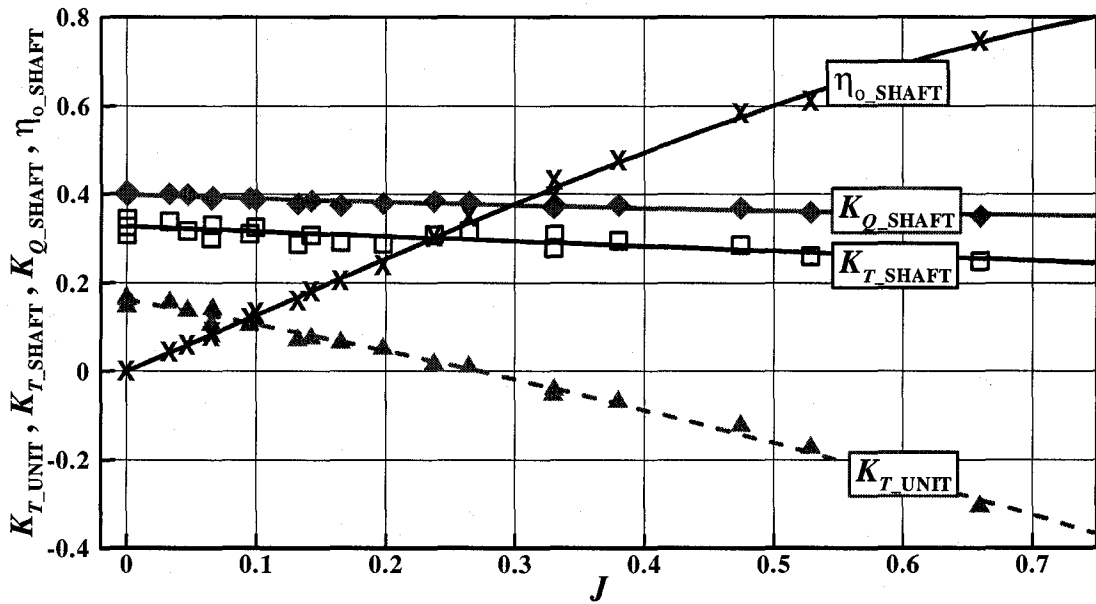
Figure B-23: Open water characteristics for tractor mode at 120° azimuthing angle

Tractor Mode, 90 Azimuthing Angle
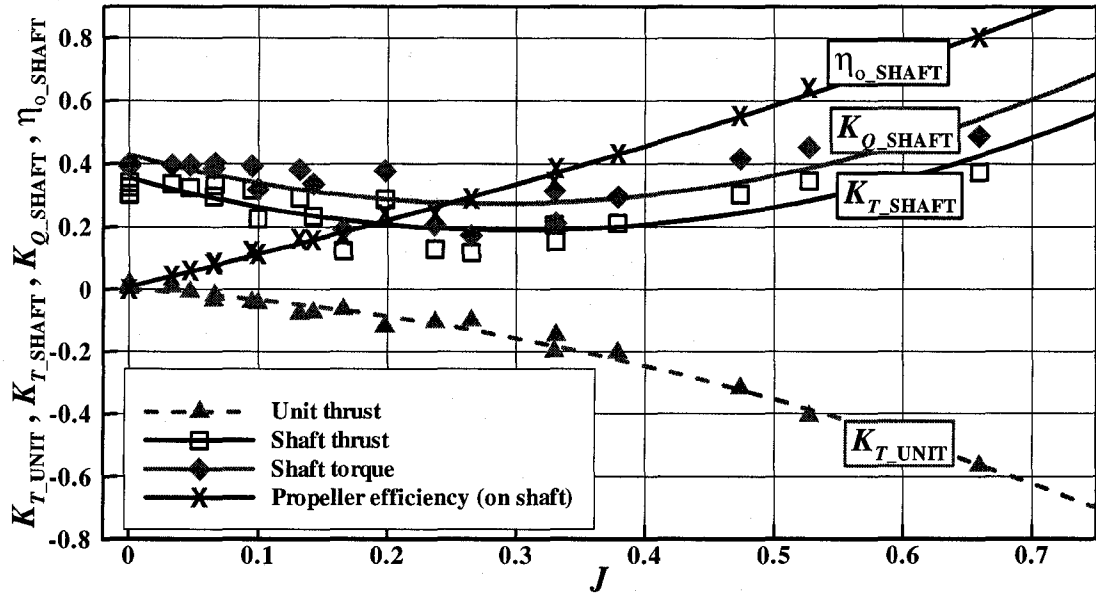
Figure B-24: Open water characteristics for tractor mode at 90° azimuthing angle

Tractor Mode, 60 Azimuthing Angle
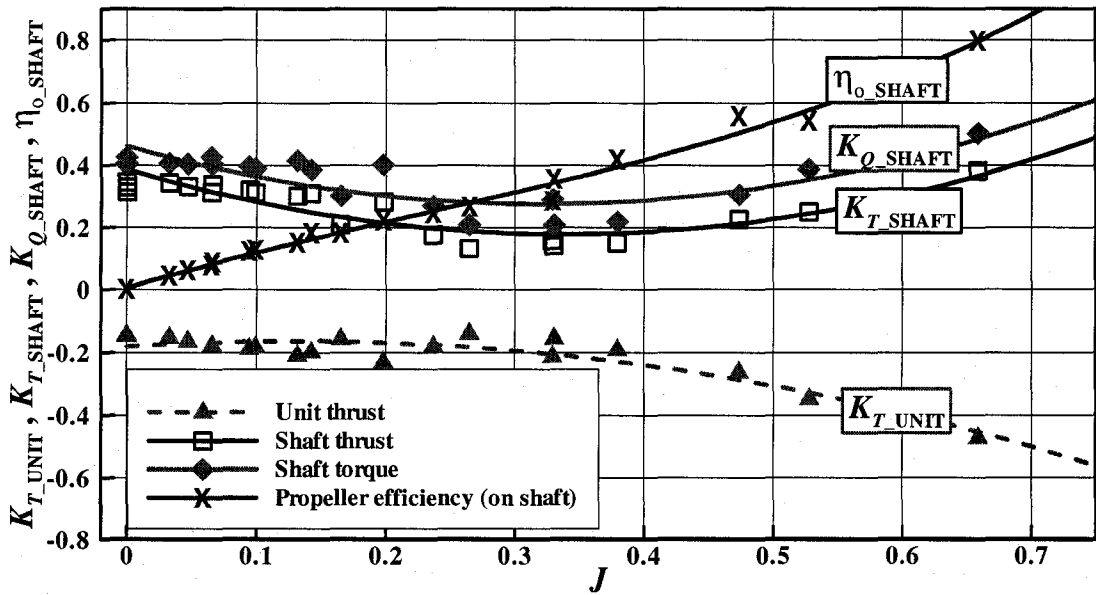
Figure B-25: Open water characteristics for tractor mode at 60° azimuthing angle

Tractor Mode, 30 Azimuthing Angle
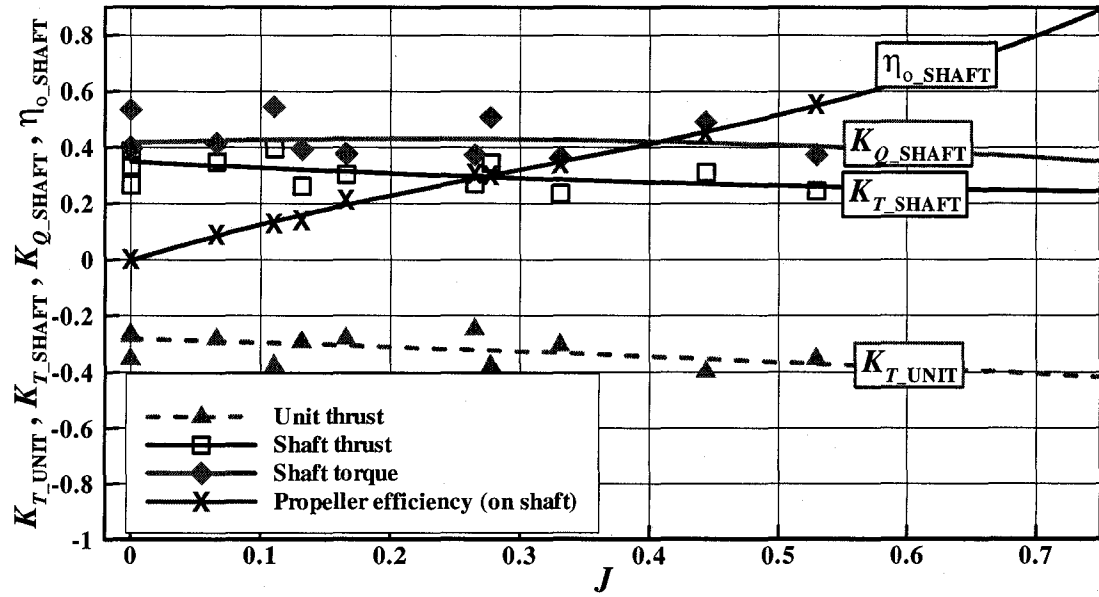
Figure B-26: Open water characteristics for tractor mode at 30° azimuthing angle

196

Appendix C Ice Related Loads (Experim ental Results in Ice Covered Water)

Experimental results for the ice related loads are shown including shaft thrust/torque and blade thrust/torque with maximum, minimum, and average in tractor mode at the azimuthing angle of 180 degrees and depth of cut of 35 mm. The results are plotted with non-dimensional coefficients with error bars, which represent the confidence level of 95 %.
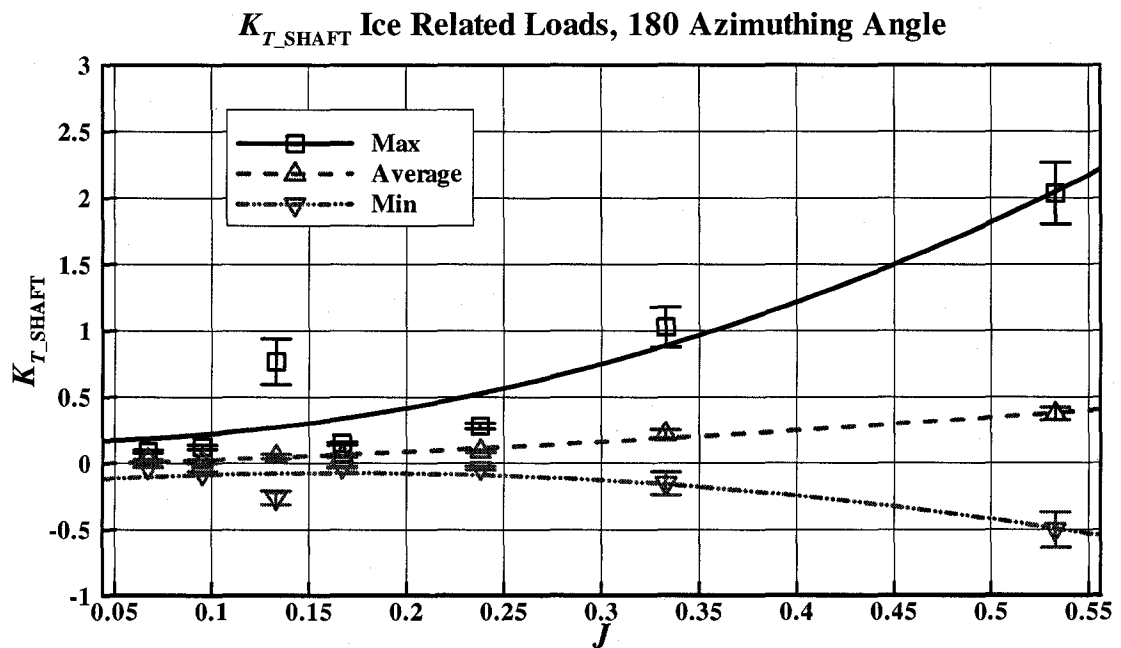
Figure C-1: K_{T_SHAFT} vs. J, maximum-average-minimum ice related loads with error bars

K_{Q_SHAFT}, **Ice Related Loads, 180 Azimuthing Angle**
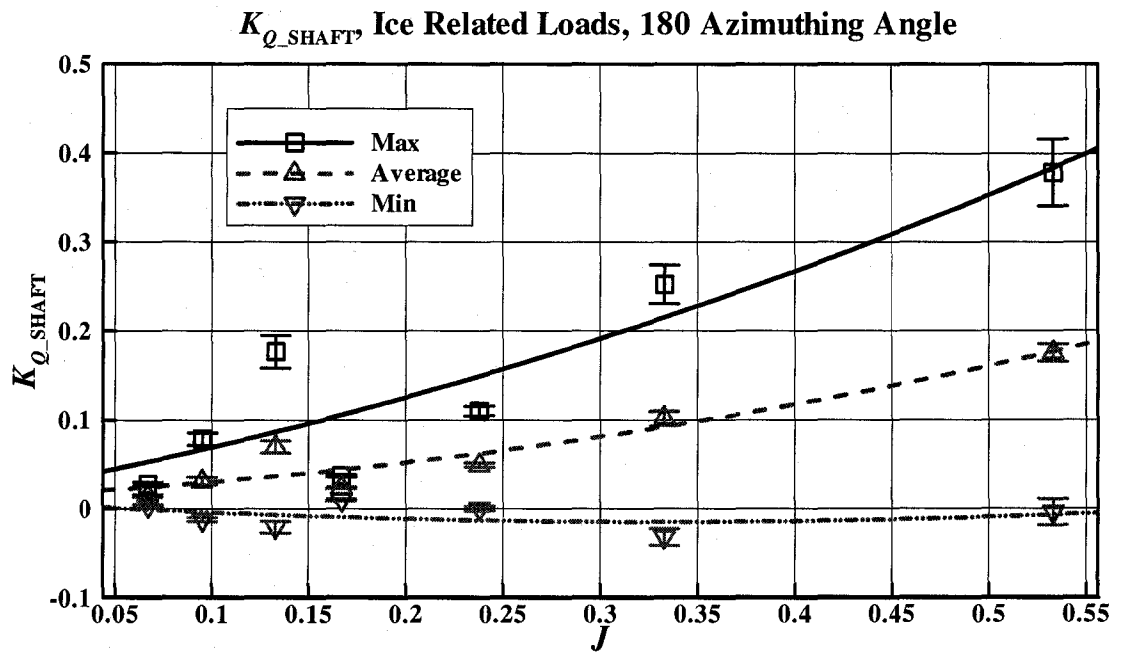
Figure C-2: K_{Q_SHAFT} vs. J, maximum-average-minimum ice related loads with error bars

K_{T_BLADE}, **Ice Related Loads, 180 Azimuthing Angle**
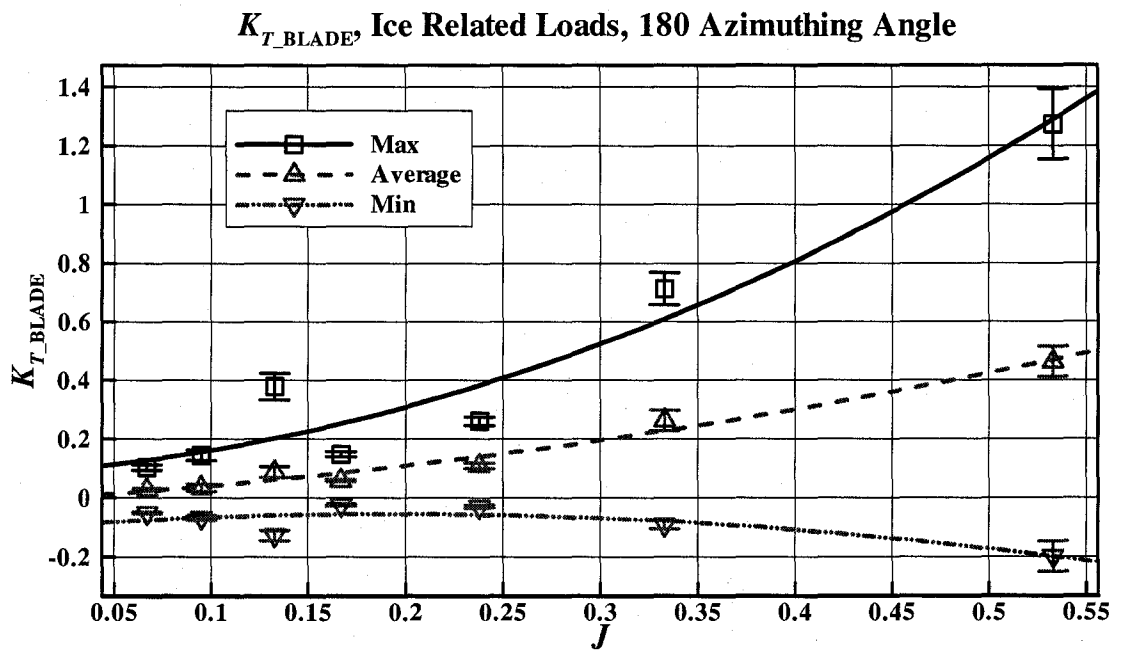
Figure C-3: K_{T_BLADE} vs. J, maximum-average-minimum ice related loads with error bars
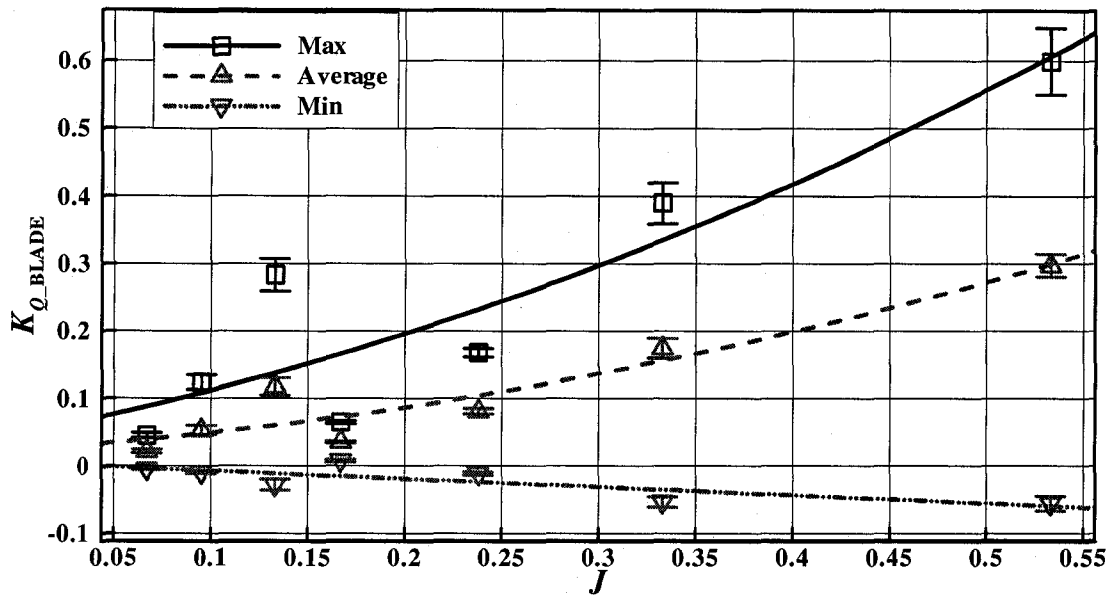
Figure C-4: K_{Q_BLADE} vs. J, maximum-average-minimum ice related loads with error bars
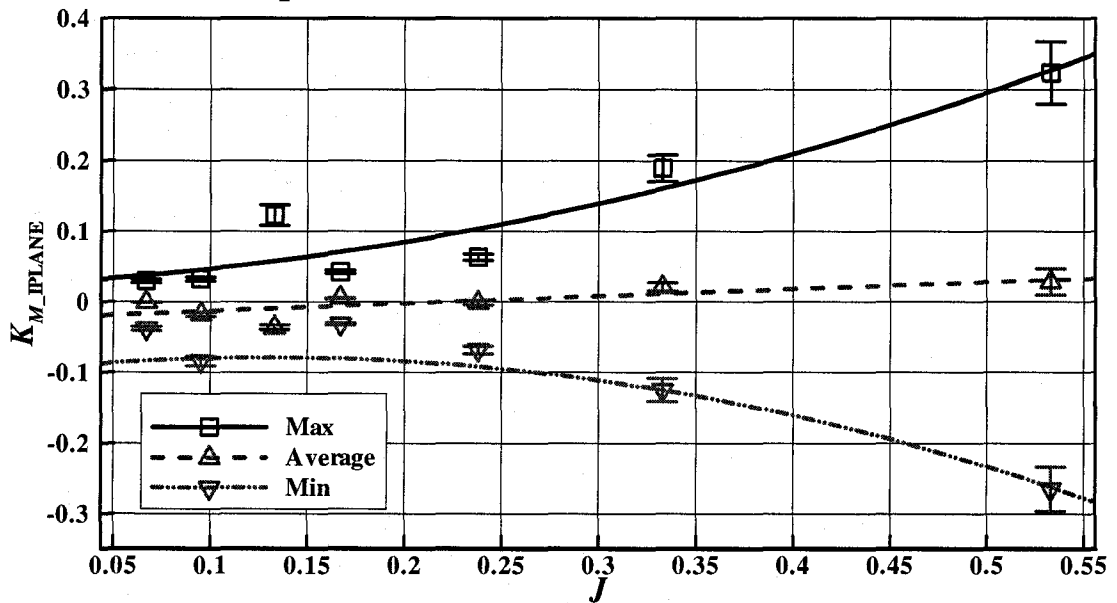
Figure C-5: K_{M_IPLANE} vs. J, maximum-average-minimum ice related loads with error bars
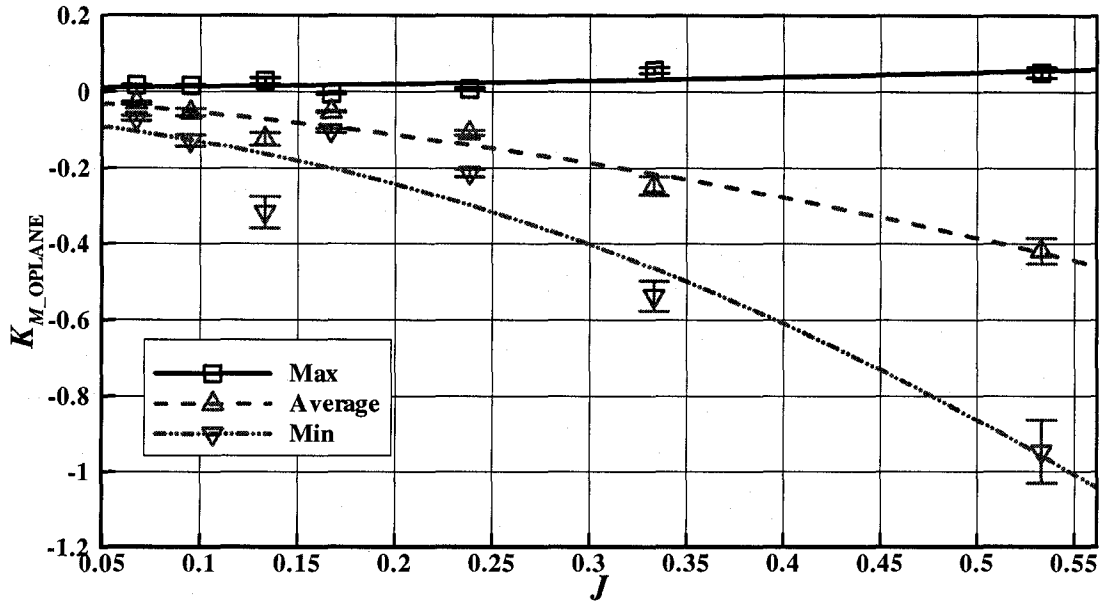
Figure C-6 : K_{M_OPLANE} vs. J, maximum-average-minimum ice related loads with error bars
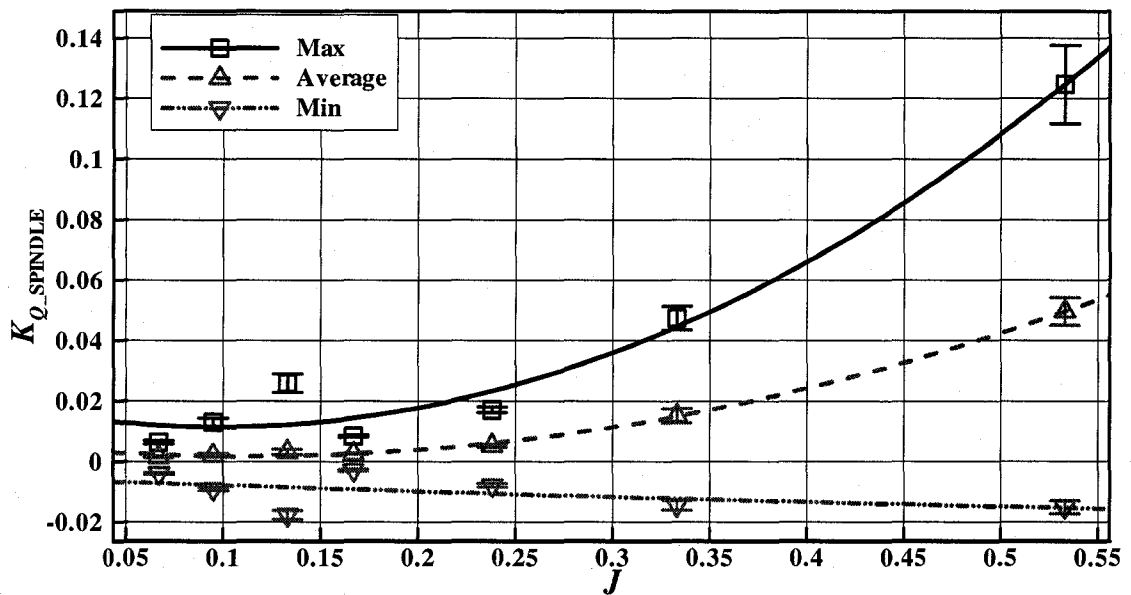
Figure C-7: $K_{Q\_SPINDLE}$ vs. J, maximum-average-minimum ice related loads with error bars

200

C.1. Average Ice Related Loads at Various Azimuthing Angles (35mm Depth of Cut)

Experimental results for the average ice related loads are shown including shaft thrust/torque and blade thrust/torque, and blade in plane bending moment/out of plane bending moment/ spindle torque in tractor mode at various azimuthing angles (180-60 degrees). The results are plotted with non-dimensional coefficients.
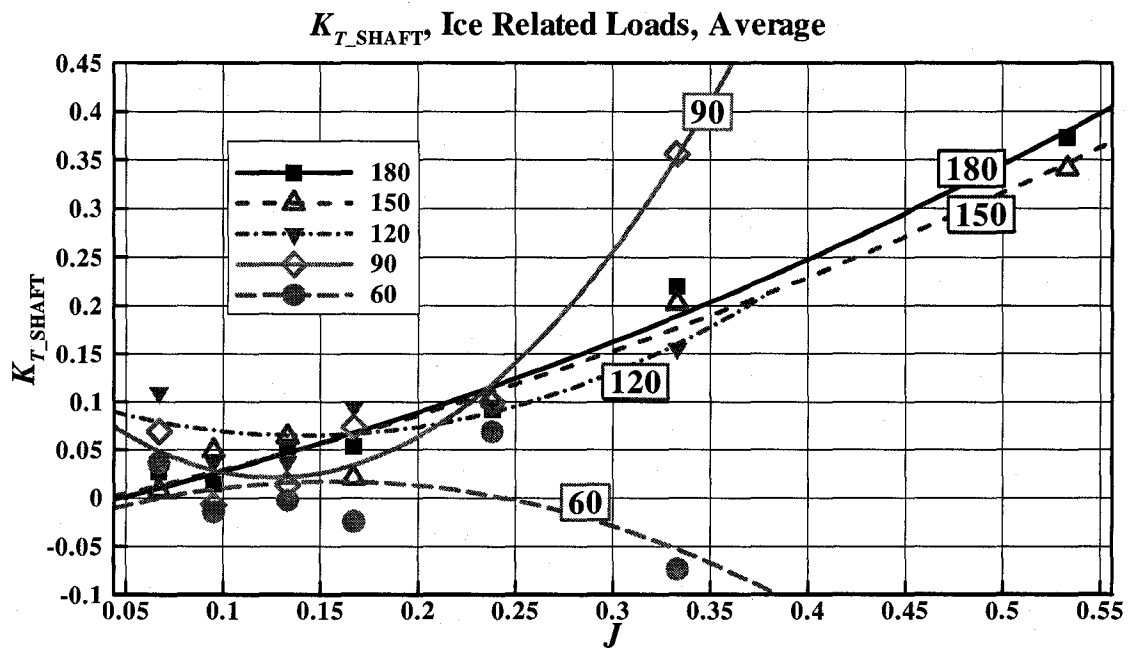
Figure C-8: K_{T_SHAFT} vs. J, average ice related loads at various azimuthing angles (180 ~ 60 degrees)

K_{Q_SHAFT}, Ice Related Loads, Average
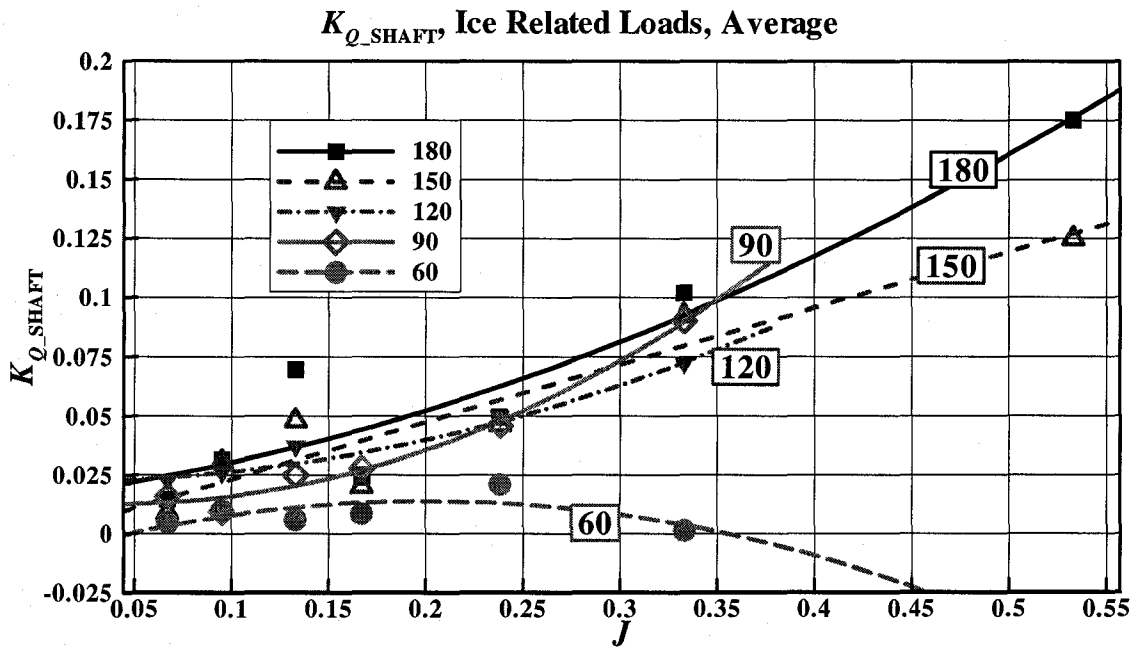
Figure C-9: K_{Q_SHAFT} vs. J, average ice related loads at various azimuthing angles (180 ~ 60 degrees)

K_{T_BLADE}, Ice Related Loads, Average
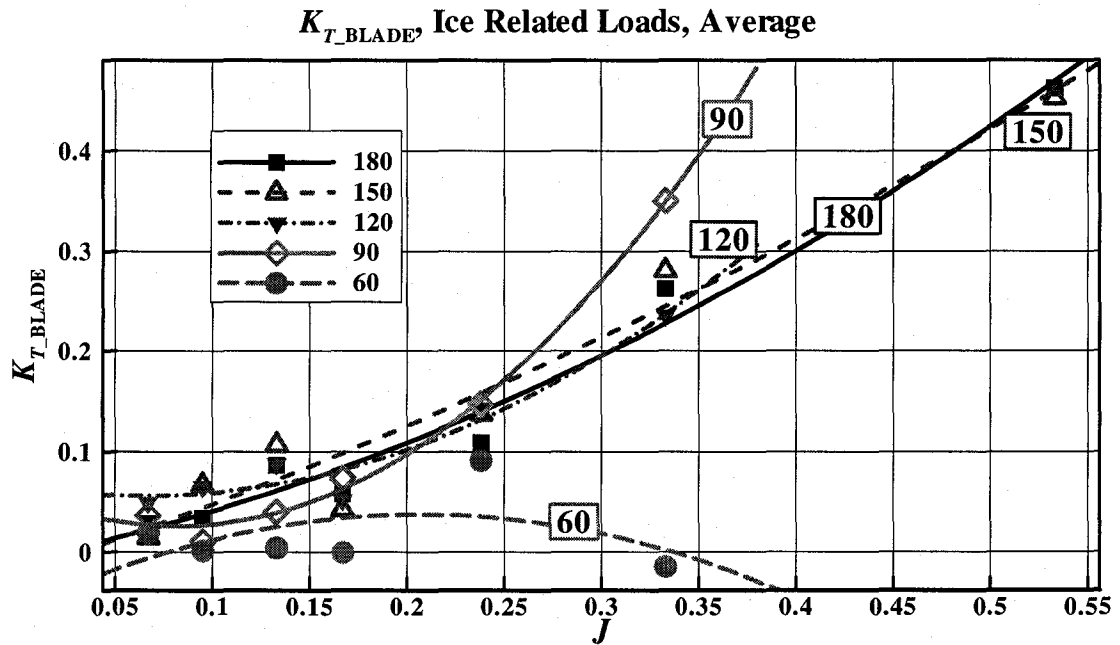
Figure C-10: K_{T_BLADE} vs. J, average ice related loads at various azimuthing angles (180 ~ 60 degrees)
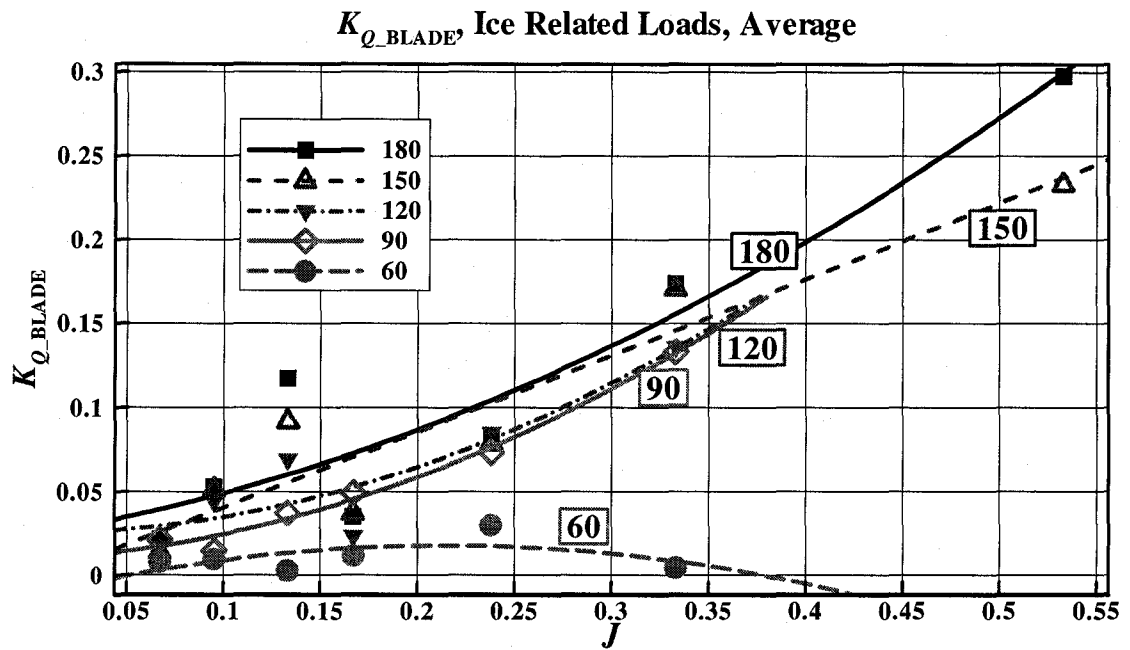
Figure C-11: K_{Q_BLADE} vs. J, average ice related loads at various azimuthing angles (180 ~ 60 degrees)
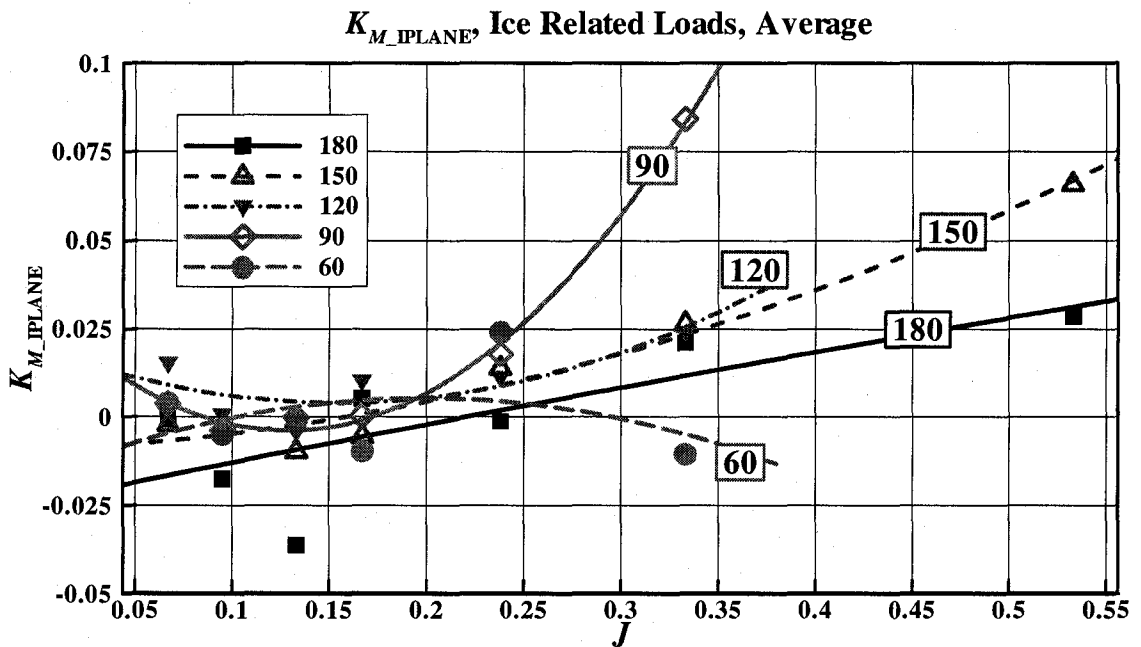
Figure C-12: K_{M_IPLANE} vs. J, average ice related loads at various azimuthing angles (180 ~ 60 degrees)
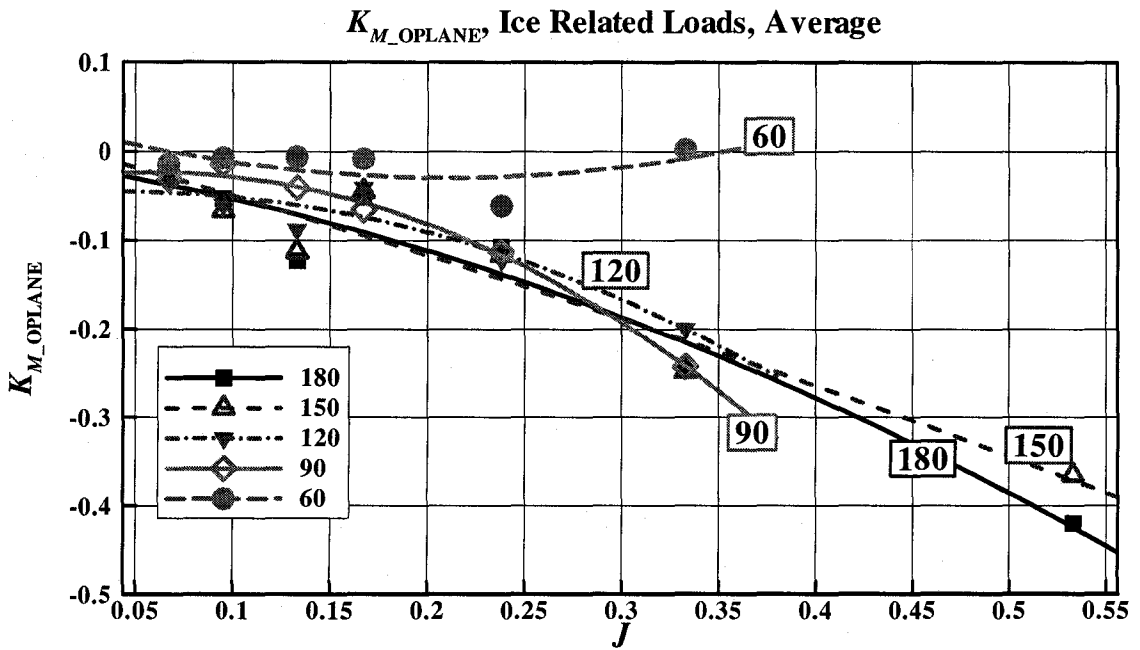
Figure C-13: K_{M_OPLANE} vs. J, average ice related loads at various azimuthing angles (180 ~ 60 degrees)
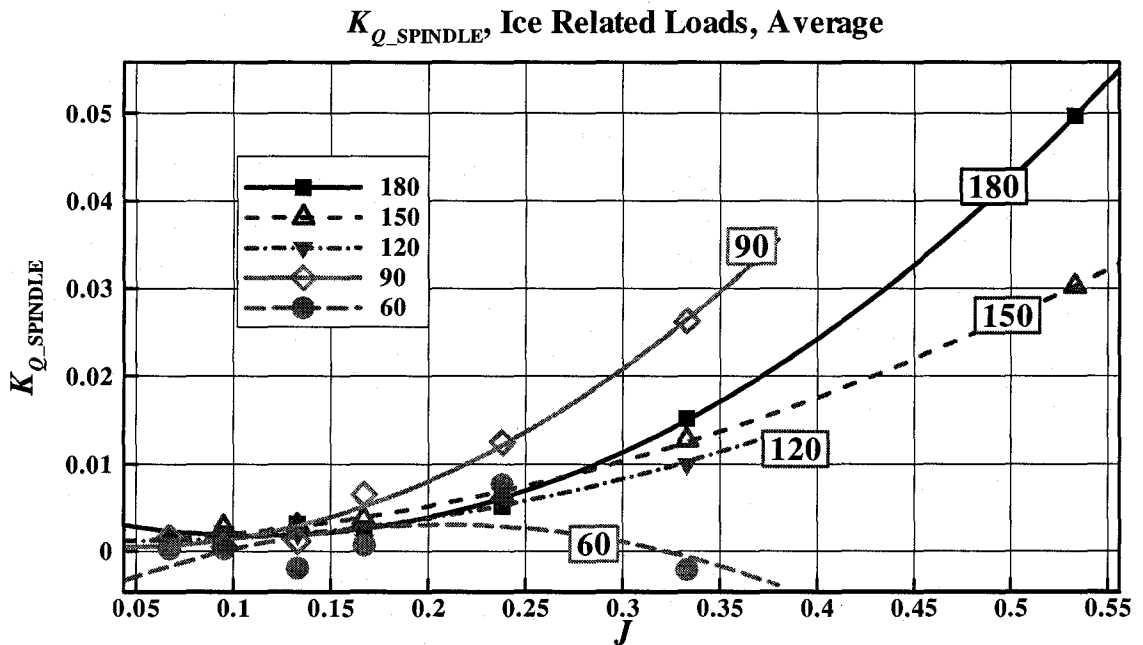
Figure C-14: $K_{Q\_SPINDLE}$ vs. J, average ice related loads at various azimuthing angles (180 ~ 60 degrees)

C.2. Maximum Ice Related Loads at Various

Azimuthing Angles (35 mm Depth of Cut)

Experimental results for the maximum ice related loads are shown including shaft

thrust/torque and blade thrust/torque, and blade in plane bending moment/out of plane

bending moment/ spindle torque in tractor mode at various azimuthing angles (180-60

degrees). The results are plotted with non-dimensional coefficients.
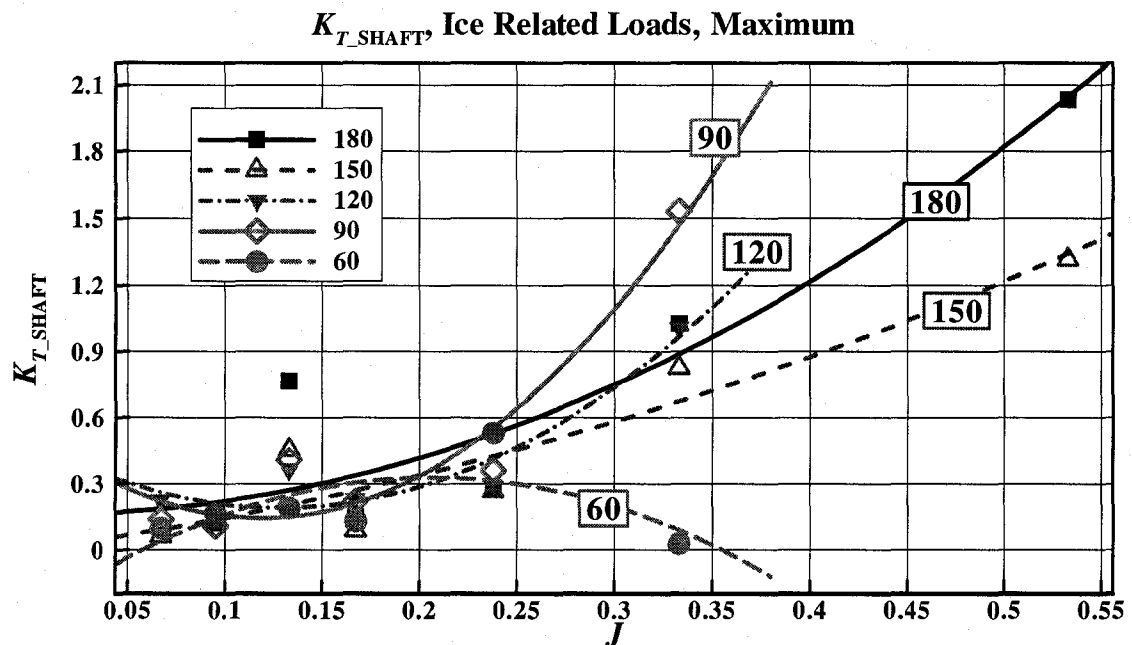
Figure C-15: K_{T_SHAFT} vs. J, maximum ice related loads at various azimuthing angles (180 ~ 60 degrees)
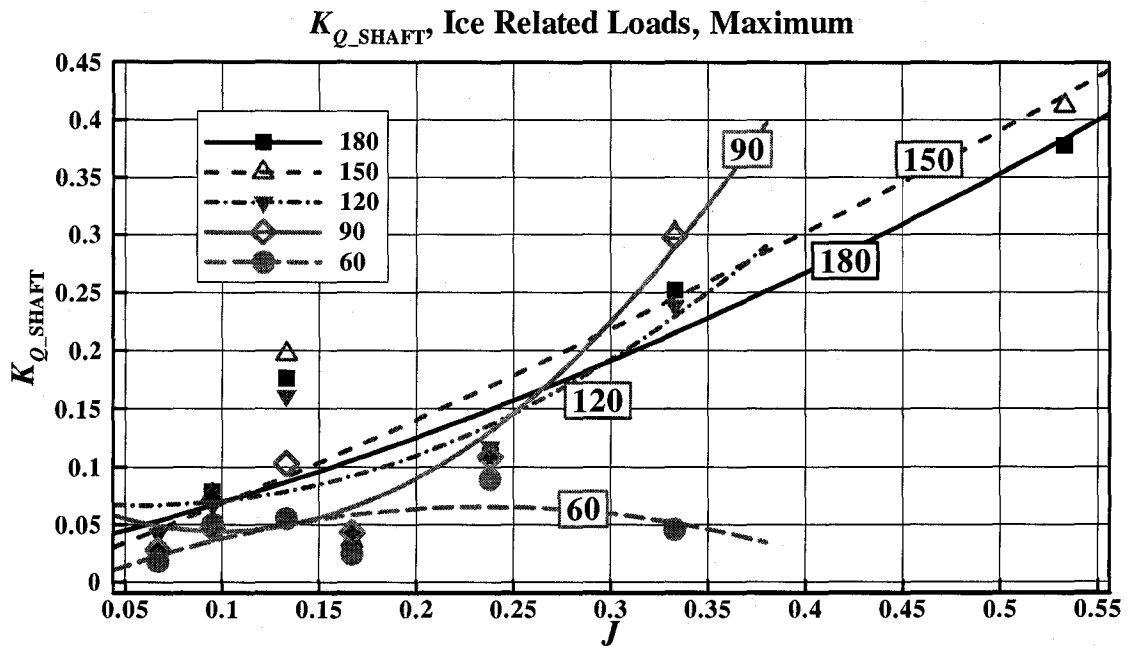
Figure C-16: K_{Q_SHAFT} vs. J, maximum ice related loads at various azimuthing angles (180 ~ 60 degrees)
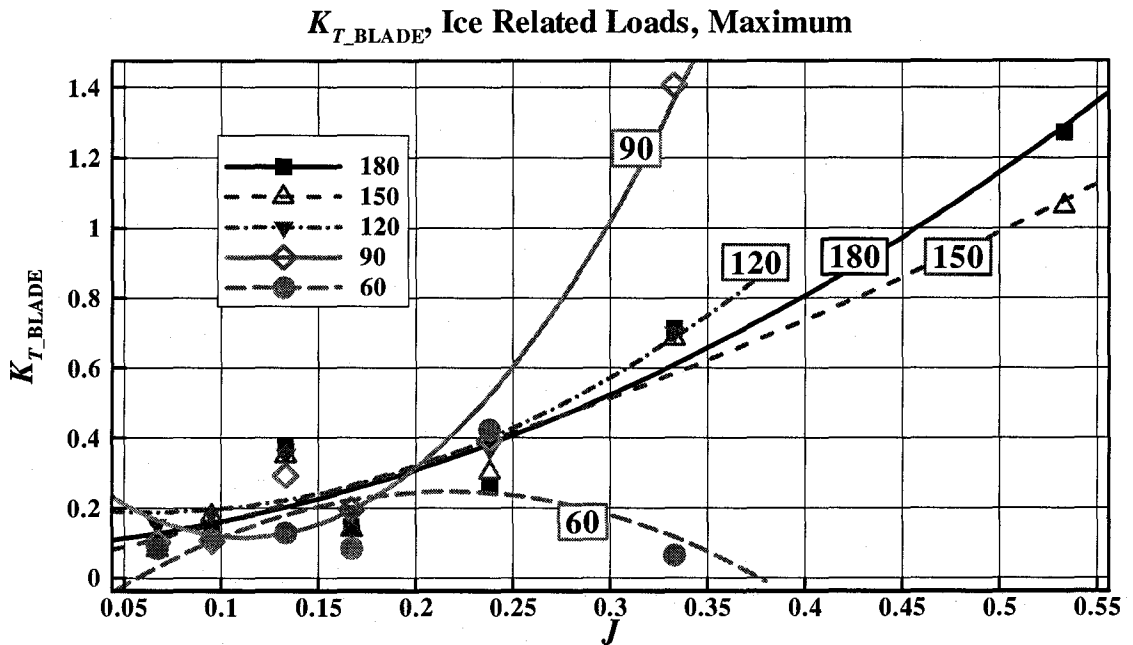
Figure C-17: K_{T_BLADE} vs. J, maximum ice related loads at various azimuthing angles (180 ~ 60 degrees)
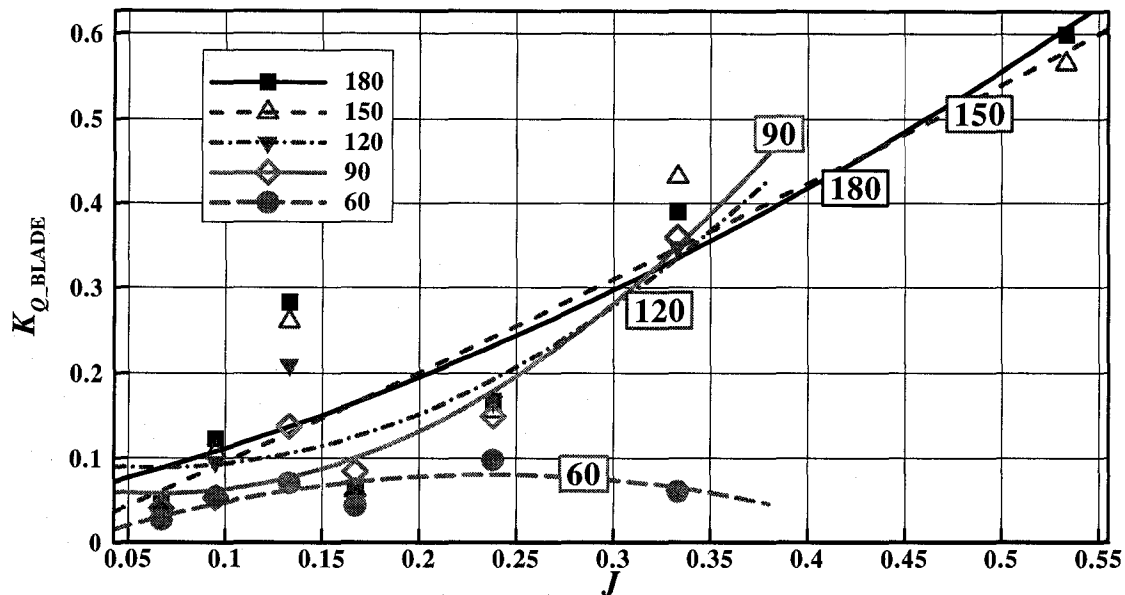
Figure C-18: K_{Q_BLADE} vs. J, maximum ice related loads at various azimuthing angles (180 ~ 60 degrees)
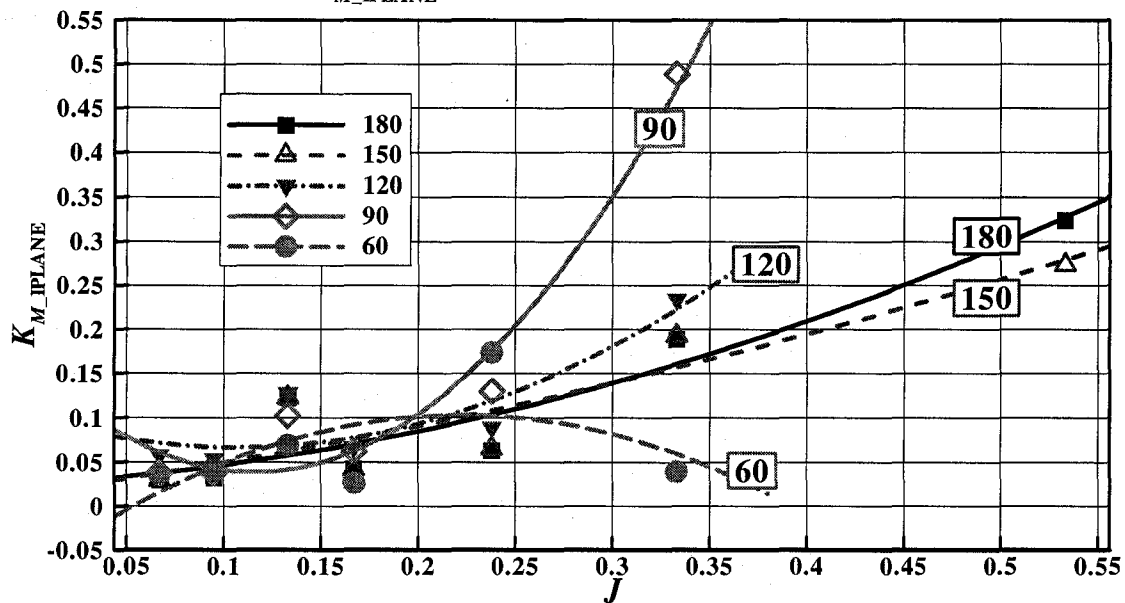
Figure C-19: K_{M_IPLANE} vs. J, maximum ice related loads at various azimuthing angles (180 ~ 60 degrees)
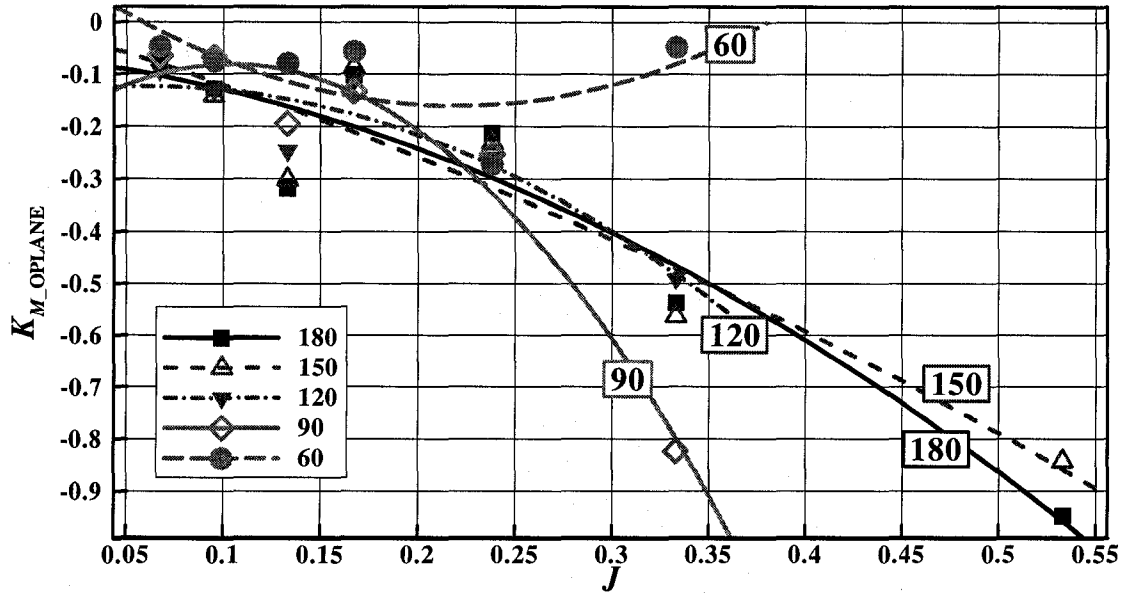
Figure C-20: K_{M_OPLANE} vs. J, negative maximum ice related loads at various azimuthing angles (180 ~ 60 degrees)
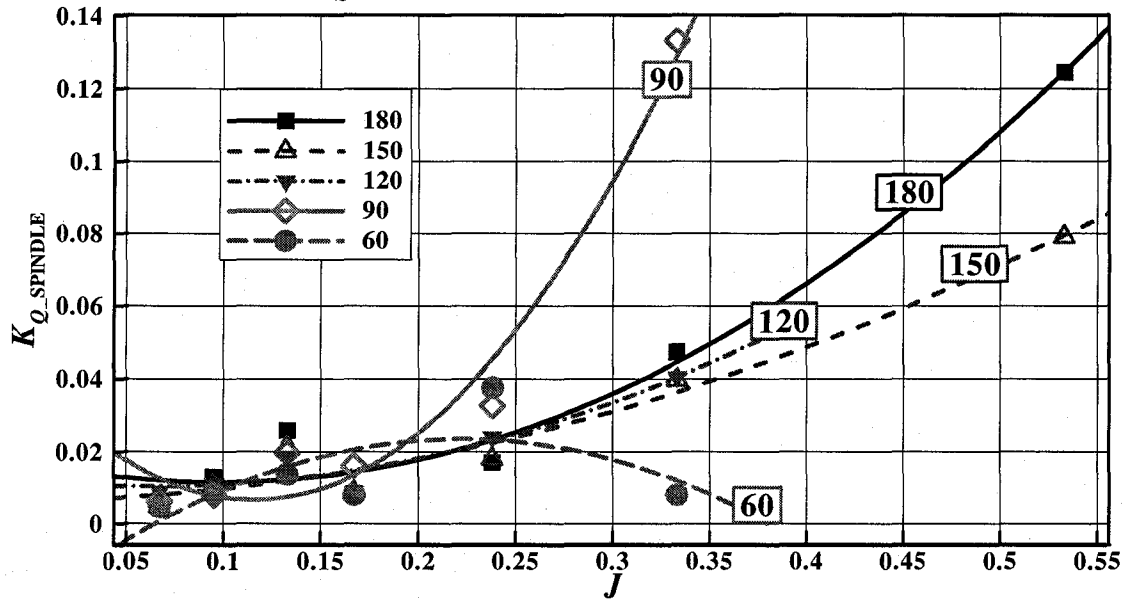
Figure C-21: $K_{Q\_SPINDLE}$ vs. J, maximum ice related loads at various azimuthing angles (180 ~ 60 degrees)

C.3. Average Ice Related Loads at Various Azimuthing Angles (15mm Depth of Cut, Repeat Runs)

Experimental results for the average ice related loads are shown including shaft thrust/torque and blade thrust/torque, and blade in plane bending moment/out of plane bending moment/ spindle torque in tractor mode at various azimuthing angles (180-60 degrees). Tests were repeated three times in 15mm depth of cut. The results are plotted with non-dimensional coefficients.
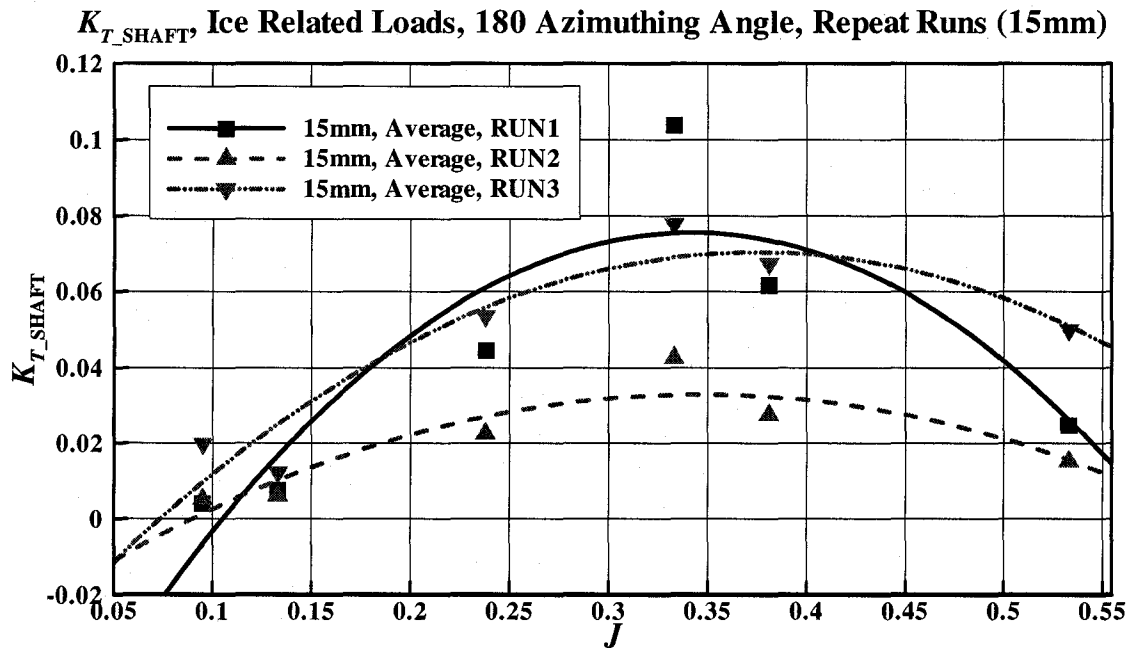
Figure C-22: K_{T_SHAFT} vs. J, average ice related loads at 15mm depth of cut (repeated)
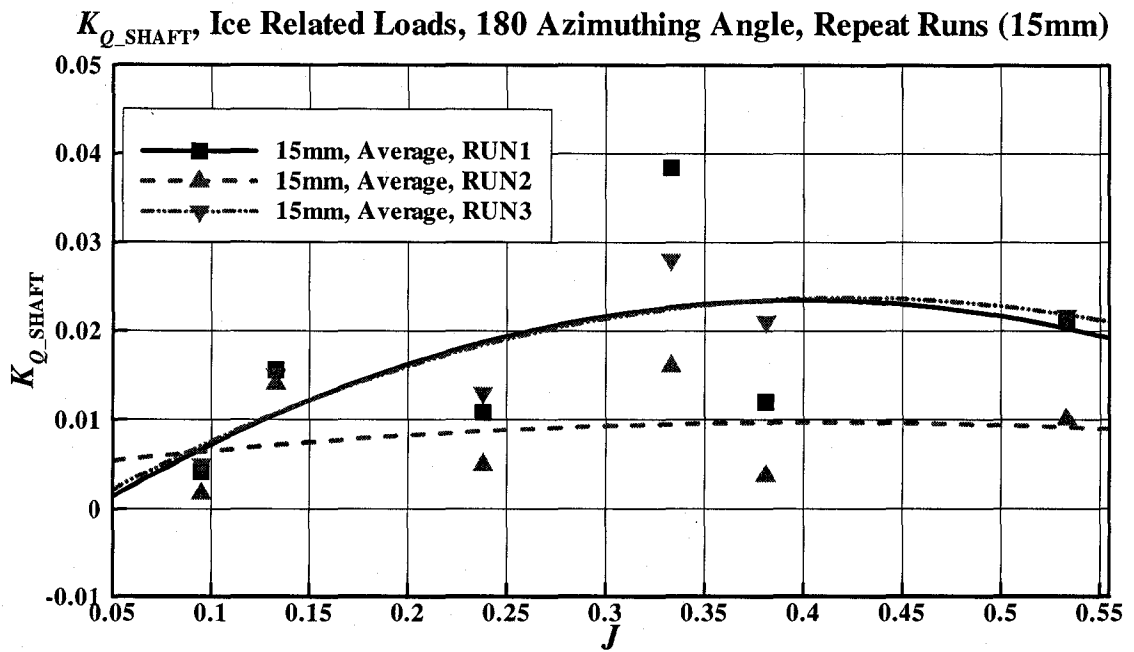
Figure C-23: K_{Q_SHAFT} vs. J, average ice related loads at 15mm depth of cut (repeated)
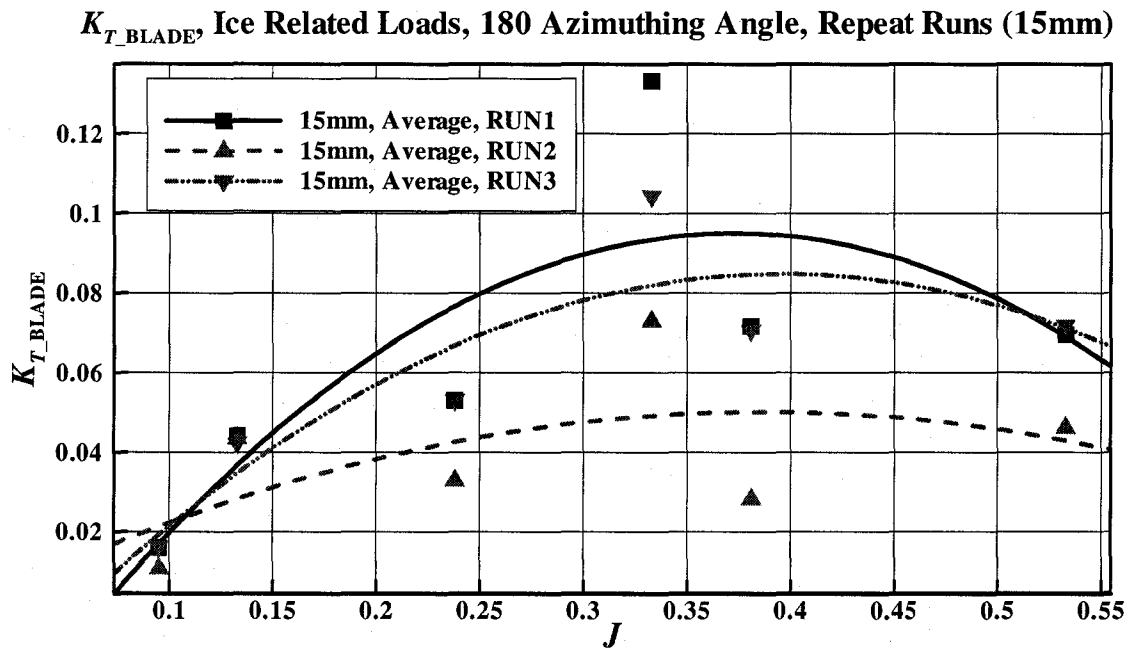
Figure C-24: K_{T_BLADE} vs. J, average ice related loads at 15mm depth of cut (repeated)
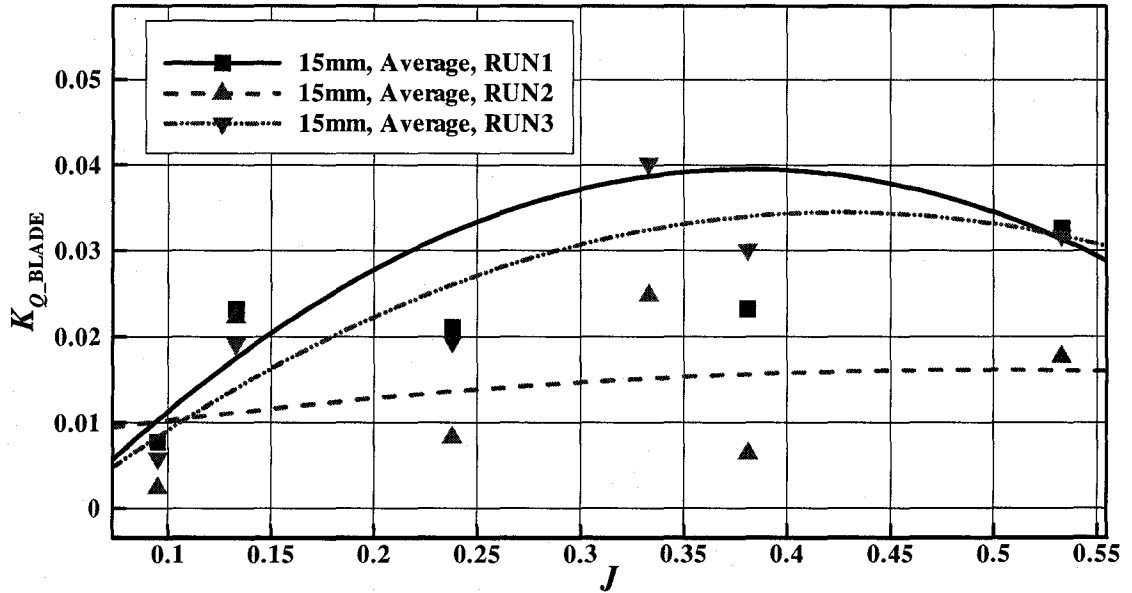
Figure C-25: K_{Q_BLADE} vs. J, average ice related loads at 15mm depth of cut (repeated)
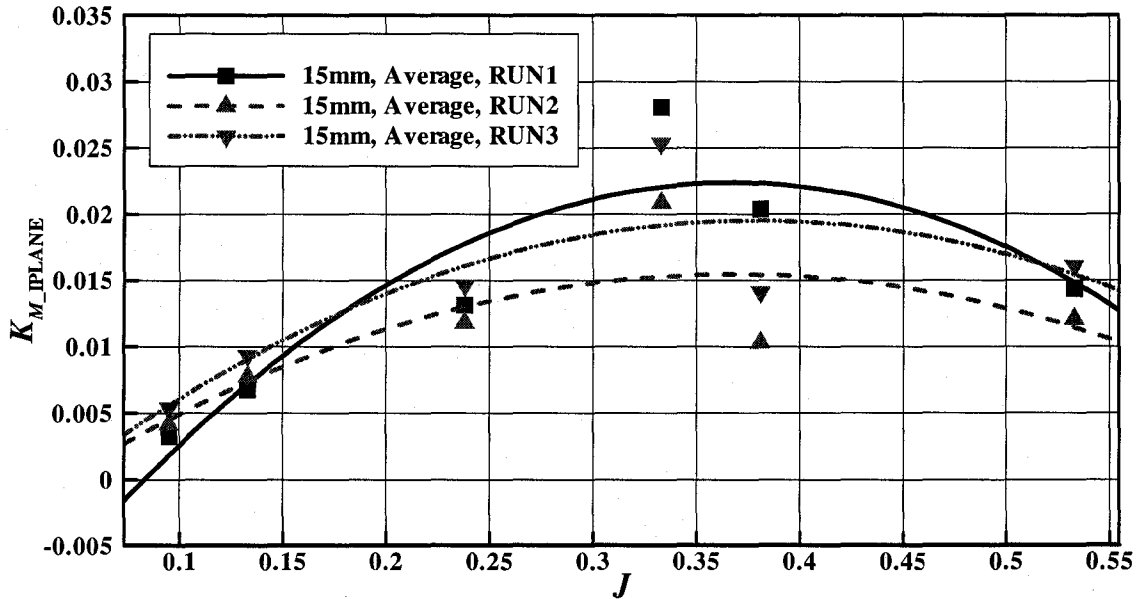
Figure C-26: K_{M_IPLANE} vs. J, average ice related loads at 15mm depth of cut (repeated)
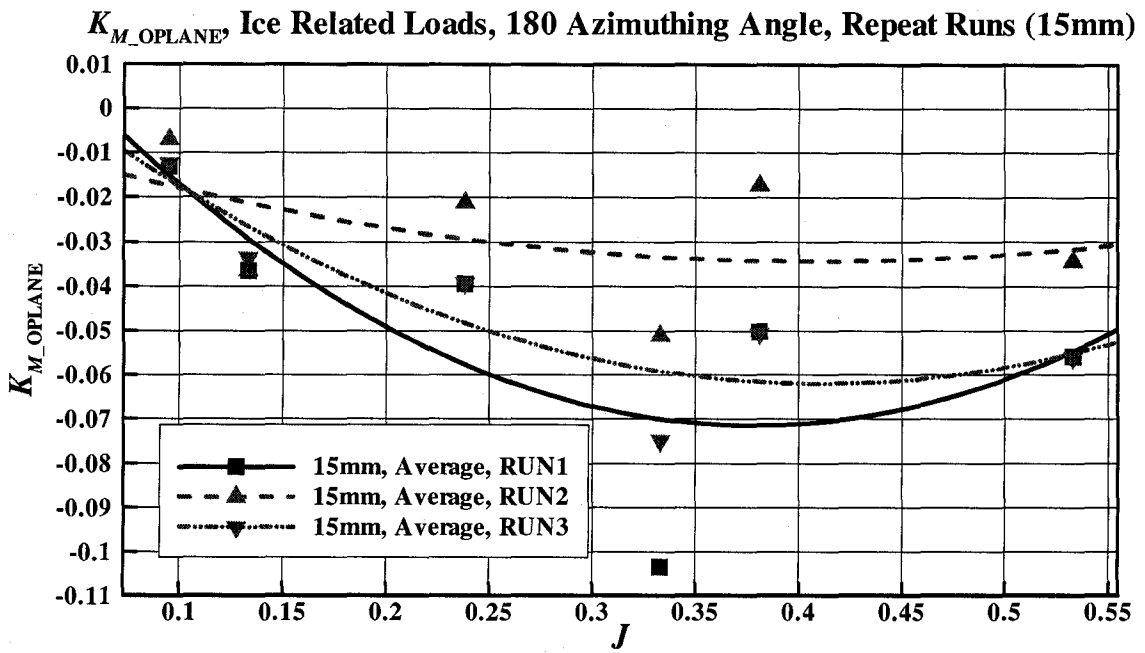
Figure C-27: K_{M_OPLANE} vs. J, average ice related loads at 15mm depth of cut (repeated)
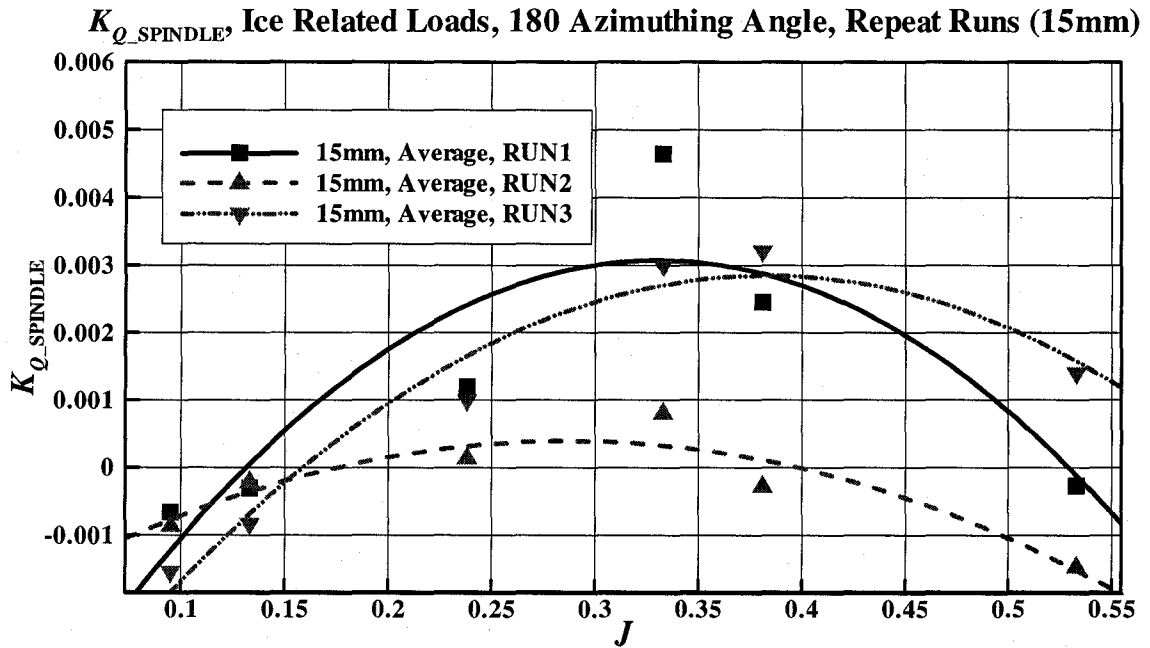
Figure C-28: $K_{Q\_SPINDLE}$ vs. J, average ice related loads at 15mm depth of cut (repeated)

212

Appendix D   Total Loads (Experimental Results in Ice Covered Water)

Experimental results for total loads in ice covered water are shown including unit thrust, transverse/vertical force on unit, shaft thrust/torque and blade thrust/torque with maximum, minimum, and average in tractor mode at the azimuthing angle of 180 degrees. The results are plotted with non-dimensional coefficients.
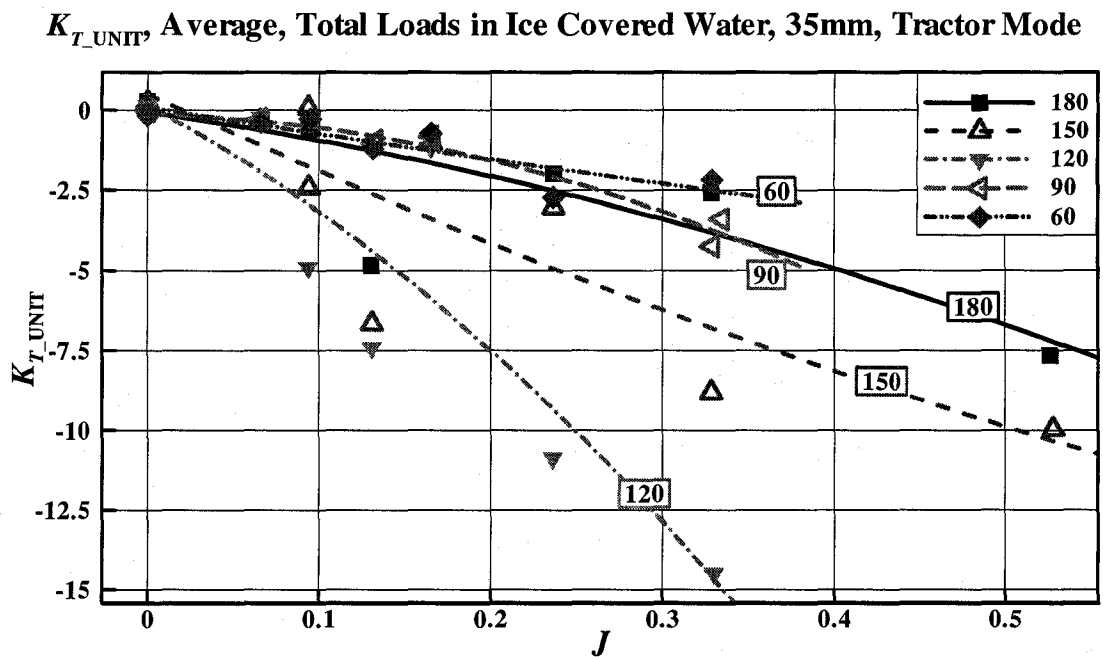
K_{T_UNIT}, Total Loads in Ice Covered Water, Tractor Mode, 180 Azimuthing Angle
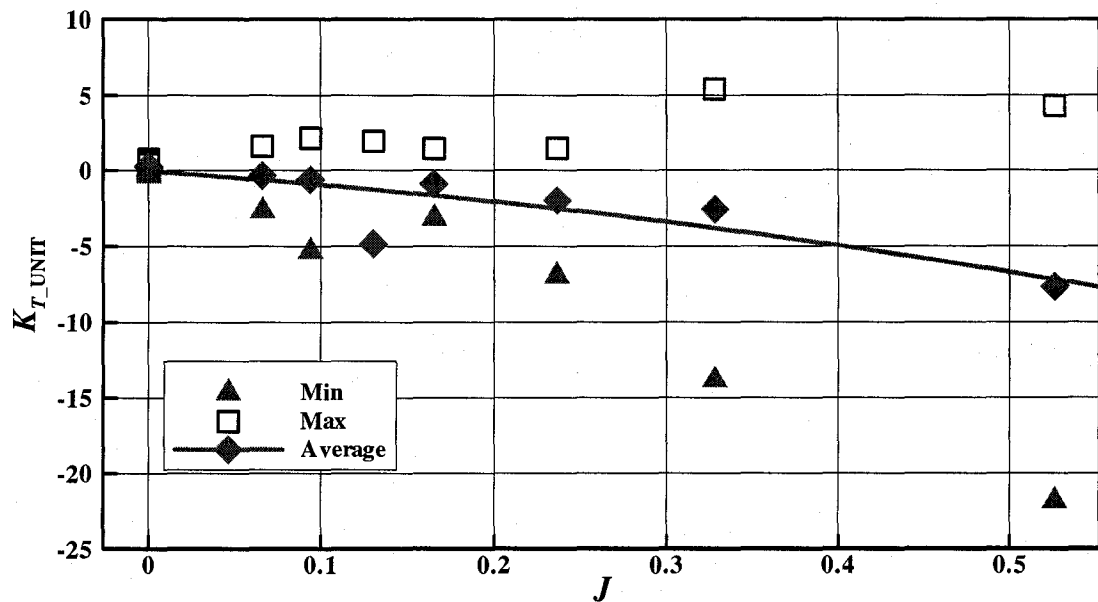
Figure D-1: K_{T_UNIT} vs. J, an azimuthing angle of 180 degrees in ice covered water

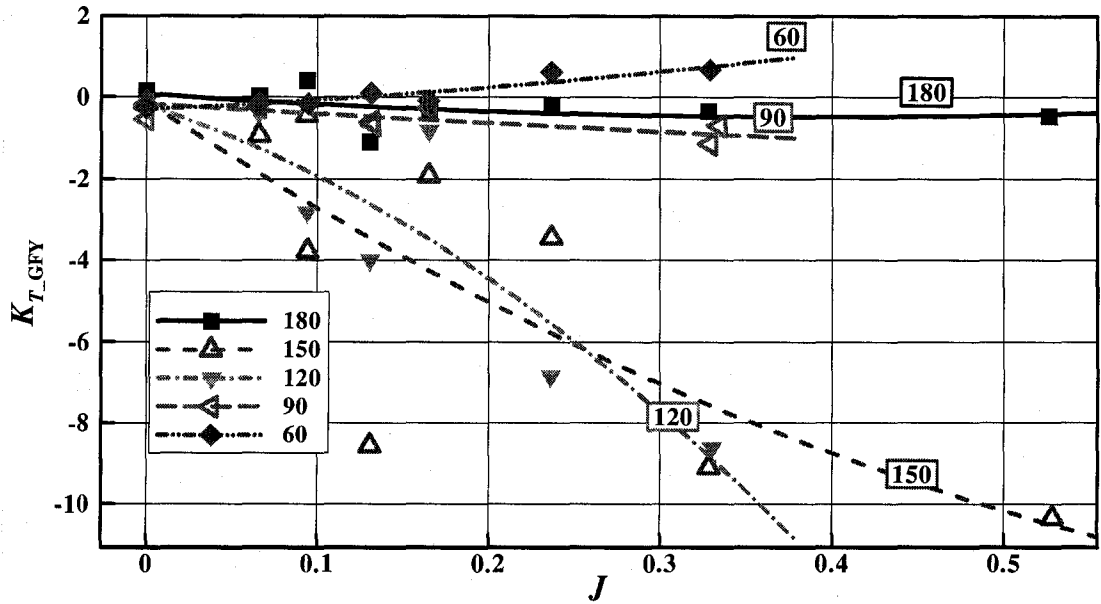K_{T_GFY}, **Total Loads in Ice Covered Water, Tractor Mode, 180 Azimuthing Angle**
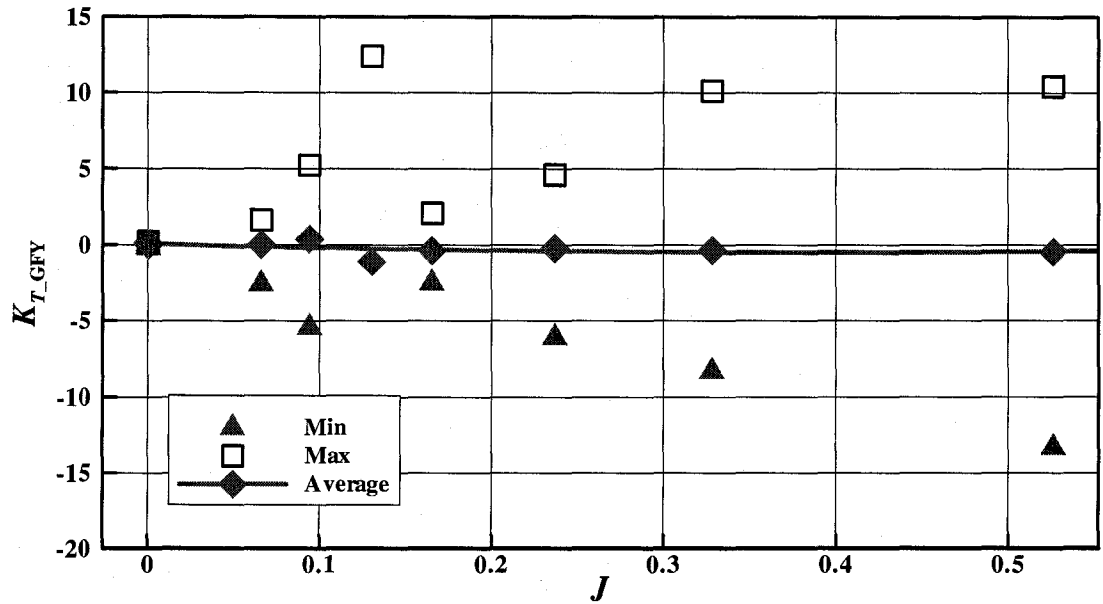
Figure D-2: K_{T_GFY} vs. J at an azimuthing angle of 180 degrees in ice covered water

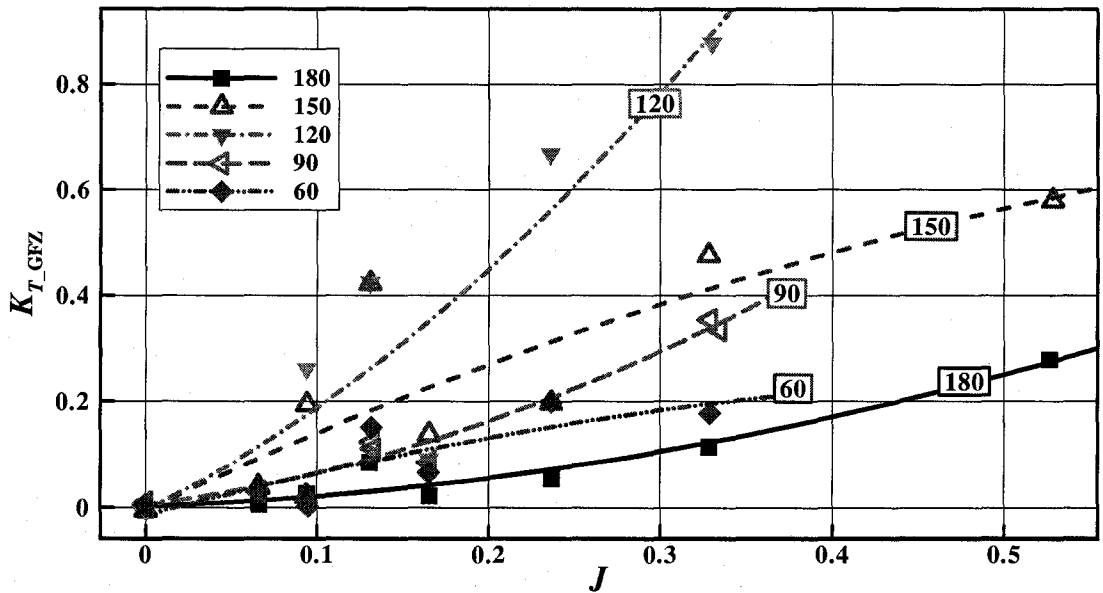K_{T_GFZ}, **Total Loads in Ice Covered Water, Tractor Mode, 180 Azimuthing Angle**
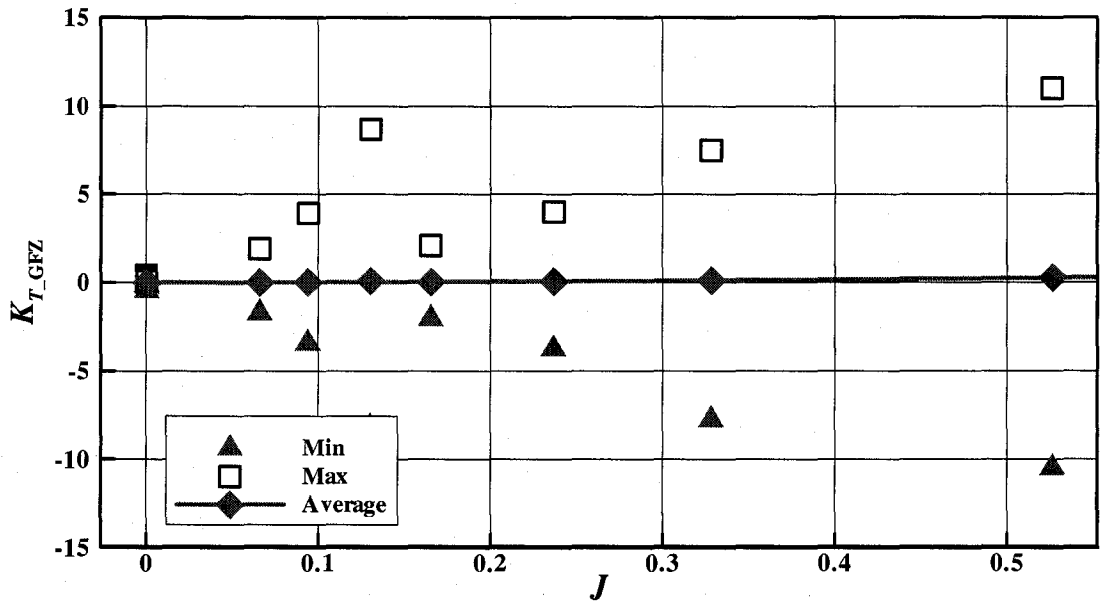
Figure D-3: K_{T_GFZ} vs. J at an azimuthing angle of 180 degrees in ice covered water

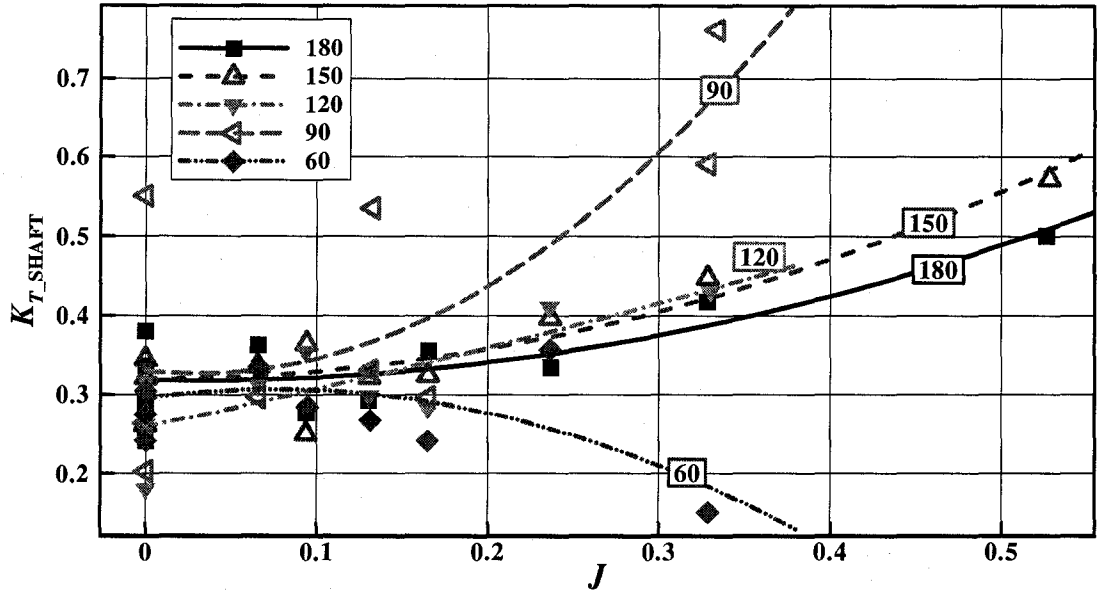K_{T_SHAFT}, **Total Loads in Ice Covered Water, Tractor Mode, 180 Azimuthing Angle**
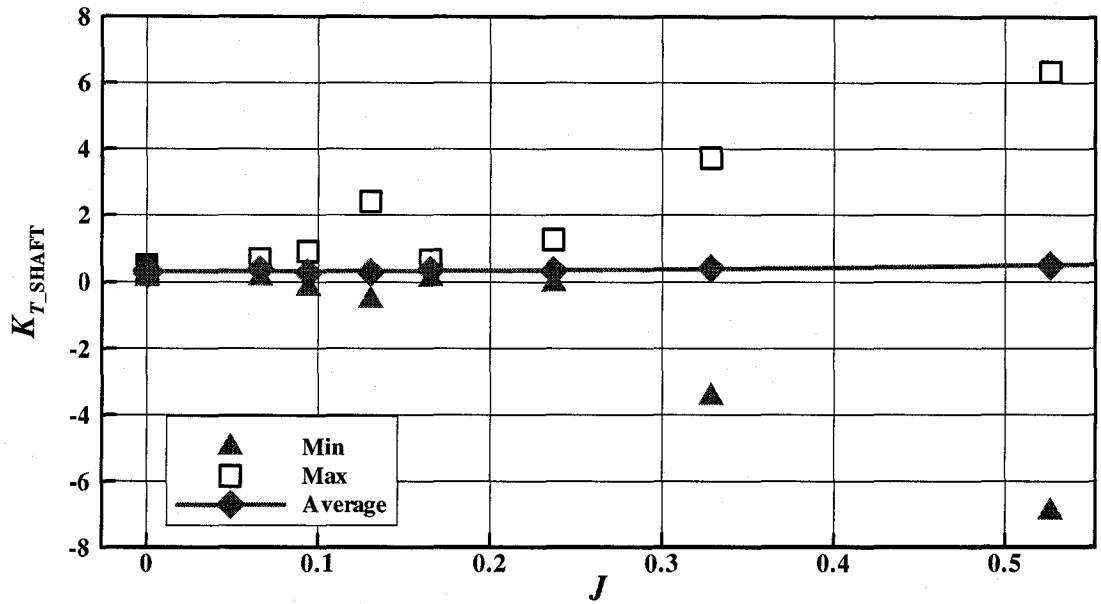
Figure D-4: K_{T_SHAFT} vs. J at an azimuthing angle of 180 degrees in ice covered water

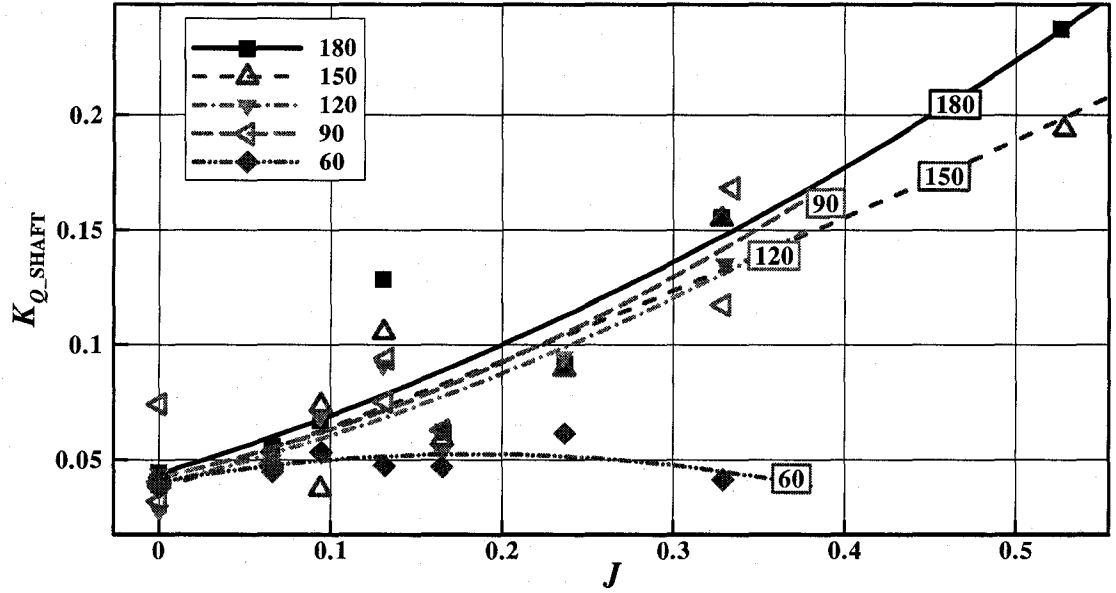K_{Q_SHAFT}, **Total Loads in Ice Covered Water, Tractor Mode, 180 Azimuthing Angle**
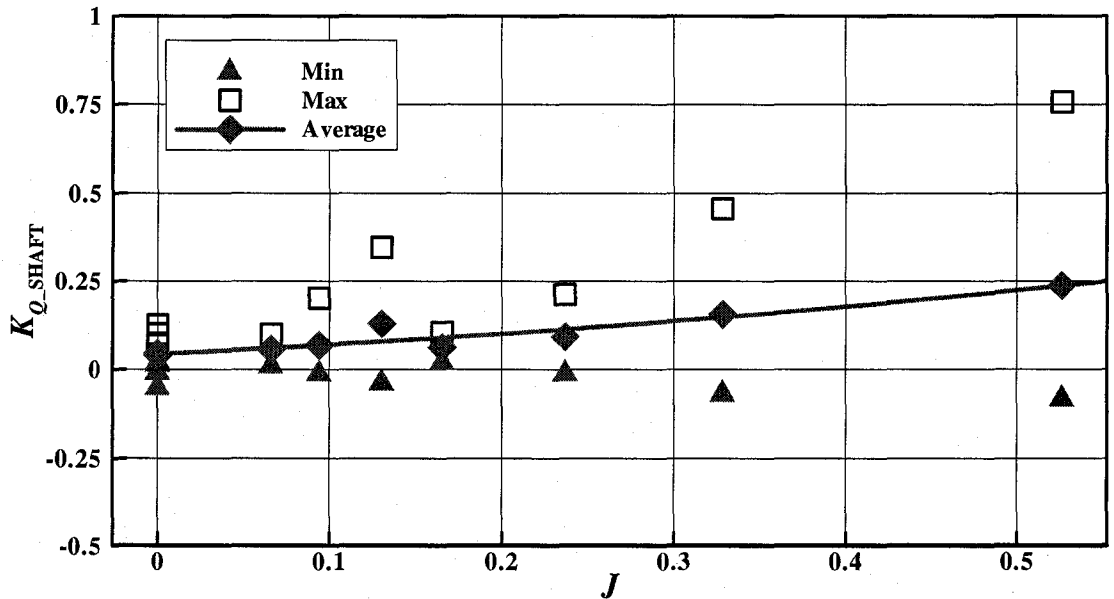
Figure D-5: K_{Q_SHAFT} vs. J at an azimuthing angle of 180 degrees in ice covered water

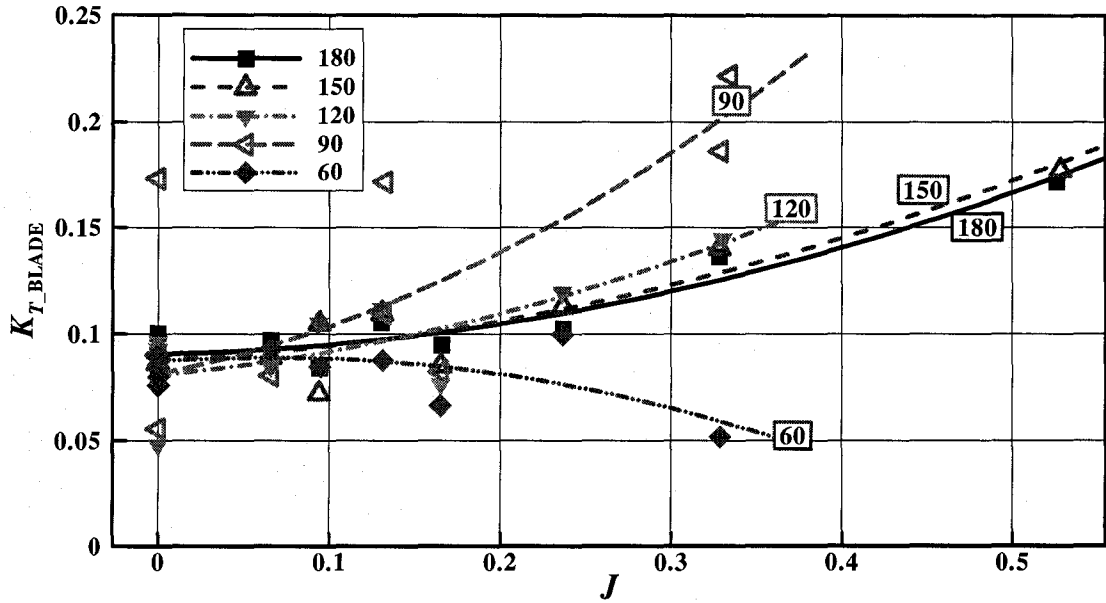K_{T_BLADE}, **Total Loads in Ice Covered Water, Tractor Mode, 180 Azimuthing Angle**
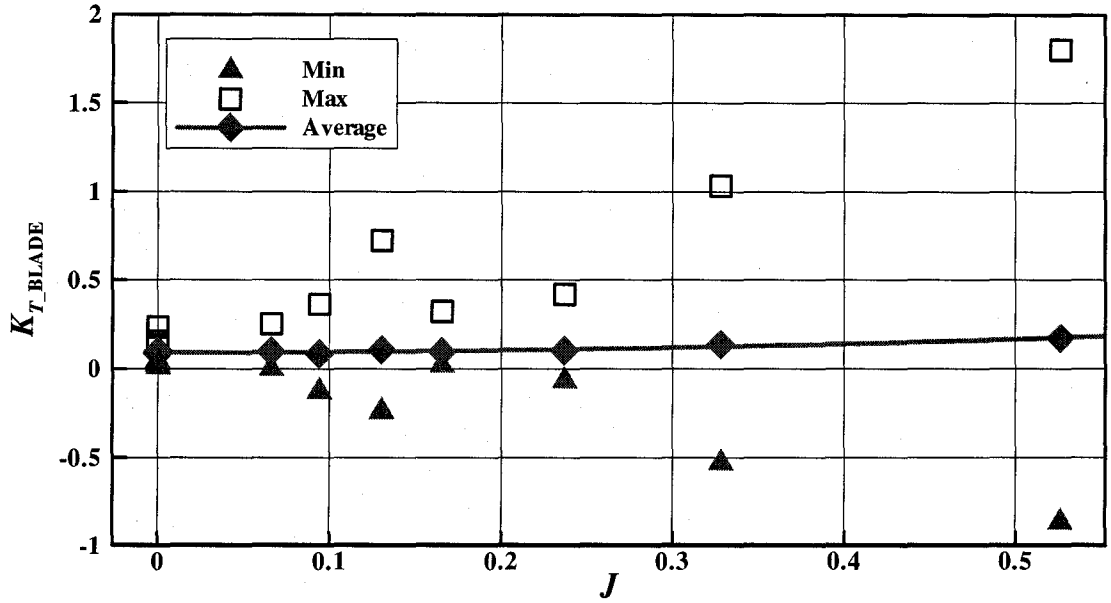
Figure D-6: K_{T_BLADE} vs. J at an azimuthing angle of 180 degrees in ice covered water

K_{Q_BLADE}, **Total Loads in Ice Covered Water, Tractor Mode, 180 Azimuthing Angle**
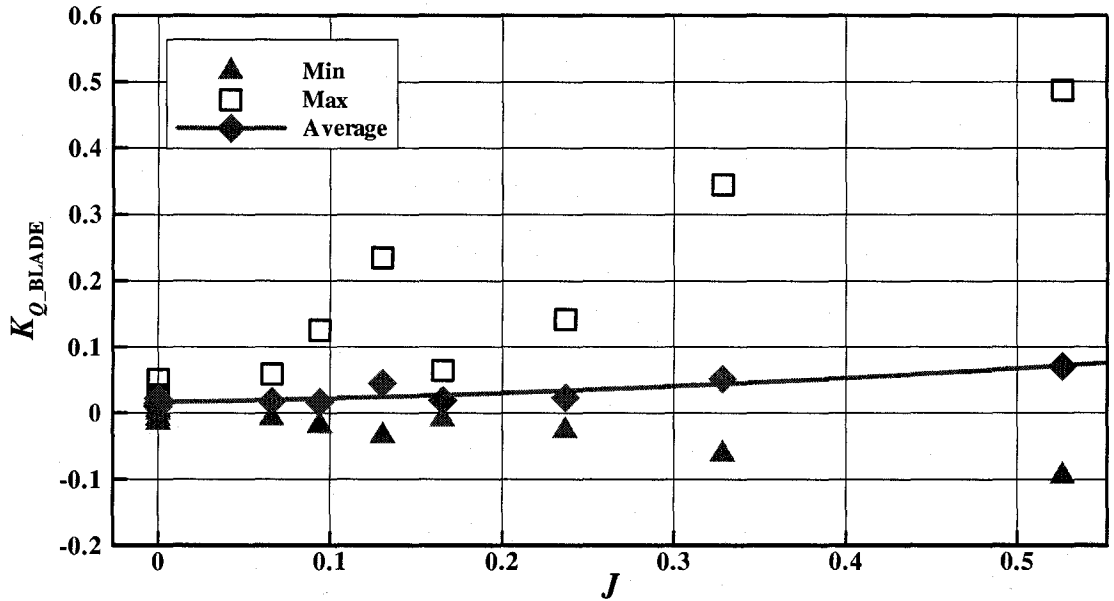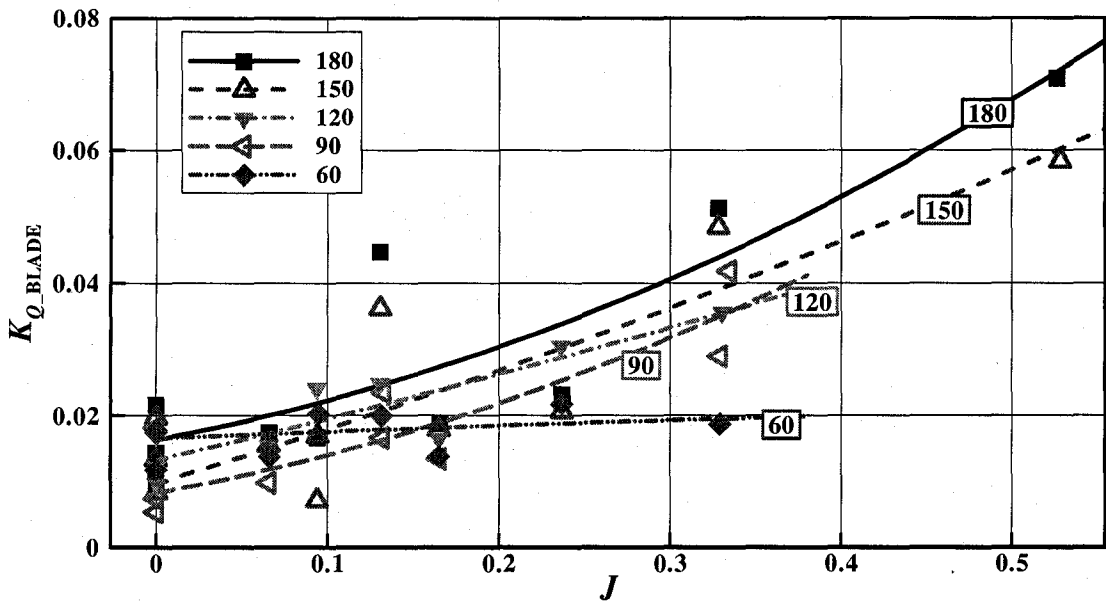

Figure D-7: K_{Q_BLADE} vs. J at an azimuthing angle of 180 degrees in ice covered water

D.1. Total Loads at Various Azimuthing Angles

Experimental results for the average total loads in ice covered water are shown including unit thrust, transverse/vertical force on unit, shaft thrust/torque and blade thrust/torque in tractor mode at various azimuthing angles (180-60 degrees). The results are plotted with non-dimensional coefficients.

K_{T_UNIT}, Average, Total Loads in Ice Covered Water, 35mm, Tractor Mode

Figure D-8: K_{T_UNIT} vs. J at an azimuthing angle of 180 ~ 60 degrees in ice covered water

K_{T_GFY}, Average, Total Loads in Ice Covered Water, 35mm, Tractor Mode

Figure D-9: K_{T_GFY} vs. J at an azimuthing angle of 180 ~ 60 degrees in ice covered water

K_{T_GFZ}, Average, Total Loads in Ice Covered Water, 35mm, Tractor Mode

Figure D-10: K_{T_GFZ} vs. J at an azimuthing angle of 180 ~ 60 degrees in ice covered water

Figure D-11: K_{T_SHAFT} vs. J at an azimuthing angle of 180 ~ 60 degrees in ice covered water

Figure D-12: K_{Q_SHAFT} vs. J at an azimuthing angle of 180 ~ 60 degrees in ice covered water

Figure D-13: K_{T_BLADE} vs. J at an azimuthing angle of 180 ~ 60 degrees in ice covered water

Figure D-14: K_{Q_BLADE} vs. J at an azimuthing angle of 180 ~ 60 degrees in ice covered water

220

D.2. Ice Covered water Characteristics for Tractor

Mode with Varied Azimuthing Angles

Experimental results for the average total loads in ice covered water are shown including shaft thrust/torque and efficiency on the shaft in tractor mode at various azimuthing angles (180-60 degrees). The results are plotted with non-dimensional coefficients.

Average, Ice Covered Water, Tractor Mode, 180 Azimuthing Angle
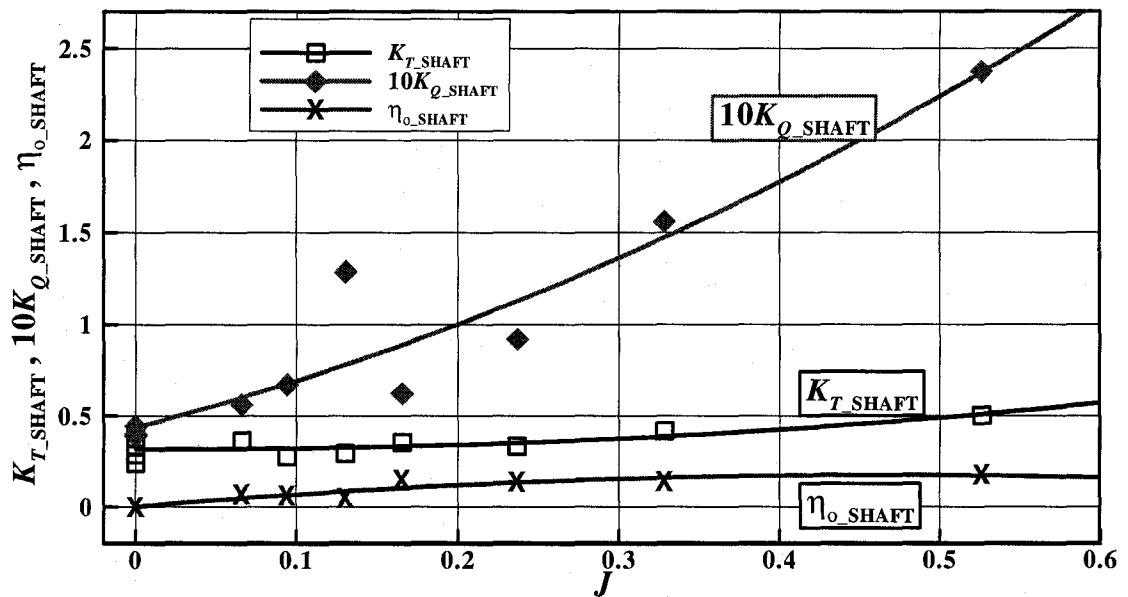
Figure D-15: Ice covered water characteristics for a tractor mode at an azimuthing angle of 180 degrees

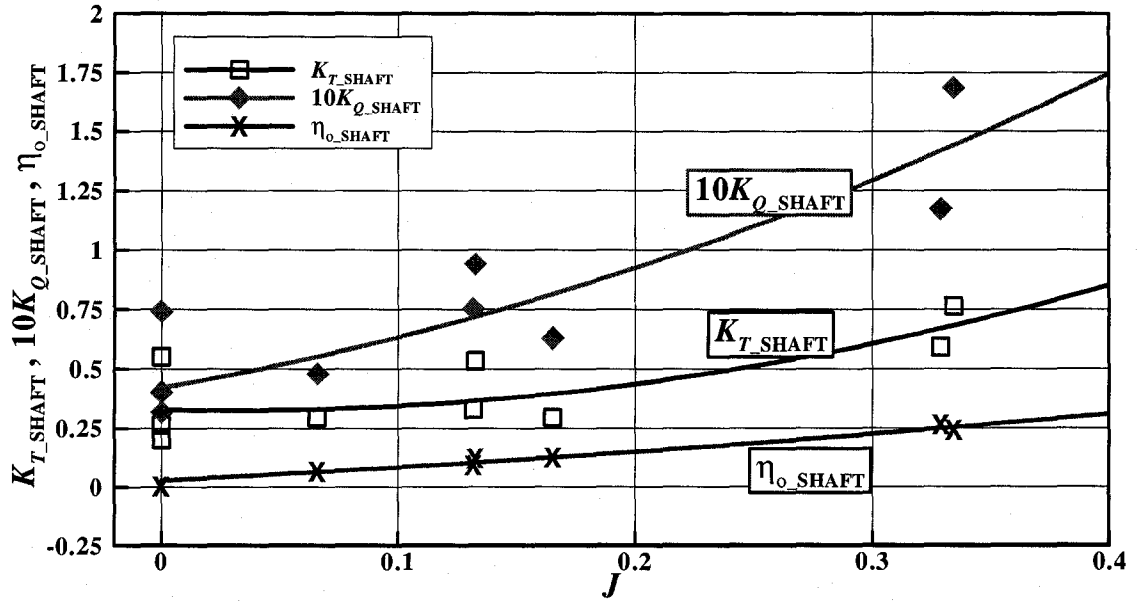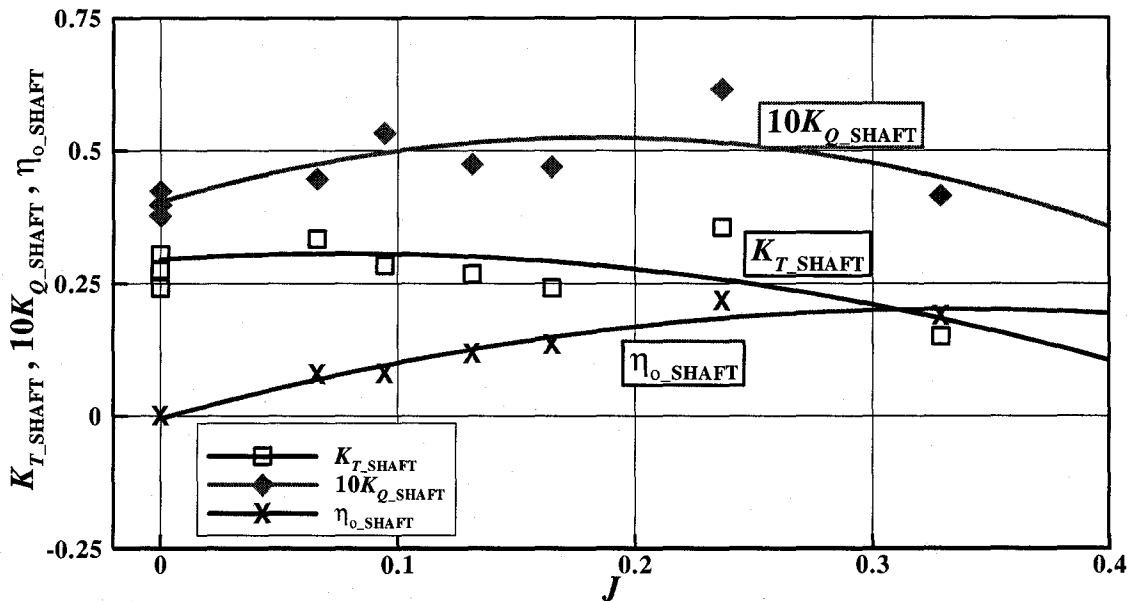**Average, Ice Covered Water, Tractor Mode, 150 Azimuthing Angle**
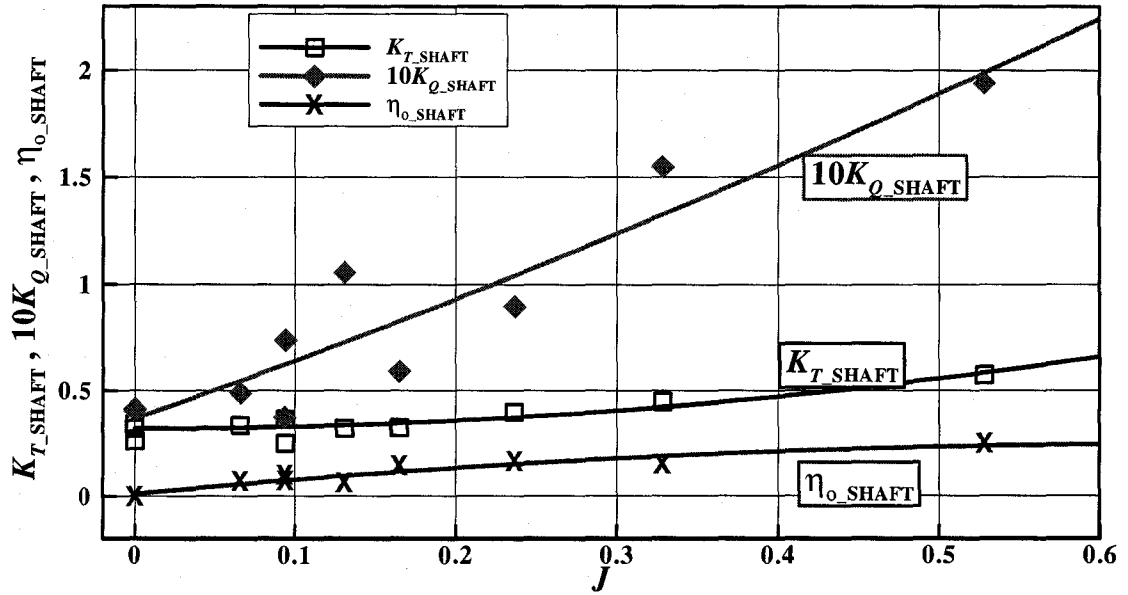
Figure D-16: Ice covered water characteristics for a tractor mode at an azimuthing angle of 150 degrees

Average, Ice Covered Water, Tractor Mode, 120 Azimuthing Angle
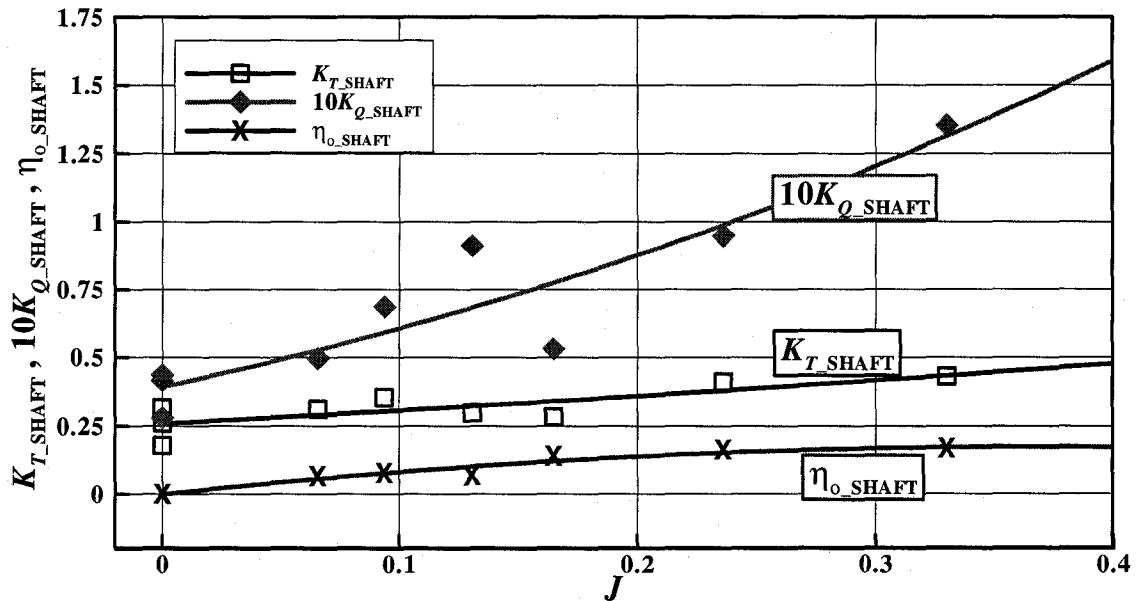
Figure D-17: Ice covered water characteristics for a tractor mode at an azimuthing angle of 120 degrees

222

Average, Ice Covered Water, Tractor Mode, 90 Azimuthing Angle

Figure D-18: Ice covered water characteristics for a tractor mode at an azimuthing angle of 90 degrees

Average, Ice Covered Water, Tractor Mode, 60 Azimuthing Angle

Figure D-19: Ice covered water characteristics for a tractor mode at an azimuthing angle of 60 degrees

Appendix E   Maximum Ice Related

Loads from PROPICE

Numerical results for the maximum ice related loads are shown including shaft

thrust/torque and blade thrust/torque in tractor mode at various azimuthing angles. The

results are plotted with non-dimensional coefficients.

Maximim K_{T_SHAFT}, Ice Related Loads, Tractor Mode, 180 Azimuthing Angle
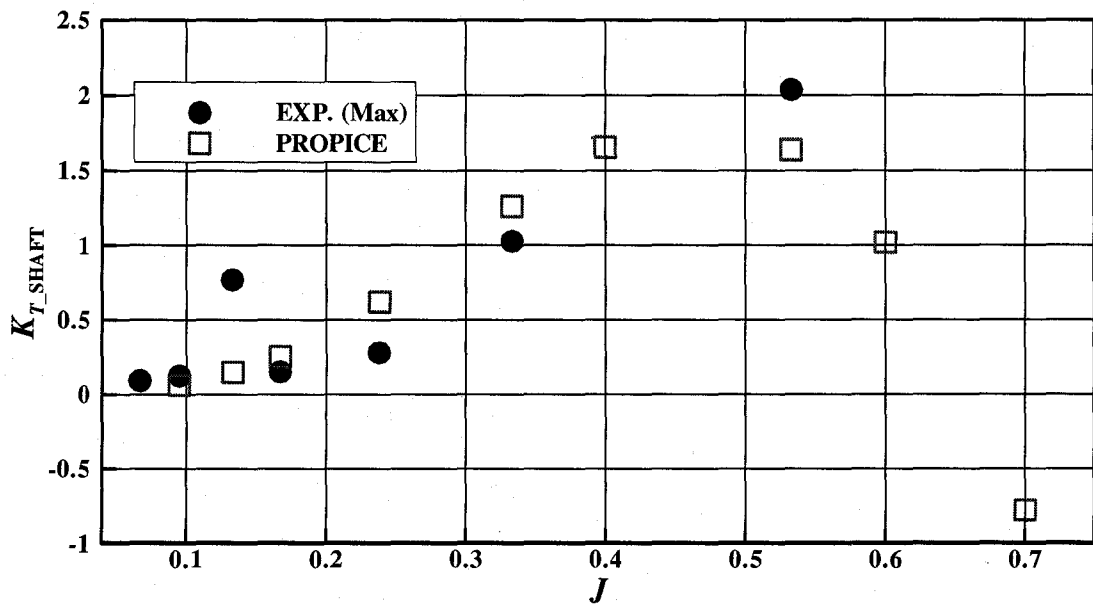
Figure E-1: Maximum K_{T_SHAFT} comparison (ice related loads, azimuthing angle of 180 degrees, 35 mm depth of cut)

Maximim K_{T_SHAFT}, Ice Related Loads, Tractor Mode, 150 Azimuthing Angle
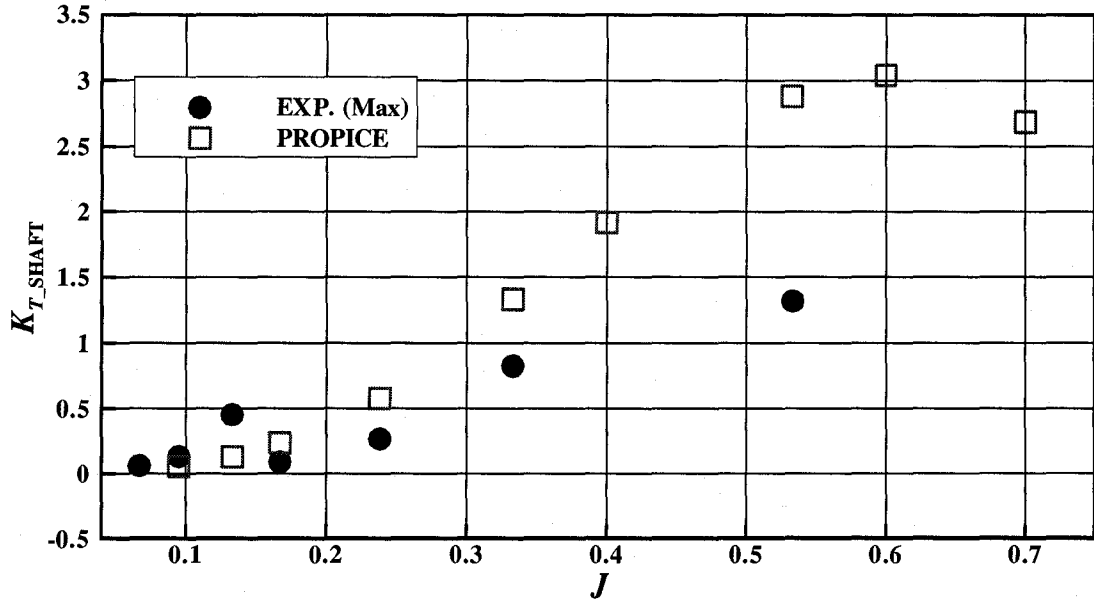
Figure E-2: Maximum K_{T_SHAFT} comparison (ice related loads, azimuthing angle of 150 degrees, 35 mm depth of cut)

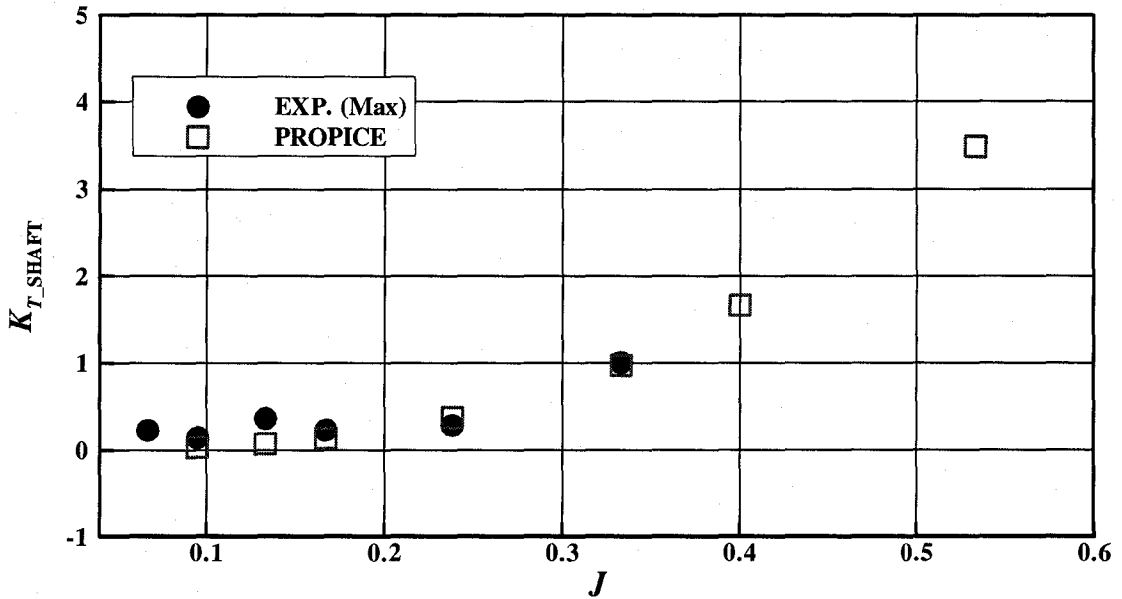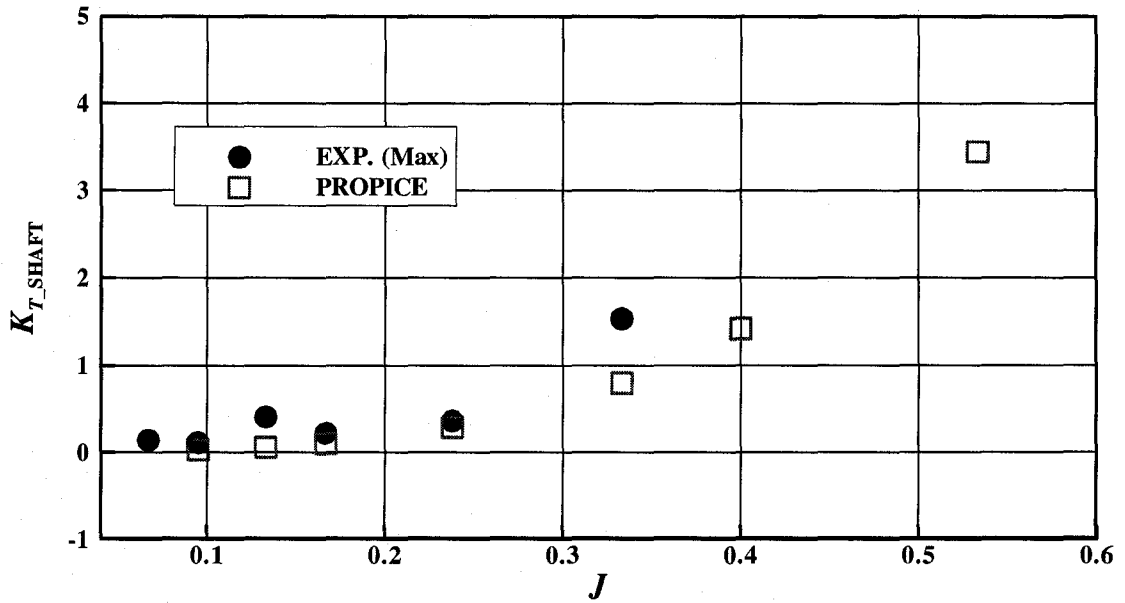**Maximum K_{T_SHAFT}, Ice Related Loads, Tractor Mode, 120 Azimuthing Angle**

Figure E-3: Maximum K_{T_SHAFT} comparison (ice related loads, azimuthing angle of 120 degrees, 35 mm depth of cut)

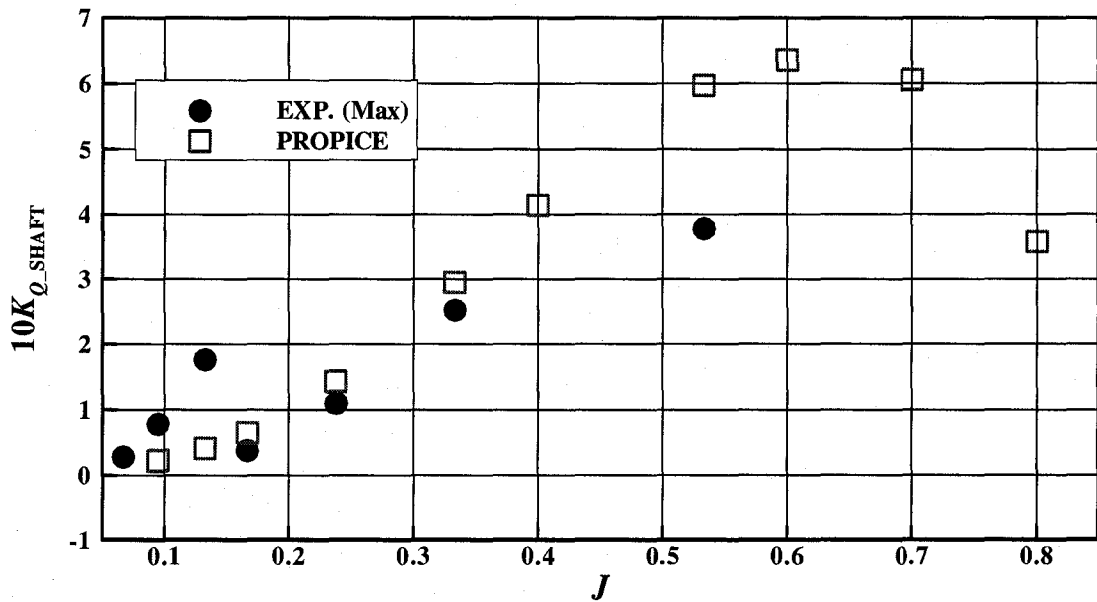**Maximum K_{T_SHAFT}, Ice Related Loads, Tractor Mode, 90 Azimuthing Angle**

Figure E-4: Maximum K_{T_SHAFT} comparison (ice related loads, azimuthing angle of 120 degrees, 35 mm depth of cut)

Maximim $10K_{Q\_SHAFT}$, Ice Related Loads, Tractor Mode, 180 Azimuthing Angle

Figure E-5: Maximum $10K_{Q\_SHAFT}$ comparison (ice related loads, azimuthing angle of 180 degrees, 35 mm depth of cut)

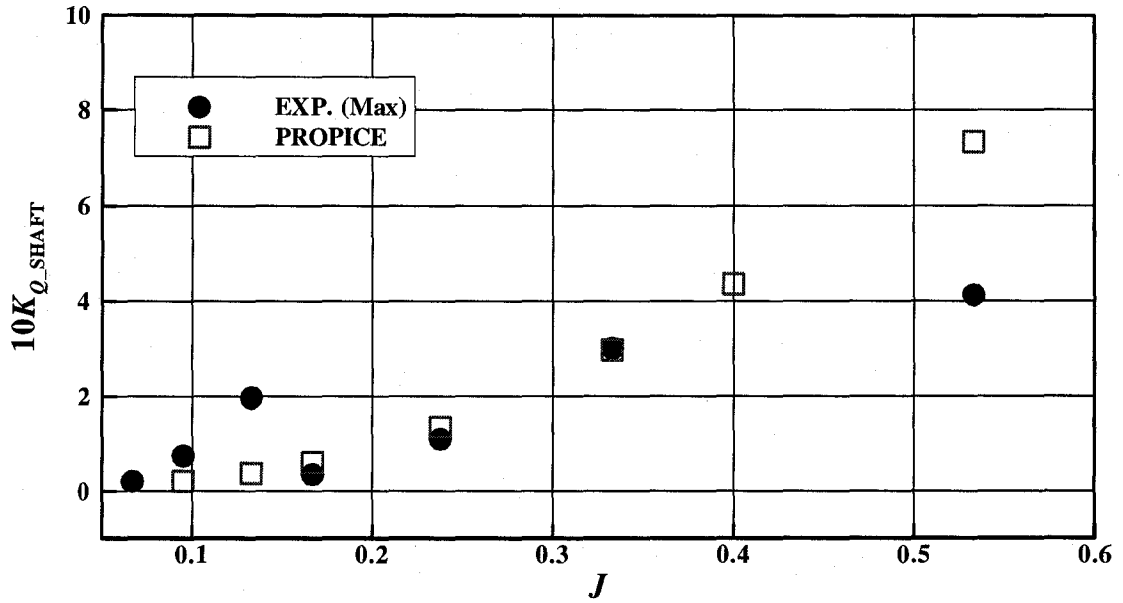**Maximum $10K_{Q\_SHAFT}$, Ice Related Loads, Tractor Mode, 150 Azimuthing Angle**

Figure E-6: Maximum $10K_{Q\_SHAFT}$ comparison (ice related loads, azimuthing angle of 150 degrees, 35 mm depth of cut)

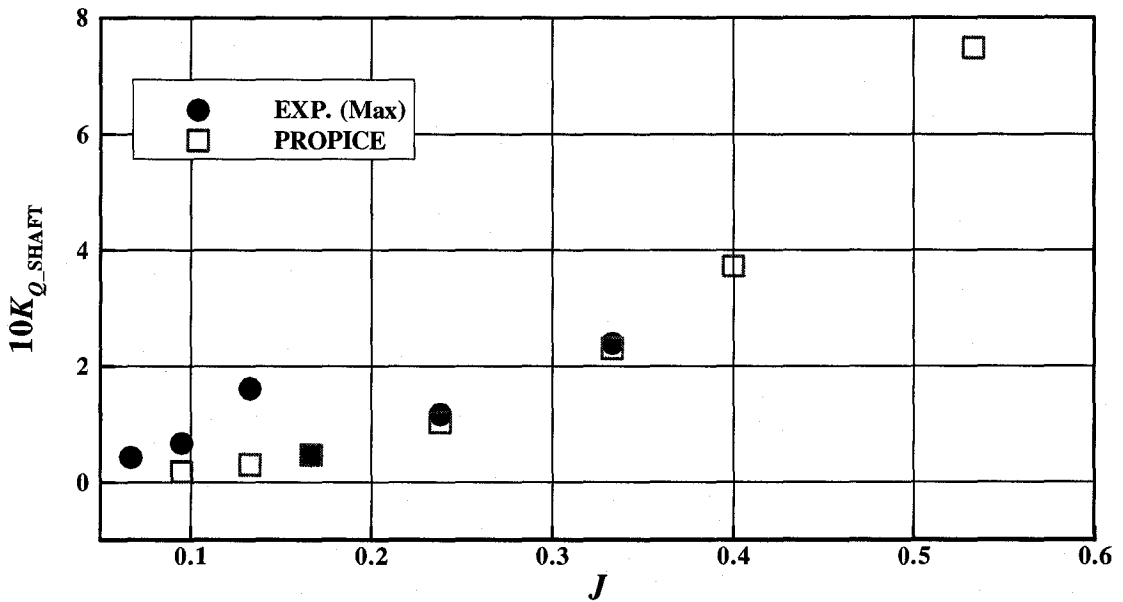**Maximum $10K_{Q\_SHAFT}$, Ice Related Loads, Tractor Mode, 120 Azimuthing Angle**

Figure E-7: Maximum $10K_{Q\_SHAFT}$ comparison (ice related loads, azimuthing angle of 120 degrees, 35 mm depth of cut)

Maximum $10K_{Q\_SHAFT}$, Ice Related Loads, Tractor Mode, 90 Azimuthing Angle
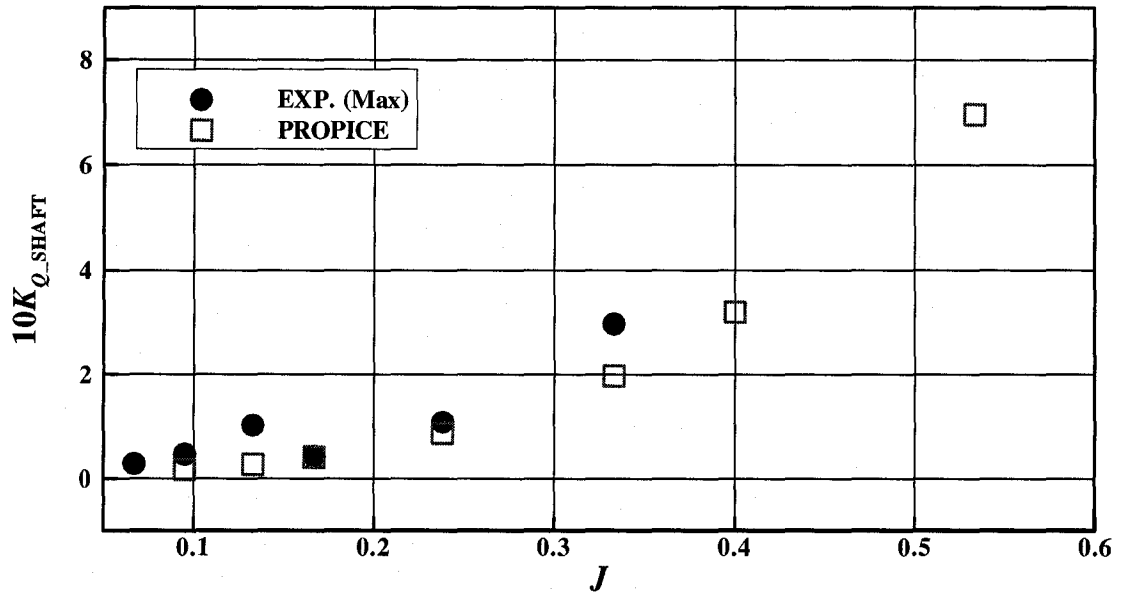
Figure E-8: Maximum $10K_{Q\_SHAFT}$ comparison (ice related loads, azimuthing angle of 120 degrees, 35 mm depth of cut)